

7-1-2016

COMPUTER-AIDED QUANTITATIVE EARLY DIAGNOSIS OF DIABETIC FOOT

Viktor Chekh

Follow this and additional works at: https://digitalrepository.unm.edu/cs_etds

Recommended Citation

Chekh, Viktor. "COMPUTER-AIDED QUANTITATIVE EARLY DIAGNOSIS OF DIABETIC FOOT." (2016).
https://digitalrepository.unm.edu/cs_etds/75

This Dissertation is brought to you for free and open access by the Engineering ETDs at UNM Digital Repository. It has been accepted for inclusion in Computer Science ETDs by an authorized administrator of UNM Digital Repository. For more information, please contact disc@unm.edu.

Viktor Chekh

Candidate

Computer Science

Department

This dissertation is approved, and it is acceptable in quality and form for publication:

Approved by the Dissertation Committee:

Shuang Luan, Chairperson

Trilce Estrada-Piedra

Yin Yang

Peter Soliz

**COMPUTER-AIDED QUANTITATIVE EARLY DIAGNOSIS
OF DIABETIC FOOT**

by

VIKTOR CHEKH

Radio Engineer
Kiev Polytechnical Institute
Kiev, USSR (now Ukraine). 1986
Master of Science in Electrical and Computer Engineering
University of New Mexico
Albuquerque, NM, USA. 2008

DISSERTATION

Submitted in Fulfillment of the
Requirements for the Degree of

**Doctor of Philosophy
in
Computer Science**

The University of New Mexico
Albuquerque, New Mexico

July, 2016

DEDICATION

In sweet memory of my parents Louisa and Yuri.

ACKNOWLEDGEMENTS

I want to acknowledge all my collaborators and advisors for this research that include: Dr. Pete Soliz, VisionQuest Biomedical LLC, Prof. Phil Heintz, UNM Radiology Department, Prof. Marc Burge, UNM Internal Medicine Department, Mr. Greg Iven, UNM Computer Science Graduate Student, Prof. Nancy Kanagy, UNM Cell Biology and Physiology Department, Prof. Majeed Hayat, UNM ECE Department, Dr. Simon Barriga, VisionQuest Biomedical, Dr. Gilberto Zamora, VisionQuest Biomedical, Mr. Caesar Carranza, VisionQuest Biomedical, Ms. Ana Edwards, VisionQuest Biomedical, Miss. Elizabeth McGrew, VisionQuest Biomedical LLC, and last but not least, Prof. Shuang (Sean) Luan, my PhD advisor of UNM Computer Science Department.

Specially, I'd like to mention that Dr. Peter Soliz, for his pioneering idea of using infrared thermography to measure temperature differential as a means for diagnosing diabetic foot, his constructive criticism and inspiring suggestion throughout the course of this research, and his dedication as a subject for the experimental aspects of this research. His feet have been submerged into various degrees of cold water for over 30 times!

I also want to acknowledge my PhD defense committee that includes Prof. Shuang Luan, Dr. Pete Soliz, Prof. Trilce Estrada and Prof. Yin Yang. Prof. Phil Heintz served on my proposal defense committee before his retirement.

I would like to take this opportunity to express my gratitude to my advisor, Prof. Shuang Luan for encouraging me and guiding me throughout the graduate studies. Discussions with him always inspired me. I appreciate the different opportunities that he gave me to explore my scientific interests.

Finally, I want to acknowledge the funding agencies that supported my PhD research. The research reported in this thesis was funded in part by National Institute of Diabetes and Digestive and Kidney Diseases Grant DK093192 and NSF Grant CBET-0853157. A significant portion of the research reported here was carried out at VisionQuest Biomedical LLC.

COMPUTER-AIDED QUANTITATIVE EARLY DIAGNOSIS OF DIABETIC FOOT

by

VIKTOR CHEKH

Radio Engineer
Kiev Polytechnic Institute
Kiev, USSR (now Ukraine). 1986

Master of Science in Electrical and Computer Engineering
University of New Mexico
Albuquerque, NM. 2008

Doctor of Philosophy in Computer Science
University of New Mexico
Albuquerque, NM. 2016

Abstract

Diabetes is an incurable metabolic disease characterized by high blood sugar levels. The feet of people with diabetes are at the risk of a variety of pathological consequences including peripheral vascular disease, deformity, ulceration, and ultimately amputation. The key to managing the diabetic foot is prevention and early detection. Unfortunately, current hospital centered reactive diabetes care and the availability of inadequate qualitative diagnostic screening procedures causes physicians to miss the diagnosis in 61% of the patients. We have developed a computer aided diagnostic system for early detection of diabetic foot. The key idea is that diabetic foot exhibits significant neuropathic and vascular damages. When a diabetic foot is placed under cold stress, the thermal recovery

will be much slower. This thermal recovery speed can be a quantitative measure for the diagnosis of diabetic foot condition. In our research, thermal recovery of the feet following cold stress is captured using an infrared camera. The captured infrared video is then filtered, segmented, and registered. The temperature recovery at each point on the foot is extracted and analyzed using a thermal regulation model, and the problematic regions are identified. In this thesis, we present our research on the following aspects of the developed computer aided diagnostic systems: subject measurement protocols, a trustful numerical model of the camera noise and noise parameter estimations, infrared video segmentation, new models of thermal regulations, thermal patterns classifications, and our preliminary findings based on small scale clinical study of about 40 subjects, which demonstrated the potential the new diagnostic system.

#	Abbreviators	Meaning
1.	IR	Infrared (meaning thermal infrared as default)
2.	NIR	Near infrared
3.	ROI	Region of interest
4.	[D]PN	[Diabetic] peripheral neuropathy
5.	ODE	Ordinary differential equation
6.	PDE	Partially differential equation
7.	FLIR	FLIR model SC 305 infrared camera
8.	Heimann	Heimann 32x31 infrared array module
9.	CCD	Charge-coupled device
10.	CMOS	Complementary metal–oxide–semiconductor
11.	FOV	Field of view
12.	LED	Light emission diode
13.	PCB	Printed circuit board
14.	BB	Black body
15.	FIR	Finite impulse response (filter)
16.	ACF	Autocorrelation function
17.	CCF	Cross-correlation function
18.	MS	Microsoft (company name)
19.	VBA	Visual basic for application (programming language)
20.	RGB	Red-green-blue (color space, visible band)
21.	2D (3D)	Two-dimensional (three-dimensional)

22.	GUI	Guided user interface
23.	CAD	Computer-aided diagnosis
24.	LF (HF)	Low (high) frequency
25.	PCA	Principal component analysis
26.	ICA	Independent component analysis
27.	CIVD	Cold-induced vasodilation

Content

INTRODUCTION.....	1
CHAPTER 1 THE EXPERIMENT.....	5
1.1 THE STANDARD PROTOCOL.....	5
1.2 THE STANDARD PROTOCOL.....	8
1.3 SUMMARY.....	9
CHAPTER 2 THE CAMERAS.....	10
2.1 GENERAL REQUIREMENT	10
2.2 FLIR SC305	11
2.3 HEIMANN ARRAY MODULE	11
2.4 LOW COST IR DIAGNOSTIC SYSTEM	12
2.4.1 Power management.....	15
2.4.2 Impact of field of view.....	15
2.5 COMPARISON OF CAMERAS.....	16
2.6 CALIBRATION	20
2.7 NOISE OF THE EXPERIMENT	22
2.7.1 Separation of the noise.....	25
2.7.2 Noise correlation between the pixels of different cameras	30

2.7.3	Investigation of the noise stationarity	34
2.7.4	Ergodicity of the noise	47
2.7.5	The numerical model	47
CHAPTER 3	BASIC DATA PROCESSING.....	49
3.1	CONVERSION TO COMMON DATA FORMAT	50
3.2	FILTERING	50
3.2.1	Adaptive spatial filtering.....	50
3.2.2	ROIs	51
3.3	TEMPORAL REGISTRATION (SYNCHRONIZATION).....	53
3.4	SPATIAL REGISTRATION AND TRACKING.....	56
3.4.1	Problems and requirements.....	56
3.4.2	Affine model of the spatial feet deformation.....	56
3.4.3	Foot segmentation on the first video frame	58
3.4.4	Registration and tracking via detected markers	58
3.4.5	The cross-correlation registration and tracking	60
3.4.6	Comparison of the methods	61
CHAPTER 4	HEAT TRANSFER MODEL	65
4.1	MOTIVATION	65
4.2	THE BIO-HEAT TRANSFER EQUATION	68
4.3	THE MODEL OF THERMOREGULATION.....	71
4.3.1	The control theory approach	71

4.3.2	The control system of the second order	75
4.3.3	The control system of the first order.....	84
4.3.4	Comparison of the obtained models	88
4.3.5	Uniqueness and fullness of the obtained set of the models	91
4.4	THE BIOLOGICAL SENSE OF THE THERMOREGULATION MODELS	96
4.4.1	The biological mechanisms of human thermoregulation.....	96
4.4.2	The correspondence between the biological mechanisms and the analytical models of thermoregulation	98
4.5	ACCURACY OF THE MODEL OF THERMOREGULATION	100
CHAPTER 5 HEAT TRANSFER DURING THE COOLING PHASE.....		104
5.1	MOTIVATION.....	104
5.2	THE THERMOREGULATION MODEL OF THE COOLING PHASE.....	105
5.2.1	General solution.....	105
5.2.2	The thermoregulation term.	113
5.2.3	Important special cases.	114
5.3	EXPERIMENTAL RESULTS.....	116
5.3.1	Model verification for the recovery phase	116
5.3.2	Application of the general model to both cooling phase and recovery phase	118
5.4	PRACTICAL RECOMMENDATIONS.....	127
5.5	CONCLUSION.....	128

CHAPTER 6	CLASSIFICATION.....	129
6.1	MOTIVATION.....	129
6.2	THE FIRST NAÏVE EXPECTATION: SLOWER RECOVERY OF PN COMPARING TO THE CONTROL GROUP	130
6.3	THE PARAMETRIC CLASSIFICATION.....	133
6.3.1	Amplitude of regulation.....	133
6.3.2	Inversed speed of regulation	135
6.3.3	Advantages and disadvantages	136
6.4	THE “TAKE ATTENTION” SUPPLEMENTARY APPROACH.	137
6.4.1	Delay of capturing.....	137
6.4.2	Parameters of the cooling phase.	137
6.4.3	Parameters related to bounds.	138
6.4.4	Interpolation quality parameters.	139
6.5	RESULTS OF THE PARAMETRIC CLASSIFICATION.	139
6.5.1	Exclusion of the outliers.	141
6.5.2	Classification by the thermoregulation model parameters.....	143
6.6	THE PATTERN RECOGNITION APPROACH	155
6.7	THE FOOT SEGMENTATION APPROACH.....	161
6.7.1	Segmentation.....	161
6.7.2	Labeling	167
CHAPTER 7	CONCLUSIONS AND FUTURE WORK.....	171

7.1	CONCLUSIONS	171
7.2	FUTURE WORK.....	173
	REFERENCES.....	174

Introduction

Sing, goddess, the anger of Peleus' son Achilles and its devastation...

Homer. Iliad.

The lock has been filled with melted bronze. Who knows what's in there?

Shi Nai'an, and Luo Guanzhong. Water Margin.

According to the Center for Disease Control (CDC), diabetes afflicts an estimated 171 million people worldwide. Diabetes patients are at risk of a wide range of complications including heart disease, kidney disease (nephropathy), ocular diseases (diabetic retinopathy), and diabetic peripheral neuropathy (hereafter DPN), i.e., nerve damage [1][2][3]. Neuropathy most often affects in the lower extremities (i.e., leg and foot) and can lead to serious pathological consequences. In this research, we focus on the feet of diabetes patients, which are at risk of peripheral neuropathy. It is estimated that 50% of diabetes have some degree of neuropathy. Fifteen percent of them will develop a foot ulcer during the lifetime [2][4][5][6]. Foot ulcers are the main cause for 85% of lower extremity amputation in patients with diabetes [7][8][9][10].

In the US, diabetes afflicts approximately 25.8 million Americans (8.3% of US population) [11]. The cost for managing diabetes was 245 Billion USD in 2012, of which one third can be attributed to diabetic foot. The long-term management of diabetes has become one of the greatest challenges and burdens of the US Health Care System. The goal of this research is to develop a computer aided diagnostic system for the early detection

and prevention of diabetic foot conditions.

Studies have shown that neuropathy is a cause for the impairment of blood flow in the diabetic foot [12][13]. Patients with long-standing neuropathy have poor regulatory mechanisms and microcirculatory dysfunction [14][15]. This condition is linked to neuropathic complications that alter the regulatory mechanisms controlling blood flow in the extremities (e.g., foot), which is confirmed by laser Doppler studies [16][17][18].

The key to preventing the advanced stages of DPN is early detection and intervention. Traditional techniques for diagnosing peripheral neuropathy are mostly based on sensory examination. Examples of these tests include Semmes-Weinstein monofilament testing [19], i.e., a monofilament wire is used to exert about 10 gram of force against a location on plantar surface of the foot for 1 second, tuning fork [20][21], pinprick sensation [22], vibration perception threshold [23][24], just to name a few. Most of these tests are simple and noninvasive and aim to determine if a patient has lost sensation in the feet. The patients who for example, cannot reliably detect the location of a monofilament are considered to have lost sensation and have developed neuropathy. Many of these tests unfortunately present significant inter- and intra-observer variability. Studies have revealed that physicians may miss the diagnosis of diabetic peripheral neuropathy in as much as 61% of patients. A reliable and quantitative means for evaluating capillary function for early (possibly pre-clinical) diagnosis of peripheral neuropathy and the risk of foot ulcers are still lacking. A repeatable means for accurately measuring pre-clinical signs of peripheral neuropathy would reduce significantly the magnitude of morbidity from this disease.

We have developed a new system for early quantitative detection of diabetic neuropathy based on thermal imaging and bioinformatics techniques. The key to our system is to use infrared imaging to quantitatively measure the thermal response of the feet of diabetic patients following cold stress. The technique is based on the theory that neuropathy causes impairment of blood flow in the diabetic foot [13]. Patients with neuropathy will have poor thermoregulation [14]. However, unlike the previous attempts, which used thermal imaging to image diabetic foot [25][26][27][28][29], and focused on discovering skin/tissue temperature differences for individuals and spatial variations, we focused on the thermoregulation characteristics with respect to time following cold stimulus. The rationale for this, which has been hypothesized by a number of other investigators [30][31][32], is that with poor thermoregulation, a diabetic foot after being cooled or warmed should recover slower to the core body temperature.

In our new system, a dynamic technique has been employed to overcome the shortcomings of previous static thermal measurements. More specifically, a cold stimulus is first applied to the diabetic foot, which will trigger the thermal auto-regulation. The recovery of the foot to the core body temperature is then captured with a thermal imaging device. The thermal video is then processed and analyzed to produce a quantitative measure of the thermoregulation of the foot. The model parameters obtained are finally used to classify the two main categories of interests, i.e., diabetic patient with and without risk of peripheral neuropathy. It is also worthwhile to note that such studies have only been made possible in the recent decade with the availability of high resolution and high sensitivity portable thermal imaging devices. Unfortunately, even in present times these devices cannot be claimed as low cost ones. Thus, another goal we had during this research is to

develop a low cost medical embedded system that provides in-home, quantitative, objective and repeatable means for early detection of diabetic foot.

The research presented in this dissertation is multidisciplinary, and spans statistical physics, image processing, physiology and medicine, applied electronics, control theory, and of course, computer science as well. The rest of the work is organized as follows. [Chapter 1](#) describes our clinical experimental set up, which includes the IRB-approved patient study protocol and characteristics of the measuring devices. [Chapter 3](#) describes the preprocessing of the captured infrared video, registration of video frames and tracking of the feet. Chapter 4 presents our novel bio-heat transfer models based on thermoregulation for parameter extraction for the recovery phase. Chapter 5 is about the modeling of Heat transfer during the cooling phase extends the thermal model to the cooling phase of the experiment. Chapter 6 discusses different approaches of diagnosis and presents some classification results. [Chapter 7](#) concludes the thesis and discusses future work.

Chapter 1 The experiment

His hand automatically kept on making the dainty motion, practiced a thousand times over, of dunking the handkerchief, shaking it out, and whisking it rapidly past his face, and with each whisk he automatically snapped up a portion of scent-drenched air, only to let it out again with the proper exhalations and pauses. Until finally his own nose liberated him from the torture, swelling in allergic reaction till it was stopped up as tight as if plugged with wax. He could not smell a thing now, could hardly breathe.

Patrick Süskind, *The Perfume*.

1.1 The standard protocol

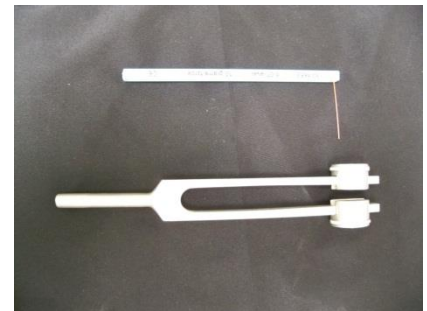
The general idea of the experiment is to take a thermal infrared video of the foot before and after the cold stress. The following equipment has been used for the experiment, see [Figure 1.1.](#) :

- A water basin for 2 gallons of cooled water with a digital thermometer for tracking the water temperature, [Figure 1.1.](#) .c)
- A chair
- A feet support.
- Infrared cameras (see detail described below). (We used a Panasonic RGB camera during the early stage of the experiments. We have later on decided that the RGB video is not useful to our purpose.)

- The tripod[s] for the cameras.
- Semmes-Weinstein monofilament, see [Figure 1.1. b\).](#)
- 128-Hz vibration tuning fork, see [Figure 1.1. b\).](#)
- Computer for camera control and data storage and processing.



a)



b)



c)

Figure 1.1. a) the natural experiment setup
b) the 10 g. Semmes-Weinstein monofilament (above) and the 128-Hz vibration tuning fork (below)
c) the bagged foot in the water bassin

The subject study protocol approved by West Cost Institutional Review Board (IRB) includes the following steps.

1. Reviewing of the subject including the existed diagnosis and current medication used.
2. Visual inspection of the feet and toes; any existence of reddened, pale, blue or shiny skin, crooked toes, plantar callus, etc. must be noted.

3. 10-gram monofilament test. The goal is to check the sensitivity of the skin to 10 gram of force [33][34]. The inability to feel the filament indicates that patient is at risk for advanced stages of peripheral neuropathy, i.e. foot ulceration. More specifically, the monofilament is applied to the subject with eyes closed for one second (see [Figure 1.2.](#) to the pre-selected points of the foot [Figure 1.2.](#) The patient should respond “yes” each time he/she feels the stimulus.
4. Vibration tuning fork test [33][35]. The vibration perception threshold (VPT) test assesses nerve fiber function. The tuning fork is stroke and applied to the pre-selected points. The patient with eyes closed should respond when the vibration is “on” and when “off”, see [Figure 1.2.](#)
5. Clean the patient’s feet with an alcohol tissue.
6. A 3-minute thermal IR video is then taken of the patient’s foot. This video will be used as a baseline control video.
7. Put the patient’s foot into a thin waterproof plastic bag. Put the foot to the cold bath with a temperature $\sim 13^{\circ}\text{C}$ for a ~ 5 minutes, see [Figure 1.1.](#) Record the room air temperature and the water temperature before and after the cold stress.
8. Take the foot out of the cold water, remove the plastic bag, and place the foot on the feet support. Take the thermal IR video for 15 minutes.

Note that, the cooling water temperature, cooling time, and the how long the recovery process will be imaged are all experimental parameter. The numbers shown were from the original protocol. We have investigated the impact from varying these parameters. The details are presented in the Chapter 4.3.

1.2 The standard protocol

The following three types of subjects are enrolled in our study:

- Diabetes for 10 years with no peripheral neuropathy
- Diabetes for 10 years with peripheral neuropathy
- Normal (control)

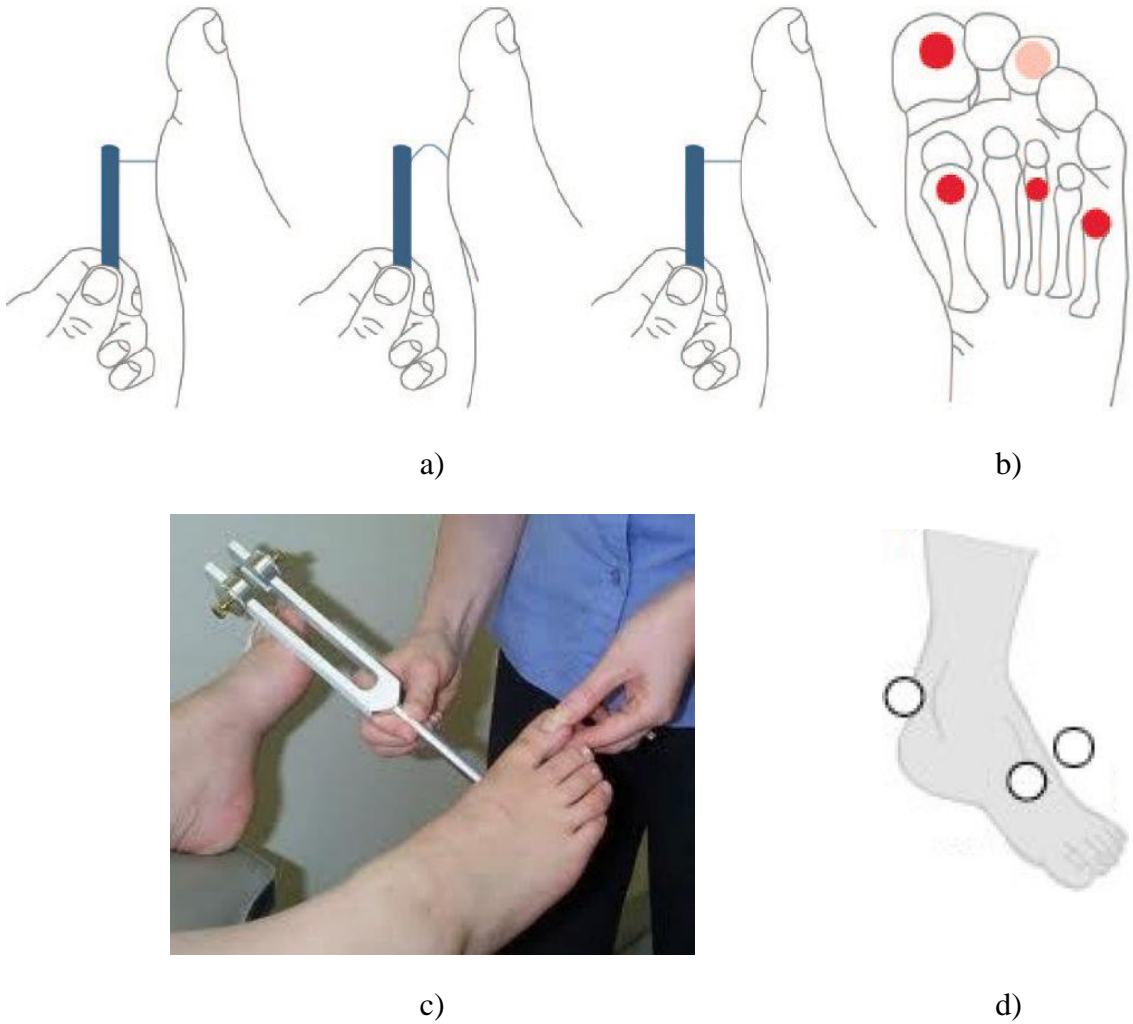


Figure 1.2. Monofilament test a) and the corresponding application points b) [34]; vibrating fork test c) and the corresponding application points d) [35].

The existed diagnosis is assumed as the ground truth for the future classification.

Visual inspections, monofilament test, and tuning fork test are included to detect the

problematic areas of the foot if any.

The points of interests for the tuning fork test correspond to the bones [2] and described in [Figure 1.2.](#) . The monofilament test was performed to the highlighted points on the foot as it is shown at [Figure 1.2.](#) , which also correspond to the bones.

1.3 Summary.

Totally the data of 70 experiments with 41 subjects have been collected. Particularly: 37 experiments with 11 control subjects (including 23 experiments with the subject VQB 04); 14 experiments with 14 subjects with diagnosed DPN for 10 years or more; 19 experiments with 16 diabetic subjects without diagnosed DPN.

Chapter 2 The cameras

2.1 General Requirement

The infrared (hereafter IR) camera is the main measuring device in our experiment. Thermal (functional) imaging can anatomically show relevant information that is useful in the assessment of local and regional function of the microvascular network. Performing regional analysis of the effects of cold provocation is equally important in the evaluation of people with diabetes. The thermal image videos present information about the blood delivery and blood extraction for a particular region as affected by damaged neurons and small vessels in that region of the body. For example, an image of the dorsal surface of the foot reflects both the systemic microvascular status and the status of the large (macrovascular) vessels supplying the leg. A pattern of the toes and plantar regions of the foot will reveal the spatial and temporal dynamics of the microvascular network, which contains information not currently analyzed for finding the relations of these parameters (spatial and temporal) to the risk of the onset or increase in the level of peripheral neuropathy.

The first main requirement to the cameras is the wavelength. We need to acquire a thermal radiant emittance within the thermal IR band, i.e., the spectral change of 7-13 μm region of the infrared spectrum. At these wavelengths, one is measuring the thermal emission from the field of view, in our case the plantar region of the subject's foot. The wavelength determines the type of optics (usually germanium vs. traditional silicon) and the type of sensors (usually uncooled or even liquid nitrogen cooled bolometers vs. widely

used CCD and CMOS ones) which both make the thermal IR cameras more expensive than the cameras working in visual or Near IR band. (Note that, the Near IR band, of NIR band if the typical spectral range for night vision applications.)

When choosing an IR camera, the following aspects were considered: (1) accuracy and the thermal sensitivity, (2) dynamic range, (3) frame rate, (4) spatial resolution, and (5) cost. The camera choice represents a tradeoff between the above parameters.

2.2 FLIR SC305

This 320x240 pixel thermal IR camera became our main measurement device. It has the frame rate ~8 Hz, 14 bpp (bit per pixel) dynamic range, 0.05°C thermal sensitivity in 7.5-13 μm range [36]. It uses uncooled bolometer with 25 μm pixel pitch as the thermal IR sensor and costs US\$ 12,000 (with the software) at the time of the experiment. It has the prime lens with 18 mm focal length and f -number 1.3 which corresponds to 25° 18.8° field of view (hereafter FOV) with the focal plane electronically adjustable from the minimum distance 0.250 m to infinity. The depth of field at 0.8 m is ~300 mm which is sufficient to keep the whole foot in focus.

2.3 Heimann array module

We have also experimented with the Heimann IR camera, which is about 1/6 of the cost of the FLIR 305 camera. The Heimann camera has the prime lens with focal distance 10 mm and f -number 1.0 which corresponds to 38.8° FOV for the 32x31 pixel sensor with 220 μm pixel pitch [37]. The depth of field is 250 mm at 350 mm distance. The Heimann camera is also sufficient for the study but is much noisier than the high-end FLIR camera, see the [Figure 2.1.](#), [Table 2.1.](#), and Chapter [2.7](#) for more details.

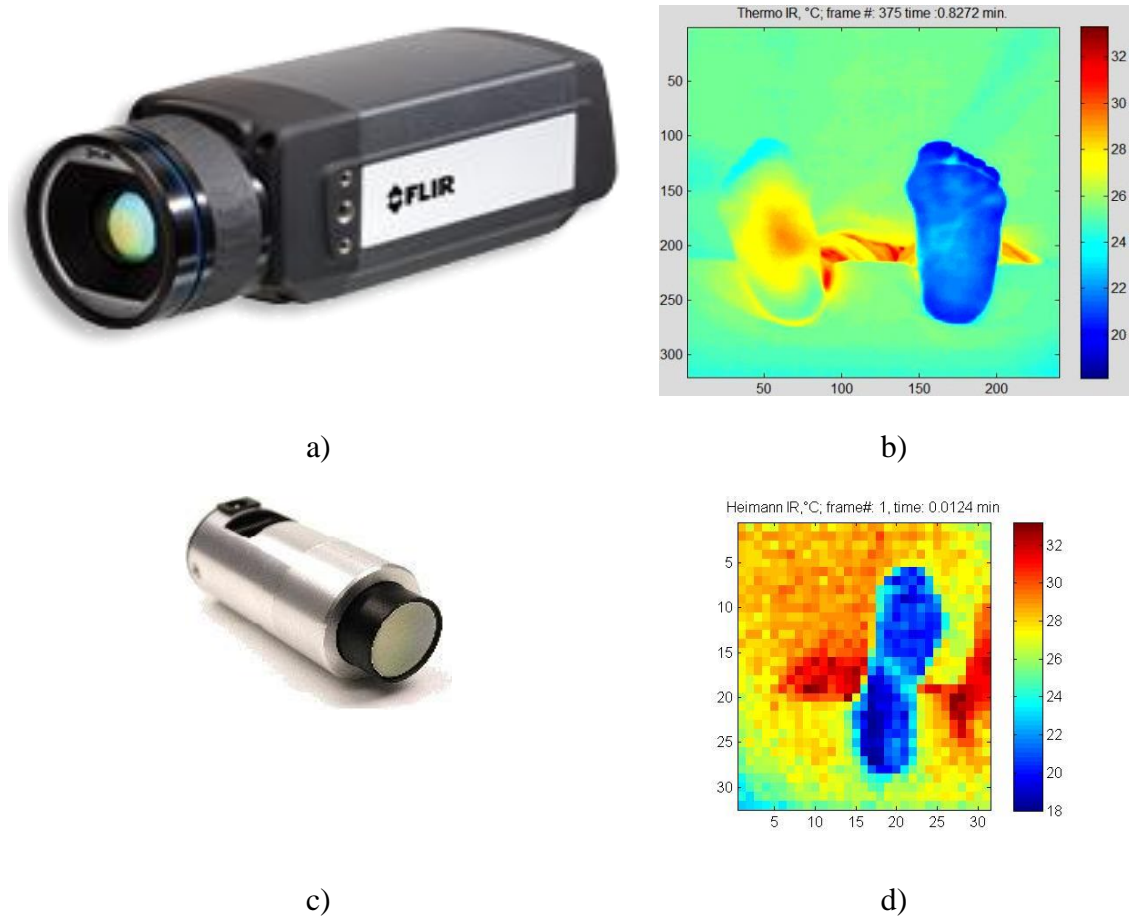


Figure 2.1. FLIR SC305 camera a) and the sample thermal IR foot pattern b);
 Heimann 32x31 array module c) and corresponding thermal IR foot pattern d)

2.4 Low cost IR diagnostic system

The high cost of the camera means that the screening is too expensive even for clinics and can only be carried out in hospitals or diabetes care centers. Early detection and prevention of diabetic foot will require routine monitoring of the foot. Thus, the solution to the long-term management of diabetic foot must be a home-oriented, patient/person centered process. It is highly demanding to develop a system that is low cost for routine in-home use. Towards that goal, we present a lightweight, foot neuropathy diagnostic system using infrared sensors [38].

[Figure 2.2.](#) shows the schematic overview of our infrared diagnostic system. The

system consists of one microcontroller (Microchip® PIC18F4550 processor), four infrared sensors (the Melexis® MLX90614-ESF-DCH infrared temperature sensors [39]), one serial communication module and a wireless Bluetooth module. Also, an LED display with push buttons is included for user control and interface (not shown in [Figure 2.2.](#)). Compared to the FLIR Infrared Camera, which is about \$12,000, the embedded system costs about \$300 (including PCB manufacturing cost), but will be significantly cheaper when mass-produced.

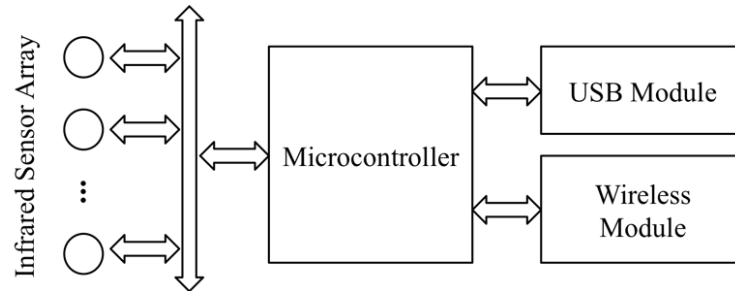


Figure 2.2. The design of the low cost IR diagnostic system

A graphical user interface application on PC is also implemented using Microsoft Visual Studio for receiving and processing data from the embedded system.

The Melexis® MLX90614-ESF-DCH infrared sensor can be used for non-contact temperature measurement. It is packaged in a TO-39 can with integrated low noise amplifier, 17-bit ADC and DSP unit. The field of view is 10-degree. The sensor supports both SMBus and PWM with 10-bit output. The maximum temperature range is -40°C~125°C and can reach up to the resolution of 0.02°C. In the range of 0°C~50°C, the sensor nominal accuracy is 0.5°C. The voltage supply of the sensor is 2.6 ~ 3.6V, and the current consumption is about 2mA. When first powered on, the sensor takes 0.65 seconds to warm up, and the response time is about 50ms in use. The sensor also supports a sleep mode for power saving. Under the sleep mode, the sensor pulls a negligible current of less

than $6\mu\text{A}$, and it will take about 33ms to wake up the sensor.

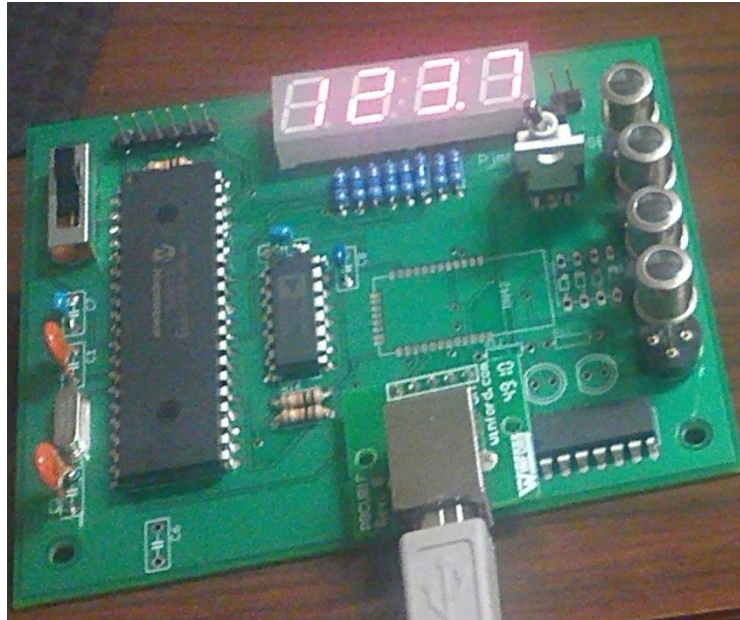


Figure 2.3. The low cost IR diagnostic system

Microchip® PIC18F4550 is a low-power microcontroller and consists of various communication and control resources, including Serial-USB adaptor, I2C (i.e., SMBus), and PWM. Its operating voltage is 2~5.5V. It has 32KB flash memory, 2KB SRAM, 256B EEPROM. It also has a high current for peripherals and can support up to 25mA as sink and source. It supports run, idle, and sleep mode. In idle mode, which is most of the time we set the controller to, the current is down to $5.8\mu\text{A}$ with all the peripherals on.

For wireless communication, we select the RN-42 Class 2 Bluetooth Module. It supports Baud rate from 1,200 bps up to 921 Kbps, where the non-standard baud rates can be programmed. The transmission range is 60 feet (20 meters). Its frequency is 2,402 ~ 2,480 MHz. It also supports 128-bit encryption and error correction. Power consumption is $26\mu\text{A}$ for sleep mode, 3mA when connected, and 30mA during transmission. However, transmission only takes a few microseconds.

An LED display is added to facilitate user operations of the device. When turned on, the display pulls about 30 ~ 40mA.

Since the diabetic foot doesn't affect the foot uniformly, the infrared sensors can also be customized to monitor different areas for different patients when prescribed for in-home monitoring. Our strategy is to use an array of TO-39 sockets, thus allowing the sensors to be custom arranged to monitor different regions.

2.4.1 Power management

When designing the device, our goal is to run the system on two AA batteries for at least a year. Assuming the patient take a measurement once every two days, each measurement takes about 15 minutes, and a usual AA battery operates at 1,800 mAh (milliamperere hour), this means the entire system should be operating at about 40mAh, i.e., pulling a current of about 40mA. Our initial measurement indicates that without any power management, the total consumption is about 50mA with 4 infrared sensors. Since we are measuring patient temperature changes, a sampling rate of 1Hz is sufficient for the application. To take advantage of this, we programed the system to put everything to sleep whenever possible. This reduces the power consumption to about 3mA on average with the LED display turned off.

It is also worth mentioning that when the system is connected to a computer via USB, all power is drawn from the USB connection, and the system is fully turned on.

2.4.2 Impact of field of view

Since the device is designed for in-home use, the set up may not always be accurate, which means the field of view, i.e., distance from the subject may change. To estimate the

impact of field of view, the system was placed at a distance of 2.5 cm, 5 cm, 12.5 cm, and 25 cm from an object with uniform temperature. For each particular distance, the average of 2-minute recording at 1 Hz sampling rate is taken for analyzing the statistical properties of the sensor. The results are shown in the table below (recall that our prototype board has 4 sensors):

Table 2.1.

Distance(cm) Sensor (°C)		2.5	5	12.5	25
#1	μ	25.65	25.61	25.61	25.75
	σ	0.06	0.06	0.05	0.06
#2	μ	25.81	25.77	25.77	25.89
	σ	0.06	0.06	0.05	0.06
#3	μ	25.88	25.80	25.80	25.89
	σ	0.05	0.06	0.05	0.06
#4	μ	25.86	25.77	25.78	25.86
	σ	0.07	0.06	0.06	0.06

As can be seen from the table, the impact of sensor to object distance is almost negligible. For a distance of about 25cm, which well beyond the range of our patient experiments, the impact of distance is only about 0.15°C.

2.5 Comparison of cameras

The [Table 2.2.](#) collects the main attributes of the specification of the cameras described above.

Table 2.2. Specifications of the cameras

Camera name	FLIR SC 305	Heimann 32x31 array	Low cost IR diagnostic system
Optical			
Wavelength, μm	7.5-13	8-14	5.5-14
Focal length, mm	18	10	-
FOV	25°x18.8°	38.8°	10° for each sensor
Minimum focus distance, m	0.25	0.1	0
F-number	1.3	1.0	-
Focus	Electric (built-in motor)	$+\infty$	$+\infty$
Detector			
Detector type	Focal plane array (FPA), uncooled microbolometer	Focal plane array (FPA), uncooled microbolometer	Single uncooled microbolometers
IR resolution	320×240	32×31	4 single
Detector pitch, μm	25	220	490 (sensor area) 10000 (distance between the sensors)
Data			
Dynamic range, bpp	14	12	10
Frame rate, Hz	9	20	1
Measurement			
Thermal sensitivity, °C	0.05	0.1	0.02
Accuracy, °C	± 2 or $\pm 2\%$ of reading	± 3	± 0.5 (± 0.1 in “medical” range)
Cost			
Cost, US\$	12.000	2.000	300 (for a single test unit)

Whereas the main differences between the first two cameras are in resolution and sensitivity, the low cost diagnostic system represents a completely different approach. The closest biological analogies are: the eye of a human (or generally an animal), and the eye of an insect; see [Figure 2.4](#). The first one has one main lens, which projects the light (in some wavelength range) to the sensor. The parts of the projection corresponding to the different pixels (photoreceptors) do not overlap and almost do not have gaps in between

(more precisely, are as dense as the photoreceptors). In the second case each pixel has its own lens which are independent, i.e. virtually could be targeted anywhere. There is no focal plane for that type of sensors in principle. The “focal plane” could be assumed for the planar array of the independent sensors as the plane where the projections of the objects to the corresponding sensors are quite dense but do not overlap.

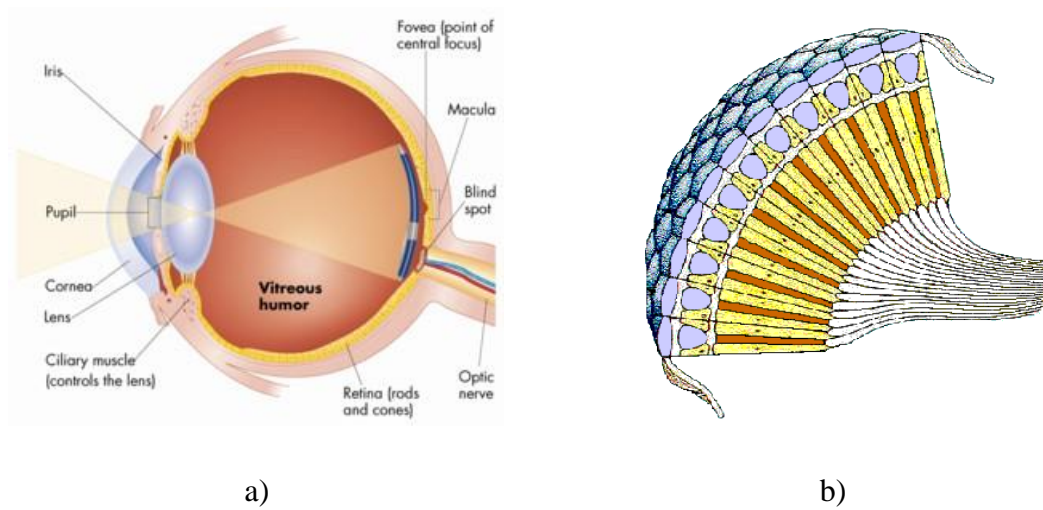


Figure 2.4. Human eye a) and facet insect eye b) [40]

Let's take a look on the synthetic “image” which actually is the superposition of the independent signals from the corresponding sensors. For the clearness let's not literally follow the current 4×1 design but generalize the concept as $N \times M$ board, which is also possible to implement on the element base described above. The minimum diameter of the spot which is just 25 mm far from the main “focal plane” for 38.8° FOV is 17.8 mm, i.e. the diameter of the spot on the inner arch foot captured by one sensor is that much bigger than the diameter of the spot from the ball, see [Figure 2.5](#).

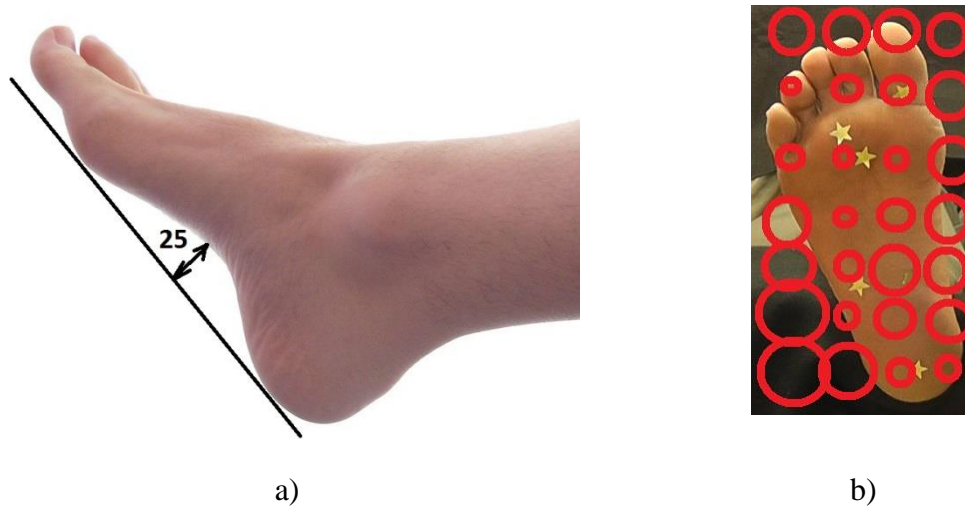


Figure 2.5. Foot shape a) and exaggerated projection of the matrix FOV to the image plane b)

This feature and corresponding inaccuracy due to 3D feet shape should be taken into account, which generally requires of a 3D foot model for the compensation. To avoid the overlapping of spots taking into account the non-parallel optical axes we need to bring the subject even closer to the “focal plane”. So, we placed the array with the 1 cm distance between 10° FOV sensors approximately to 5 cm from the object to get the non-overlapped projected spot diameter 8.7 mm, see [Figure 2.6](#).

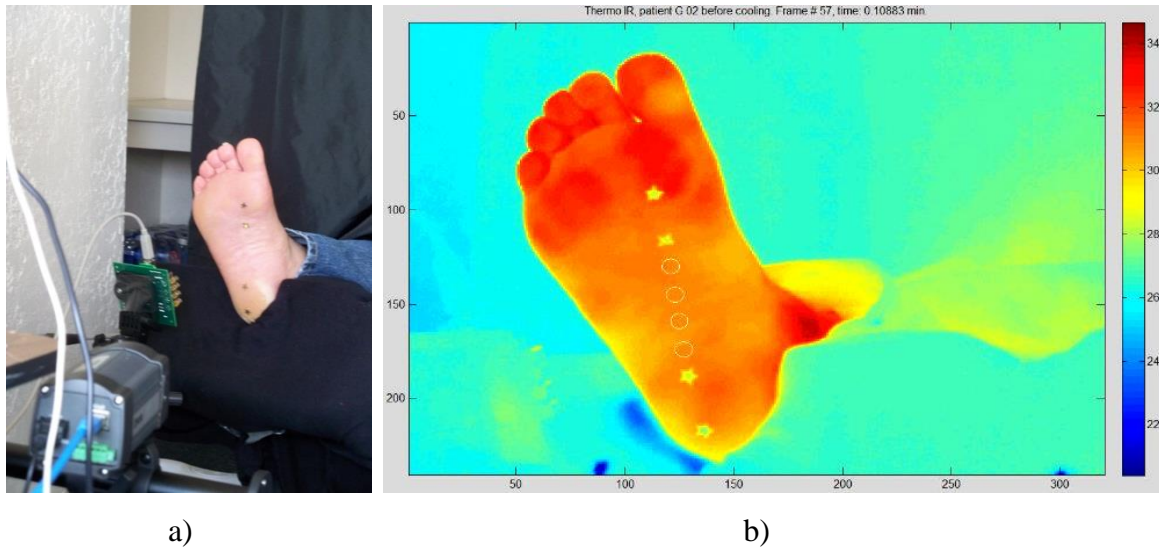


Figure 2.6. The experiment setup with the low cost IR diagnostic system a) and the approximate areas of the foot projected to the corresponding sensors (highlighted white circles), b).

However, since the embedded system is for in-home use and will be customized for tracking particular spot or spots on the foot, it is sufficient for the application.

2.6 Calibration

Generally speaking, by calibration, or radiometric calibration we aim to ensure that all measurements are accurate and precise. In a nutshell, the calibration will produce a function f , such that when applied to the measured value x , $T = f(x)$ is the true temperature (within certain pre-specified error criteria). Most cameras require frequent recalibration. For example, the FLIR SC 305 camera has to be recalibrated every 6 months as per the manufacturer requirements.

The raw output from IR cameras are 16-bit integers from analog-to-digital converters (ADC). Their raw output are not temperature readings but the measured radiant emission of the objects. From Stefan-Boltzmann Law [41], the energy radiated by a blackbody radiator per second per unit area is proportional to the fourth power of the absolute temperature and is given by $\frac{P}{A} = \epsilon \sigma T^4$, where P is the radiated power, A is the area, ϵ is the emissivity (0.98 for human tissue), σ is the Stefan-Boltzmann constant (5.6703×10^{-8} watts/m² K⁴), and the temperature, T , is in degrees Kelvin K. Thus the raw output, i.e., the radiant emission is proportional to the fourth power of the absolute temperature T .

An Omega BB703 black body [42] was used for the calibration of the cameras, see Fig. 2.8 a) below, where the black circle is the black body and the digital indicator left displays the current temperature value at 0.1°C resolution. This black body has a temperature range from ambient temperature to 100°C with 0.3°C stability; see [Figure 2.7](#).

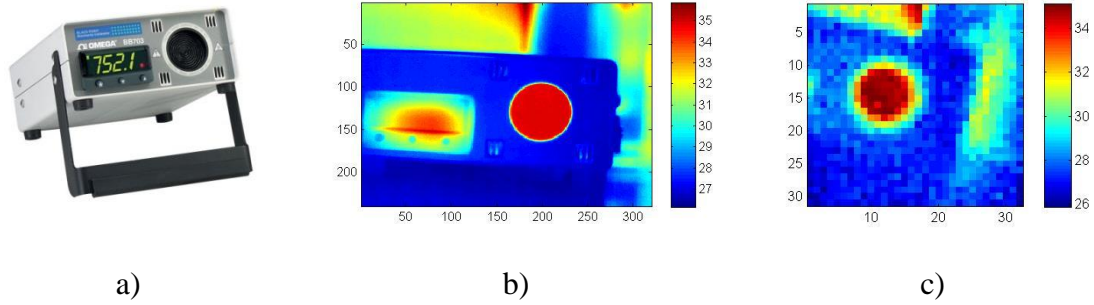
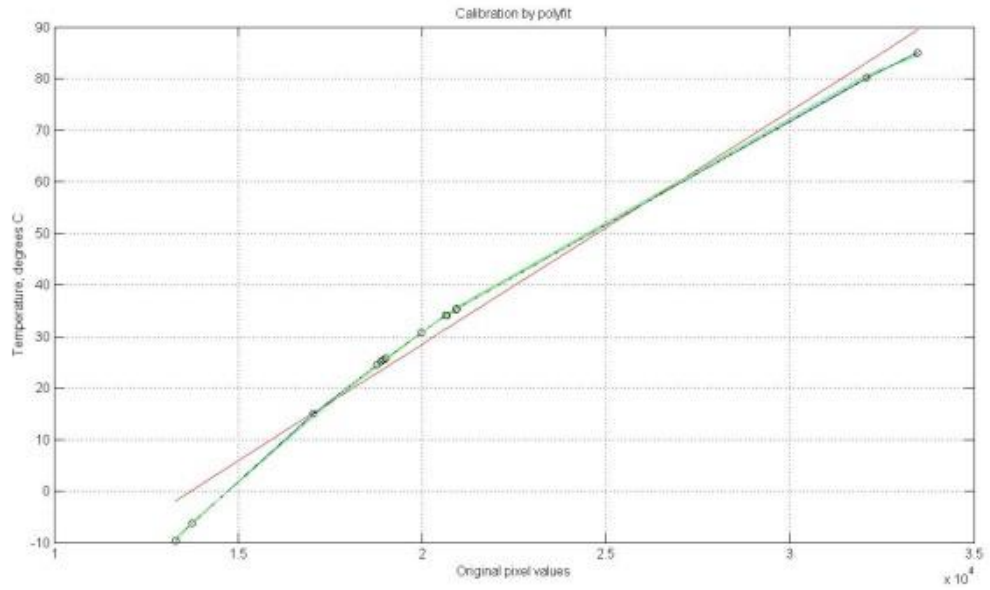


Figure 2.7. Omega BB703 black body a) and the sample thermal IR patterns during the calibration via FLIR SC305 b) and Heimann 32x31 c)

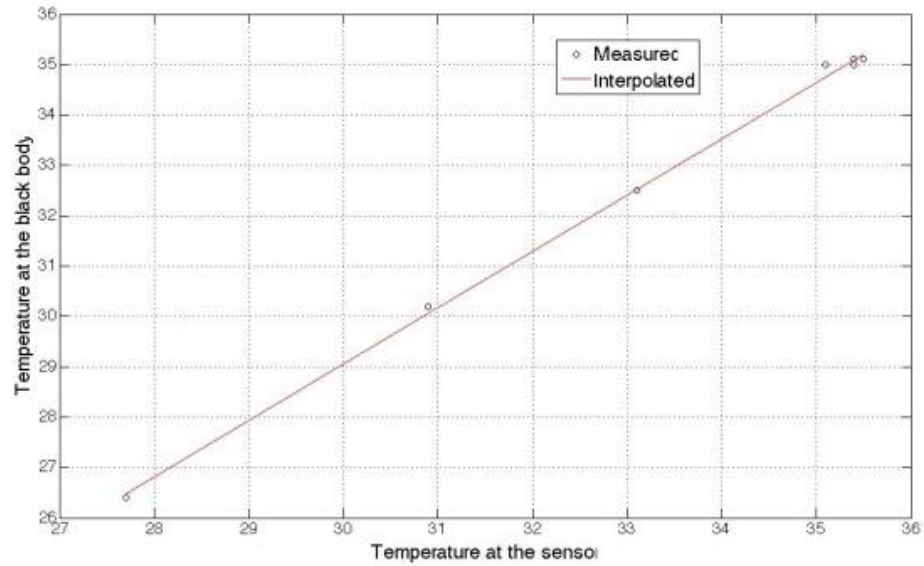
Different camera manufacturers use different calibration rules. For FLIR, a polynomial degree 4 is suggested for the entire camera, see [Figure 2.8](#).

For the experimental low cost device, we calibrated each sensor individually; 8 temperature measurements have been done within the $27 \sim 35$ °C range. During the calibration, each sensor was placed 5 cm away from the black body to ensure that the field of view of sensor is completely within the active region of the black body.

The calibration measurements indicated a linear relationship between the set temperature of the black body and the sensor readings with an accuracy of $0.2 \sim 0.4$ °C; see [Figure 2.8](#). For the temperatures below the calibrated range we used corresponding extrapolation. These calibrations gave us confidence that the sensors were indeed within the specifications from the manufacturer.



a)



b)

Figure 2.8. Sample calibration data. FLIR CS305 a); one sensor of the low cost IR diagnostic system

2.7 Noise of the experiment

Accordingly to [36] and [37], the cameras has uncooled microbolometer array thermal infrared sensor; the low cost system has independent microbolometers [39].

Following [43], the main sources of the noise in uncooled microbolometers are the following: white Johnson noise, white thermal noise, $1/f$ flicker noise due to resistance fluctuations, and drift noise with approximately $1/f^2$ spectral density. The influence of other sources of noise such as different environmental noise including microphonics (vibrations which can produce noise in electric circuits), air currents, light induced noise and electromagnetic influence are usually minimized by the manufacturers and can be neglected. Thus, the power spectrum of the noise can be written [43] as follows:

$$S(f) = a^2 + \frac{b^2}{f} + \frac{c^2}{f^2},$$

where a^2 , b^2 , and c^2 stand for the variances of the white, flicker, and drift noise, correspondingly. The drift noise could be almost filtered out with the high-pass filter. Almost in the whole bandwidth the $1/f$ noise is the most valuable component; only at the very high frequencies the spectrum becomes almost invisibly more flat due to Johnson noise.

$1/f$ noise seems to have equal power at all frequencies. The terms flicker noise, $1/f$ noise, and pink noise [44] are synonyms. “Pink” color has been chosen to emphasis that this noise it has high intensity on low frequencies and low intensity at high frequencies, but fades with frequency increasing not as fast as $1/f^2$ “red” noise. The term “pink noise” is more general and used not only for the canonic $1/f$, but also for the $1/f^{2-\alpha}$ noise, where $0 < \alpha < 2$.

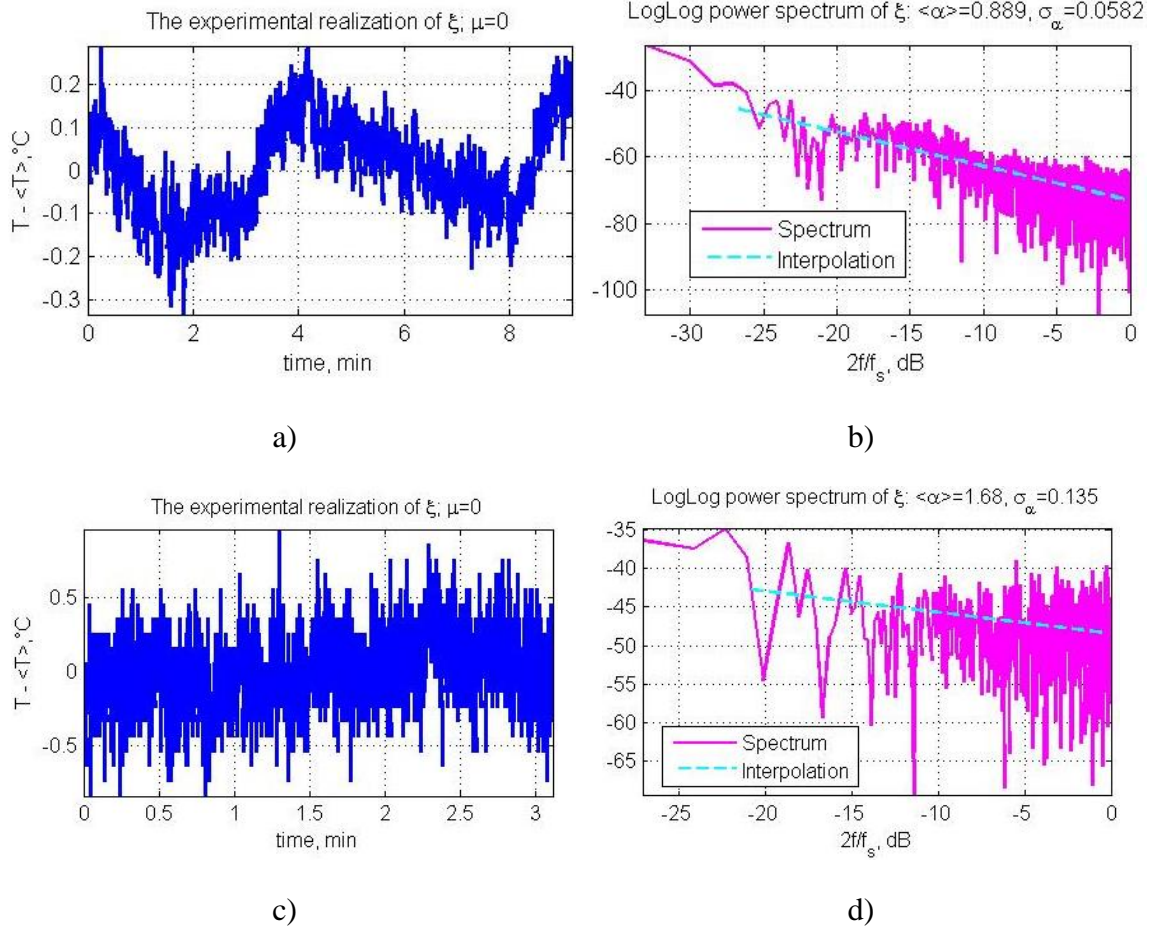


Figure 2.9. Sample realizations, i.e. zero-mean temperature dependence at one pixel in time denoted as ξ (left column, blue plots) and corresponding loglog power spectra (right column, purple plots) of thermal IR signals from FLIR SC305 a) and b), Heimann 32x31 array c) and d), correspondently. f_s stands for the sampling frequencies.

Generally, pink noise has Tweedie distribution [45], i.e. not necessarily normal. The chi-square test of the experimental data refused the normal distribution 0-hypothesis; see the plots at [Figure 2.10](#). Here and below the paragraph is illustrated with the experimental data from the FLIR SC305 camera as default (otherwise the different camera type is marked).

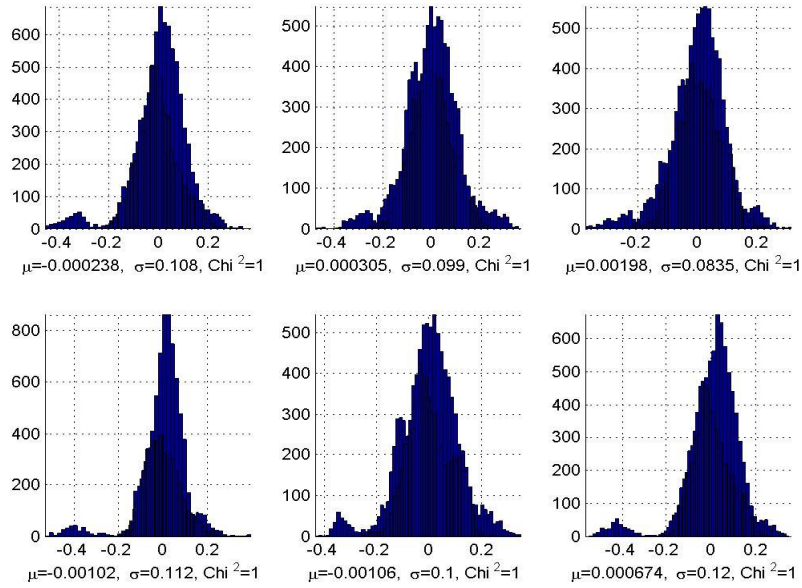


Figure 2.10. Histograms of zero-mean temperatures at 6 different ROIs with the estimated parameters of the corresponding normal random processes and all refused results of chi-square test.

2.7.1 Separation of the noise

Let's first investigate the signal to separate the sources of the noise. Take a brief look at [Figure 2.9. a\)](#) to see the slow change of the temperature with the period $\sim 4 \dots 6$ min together with the fast changes. Even the most thermostatically stable available source of the temperature, which the calibrator is, cannot keep absolutely the same temperature for a while. In the environment colder than the required temperature, the calibrator first warms up to the little bit higher temperature within the precision. The temperature changes very slowly, for a few minutes normally; observe the top-left plot at Figure 2.11. Then it cools down until the lower bound, then warms up again, and so on. The change of temperature is displayed on the digital indicator of the calibrator (see [Figure 2.7. a\)](#)). We need to determine the frequency cutoff for the actual temperature change to claim the higher frequencies as the camera noise.

Let's compare the experimental signal [Figure 2.9.](#) with the pure $1/f$ spectrum

model signal. To obtain such signal one needs just to modulate the power spectrum of the white noise and make inverse Fourier transform. [Figure 2.11.](#) below shows sample experimental and model realizations (top blue plots) and their power spectra with the linear interpolation (bottom magenta plots and dash cyan lines, correspondingly). Remind that the power spectrum density of the pink noise is $1/f^{2-\alpha}$, and the linear interpolation coefficient $\alpha = 1$ corresponds to the “canonic” flicker noise, i.e. to the pure $1/f$.

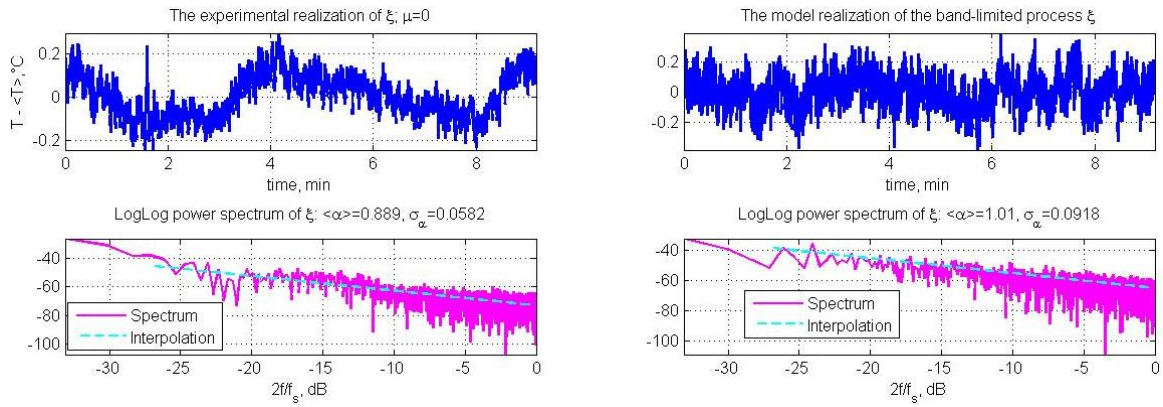


Figure 2.11. Zero-mean experimental realization (left top), the corresponding numerical model (right top), their power spectra with their linear interpolations (bottom left and right, correspondently).

Besides the spectra above look very similar, the processes are quite different. It can be detected by comparing their auto- and cross-correlation functions, see [Figure 2.12.](#) .

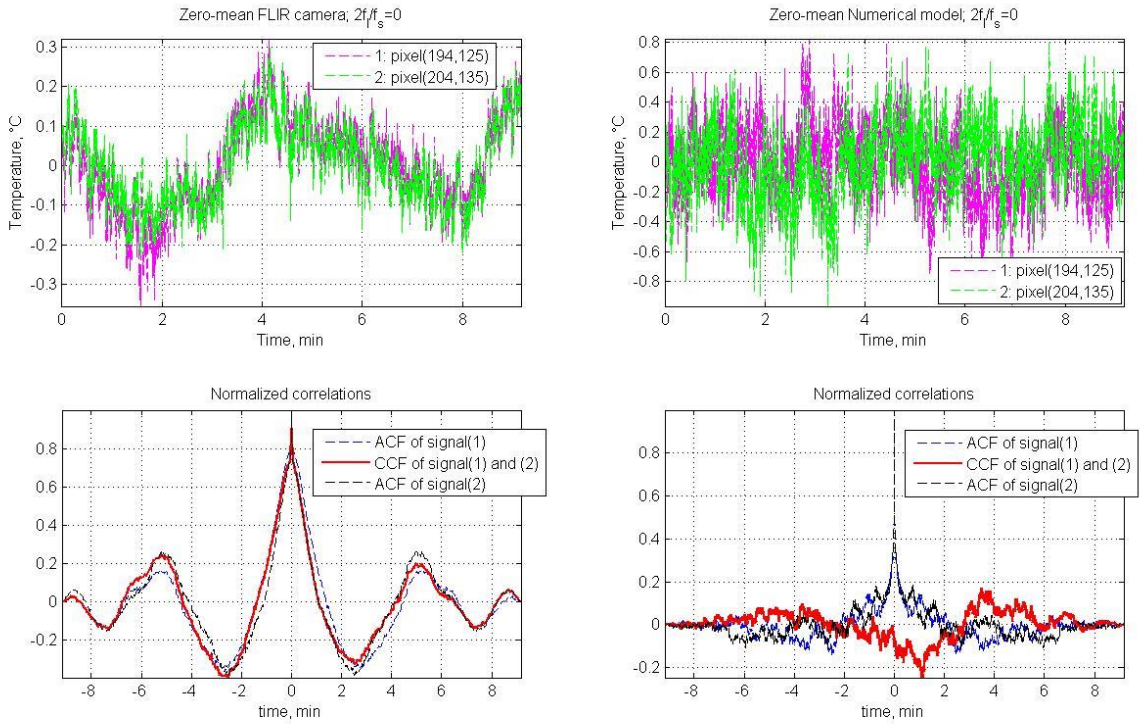


Figure 2.12. Two zero-mean realizations: experimental (left top), the corresponding numerical model (right top), their auto- and cross-correlation functions (bottom left and right, correspondently).

The cross-correlation function (red solid line bottom left) of the experimental is very similar to the low-frequency auto-correlation functions of sample realizations from the distant pixels (i.e. with the long Manhattan distance on the sensor plane). It means a presence of the low-frequency deterministic component in the experimental signal in contrary to the numerical model. It also can be confirmed by the plots [Figure 2.13](#). below. The narrow elliptic distribution of the sample experimental realizations in contrary to the near round one for the numerical model means that the experimental random process is strongly correlated.

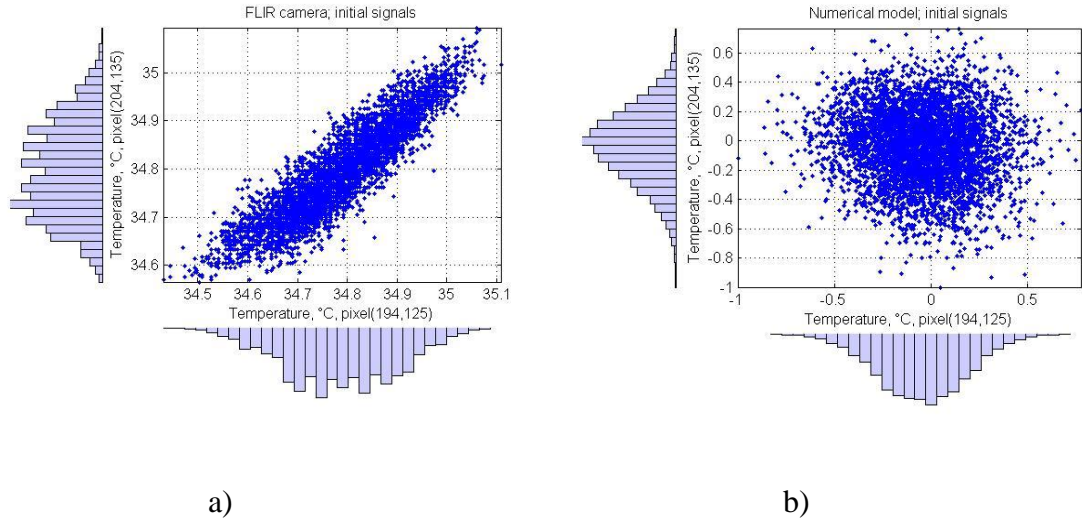
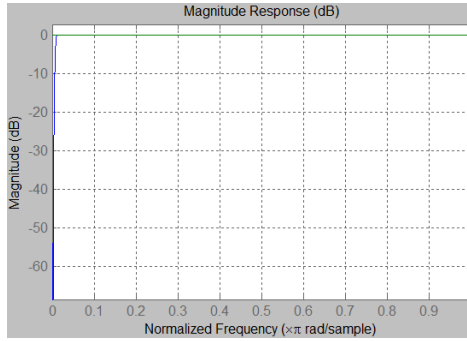


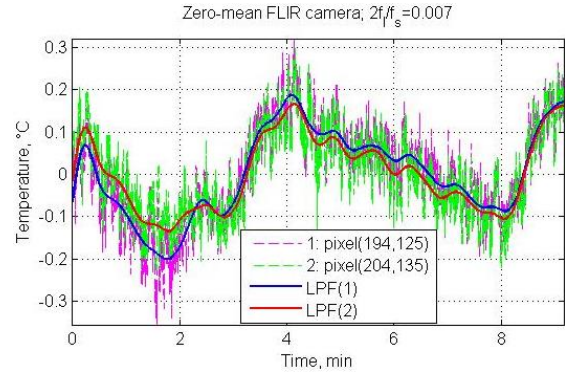
Figure 2.13. Distribution of temperatures for two sample realizations: experimental a) and uncorrelated numerical model b).

It is not a surprise, as we have noticed above. Let us filter the low frequency temperature change of the calibrator's temperature out. Let us choose the low cut frequency of the high pass FIR (finite impulse response) filter with order 777 (i.e. definitely a very high order!) as 0.007 of the sampling frequency f_s (chosen experimentally), see the magnitude response at [Figure 2.14](#).

One can see that the low pass signals are mutually almost deterministic, especially at near pixels, [Figure 2.15](#). a) with the coordinates at the sensor plane (199, 130) and (200,130), i.e. Manhattan distance = 1. The high pass signals are not as correlated as at [Figure 2.13](#). a), but also not as uncorrelated as at [Figure 2.13](#). b). The experiments have shown that one cannot fully avoid the correlation just by increasing the cutoff frequency.

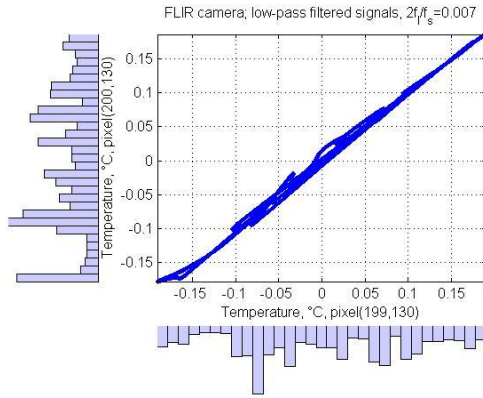


a)

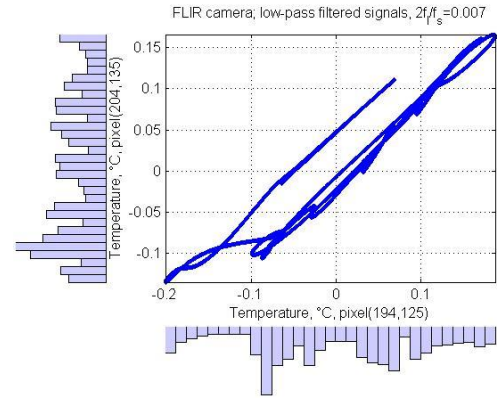


b)

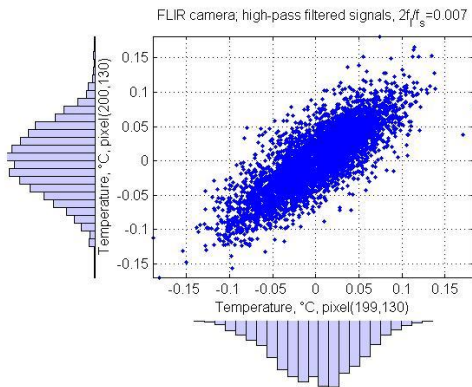
Figure 2.14. Magnitude response of high-pass FIR filter a), and the low-pass signals filtered out from the sample realizations b)



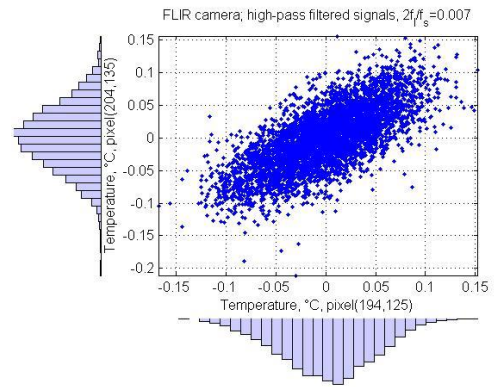
a)



b)



c)



d)

Figure 2.15. Distribution of temperatures for two sample realizations: low pass filtered near pixels a), low pass filtered distant pixels b), high pass filtered near pixels c), high pass filtered distant pixels d).

For the illustration, see the correlation functions of the high pass signals in [Figure 2.16](#). below. The ACFs of the experimental signals do not look that dramatically different to the model as at [Figure 2.12](#). but look very similar.

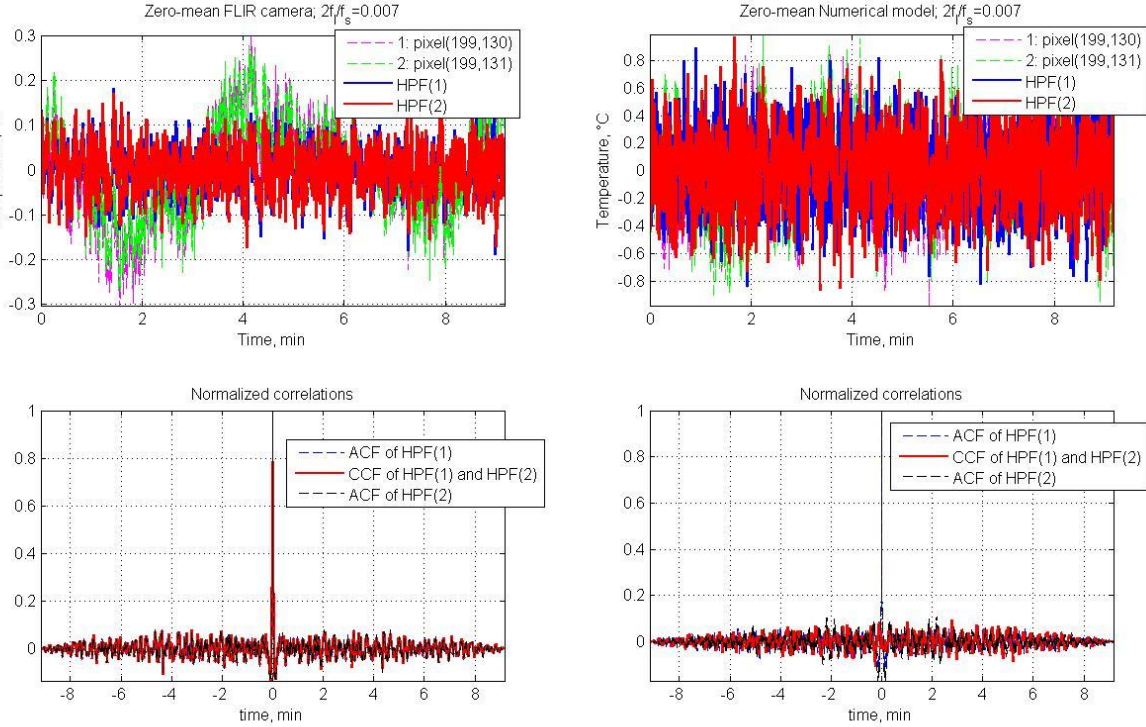


Figure 2.16. Two zero-mean realizations and their high pass filtering: experimental (left top), corresponding numerical model (right top), and their auto- and cross-correlation functions (bottom left and right, correspondently).

2.7.2 Noise correlation between the pixels of different cameras

Nevertheless, the CCFs at [Figure 2.16](#). look quite different (compare red solid curves at two bottom plots). High peak value ~ 0.8 of left CCF indicates the presence of the correlation between pixels even at high frequencies. Therefore, one cannot claim the realizations statistically independent. To make the correspondence between the model and the experiment the multivariate Gaussian random number generator is used; then the spectrum modulation is applied to the numerical model, as before. The spectra look

similarly; the correlation is illustrated at [Figure 2.17.](#) and [Figure 2.18.](#) .

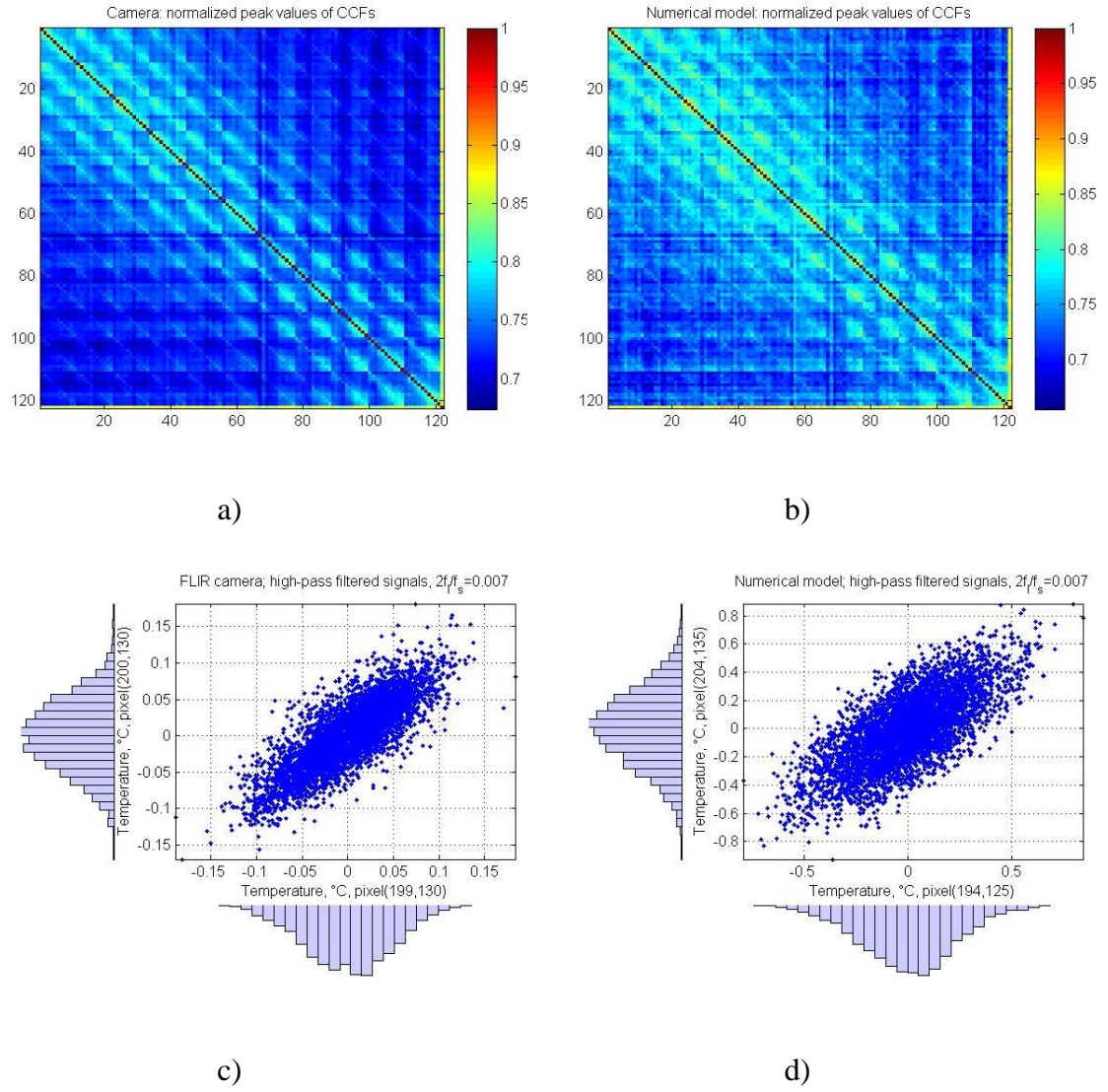


Figure 2.17. Normalized correlation coefficients of the highpass experimental a), and model b) processes; distribution of high pass realizations: experimental a), and model b).

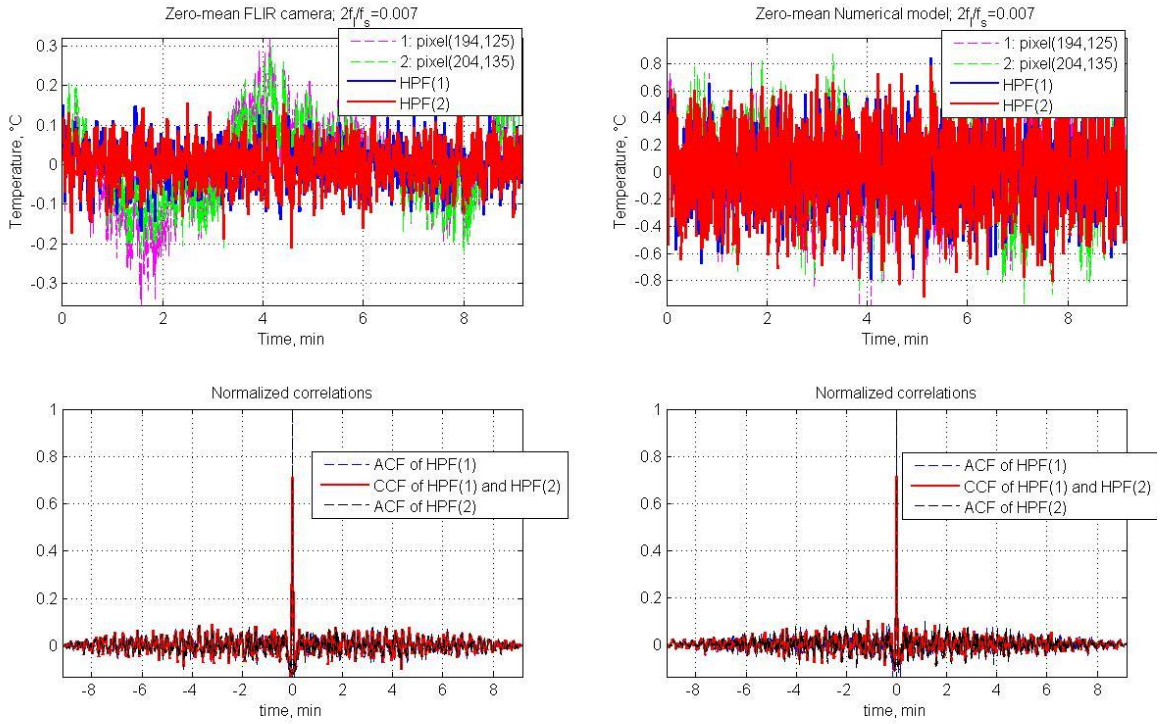


Figure 2.18. Two zero-mean realizations and their high pass filtering: experimental (left top), corresponding numerical model (right top), and their auto- and cross-correlation functions (bottom left and right, correspondently).

The really good match between spectral and correlational characteristics of the experimental and model processes gives us the promising model. Thus, we can claim the noise at FLIR SC305 thermal IR camera as the correlated band-limited pink random process.

[Figure 2.17](#), shows the normalized to one correlation coefficients of the high-pass filtered experimental signal a) and of the corresponding numerical model b). Observing the correlation coefficients one can see that the correlation between the pixels is stronger for the close pixels. It could be explained by the electrical feedback (mostly via induction) between the near pixel circuits [46]. The manufacturer company calls this “imperfection in detector read-out circuits” and gives a very promising recommendation how to overcome

it: “Live with it”. Visually it could look like a column-ordered noise.

Another possible explanation of the correlation of spatially close pixels is the lens blur, i.e. the quality of lens and/or ability of precise focusing are lower than the sensor pitch size. In this case the 2D impulse response spot overlaps not just one pixel but also its neighbors; therefore, they become correlated. The correlation coefficients of Heimann camera indirectly confirm (but not proof) this hypothesis: for the sensor with much bigger pitch size (220 μm vs. 25 μm for FLIR SC305) we don't see increasing of the correlation for the close pixels. [Figure 2.19.](#) below illustrates the statistical behavior of the noise of the Heimann infrared array. Thus, we can claim the noise at Heimann 32×31 array as the uncorrelated band-limited pink random process.

The sensors of the low cost IR diagnostic system are independent, distant and electrically isolated. Nevertheless, they could correlate as well if the distance from the device to the object will be big enough to overlap, see [Figure 2.5.](#) Unfortunately, the geometrical base of this device is greater than the size of the black body's working surface. Thus, the correlation between the sensors of the low cost system cannot be measured similarly to the other two cameras.

We don't have enough data to differentiate the correlation between pixels due to blur and due to electric circuit. Actually, for our research it is sufficient to characterize the camera noise, i.e., whether the noise is stationary.

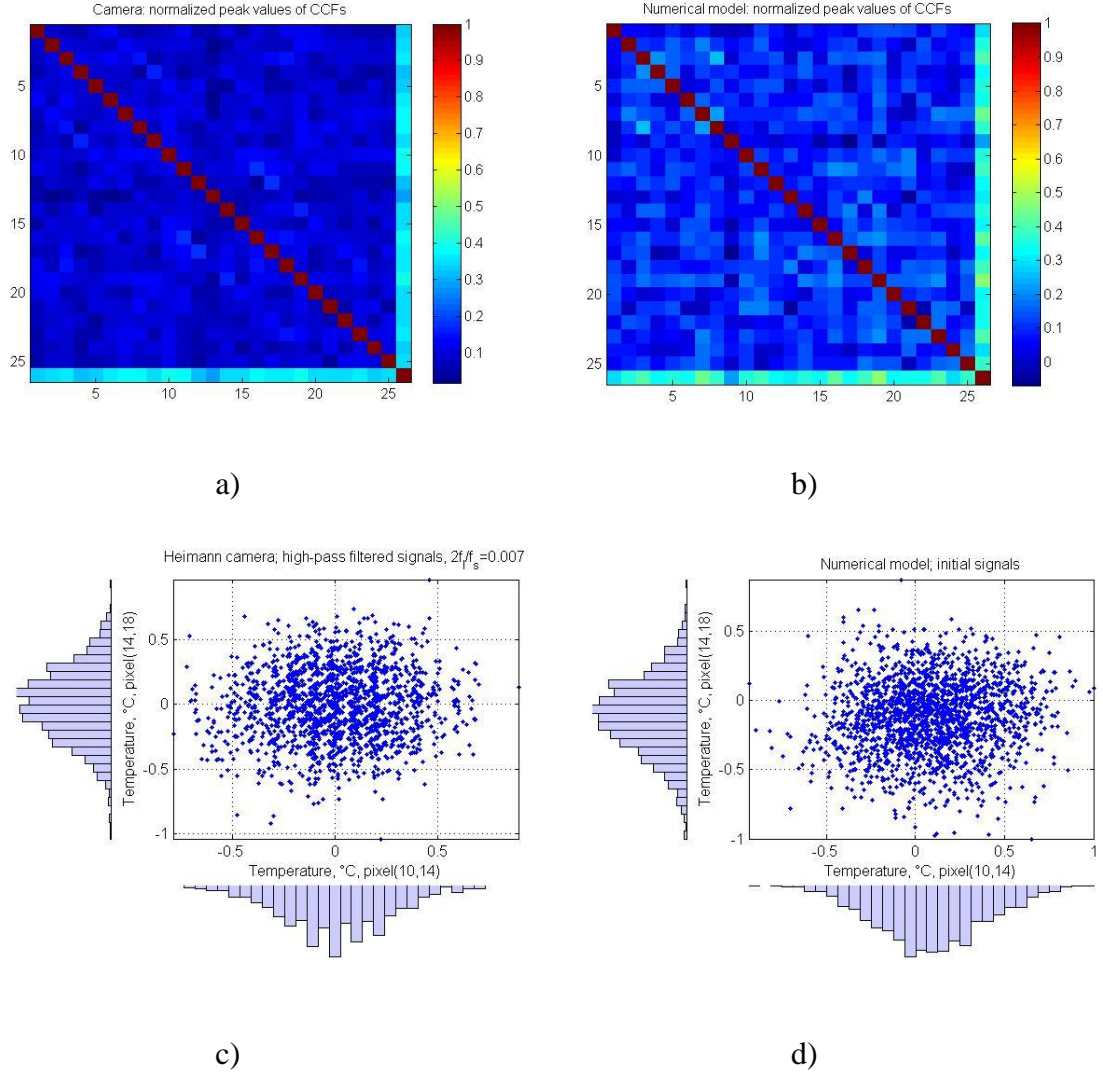


Figure 2.19. Heimann array: normalized correlation coefficients of the highpass experimental a), and model b) processes; distribution of high pass realizations: experimental a), and model b).

2.7.3 Investigation of the statistical stationarity of the camera noise

Flicker noise together with the thermal noise has been predicted by Walter H. Schottky in 1918 [47] and first time successfully measured by J.B. Johnson in 1925 [48] (and named it as the Schottky effect) and then discovered by Schottky in 1926 [49]. For almost a hundred years the number of the publications related to this effect is almost constantly growing year by year, see [Figure 2.20](#). Of course that is because pink noise effect exists – I would say – almost everywhere, from the solid state physics and

microelectronic devices to astrophysics, from car traffic to macroeconomics, from biology to geology, from music to weather behavior... On the other hand, it cannot exist by the contradiction to Parseval's theorem: the spectrum of a random process must be integrable, whereas $\int_{-\infty}^{\infty} \frac{df}{f} = +\infty$, so called cutoff paradox [51].

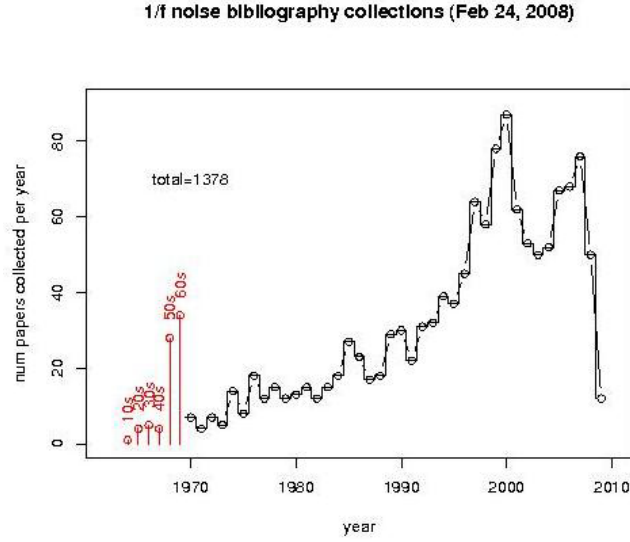


Figure 2.20. Growth of the $1/f$ noise-related publications [52].

The stationarity of the flicker noise also is an interesting question. Many researchers from Benoit Mandelbrot [50] and until present times [51] claim that $1/f$ noise can be non-stationary and consequently non-self-averaging observable, non-ergodic. Note that “can be non-stationary” does not mean that it necessarily is non-stationary. The assumption of stationarity and ergodicity is very important for our measurements. Ergodicity makes possible to get the same statistical properties for the different particular pixels and ROIs, and thus to investigate them similarly. Moreover, it makes possible to trust to the measurements made with the array of bolometers. Stationarity makes possible to trust the measurements made in a long time and also to model the noise by corresponding shaping of stationary white noise spectrum. Thus, we are doomed to check the stationarity and

ergodicity of the experimental noise to go further.

Let's check the hypothesis of stationarity and ergodicity with the method described in [53]. The non-stationarity means that the short time average of the squared noise seemed to exhibit larger statistical fluctuations than had been expected for stationary stochastic processes. Thus, the experimental signals representing the tested stochastic process were band limited with different ratios of bounding frequencies, squared, and exponentially weighted averaged. As the result, we got the variance noise. The properties of this stochastic process have been compared to the properties of similarly weighted $1/f$ -shaped normally distributed stationary and ergodic zero mean stochastic process. In contrary to the original investigation [53], we will use the advantages of digital signal processing and explicit formulas for the cross-correlation functions.

Denote a normally distributed stationary and ergodic zero mean stochastic process as $\xi(t)$. Let σ_ξ^2 stands for the variance of ξ and $\psi_{\xi\xi}(\tau) = E[\xi(t)\xi(t + \tau)]$ for its autocorrelation function. New random variable $\eta_1(t)$ proposed in [53] for exponentially weighted average square of $\xi(t)$ is

$$\eta_1(t) = \frac{1}{\tau} \int_0^\infty e^{-\frac{x}{\tau}} \xi^2(t - x) dx \quad (2.1)$$

Physically it corresponds to the integration of the square weighted average square with the integrating RC circuit, with the time constant $\tau = RC$. We have a possibility to integrate the squared $\xi(t)$ digitally, so there is no need of the exponent weighting and by this we introduce the following stochastic process:

$$\eta(t) = \frac{1}{\tau} \int_0^{\tau} \xi^2(t-x) dx \quad (2.2)$$

Mean of $\eta(t)$ is σ_{ξ}^2 and the variance is

$$\sigma_{\eta}^2 = \frac{2}{\tau} \int_0^{\tau} \psi_{\xi\xi}^2(x) dx \quad (2.3)$$

Physically the random process $\eta(t)$ means the variance noise of $\xi(t)$.

Let the $1/f$ noise be band-limited with the frequencies $\frac{f_h}{f_l} > 1$; then the power spectral density inside the band pass is $S_{\xi\xi}(f) = \frac{\sigma_{\xi}^2}{2f \ln \frac{f_h}{f_l}}$. The lower frequency limit cuts off the spectrum near 0 and makes the integral $\int_{-\infty}^{\infty} \frac{df}{f}$ finite. Physically it means that we are investigating the stationarity during the certain time limit. The noise of our cameras is naturally band-limited, as it has been shown above, so we are fine with this assumption. The normalized autocorrelation function for the band-limited pure $1/f$ noise has been derived in [54] is

$$\frac{\psi_{\xi\xi}(t)}{\psi_{\xi\xi}(0)} = \frac{\ln\left(\frac{\tau_2}{t}\right)}{\ln\left(\frac{\tau_2}{\tau_1}\right)} \quad (2.4)$$

where $\psi_{\xi\xi}(0) = \sigma_{\xi}^2$ and $\tau_{1,2} = 1/f_{h,l}$, correspondently and $\tau_1 < t < \tau_2$.

This yields the normalized variance

$$\frac{\sigma_\eta^2}{\sigma_\xi^4} = \frac{2}{\sigma_\xi^4} \int_0^\tau \left(\sigma_\xi^2 \frac{\ln\left(\frac{\tau_2}{x}\right)}{\ln\left(\frac{\tau_2}{\tau_1}\right)} \right)^2 dx = \frac{2}{\tau \ln^2 \frac{f_h}{f_l}} \int_0^\tau \ln^2 \frac{1}{f_l x} dx \quad (2.5)$$

As usually for this kind of noise we are not lucky to get the explicit formula for the integral above.

Let's now consider not only exact $1/f$ noise but also a more general case: the noise with the power spectra $f^{-2+\alpha}$, where $0 \leq \alpha \leq 2$. The case $\alpha = 1$ corresponds to case we have just discussed above. The cases with $1 \leq \alpha \leq 2$ correspond to more wideband noise, which should not appear in our experiments. The normalized autocorrelation function for the case $0 \leq \alpha < 1$ (and all other noted cases as well) has been derived by Watanabe in [\[55\]](#):

$$\frac{\psi_{\xi\xi}(t)}{\psi_{\xi\xi}(0)} = \begin{cases} 1 - \left(\frac{t}{\tau_0}\right)^{1-\alpha}, & t \leq \tau_0 \\ 0, & t > \tau_0 \end{cases} \quad (2.6)$$

where

$$\tau_0 = \{(\tau_2^{1-\alpha} - \tau_1^{1-\alpha})/\Gamma(\alpha)\}^{\frac{1}{1-\alpha}}, \quad (2.7)$$

and $\Gamma(\cdot)$ is the gamma-function: $\Gamma(\alpha) = \int_0^\infty x^{\alpha-1} e^{-x} dx$.

More precisely, this ACF as well as the ACF of the canonic $1/f$ pink noise has been computed assuming Lagrangian [\[54\]](#) and multi-Lagrangian [\[55\]](#) noise model. Other examples of $1/f$ noise such as fractional Gaussian noise [\[56\]](#) [\[57\]](#), fractional Brownian motion [\[58\]](#)[\[59\]](#)[\[60\]](#)[\[61\]](#), Cauchy-class process [\[63\]](#), generalized Cauchy process [\[64\]](#),

and some other ones are not considered here. It means that their ACFs are not substituted to (2.3), mostly because, looking a bit forward, we have been enough satisfied with the results with the multi-Lagrangian model; also they don't have the explicit formulas of ACFs for the band-limited process. See the observation [65] for the comparison of the above mentioned models.

Similarly, substituting the correlation function to the expression for the normalized variance of $\eta(t)$ (2.3) one get:

$$\frac{\sigma_{\eta}^2}{\sigma_{\xi}^4} = \frac{2}{\sigma_{\xi}^4} \int_0^{\tau_0} \left(\sigma_{\xi}^2 \left(1 - \left(\frac{\tau x}{\tau_0} \right)^{1-\alpha} \right) \right)^2 dx. \quad (2.8)$$

We need to compare normalized variance of $\eta(t)$ (2.5) or (2.8) depending on the noise power α with the experimental results in the range of $\frac{f_h}{f_l}$. Good correspondence between the measured and calculated data should mean that the noise could be assumed as the stationary.

The Omega calibrator has been targeted by the FLIR and Heimann cameras, as it shown in [Figure 2.21](#). The regions of interest are highlighted as white rectangles. The sizes of ROIs are 11×11 for FLIR and 5×5 for Heimann. Time series for each pixel corresponds to the particular realization of the stochastic processes $\xi(t)$, which covers the whole ROI. The bandpass FIR filter order 777 has been chosen to cutoff the frequency; [Figure 2.22](#), clearly demonstrates the quality of the filtering.

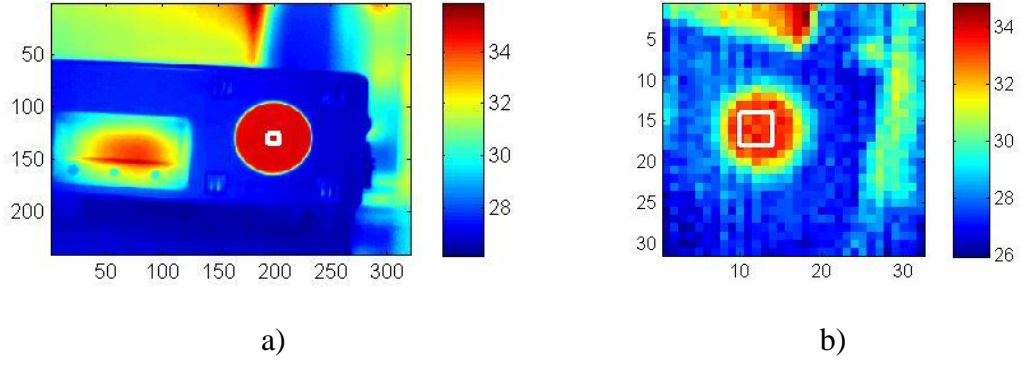


Figure 2.21. Selected ROIs for FLIR SC305 a) and Heimann 32x31 b)

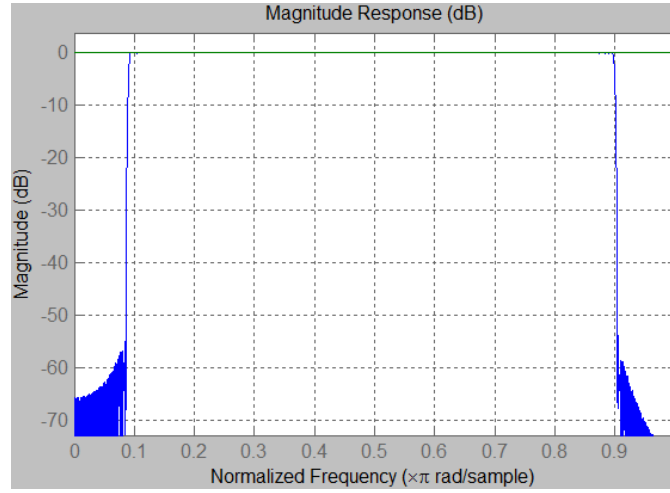


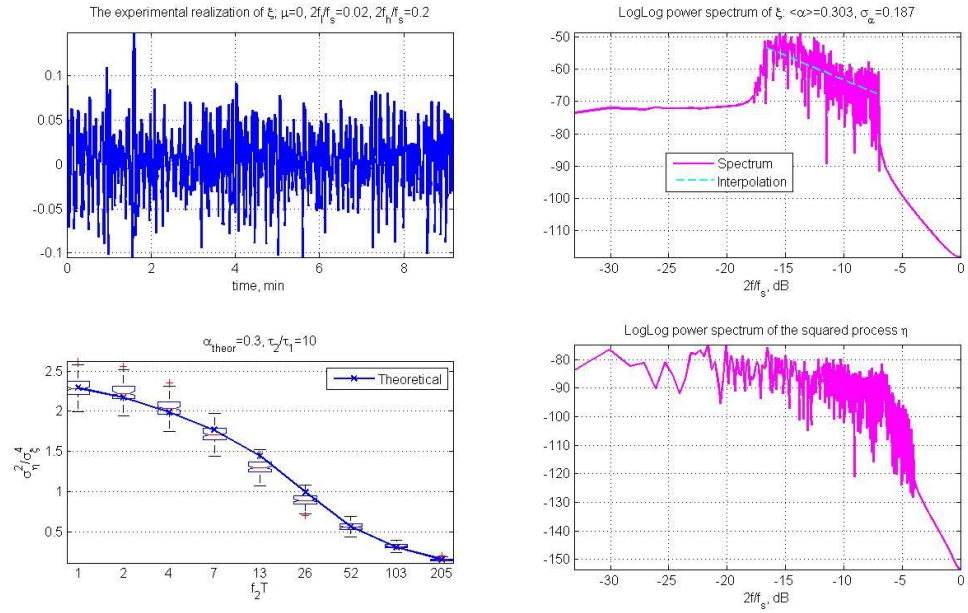
Figure 2.22. Frequency response of sample bandpass FIR filter order 777

[Figure 2.23.](#) and [Figure 2.24.](#) illustrate the results of the investigation of the band-limited noise of FLIR SC305 camera and Heimann 32x31 array correspondently. The plots containing 4 subplots correspond to the different ratio $\frac{f_h}{f_l} = \frac{\tau_2}{\tau_1}$. The top-left subplot represents a sample realization of the zero-mean band-limited stochastic process $\xi(t)$, the top-right one shows its power spectrum and linear interpolation in the frequency band, bottom right one stands for the power spectrum of $\eta(t)$, and the bottom left shows the correspondence between the experimental measurements of $\frac{\sigma_\eta^2}{\sigma_\xi^4}$ (box plots) and the corresponding theoretical values (solid blue line). In our investigation we didn't limit ourselves by fixing of the upper cutoff frequency f_h as has been proposed in [53], but did

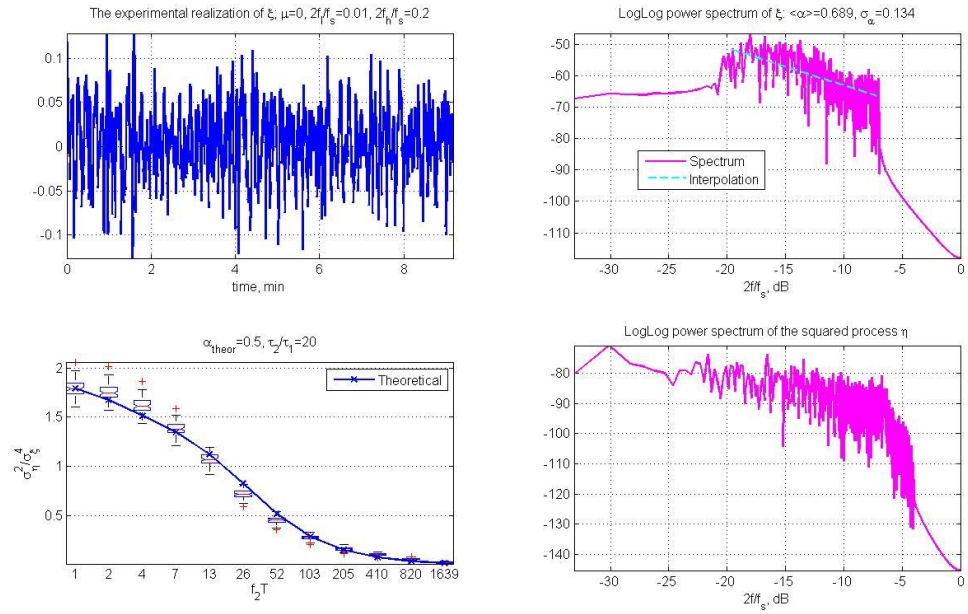
the investigations in the wide range of frequencies. Many similar plots are missed to save some space.

Observing the plots at [Figure 2.23.](#) and [Figure 2.24.](#) we made the following conclusions.

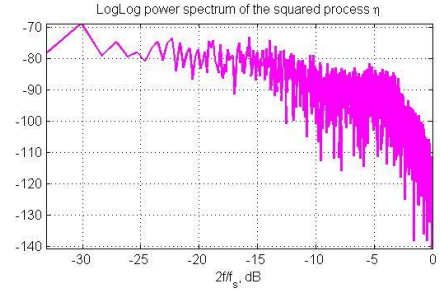
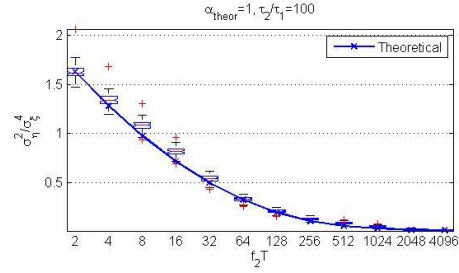
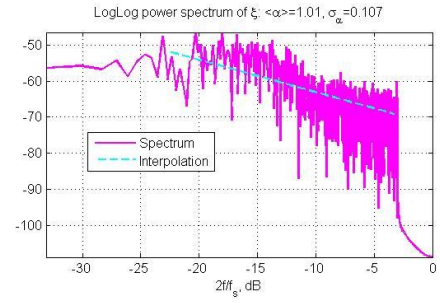
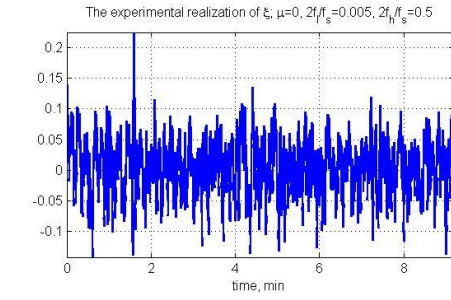
1. The experimental box plots are intersected by the theoretical curves in a wide range of frequencies. It means that the process can be assumed as the stationary, which is the most important conclusion.
2. The parameters α corresponding to the best fits are generally different for different frequency bands. They are within $0 < \alpha \leq 1$, so the assumption of the flicker noise is correct. α is greater for the higher frequencies, so the thermal noise is valuable on low frequencies, especially for the FLIR camera.
3. Unsurprisingly that the linear interpolation of the very noisy spectrum not always give a perfect estimation of α , especially for the less precise Heimann camera with the lower sampling frequency. The variance of the estimation is very big, see the header of the top right subplots. Instead of this, the power parameter α can be robustly estimated as the best fit of the theoretical curve and experimental values.



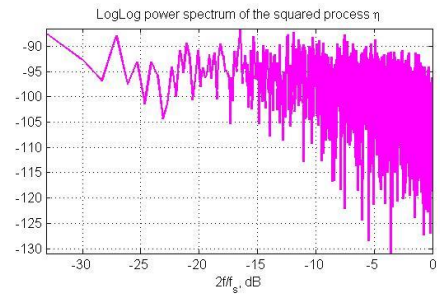
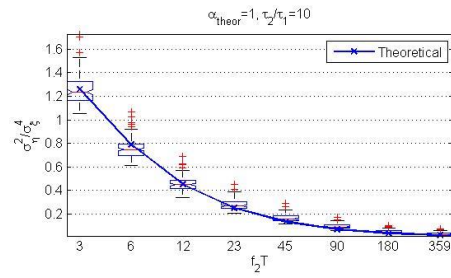
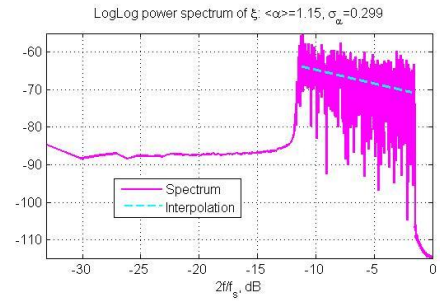
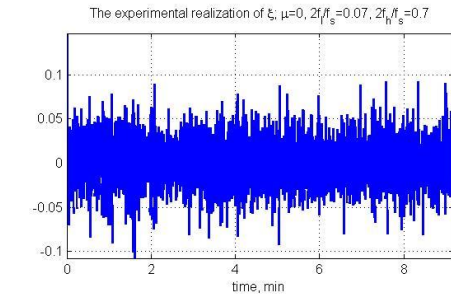
a) $\frac{2f_l}{f_s} = 0.02$, $\frac{2f_h}{f_s} = 0.2$, $\frac{f_h}{f_l} = 10$, $\alpha = 0.3$



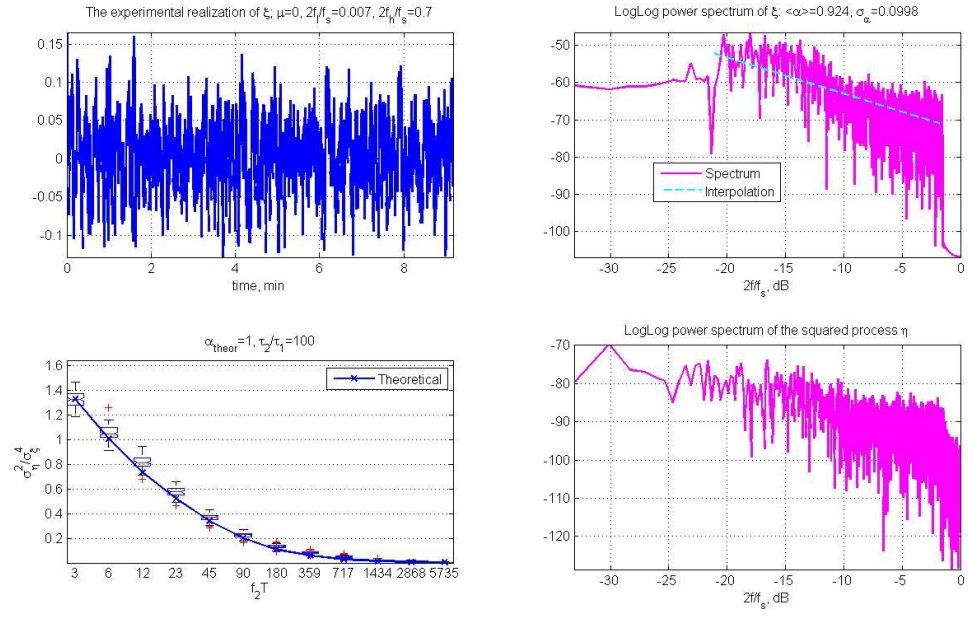
b) $\frac{2f_l}{f_s} = 0.01$, $\frac{2f_h}{f_s} = 0.2$, $\frac{f_h}{f_l} = 20$, $\alpha = 0.5$



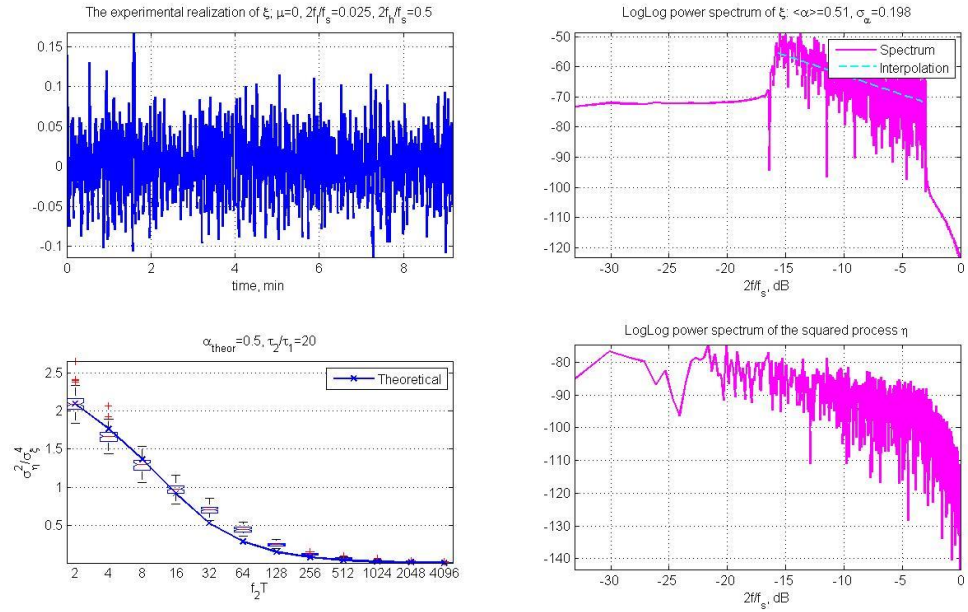
c) $\frac{2f_l}{f_s} = 0.005$, $\frac{2f_h}{f_s} = 0.5$, $\frac{f_h}{f_l} = 100$, $\alpha = 1.0$



d) $\frac{2f_l}{f_s} = 0.07$, $\frac{2f_h}{f_s} = 0.7$, $\frac{f_h}{f_l} = 10$, $\alpha = 1.0$

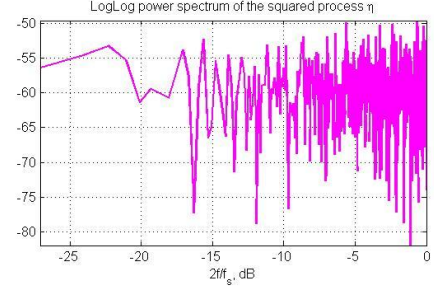
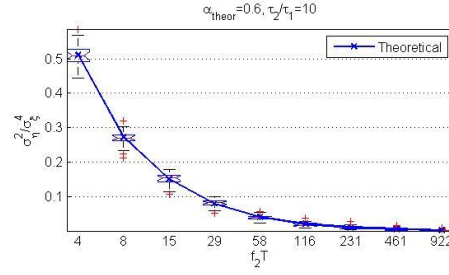
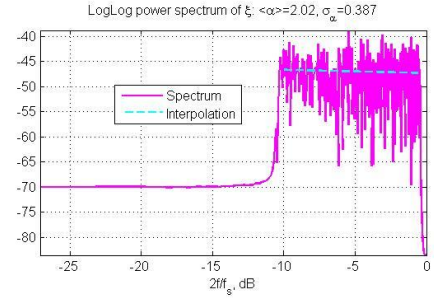
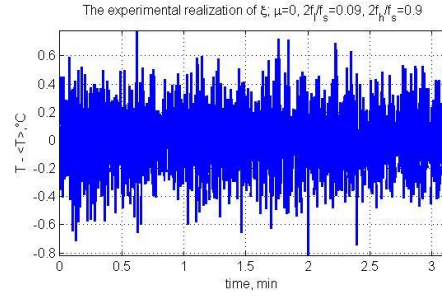


e) $\frac{2f_l}{f_s} = 0.007$, $\frac{2f_h}{f_s} = 0.7$, $\frac{f_h}{f_l} = 100$, $\alpha = 1.0$

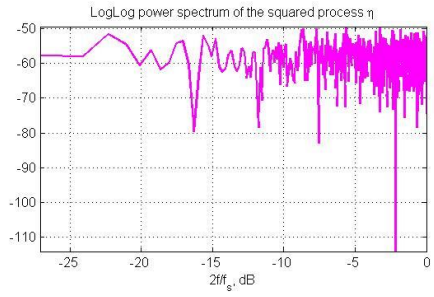
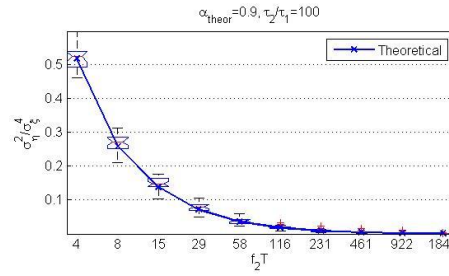
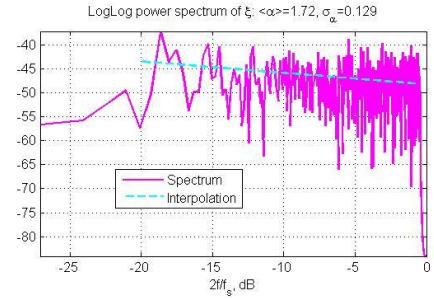
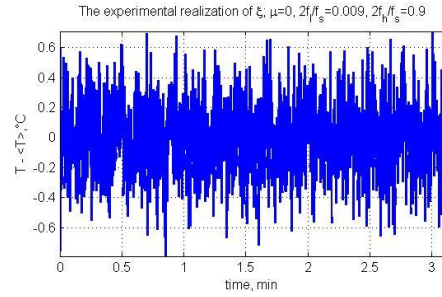


f) $\frac{2f_l}{f_s} = 0.025$, $\frac{2f_h}{f_s} = 0.5$, $\frac{f_h}{f_l} = 20$, $\alpha = 0.5$

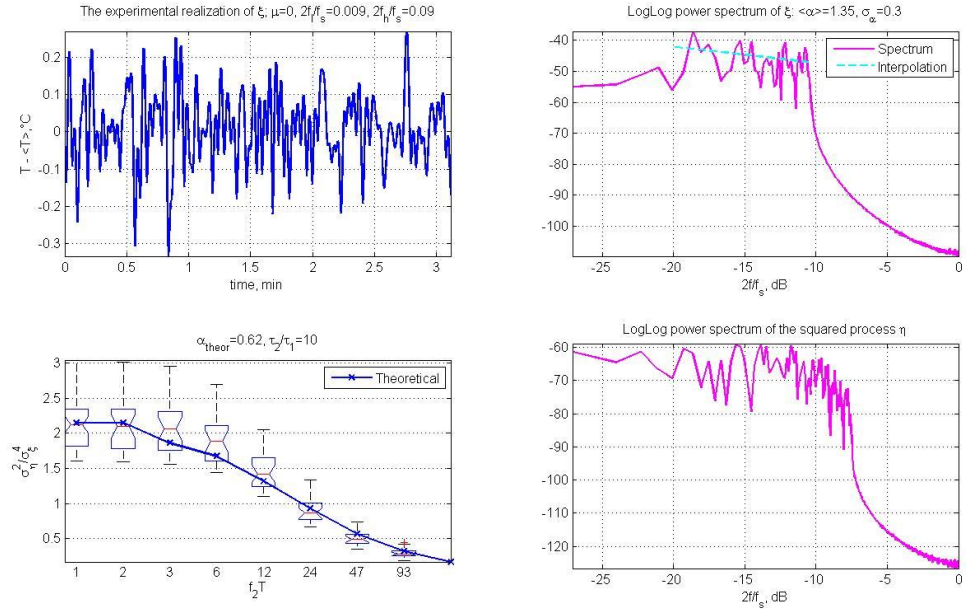
Figure 2.23. Invertigation of the stationarity of the FLIR SC305 camera noise.



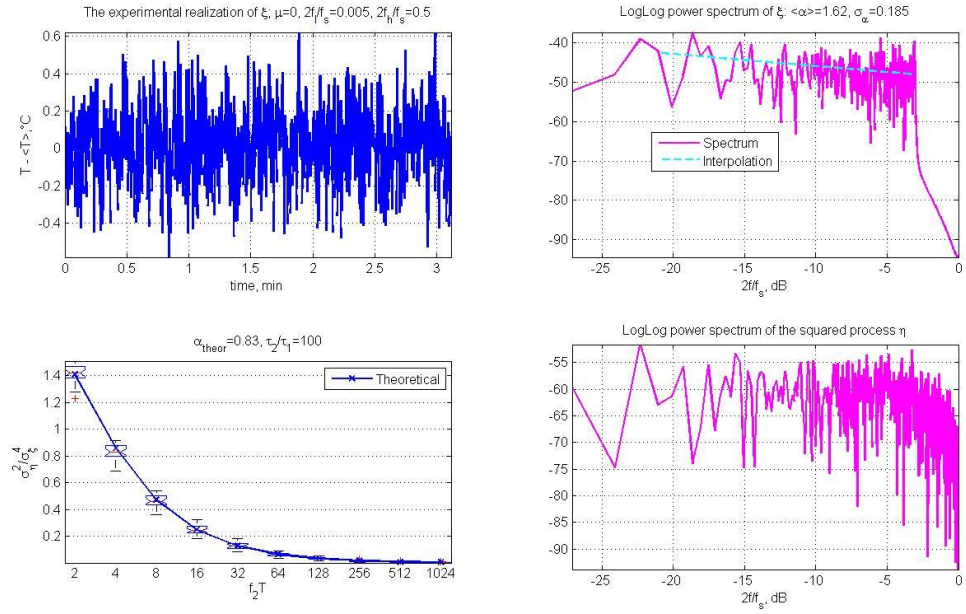
a) $\frac{2f_l}{f_s} = 0.09$, $\frac{2f_h}{f_s} = 0.9$, $\frac{f_h}{f_l} = 10$, $\alpha = 0.6$



b) $\frac{2f_l}{f_s} = 0.009$, $\frac{2f_h}{f_s} = 0.9$, $\frac{f_h}{f_l} = 100$, $\alpha = 0.9$



$$c) \frac{2f_l}{f_s} = 0.009, \frac{2f_h}{f_s} = 0.09, \frac{f_h}{f_l} = 10, \alpha = 0.62$$



$$d) \frac{2f_l}{f_s} = 0.005, \frac{2f_h}{f_s} = 0.5, \frac{f_h}{f_l} = 100, \alpha = 0.83$$

Figure 2.24. Invertigation of the stationarity of the Heimann 32x31 array noise.

2.7.4 Ergodicity of the noise

Proven the stationarity of the noise, we can simply prove the ergodicity in the mean just by comparing of means for different realizations. We should not anticipate the noise variance to be neither less than the cameras' accuracy, nor less than the black body's precision. BB is much more precise than the cameras, as it required for the calibration device, so we should be within the cameras' accuracy, and we are for all cameras we use.

2.7.5 The numerical model

As it has been noticed above, the $1/f$ power spectrum of the numerical model is modulated from the power spectrum of Gaussian white noise. We use the multivariate noise with the same correlation between the “pixels” of the model as we have for the experimental model. It is as stationary as the experimental signal, see for the illustration [Figure 2.25.](#) , and also naturally ergodic in mean. Thus, we have got numerical model of the random process, which has a very good correspondence with the original random process specific for each camera in the following terms.

- spectral density;
- auto-correlation and cross-correlation between the realizations, i.e. in multivariate statistical property;
- stationarity;
- ergodicity.

In other words, we have got the trustful numerical model, which can be used for the numerical simulation of the natural experiment.

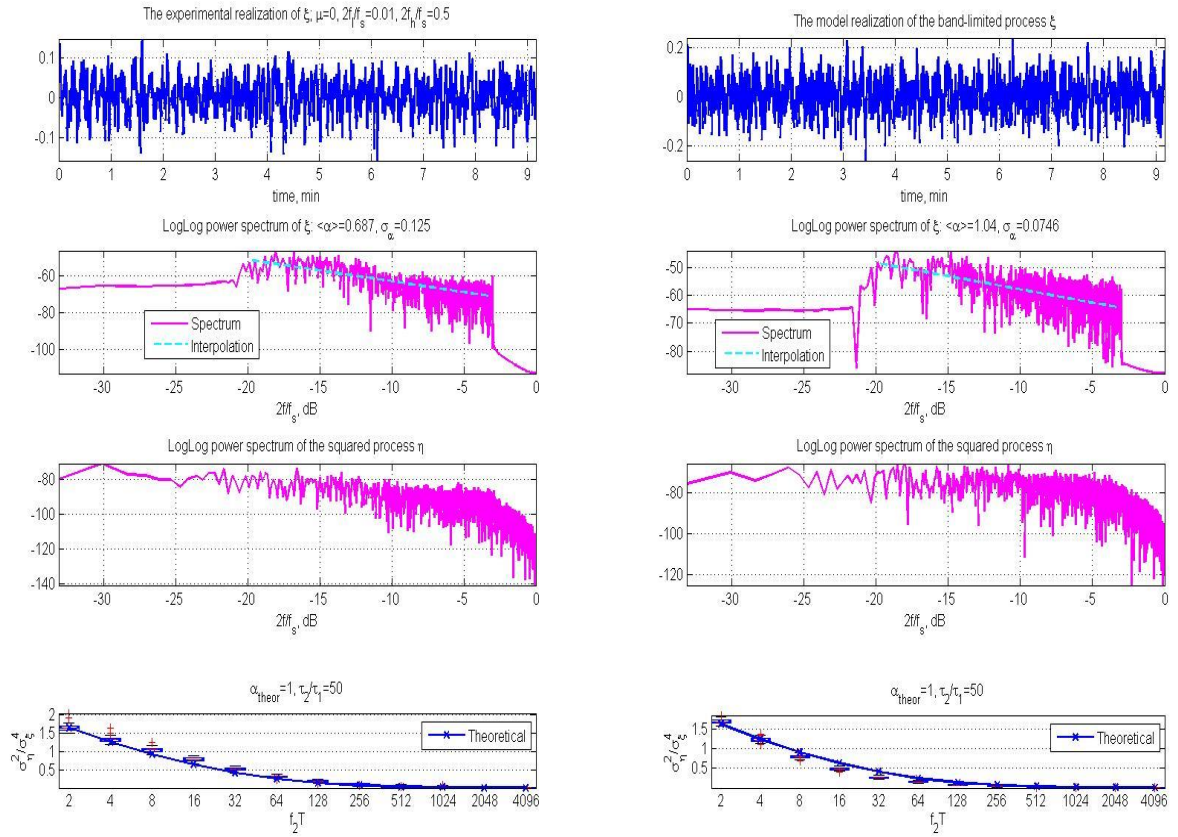


Figure 2.25. Comparison of the experimental data (left) and the numerical model (right) band-limited random processes: signals (up plots), power spectra (the 2-nd and the 3-rd ones), and variance of the $\eta(t)$ (lower ones) for stationarity.

Chapter 3 Basic Data Processing

After choosing the name for his Marionette, Geppetto set seriously to work to make the hair, the forehead, the eyes. Fancy his surprise when he noticed that these eyes moved and then stared fixedly at him.

Carlo Collodi. The Adventures of Pinocchio.

The basic data type is thermal IR video sequence. The nature of the input data determines the specifics of the processing. The current flowchart of the data processing is shown at [Figure 3.1](#). The “Capturing” block of the flowchart has been discovered in Chapter 2. This chapter describes next 5 blocks, namely “Preprocessing”, “Synchronization”, “Intermediate output”, “Registration”, and “Data extraction”.

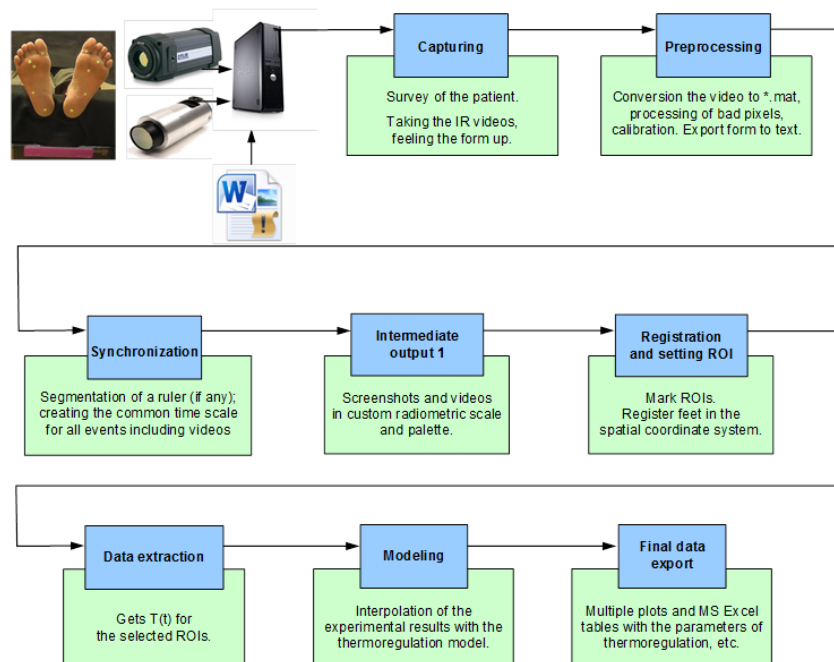


Figure 3.1. The flowchart of the data processing

3.1 Conversion to common data format

Some processing steps are not enough interesting to be described into the dissertation but necessary so must be at least mentioned. The main processing software tool is MatLab™ whereas the data from the cameras come in their original formats: binary for FLIR camera and text for other two ones. Thus, the first preprocessing step is conversion from these formats to *.mat MatLab™ format. Second, some data comes from the Word form. It includes the patient's diagnosis, age, sex and other survey parameters filled up manually. The form also contains the experiment parameters including the air temperature, the cold bath temperature, the beginning and end times of the cold stress. All this data is exported to the text format with the MS VBA script and later imported to MatLab. After all these steps, the MatLab data becomes a relatively complex structure with the fields containing contained video header, body, times of each frame, and the general parameters of the experiment.

3.2 Filtering

3.2.1 Adaptive spatial filtering

The “hot pixels” effect is known from the very first years of digital imaging [\[66\]](#). The same might happen with the particular microbolometers in the camera sensor array. Also it might happen not due to the hardware but because of the reflection. In our case the target, i.e. the feet assumed having pretty smooth surface temperature distribution. If one single pixel has very different intensity comparing to its neighbors, we assume that it should be filtered out. It might happen also on the sharp edge, so this case must be considered to prevent not required smoothing of the edge. The adaptive filtering algorithm

has been developed.

The term “adaptive filtering” means that the pixels should be processed quite not similarly but depending on their local properties [67][68]. In this case we want to process only detected “hot” pixels and leave all other pixels without any change.

The pseudocode of the algorithm is shown at [Figure 3.2](#).

```
For every image frame do
  Apply 5x5 median filter to the initial frame;
  Take the difference between the filtered and initial frames;
  Mark the pixels of the difference frame brighter than the given threshold as “noisy”;
  If any noisy pixels found
    Apply the Canny edge detector filter to the initial frame;
    Unmark the noisy pixels which belong to the edge;
  If any noisy pixels exist
    Exchange the values of the noisy pixels on the initial frame to the corresponding
    value of the median filter.
```

Figure 3.2. The algorithm of adaptive filtering

It must be noticed that the occasion of real hot pixels happen really rarely. See [Figure 3.3](#). for illustration.

3.2.2 ROIs

The points of the standard monofilament test (see Chapter [1.1](#)) can be pointed enough approximately. To reflect this and also to average the noise the temperature is averaging in the selected regions of interest (hereafter ROIs). It is possible due to the proven stationarity and ergodicity of the camera noise, see Chapter [2.7](#).

The chosen ROIs correspond to the one of the schemes of the monofilament test, namely the following: 1) big toe, 2) third toe, 3) ball, 4) inside arch, 5) lateral (outside) arch, and 6) heel. The ROIs placed above the foil stars used at the early set of experiments, see [Figure 3.4](#).

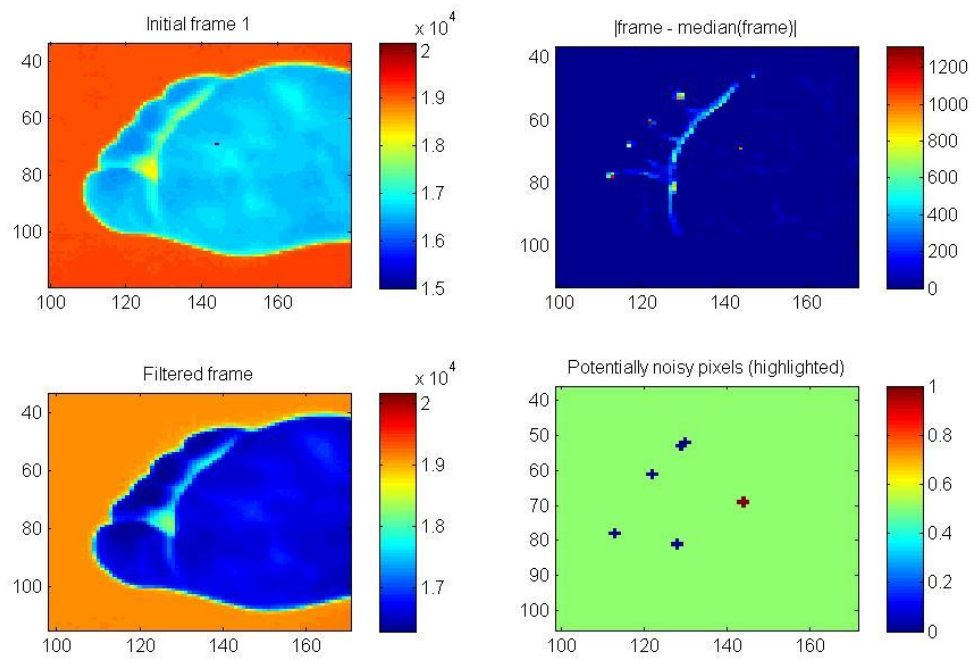


Figure 3.3. Adaptive filtering. Only one potentially noisy pixel (marked as red at the lower right plot) has been removed.

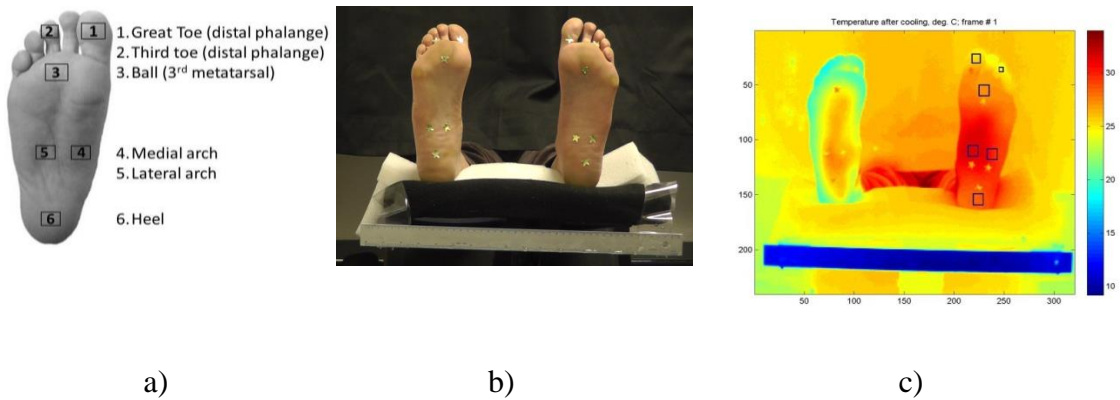


Figure 3.4. ROIs on foot a); feet images in visible band b) and FLIR SC305 screenshot c). ROIs marked with the black rectangles on a) and blue ones on c).

The filtering therefore means the averaging of each frame in ROIs. For the averaging, the round shape of ROIs has been chosen with the diameters 9 pixels for the big toe, 5 for the third toe and 21 for all other ROIs. Smaller size for the toe ROIs has been chosen to fit the toes and not to process the temperature in the space between them. These

sizes relate to the FLIR SC305 camera. Much lower resolution of the Heimann camera excludes the possibility to process the toes – they cannot be differentiated. Greater diameter of the ROI means less sensitivity to the spatial inaccuracy of registration. On the other hand, increasing the diameter reduces potential resolution. Thus, there is a technical contradiction for the relatively noisy and low resolution Heimann camera. The accuracy of registration for our Heimann camera is definitely worse than for FLIR SC305 due to noise and resolution; it requires increasing the diameter of ROIs, which contradicts with the lower resolution. Therefore, FLIR SC305 camera became the main measurement tool.

3.3 Temporal registration (synchronization)

All three cameras, i.e. FLIR, Heimann and low-cost IR screening system send the data to the computer, so they have common time scale. Each frame has the time of recording in the file headers. The events of beginning and ending of the cold stress registered manually by hitting the dedicated button at the MS Word experiment form with the VBA script, i.e. with 1 second accuracy. These data is automatically saved to text file after the end of the experiment and then imported to the main MatLab program. The sequence of the events in time for the setup with both FLIR and Heimann cameras looks like it is shown in [Figure 3.5.](#) . Zero ordinate values on plots correspond to absence of the corresponding event. First 3 minutes are for the control measurement (both cameras are on and overlapping in time, the Heimann camera has been switched off some later), 5 minutes for the cooling event, and then 15 minutes for the recovery after the cold stress.

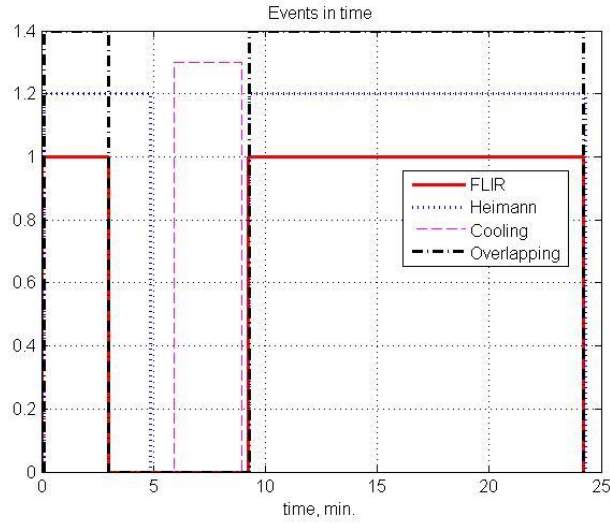


Figure 3.5. Sequence of the events during the experiment in time.

It might also happen that the setup includes the cameras without common time scale. For example, one of them could save the video to the internal memory. It is possible to synchronize the times on computer and external camera, but usually within 1-second accuracy. It could be enough for some applications, but not enough, say, for stereo video. For this case the “clapperboard event” should be introduced.

We used Panasonic RGB camera with internal memory at the early stage of the experiments. Thus, the clapperboard event should be easily recognizable and automatically detectable with both visual and thermal infrared bands. To satisfy this requirement, we either put the cold ruler or the hand with the piece of ice into the field of view trying not to shade the target, i.e. the foot.

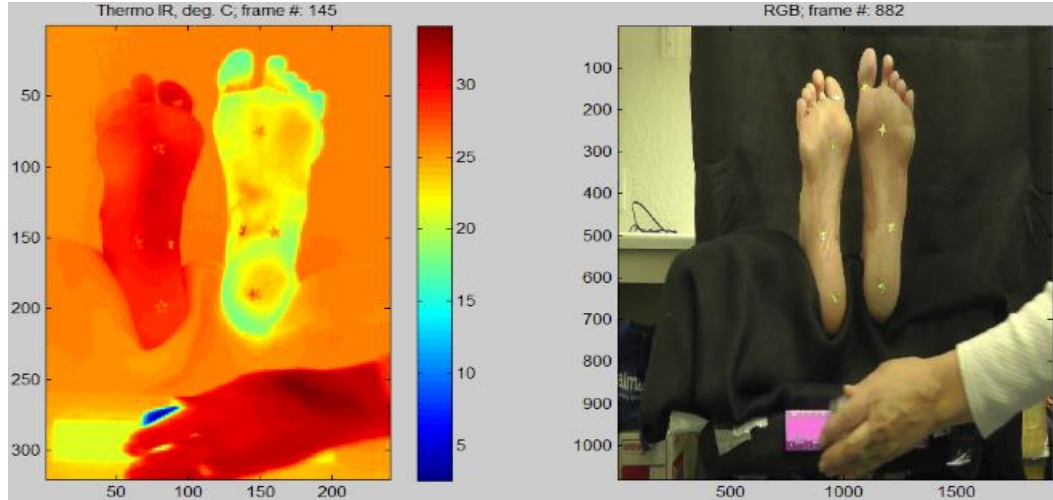


Figure 3.6. Synchronization of IR (left) and RGB (right) videos.
Observe a cold piece of ice (dark blue, colder than 5°C on the left subplot) in the warm hand.

The videos can be synchronized automatically by correlating the intensity change in IR and RGB. To increase the accuracy and robustness and also to simplify it, the event should happen in the certain part of the field of view. In our case we analyze the intensity change on the metal ruler at the low part of the frames. It is very contrast in both visible and thermal IR bands, see [Figure 3.6.](#) and [Figure 3.7.](#) .

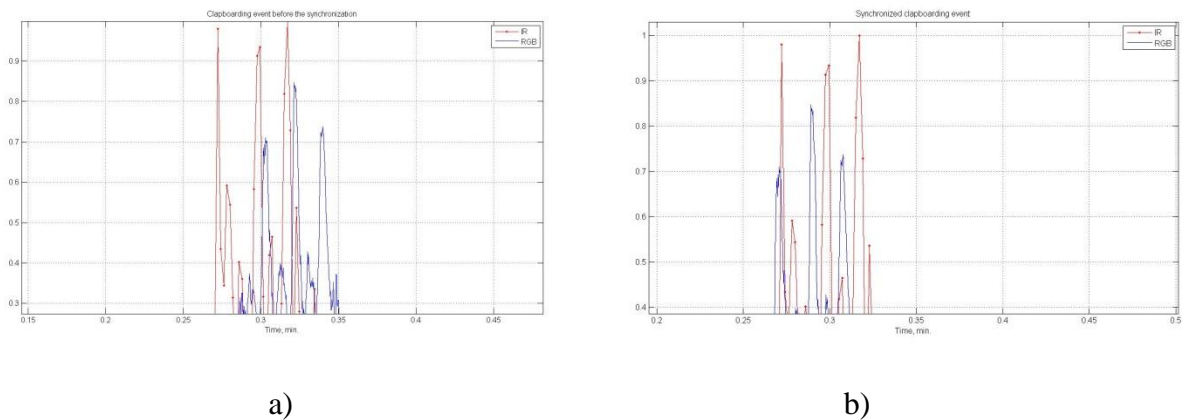


Figure 3.7. Intensity change due to the clapperboard event before a) and after b) the synchronization.
Red plots are for the thermal IR, blue ones for the visible band.

3.4 Spatial registration and tracking

3.4.1 Problems and requirements

In the current experiment setup, the patient's feet are placed on the feet support with no location. It is impossible for the subject to keep the feet still for 15 minutes while the IR camera is videotaping the recovery. Thus in order to extract the temperature recovery for each point on the foot, the IR video needs to be segmented and registered to establish the correspondence between the same position on different frames. We call this process spatial registration and tracking. Precisely, by registration, we need to segment (i.e., delineate) the foot on each IR video frame and transform (i.e., translate, rotate, scale, shear, *etc.*) the segmented foot to a common coordinate system [69], so that the same point on the foot can be tracked.

The main requirement to the registration is spatial accuracy. The six ROIs as described in the previous chapters can be used to quantify the accuracy of the registration process. Ideally, one would like to achieve a one-pixel spatial accuracy.

Note that one-pixel accuracy means approximately $\frac{1}{2}$ overlap of the true and measured ROIs with the diameter 5 pixels for the small toe; $\sim\frac{1}{4}$ for the big toe with the diameter 9 pixels, and $\sim\frac{1}{10}$ for the rest 4 ROIs with the diameter 21 pixels. That's why the smallest ROIs - the toes - are the most sensitive to the motion, especially if their motion is quite independent to the motion of whole foot.

3.4.2 Affine model of the spatial feet deformation

The IR image of a subject's foot is obtained by projecting the foot, a 3D object onto the 2D sensor plane of the camera along the optical axis. From our experience, the

dominating movement of the foot during the imaging process is clockwise or counterclockwise rotation around the heel. Assuming that the optical axis of the camera is perpendicular to the foot plantar, the rotation of the foot is best modeled by translation and rotation. Another type of motion that also occurs is the inclination of the foot toward and away from the imaging plane along the optical axis due to muscle relaxation. The inclination is best modeled to scaling.

From the above discussion, it is clear that the foot movement should be represented using affine transform [70]. Let $f_R^1(x, y)$ to be the reference image of segmented foot on the 1-st video frame, $f^i(x, y)$ be the segmented foot on i -th frame, and $A(x, y|\mathbf{a}) = \begin{bmatrix} a_1 & a_2 & a_3 \\ a_4 & a_5 & a_6 \\ 0 & 0 & 1 \end{bmatrix}$, be the affine transformation from $f_R^1(x, y)$ from the 1st frame to the i -th frame $f^i(x, y)$, where \mathbf{a} is the set of the parameters a_1, a_2, \dots, a_6 . It is clear that the optimal affine transformation A should minimize the difference or discrepancy between the transformed foot $A \circ f_R^1$ and the segmented foot f^i , i.e.,:

$$\mathbf{a} = \operatorname{argmin} \|f^i, A(x, y|\mathbf{a}) \circ f_R^1\|, \quad (3.1)$$

where $\|f^i, A(x, y|\mathbf{a}^i) \circ f_R^1\|$ is the metric for measuring image discrepancy. As a concrete example, for the simplest case the affine transformation accounting for only translation and rotation is:

$$A = \begin{bmatrix} \cos(\theta) & -\sin(\theta) & a_x \\ \sin(\theta) & \cos(\theta) & a_y \\ 0 & 0 & 1 \end{bmatrix}, \quad (3.2)$$

and

$$\mathbf{a} = \{a_x, a_y, \theta\}. \quad (3.3)$$

It must be noted that the affine transform approach assumes the foot is a rigid body and cannot account for motions such as bending of the foot arch or toe movement. These types of motions can only be accounted for using more complex model (like, for example, morphing [71]). Fortunately, from our experience, affine models are sufficient for our purpose.

3.4.3 Foot segmentation on the first video frame

Rough segmentation of the feet requires Canny edge detecting [72], filling the contours up, analysis of the size and position of the filled contours. The idea is to minimize false positives for the markers at the background analyzing just the segmented areas.

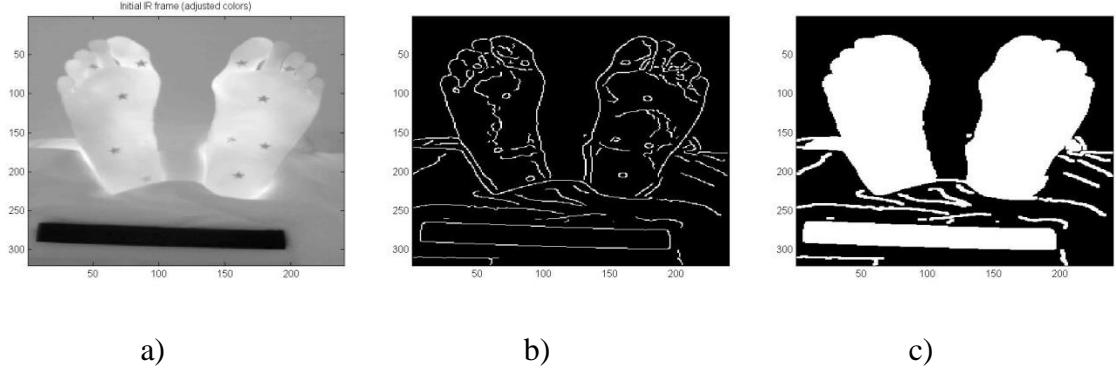


Figure 3.8. Step 1. Segmentation of feet and ruler.
Initial image a), Canny filtered b), and segmented objects c).

3.4.4 Registration and tracking via detected markers

We have experimented with several different techniques of calculating the affine transformation matrix. Our first idea is to take advantage of the ROIs, which are marked with reflective foils. The main idea to segment these ROIs on each video frames and use the locations of the ROIs to calculate the transformation matrix.

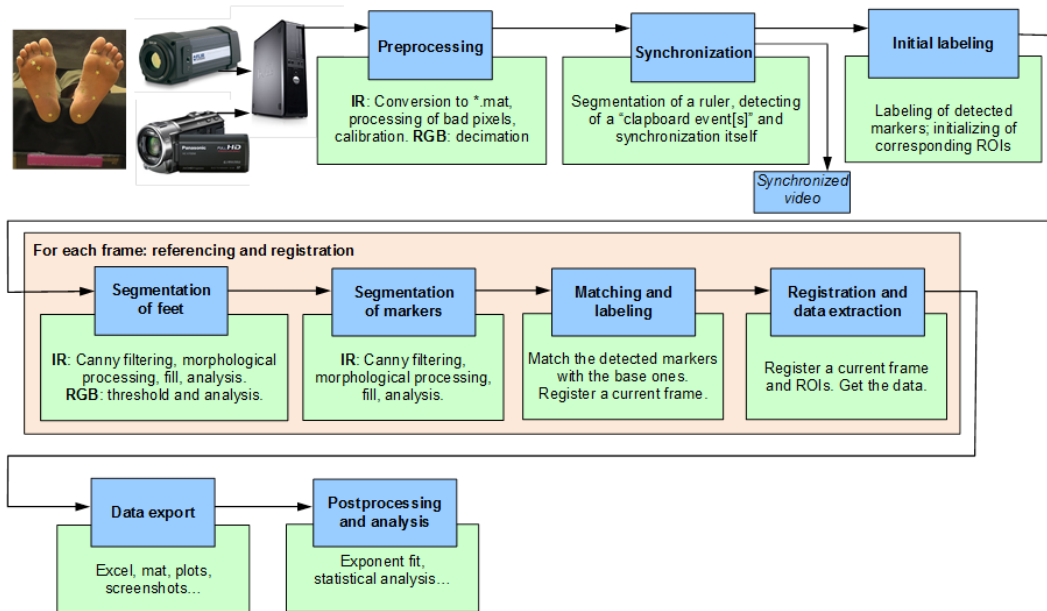


Figure 3.9. The flowchart of the data processing.
Referencing and registration via detected markers highlighted at the second row of blocks.

The main challenge for this method is the segmentation of the reflective foils. Since the foot temperature changes throughout the recovery phase, the reflecting marker may be different on the next frame because it is reflecting a very different environment. The markers are not flat, so additional fragmentation of the markers is possible as well. Markers are less contrast on the cooled feet because the feet temperature becomes closer to the temperature of environment.

To segment the markers, we use Canny edge detection and morphological processing to obtain closed contours of the reflecting stars. This may produce false positives (marked as blue dots at [Figure 3.10.](#)). The temporal information from adjacent video slices has been used to filter out the false positives.

The frames with the number of matched objects less than 3 to be omitted. It could happen by obstacles or just by bad reflection of some markers at particular frame.

Nevertheless, some frames could be taken into account even with the obstacles.

So, the next step is matching of the detected markers to the initial set. Assuming smooth feet movement, we first find the detected potential markers closest to the given set of labeled markers (base points); select by distance. By this we clear away some dots distant from the previous set of markers.

Our final affine transformation is calculated with Procrustes analysis, which determines a linear transformation of the points from the initial video frame to best conform them to the points in the other frames [73][74]. The goodness-of-fit criterion is the sum of squared errors. Note that, we opted not to perform a frame-by-frame transform to avoid the cumulative errors.

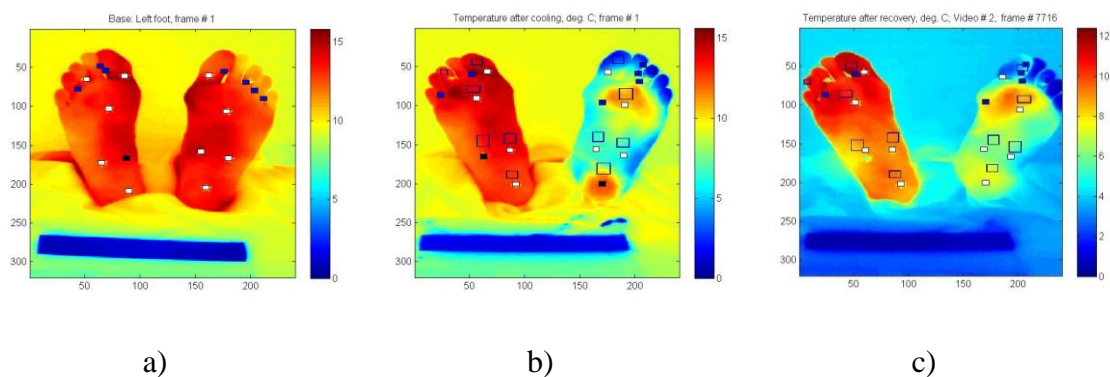


Figure 3.10. Detected markers a), markers and initial ROIs b), and ROIs at the last frame.
True markers highlighted as white dots, omitted one as blue and non-recognized as black ones.
ROIs highlighted as blue rectangles.

3.4.5 The cross-correlation registration and tracking

The other method for generating the affine matrix that we have tried is the cross-correlation method [73][74]. In this method, a rectangular reference window is first selected on the first frame of the video. The goal of the registration is to identify the windows corresponding to this reference window on each subsequent video frames. This

is achieved by “shifting” the reference window around on each remaining frame to maximize Person’s correlation coefficient [75], [76]:

$$R = \frac{1}{n-1} \sum_{j=1}^n \left(\frac{X_j - \bar{X}}{s_X} \right) \left(\frac{Y_j - \bar{Y}}{s_Y} \right), \quad (3.4)$$

where X, Y are the two rectangular regions in two different frames, \bar{X}, \bar{Y} are the means, and s_X and s_Y are the standard deviations. The rectangular regions identified on each image frame will produce the affine transformation matrix that accounts for translation and rotate between successive frames and thus register all the frames. In our research, the reference window(s) were the regions of the feet with high contrast such the big toe and the heel.

3.4.6 Comparison of the methods

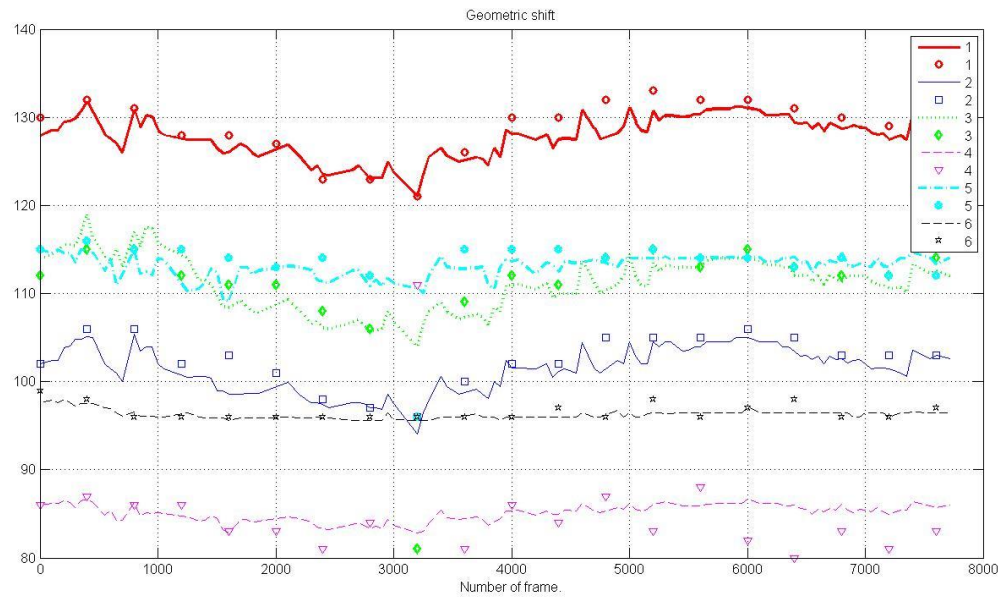
To quantify the accuracy of the two tracking algorithms, we have manually segmented the reflecting foils on each video frames, and applied the affine transformation matrix calculated by the tracking algorithm. The results are shown in Figure 3.11. As can be seen, both tracking algorithms works well and fast and can achieve within 1-2 pixels accuracy. It is also worth noting that the correlation based tracking algorithm is much faster than the ROI based algorithm. However, the correlation-based algorithm doesn’t take into account of scaling and shear.

Tracking by detection of markers program is less sensitive to the warming because the algorithms based onto the contour segmentation are used, but is more sensitive to the noise, which affects the shape and contrast of the stars, like the speckle noise. The cross-correlation registration program is more sensitive to the smooth change of intensity, i.e. cooling. To avoid this, the shifted referencing frame number has been introduced, i.e. not

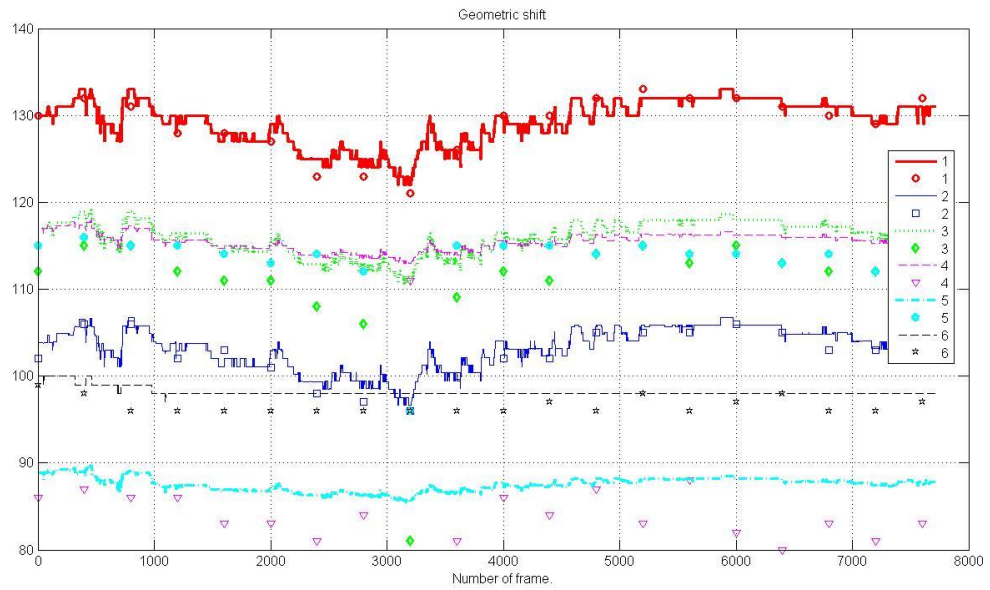
necessarily 1-st, default is 1500 (of ~7720 total). The program is also sensitive to the changes behind the feet as far it can be within the regions of cross-correlation.

By manual testing of the cases above (measuring the distance from the center of the corresponding star to the position of the label in the selected frames, see [Figure 3.11.](#)) one can conclude that in the case of smooth and contrast images, both programs are almost equally precise.

The cross-correlation registration program is more sensitive to the smooth change of intensity, i.e. cooling. To avoid this, the shifted referencing frame number has been introduced, i.e. not necessarily 1-st, default is 1500 (of ~7720 total). The program is also sensitive to the changes behind the feet as far it can be within the regions of cross-correlation. The geometric accuracy of the segmentation is within 1-2 pixels, which is sufficient considering the diameters of the ROIs are around 11-13 pixels. The impact of radiometric error due to the geometric inaccuracy is about 0.1 °C.



a)



b)

Figure 3.11. Geometric shifts in horizontal direction for the tracking by detection of markers a) and CCF b). Solid lines are the coordinates of the markers detected by the programs; dot lines for the actual coordinates measured manually.

The cross-correlation registration program runs for less than 13 minutes. Is a clear winner – more than 10 times faster even taking into account that other program process two files and two feet. For the acceleration the decimation parameter is introduced into the tracking by detection of markers program, i.e. it may track not each frame. It works well for the smooth movement but not for the sharp ones. The cross-correlation registration code is also much simple: just two functions vs. 50. Therefore, the cross-correlation program has been chosen as default registration and tracking tool. In the problematic cases the detection of markers program should be tried. If it not helps the whole video should not be considered.

Chapter 4 Heat transfer model

“Kant’s proof,” objected the educated editor with a thin smile “is also unconvincing. And not for nothing did Schiller say that the Kantian arguments on the question could satisfy only slaves, while Strauss simply laughed at that proof...”

“This Kant should be taken and sent to Solovki [*the concentration camp*] for two or three years for such proofs!” Ivan Nikolayevich blurted out quite unexpectedly...

“Precisely, precisely,” the foreigner shouted, and a twinkle appeared in his green left eye, which was turned towards Berlioz, “that’s the very place for him! I said to him then over breakfast, you know: ‘As you please, Professor, but you’ve come up with something incoherent! It may indeed be clever, but it’s dreadfully unintelligible. They’re going to make fun of you.’”

Berlioz opened his eyes wide. “Over breakfast... to Kant? ... What nonsense is this he’s talking?” he thought.

Mikhail Bulgakov, *The Master and Margarita*.

4.1 Motivation

Once the thermal infrared video is processed, the temperature changes of each point on the foot is extracted (see [Figure 4.1](#)). Time zero on the plot marks the end of the cold stress and the beginning of the recovery. In this chapter, we discuss how to extract quantitative properties of these curves for differentiating diabetic foot subjects using our heat transfer model.

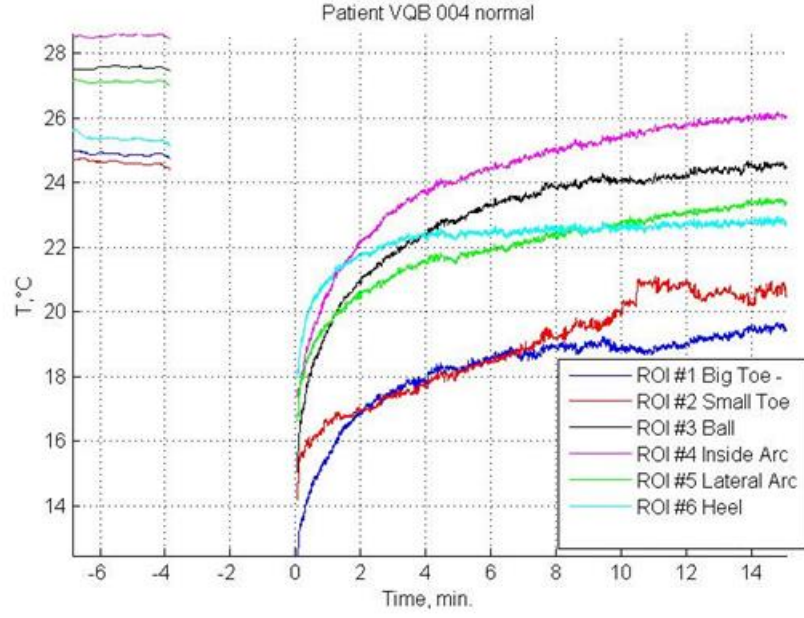


Figure 4.1. Sample set of temperature curves extracted for 6 ROIs.

The temperature data extracted are noisy. In addition to the high frequency $1/f$ camera noise discussed at Chapter 2.4 there is low frequency (LF) noise induced by the movement of feet, which is not fully compensated by the tracking. The data must be further processed before classification. This is clearly a model-based curve-fitting problem. Our first model used is the Newton's Law of Cooling [105]:

$$\frac{\partial T(t)}{\partial t} = -k(T(t) - T_A) \quad (4.1)$$

In this ordinary differential equation (ODE), $T(t)$ describes the temperature changes over time t , T_A is the ambient temperature, i.e., core body temperature, and k is a constant.

The differential equation (4.1) has a simple analytical solution (4.2), illustrated with Figure 4.2:

$$T(t) = T_A + (T_0 - T_a)e^{-kt} \quad (4.2)$$

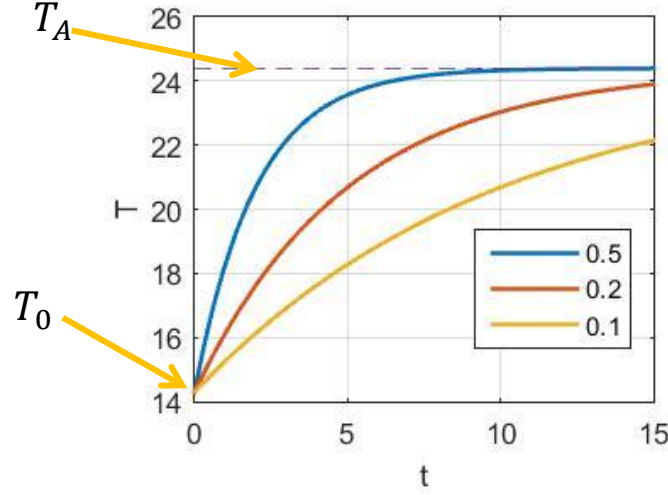


Figure 4.2. Illustration of the Newton's Law of cooling: the set of plots with different k .

The curve fitting is modeled using the following least square optimization:

$$\{k, T_0, T_A\} = \underset{\text{subject to } lb \leq \{k, T_0, T_A\} \leq ub}{\operatorname{argmin}} \{\|T(t) - T_{measured}(t)\|_2^2\} \quad (4.3)$$

where lb and ub are lower and upper bounds for the vector of parameters.

The curve fitting results using the Newton's Law of Cooling is shown in [Figure 4.3](#), where the X-axis is time in minutes and the Y-axis is temperature in °C. The experimental data is the zigzagged curve in red and the extrapolation is smooth curve in blue. The parameters T_0, T_A, k are determined using nonlinear least square (4.3) [78]. To verify the quality of the curve fitting, we removed the first 0, 0.5, 1 and 1.5 minutes of temperature data and compared the extrapolations with original data. The extrapolation error for T_0 at the beginning of recovery is 0.5-1.5 °C is much greater than the camera accuracy, making the extrapolation result not satisfactory. We believe the reason is that the Newton's Law of Cooling only considers heat transfer between objects of different temperature, but doesn't consider thermal regulation such as increasing or decreasing the

blood flow as in the human body. To overcome this, we decided to use the Pennes' Bio-heat Transfer Equation to model the recovery process.

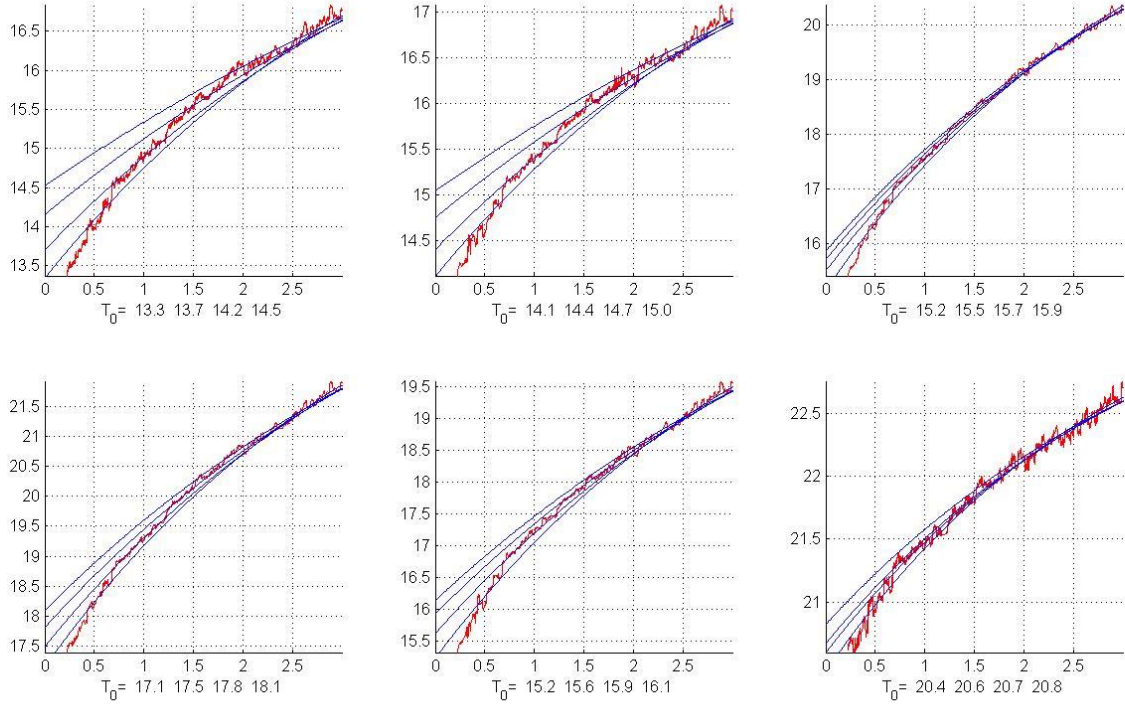


Figure 4.3. Extrapolation of the experimental data with Newton's Law of Cooling. The same experiment, 6 plots for 6 ROIs. T_0 -s are the extrapolated temperatures at $t = 0$ for removed 0, 0.5, 1 and 1.5 min. of the experimental data.

4.2 The Bio-heat Transfer equation

The heat transfer between the tissue, blood and environment is commonly described by the Pennes' Bio-heat Transfer Equation [79][80] with the assumption of uniform environment and tissue-independent blood temperature. We will modify it to fit the conditions of our experiment, and to take the thermoregulation effect into account.

$$\begin{cases} V\rho c \frac{\partial T}{\partial t} = \nabla(\chi \nabla T) + (\rho c)_b \omega_b (T_b - T) + (\rho c)_e \omega_e (T_e - T) \\ \quad \quad \quad + q_m + q_{rad} + q_{vap} \\ V_e(\rho c)_e \frac{\partial T_e}{\partial t} = (\rho c)_e \omega_e (T - T_e) - q_{rad} - q_{vap} \end{cases} \quad (4.4)$$

In the above equation, $V [m^3]$ is volume, $T [^\circ K]$ is temperature, $c [J * kg^{-1} * ^\circ K^{-1}]$ is heat capacity, $\rho [kg * m^{-3}]$ is density, and $\chi [J * m^2 * sec^{-1} * ^\circ K^{-1}]$ is surface thermal conductivity. The variables without subscript are related to tissue. The subscripts b and e stand for blood and environment, correspondently; $\omega_b [m^3 * sec^{-1}]$ represents blood perfusion, and $\omega_e [m^3 * sec^{-1}]$ is environment (air) perfusion. $q_{rad} [J * sec^{-1}]$ is the radiant heat, $q_m [J * sec^{-1}]$ is metabolic volumetric heat, and $q_{vap} [J * sec^{-1}]$ (always negative) is the evaporative heat.

The equation (4.4) has too many unknowns and is too complicated to be directly useful. Moreover, in our experiments we measure just a few variables, so just we don't have enough data to estimate the parameters in such a multiparametric equation. Our approach is to simplify it by emphasizing the main thermoregulation mechanisms.

The first equation of (4.3) shows the energy transfer in tissue per unit time. The radiant term following Stefan-Boltzmann law [\[81\]](#) is:

$$q_{rad} = \varepsilon \sigma (T^4 - T_e^4) A_e \quad (4.5)$$

In our experiments, minimal value for T is $13 ^\circ C$; maximum for T_e is $25 ^\circ C$. Assume the foot surface area $A_e = 0.03 m^2$, $\varepsilon=1$, and a foot mass of 1 kg with its mass-specific capacity close to the mass-specific capacity of water $c_w = 4181.3 J/kg/^\circ K$, σ is a Stephan-Boltzmann constant, we can estimate the warming up from the radiant heat to be no more

than 0.03 °C per minute, which is negligible.

The evaporation term is:

$$q_{vap} = m_w c_w / dH \quad (4.6)$$

where m_w is the mass of evaporated water, and dH is the enthalpy of vaporization.

Thus, assuming $c \approx c_w$, about 2g of water need to be evaporated to cool down 1 kg foot by 1 °C, and therefore can also be ignored in the frames of our experiment (for example, compare this value with [Figure 4.1](#)).

Further, we also can ignore the metabolic heat term due to the relative short time process [\[82\]](#).

Since, we are only measuring the surface temperature, 2-dimensional diffusion can be used. For the relatively small surface areas like ROIs we can ignore the diffusion term $\nabla(\chi \nabla T)$ assuming locally uniform surface temperature distribution. It means that we assuming the influence of near branch or branches of thermally significant blood vessels under the skin is much higher than the diffusion between the near pieces of skin surface.

The second equation of (4.4) shows the energy transfer in the environment per unit time. Our environment is the air-conditioned room; the room temperature almost does not change during the experiment. Thus let us assume $V_e \gg$, i.e. the perfusion of the air thermally interacted with the tissue ω_e is relatively slow to change the environment temperature in the room. Therefore, the environment temperature becomes constant: $T_e(t) = T_e(0)$, $\frac{\partial T_e}{\partial t} = 0$, and the second equation is neglected, too.

To summarize, the main contribution to heat transfer is given by the thermally significant blood vessels with diameter 0.08...1 mm [82],[83],[83]. Thus, the boundary-value problem in 3D space and time for the initial PDEs [85],[86] is reduced to the Cauchy problem for the set of ODEs with the given initial conditions: $T(0) = T^0$, and $T_e(0) = T_e^0$. Assuming that the regions of interests (ROIs) are mutually independent we obtain the number of similar ODEs each describing the particular ROI. The actual dependence between them, if any, could be determined later by statistical analysis.

Finally, the set of equations becomes the following ODE:

$$\frac{dT}{dt} = -r_b(T - T_b) - r_e(T - T_e) \quad (4.7)$$

where $r_e = \frac{(\rho c)_e}{V \rho c} \omega_e$ [sec⁻¹] is the characteristic of the body (foot) with respect to the external media, $r_b = \frac{(\rho c)_b}{V \rho c} \omega_b$ [sec⁻¹] that accounts for all the biological and thermal dynamical parameters responsible for the heat transfer between the blood and body, which will be discussed in details in the next section. Note that the equation (4.7) is equivalent to (4.1) so far.

4.3 The model of thermoregulation

4.3.1 The control theory approach

As it has been noted above, thermoregulation in humans exists and it is determined by microcirculatory function. We will model the thermal regulation in the terms of control theory.

The scheme of thermoregulation is shown in [Figure 4.4. a](#)). The foot (as a part of

a human body which shares the feedback via the nervous system) is assumed under the heat disturbance $T_e(t) = 1(t)$ at the zero time, i.e. at the end of the cold stress, see [Figure 4.4](#) a) and b). The controlled variable $T(t)$ is the foot temperature which is registered with the thermal IR camera, see [Figure 4.4](#) c). Here $1(t)$ is the unit step function, or the Heaviside function (also denoted sometimes as $u(t)$), i.e.

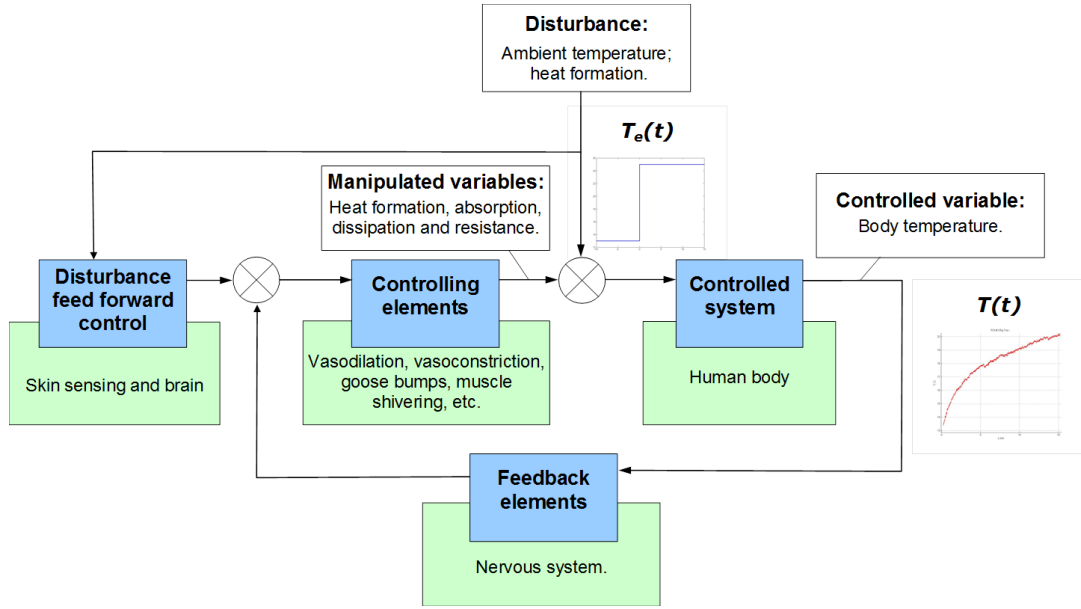
$$1(t) = \int_{-\infty}^{\infty} \delta(t) dt,$$

where $\delta(t)$ is the Dirac unit function.

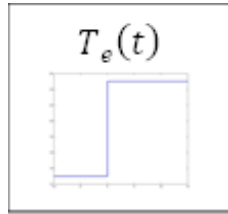
The transmitting response $W(p)$ of the scheme [Figure 4.4](#) a) is [\[87\]](#), [\[88\]](#):

$$W(p) = \frac{W_1(p)}{1 - W_1(p)W_0(p)} \quad (4.8)$$

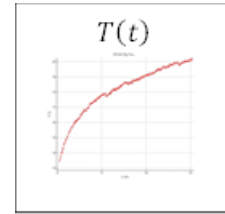
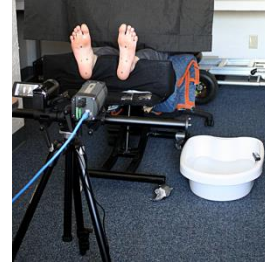
where $W_0(p)$ is the transmitting response of the feedback elements, $W_1(p)$ is the transmitting response of the rest elements, and p is the Laplace operator, i.e. $\frac{d}{dt}$. Thus, one needs just to describe the corresponding elements of the controlling system. Since we can't measure the transmitting responses, we cannot measure the contribution of each particular controller such as vasomotion, sweating, or heat production separately. We can monitor just one controlled variable T and one disturbance variable T_e . Thus we must describe the thermoregulation system as a black box with the parameters noted above. For the modeling we may start from the simplest description of $W(p)$ as elementary plants.



a)



b)



c)

Figure 4.4. The model of human thermal regulation. The scheme a) illustrated with: input b) - environment temperature $T_e(t)$ at the end of cold stress as a unit step function, and controlled variable c) - measured tissue temperature $T(t)$.

The equations (4.1) and (4.7) have the same view of the transmitting response:

$$W_{\text{Newton's Law of Cooling}}(p) = \frac{b_0}{a_0 + a_1 p}, \quad (4.9)$$

where a_0 , a_1 , and b_0 are the coefficients. As far as we have a unit step function as

the input, our output is just the step response, which is:

$$h(t) = \frac{b_0}{a_0} (1(t) - e^{-a_0 t/a_1}) \quad (4.10)$$

Compare (4.2) and (4.10) to see that they are equivalent.

If the physical meaning of all above is clear, one may not read this paragraph. If this looks not very clear in terms of thermodynamics, let me describe the behavior of the electrical RC-circuit, [Figure 4.5a](#)), which is absolutely equivalent to our system in terms of control systems, i.e. it has the same transmitting response (4.8). The only difference is that for the electrical circuit the input and output have the physical sense of voltage, not temperature. In the terms of control systems this circuit is the system of the 1-st order and is the one of base plants, namely the inertial plant.

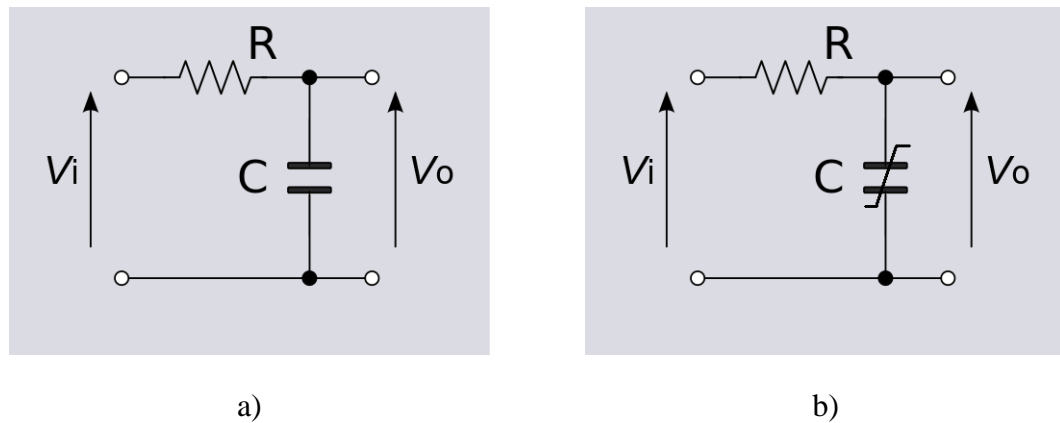


Figure 4.5. The 1-st order systems or inertial elementary plants: simple RC circuit a) and RC circuit with the parametrically changing capacity b).

The transmitting response of RC circuit is $W_{RC}(p) = \frac{b_0}{1+RCp}$ and the step response is $h_{RC}(t) = b_0(1(t) - e^{-t/RC})$. Compare these formulae with (4.9), (4.2), and (4.10) to see that they are correspondently equivalent. The physical (here electrical) meaning is the

following. RC -circuit is an analogous low-pass filter with the cutoff frequency $\frac{1}{RC}$. The high frequencies near the zero time pass through the capacity; later on, with some inertia, the capacity charges up. Or, if the input step is negative, the capacity is discharging through the resistivity by exponent with the same time constant factor equal to RC .

4.3.2 The control system of the second order

Let us come back to the experiment. Let us observe [Figure 4.3](#) again. At the beginning of recovery, the extrapolated temperature goes above the real one; later on it gives a good approximation. It means that the temperature stress turns the additional regulation on, and later it comes to naught. There is just one source of heat in (4.1) but two ones at (4.7): environment temperature and blood temperature. Thermoregulation means that the amount of heat exchange between blood and tissue is changeable, i.e. $r_b = \frac{(\rho c)_b}{V \rho c} \omega_b$ should be the function of time. For the liquid, which the human blood is, the change of density and thermal capacity $(\rho c)_b$ definitely can be neglected for such narrow temperature range; thus, we have to consider the change of blood perfusion $\omega_b(t)$. It makes the equation (4.7) parametric (don't confuse with non-linear!) [\[86\]](#). Similarly, comparing (4.7) and (4.1), we conclude the change of the cooling speed in time. Therefore, we can substitute the regulation parameter $r(t)$ instead of k to (4.1). By the way, in terms of electric circuits it corresponds to the RC circuit with the nonlinear capacity [Figure 4.5b](#)), and the capacity is the controlling object of the thermoregulation system.

Let us be more specific. Initial rapid increasing of the speed of cooling (or warming in our case) can be described with the following modification of (4.2) trying to keep it as simple as possible:

$$T(t) = T_A + (T_0 - T_A)e^{-k(1+Qe^{-st})t}. \quad (4.11)$$

So, we guessed the possible solution; let's find the corresponding parametric differential equation of the 1-st order. The following equation has (4.11) as the explicit solution:

$$\frac{dT(t)}{dt} = -k \left(1 + (Qe^{-st}(1 - st)) \right) (T(t) - T_A). \quad (4.12)$$

Denote the thermal interaction term $r_2(t)$ [sec^{-1}], i.e. the thermoregulation parameter as

$$r_2(t) = k \left(1 + (Qe^{-st}(1 - st)) \right). \quad (4.13)$$

The subscript “2” stands for the second order of the control system corresponding to this model. Let's describe the obtained heat transfer model with thermoregulation (4.11-13). As before, T_0 is the initial temperature, T_A is ambient temperature, dimensionless k is the stationary exponent factor, dimensionless Q is the intensity of regulation, and s [sec^{-1}] is the speed of regulation. The thermoregulation parameter has a view shown in [Figure 4.6 b](#)). Greater values of $|Q|$ mean bigger thermoregulation whereas the case $Q \approx 0$ should indicate absence of the thermoregulation, i.e. it exactly corresponds to the Newton's Law of Cooling (4.1). Also, greater values of s mean faster thermoregulation whereas $s \approx 0$ corresponds to the absence of regulation, which in our case may indicate peripheral neuropathy. It is easier to imagine values of s^{-1} in time units. One can observe that $r_2(t)$ asymptotically converges to the stationary value equal to k .

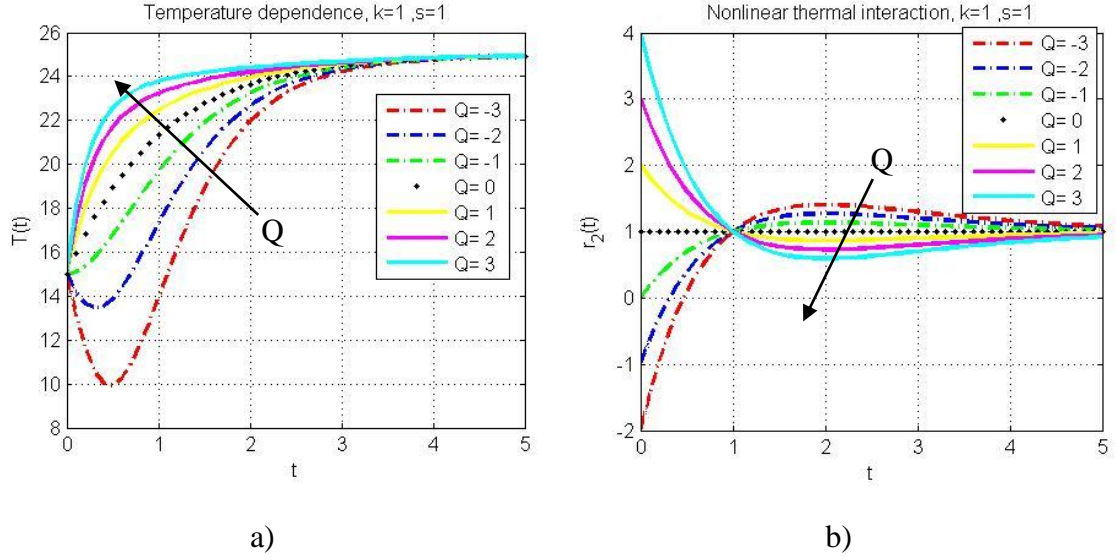


Figure 4.6. Sample plots (not related to any experiment) illustrating (4.10) a), and (4.12) b).

The scheme of the control system describing the thermoregulation exactly corresponds to the [Figure 4.4](#) a) except the controlled variable is not $T(t)$ but $r_2(t)$. One more time but in other words: this control system controls thermoregulation, not temperature. Also, the transmitting response $W_r(p)$ does not have a view (4.9) as far as (4.13) is not equivalent to (4.2). Generally, the intersection of $r_2(t)$ and the asymptotic line $t = k$ called overregulation or overshoot [89], [90] indicates that the control system has the order greater than 1 [88], [89], [90], [91], i.e. 2 in our simplest case. Thus,

$$W_{r_2}(p) = \frac{b_0 + b_1 p}{a_0 + a_1 p + a_2 p^2}. \quad (4.14)$$

At this point it is a good time to understand the physical meaning of the control system parameters. Let us re-parameterize (4.14) to the following view:

$$W_{r_2}(p) = \frac{\omega_0}{\beta} * \frac{p + \beta \omega_0}{p^2 + 2\zeta \omega_0 p + \omega_0^2}. \quad (4.15)$$

Here dimensionless β^{-1} is the coefficient of amplification, $\omega_0 = 2\pi f_0$ [rad *

sec^{-1}] is the resonant frequency parameter and determines the speed of response of the control system. Dimensionless ζ is the damping ratio (in mechanical terms) or inverse quality factor (in electrical circuit terms); it's very visual physical meaning is the ratio of the band pass to the resonant frequency. It determines the shape of response. So, a zero damping ratio, i.e. no damping in the systems of the second order correspond to non-decaying oscillations at the resonant frequency, or, if one wish, an infinite quality factor; increasing the damping ratio $0 < \zeta < 1$ means faster decay of the oscillations; the values $\zeta \geq 1$ correspond to non-oscillating systems.

Recall [88], [91] that formally the step response can be obtained as the inverse Laplace transform \mathcal{L}^{-1} :

$$\begin{aligned} h(t) = \mathcal{L}^{-1}[W(p)/p] &= \frac{1}{2\pi i} \int_{\rho-i\infty}^{\rho+i\infty} \frac{W(p)}{p} e^{pt} dp = \\ &= \sum_{j=1}^n \text{Res} \frac{W(p)}{p} e^{pt} \Big|_{p=\lambda_j}. \end{aligned} \quad (4.16)$$

Here λ_j is the j -th pole of the integrand (including of course the repeating ones, if any), n is the number of the poles, and

$$1/p = \mathcal{L}[1(t)]. \quad (4.17)$$

Thus, the step response of $W_{r_2}(p)$ is:

$$h_{r_2}(t) = \mathcal{L}^{-1}[W_{r_2}(p)/p] = \mathcal{L}^{-1} \left[\frac{\omega_0}{\beta} * \frac{p + \beta\omega_0}{p(p^2 + 2\zeta\omega_0 p + \omega_0^2)} \right] = \quad (4.18)$$

$$\mathcal{L}^{-1} \left[\frac{\omega_0^2}{p(p^2 + 2\zeta\omega_0 p + \omega_0^2)} \right] + \frac{1}{\beta\omega_0} \frac{d}{dt} \left(\mathcal{L}^{-1} \left[\frac{\omega_0^2}{p(p^2 + 2\zeta\omega_0 p + \omega_0^2)} \right] \right).$$

Obviously, the transmitting response of the 2-nd order system has two poles:

$$\lambda_{1,2} = -\zeta\omega_0 \pm \omega_0\sqrt{\zeta^2 - 1}. \quad (4.19)$$

If $\zeta < 1$ they are complex conjugate

$$\lambda_{1,2} = -\zeta\omega_0 \pm i\omega_0\sqrt{1 - \zeta^2}, \quad (4.20)$$

and thus the step response is:

$$h_{r_2}^{\zeta < 1}(t) = c_1 1(t) \quad (4.21)$$

$$+ c_2 e^{-\zeta\omega_0 t} \left(c_3 \sin(\sqrt{1 - \zeta^2}\omega_0 t) + \cos(\sqrt{1 - \zeta^2}\omega_0 t) \right).$$

Hereafter c_j are the constants depending on the initial conditions. It is clear that the $\sin(\sqrt{1 - \zeta^2}\omega_0 t)$ and $\cos(\sqrt{1 - \zeta^2}\omega_0 t)$ functions give the oscillations around the resonant frequency fading due to the real exponential term $e^{-\zeta\omega_0 t}$.

In the case $\zeta > 1$ the transmitting response has two different real poles and the 2-nd order control system can be decomposed to the sequence of two 1-st order plants. The step response is:

$$h_{r_2}^{\zeta > 1}(t) = c_4 1(t) + c_5 e^{-(\zeta + \sqrt{\zeta^2 - 1})\omega_0 t} + c_6 e^{-(\zeta - \sqrt{\zeta^2 - 1})\omega_0 t}. \quad (4.22)$$

The sum of two real exponents does not have oscillations; it is a monotonic function for big values of ζ .

Finally, $\zeta = 1$ gives two repeating poles; in this case the step response is the following:

$$h_{r_2}^{\zeta=1}(t) = c_7 1(t) + c_8 e^{-\omega_0 t} + c_9 \omega_0 t e^{-\omega_0 t}. \quad (4.23)$$

[Figure 4.8](#) shows the frequency response functions, the zero-pole maps and the step responses for all three cases. The parameters of the corresponding systems following (4.14) are shown in Table 4.1. Observing the step responses here and comparing them with [Figure 4.6 b](#)) one can see that $r_2(t)$ has overshooting but not oscillating, unlike the oscillating step response for $\zeta < 1$, also unlike the smooth step response for $\zeta > 1$, and exactly like the step response for $\zeta = 1$. Thus one can decide the transmitting response (4.15) has two repeated poles, and by substituting $\zeta = 1$ it can be simplified to:

$$W_{r_2}(p) = \frac{\omega_0}{\beta} * \frac{p + \beta\omega_0}{p^2 + 2\omega_0 p + \omega_0^2} = \frac{\omega_0}{\beta} * \frac{p + \beta\omega_0}{(p + \omega_0)^2}. \quad (4.24)$$

One can create the control system (4.24) by the superposition of two elementary plants of the 1-st order; the corresponding scheme is shown at [Figure 4.7](#). The correspondence between the feedback coefficients in [Figure 4.7](#) and (4.24) one can get by the simple substituting to (4.8):

$$\frac{b_0 + b_1 p}{1 + (b_0 + b_1 p)(a'_0 + a'_1 p)} = \frac{\omega_0}{\beta} * \frac{p + \beta\omega_0}{p^2 + 2\omega_0 p + \omega_0^2}. \quad (4.25)$$

Therefore $a_0 = 1 + a'_0 b_0$, $a_2 = a'_1 b_1$, and $2a'_1 b_1 (1 + a'_0 b_0) = a'_0 b_1 + a'_1 b_0$.

#	$\omega_0, [rad * sec^{-1}]$	$\zeta, [rad * sec^{-1}]$	β	Poles	Zero	$h(t)$
1.	0.0191	1	0.25	$\lambda_{1,2} = -0.0095$	$\varsigma = -0.0048$	(4.22)
2.		1.4		$\lambda_1 = -0.0227$ $\lambda_2 = -0.0040$	$\varsigma = -0.0048$	(4.21)
3.		0.6		$\lambda_{1,2} = -0.0057 \pm 0.0076i$	$\varsigma = -0.0048$	(4.20)

Table 4.1. The parameters of the systems reflected in [Figure 4.7](#).

The physical meaning of the parameters became clear by comparing (4.23) and (4.13): s and Q in (4.13) are ω_0 and β^{-1} in (4.23-4.24), correspondently.

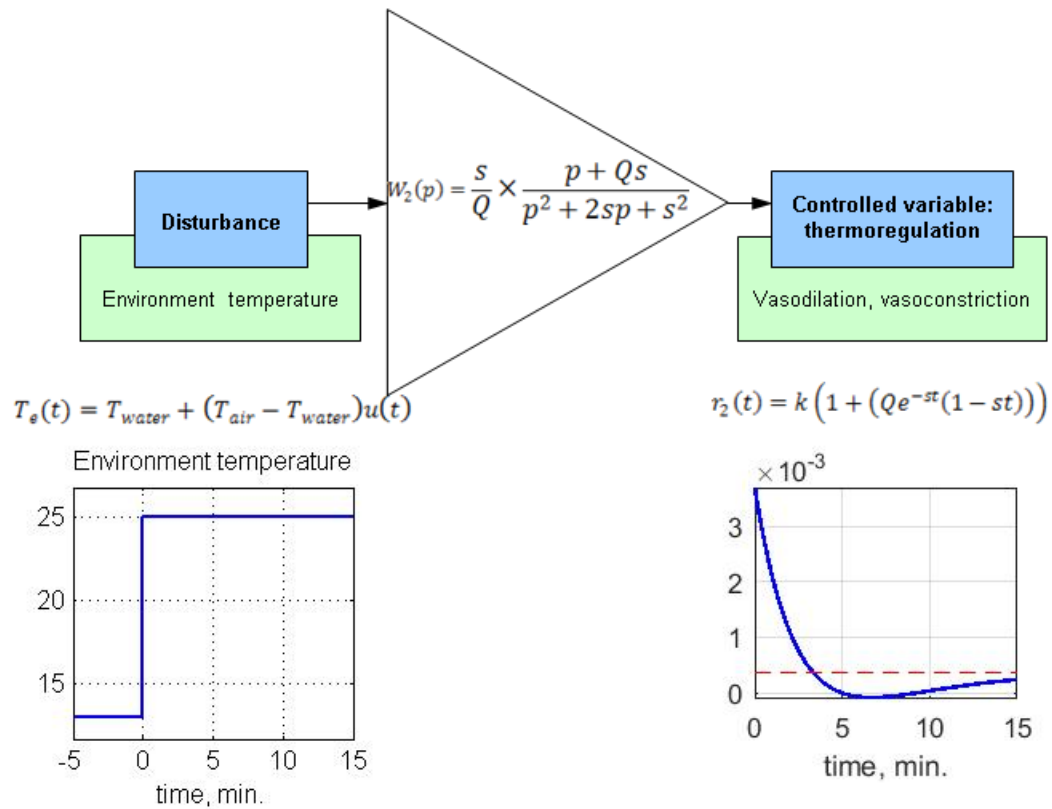
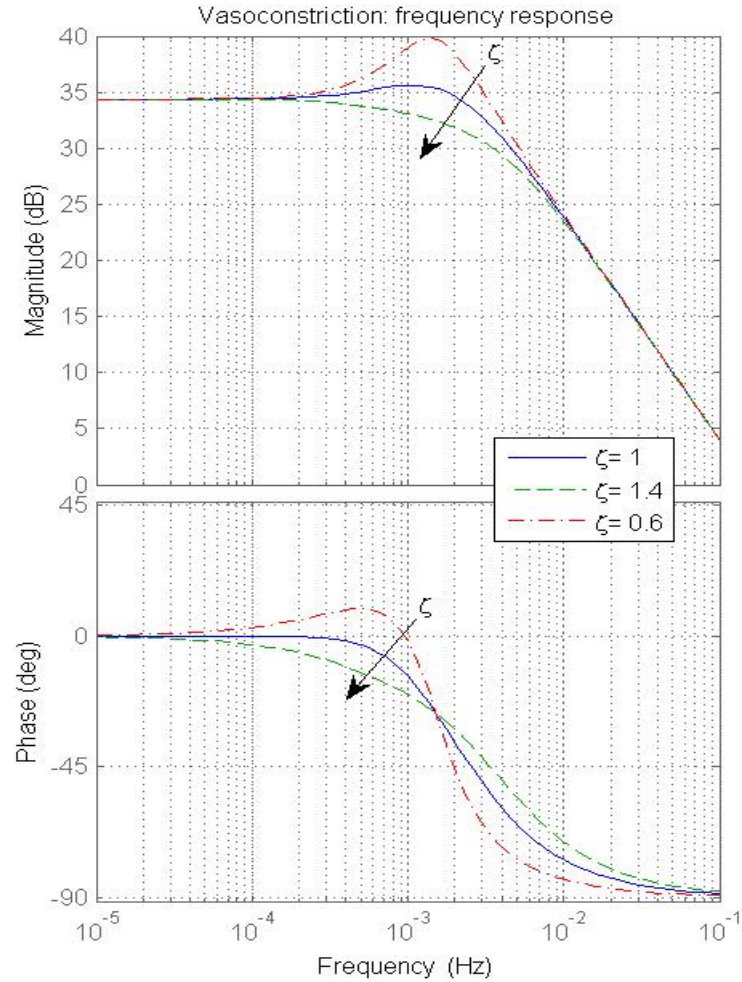
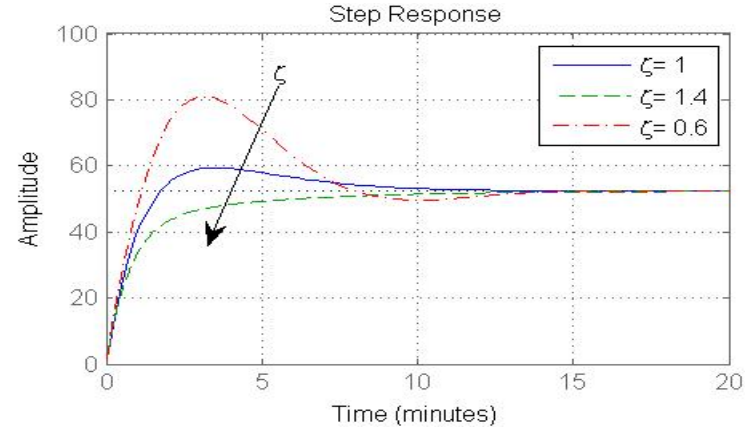


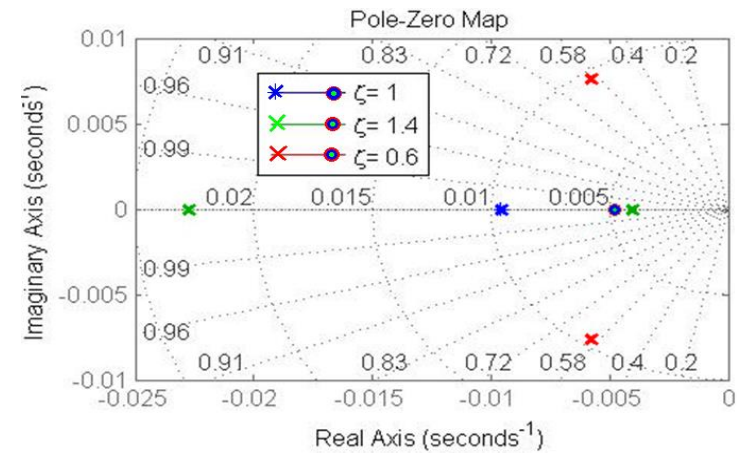
Figure 4.7. Scheme of the sample 2-nd order control system (4.13).



a)



b)



c)

Figure 4.8. Sample 2-nd order control system (4.14) with different damping factor ζ : frequency responses a), step response b), and pole-zero map c). The poles marked with x-crosses; all zeros are the same for all 3 systems marked with the circle.

In our experiments we don't measure $r_2(t)$, so we can prove our conclusions only indirectly. Let us do the extrapolation of the experimental data but with the new function (4.10). Also like the tests as presented in [Figure 4.3](#), we manually remove the first 0, 0.5, 1 and 1.5 minutes of temperature data and compared the extrapolations obtained our model with original experimental data. As it can be seen from [Figure 4.9](#), the extrapolation with thermal regulation is much more accurate. The maximum extrapolation error at zero time is about $0.1 - 0.2$ °C with thermoregulation, which is sufficiently accurate for this research. A metric that indicates the goodness of fit is the coefficient of determination R^2 [92]. As we will see later, R^2 is mostly above 99.9%, i.e. the accuracy is really good at the whole range of time of the experiments.

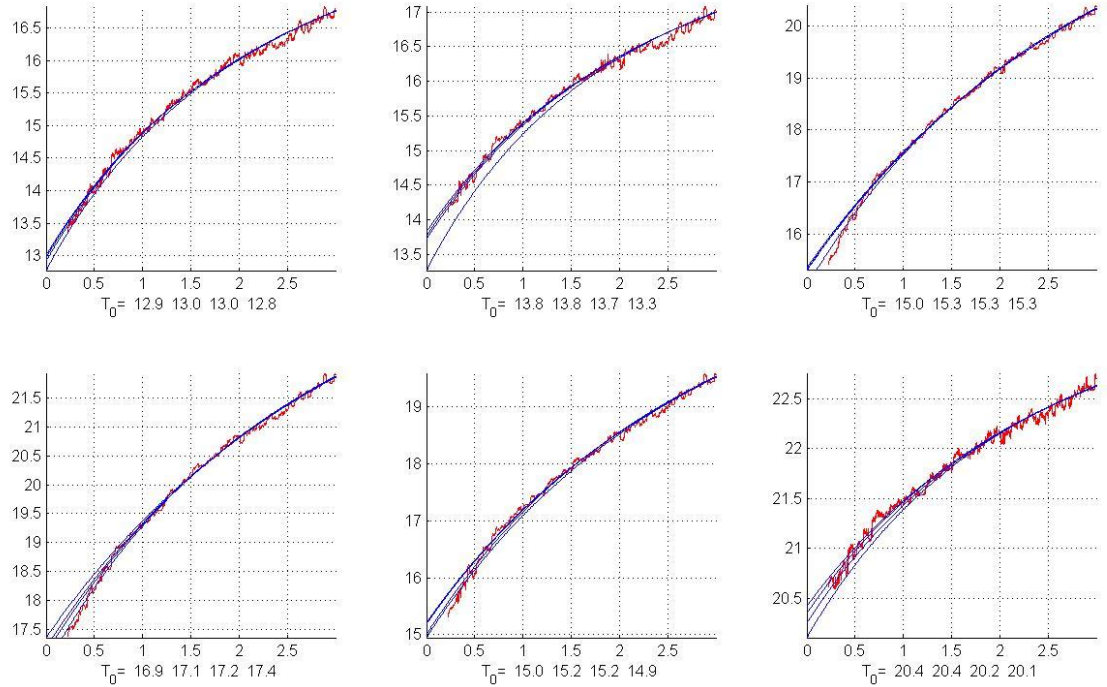


Figure 4.9. Extrapolation of the experimental data with (4.10). The same experiment, 6 plots for 6 ROIs. T_0 -s are the extrapolated temperatures at $t = 0$ for removed 0, 0.5, 1 and 1.5 min. of the experimental data.

4.3.3 The control system of the first order

We like the robust results, and generally could trust the obtained model. To be absolutely sure let's try to simplify it by the Occam's blade principle: investigate the 1-st order model, and compare it with the second one observed above. Assume the equation with thermoregulation to be:

$$\frac{dT(t)}{dt} = -k(1 - Qe^{-st})(T(t) - T_A), \quad (4.26)$$

and thus a new thermoregulation parameter to be:

$$r_1(t) = k(1 - Qe^{-st}). \quad (4.27)$$

The transmitting response of the control system with the step response (4.27) is the same very familiar 1-st order system (4.9) which is simple than the 2-nd order one (4.14). The frequency response, the step response, and the pole-zero map of the system corresponding to (4.9) are shown at [Figure 4.11](#). The explicit solution of (4.15) is:

$$T(t) = T_A + (T_0 - T_A)e^{-k\left(t + \frac{Q}{s}(e^{-st} - 1)\right)}. \quad (4.28)$$

The scheme of the corresponding control system is shown at [Figure 4.10](#). The sample plots including frequency response, step response, and pole-zero map are in [Figure 4.8](#); for this example, the coefficients of (4.9) are: $b_0 = 1$, $a_0 = 1$, $a_1 = 1$ [sec].

$$W_1(p) = \frac{s/Q}{p + s}$$

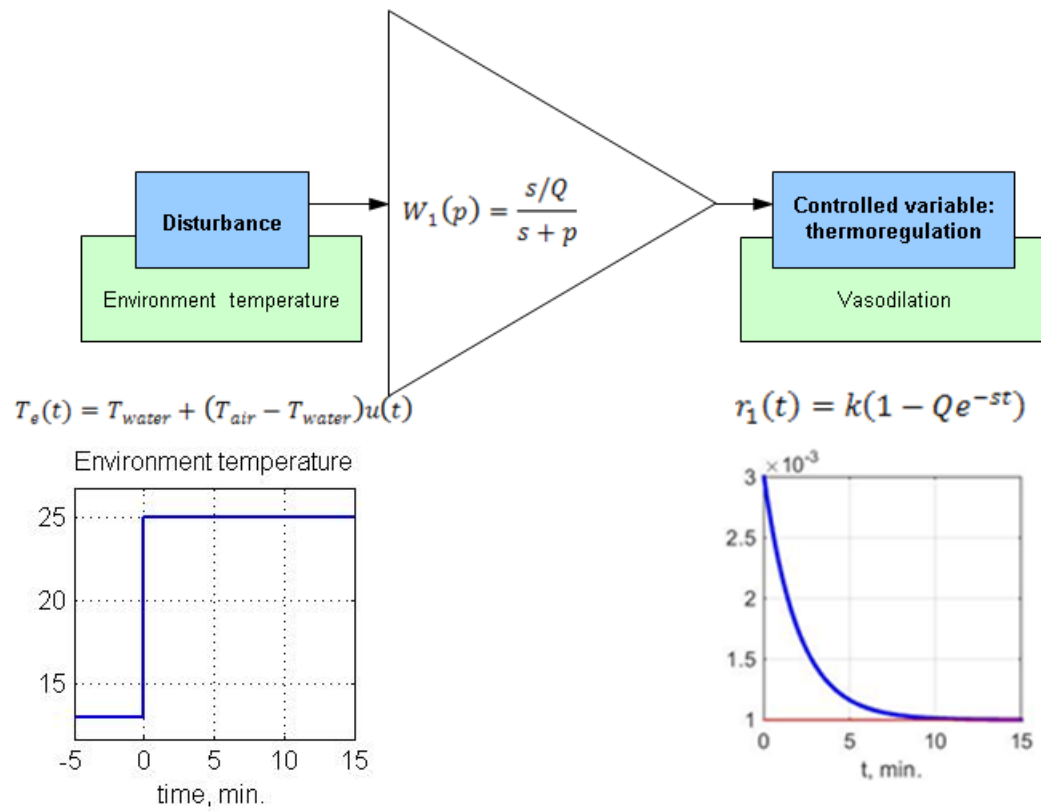
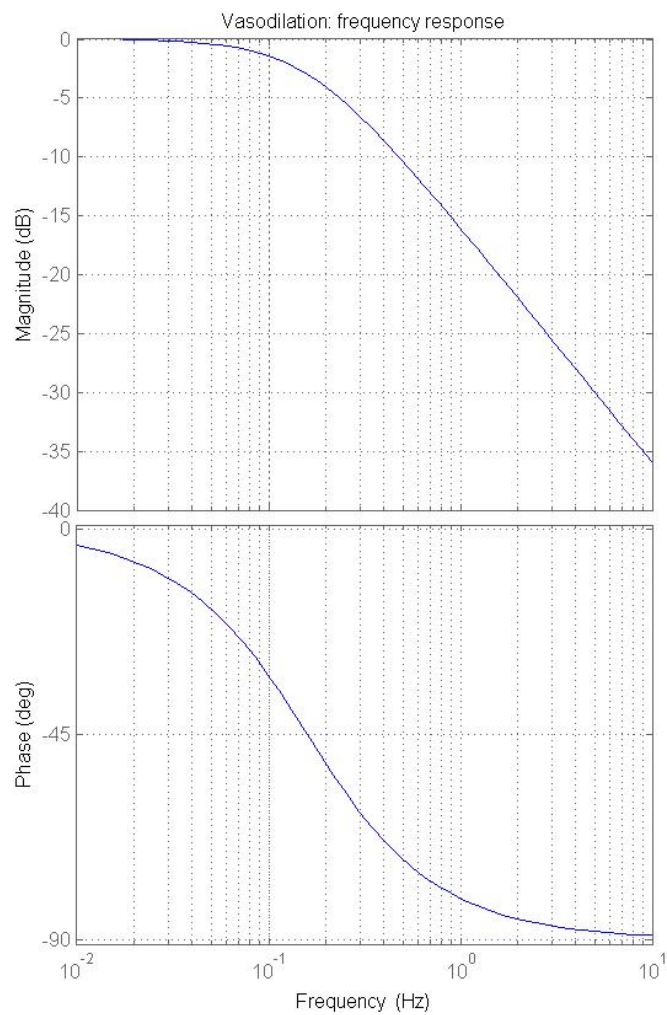
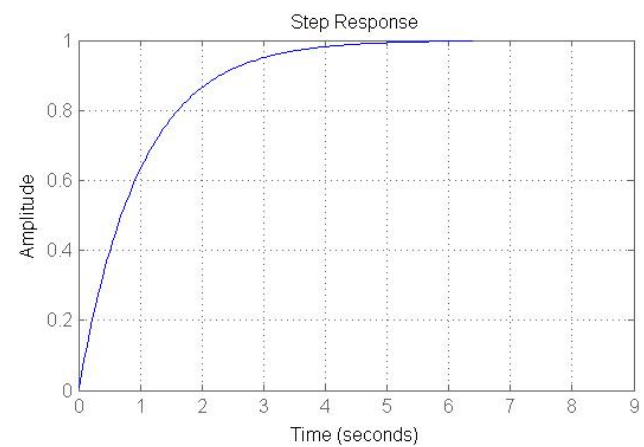


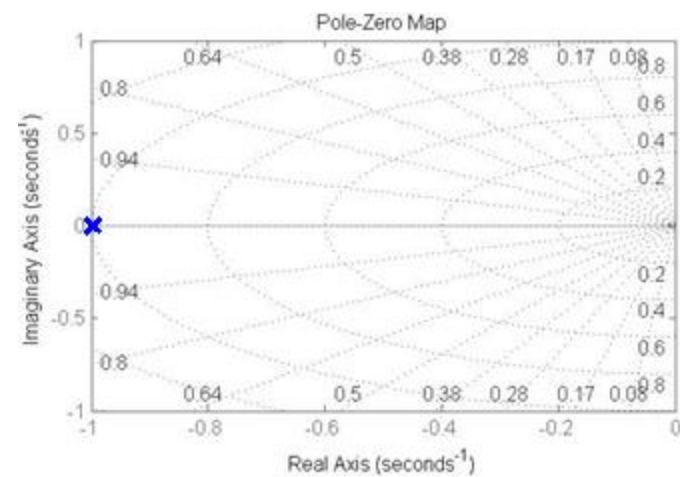
Figure 4.10. Scheme of the 1-st order control system (4.9).



a)



b)



c)

Figure 4.11. A sample 1-st order control system (4.9): frequency response a), step response b), and pole-zero map c). No zeros, one pole at $-1 + i0$.

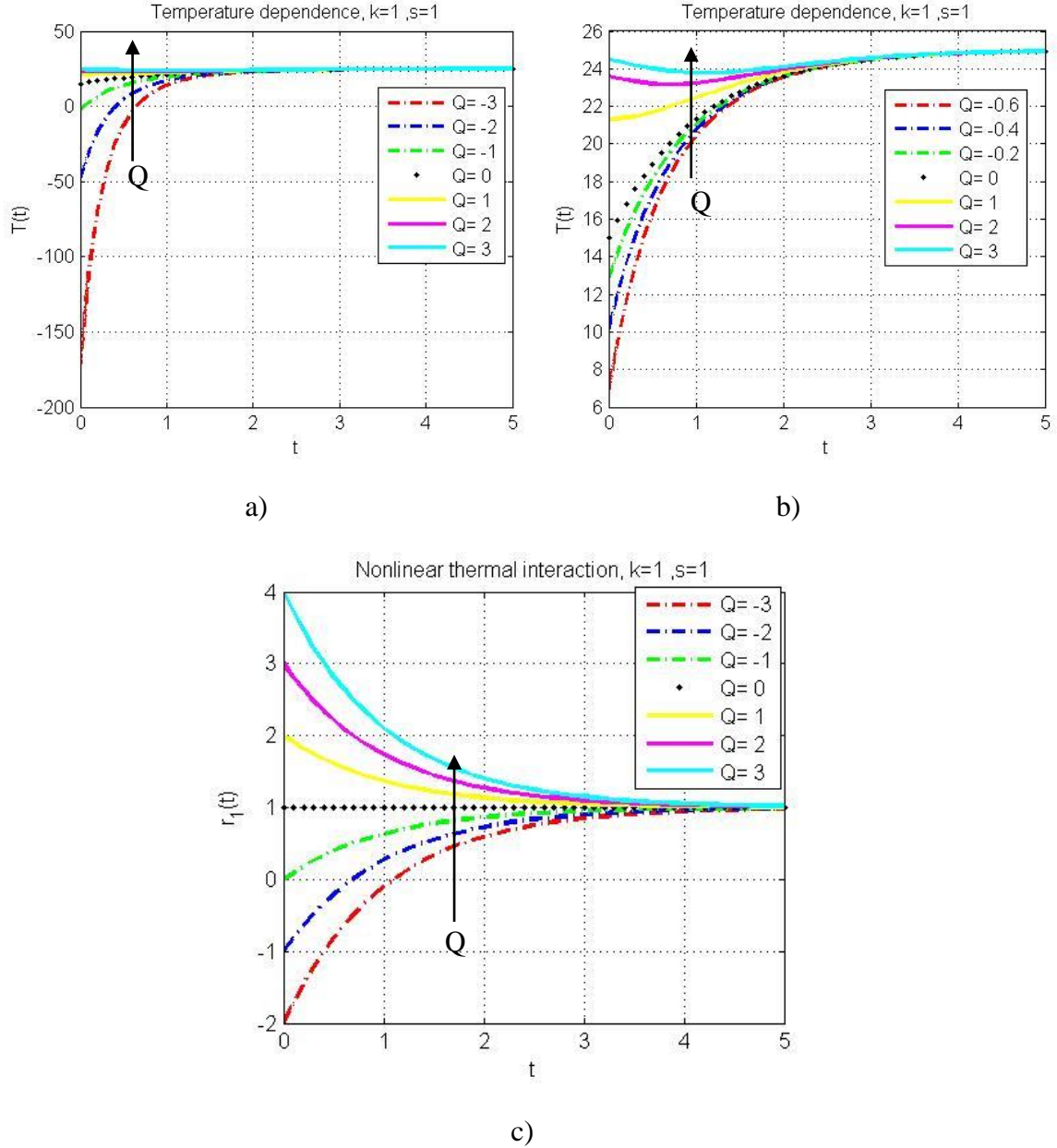


Figure 4.12. Sample plots (not related to any experiment) illustrating (4.16) a, b), and (4.15) c).

The physical meaning and the dimensions of the parameters k , Q , and s are the same as for the second order model described above. One thing should be noticed, that this type of regulation (4.27) is slower than (4.13) given the same values of the model parameters; compare the plots [Figure 4.6b\)](#) and [Figure 4.12c\)](#). As far as we are finding these parameters as the best fit for the same experimental data, one should expect greater

value of s for the slower first order model.

4.3.4 Comparison of the obtained models

Table 4.2 below summarizes the mathematical description of the models also compared with the Newton's law of cooling.

Let us compare the interpolation quality for the 3 models we have: Newton's law of cooling without any thermoregulation, the thermoregulation system of the 1-st order, and the thermoregulation system of the 2-nd order, see [Figure 4.13](#)

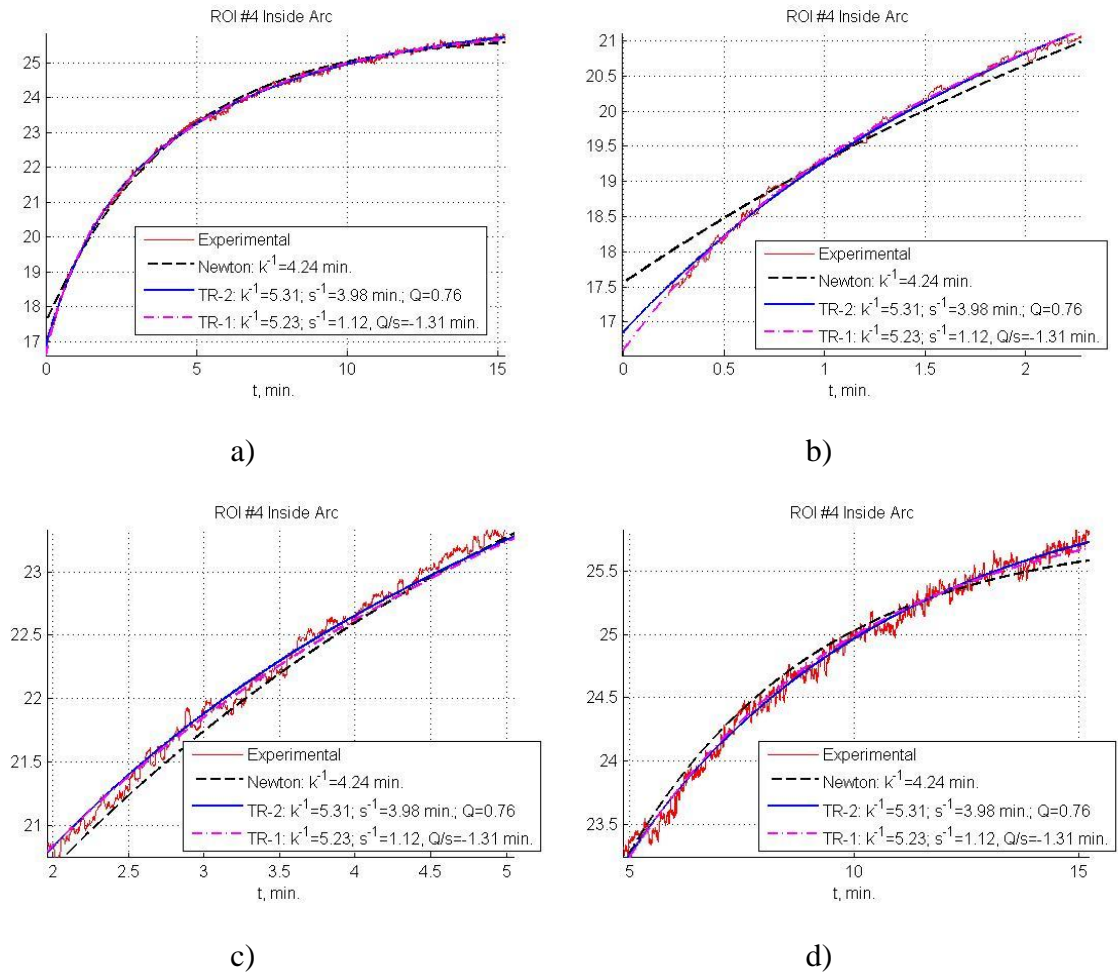


Figure 4.13. Nonlinear fit for 3 models: in the whole time range a) for 0...2 min b), 2...5 min c), and 5...15 min d).

Both models with thermoregulation demonstrate really good interpolation quality. They both grow faster than Newton's law of cooling, see [Figure 4.13 b](#)). At the same time they both have the value of k some smaller than the correspondent values of Newton's law of cooling. There is no contradiction in it, because they are faster due to the thermoregulation. The parameter s which is the speed of thermoregulation is always greater for the 1-st order system as far as for the same parameters the plots [Figure 4.12c](#)) are slower than the correspondent plots [Figure 4.6b](#)) for the 2-nd order system. See the sample values of k^{-1} and s^{-1} in the legend of the plot.

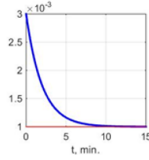
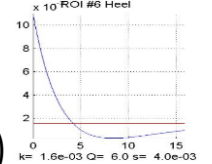
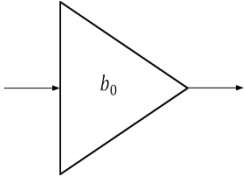
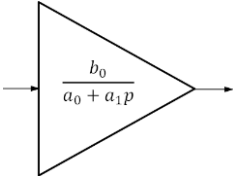
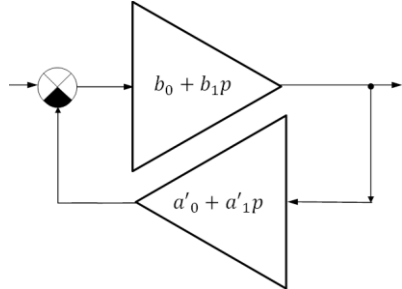
Model of thermoregulation	Newton's law of cooling (0 order)	The 1-st order thermoregulation system	The 2-nd order thermoregulation system
Equation $\frac{dT(t)}{dt} =$	$-k(T(t) - T_A)$	$-k(1 - Qe^{-st})(T(t) - T_A)$	$-k(1 + (Qe^{-st}(1 - st))) (T(t) - T_A)$
Solution $T(t) =$	$T_A + (T_0 - T_A)e^{-kt}$	$T_A + (T_0 - T_A)e^{-k(t + \frac{Q}{s})e^{-st}}$	$T_A + (T_0 - T_A)e^{-k(1 + Qe^{-st})t}$
Thermoregulation parameter $r(t) =$	k	$k(1 - Qe^{-st})$ 	$k(1 + (Qe^{-st}(1 - st)))$ 
Transmitting response $W(p) =$	b_0	$\frac{b_0}{a_0 + a_1p}$	$\frac{b_0 + b_0p}{a_0 + a_1p + a_2p^2}$
Control system			

Table 4.2. The models of thermoregulation.

4.3.5 Uniqueness and fullness of the obtained set of the models

So far we have proposed two thermoregulation models, and found the biological explanation for both. Should one try to find more models and explain them then?

The answer is: fortunately, no, at least if the maximum order of the system will be bounded by 2. Look at the logarithmic frequency responses of the systems [Figure 4.8 a\)](#) and [Figure 4.11 a\)](#). They are low pass, i.e. asymptotically flat at low frequencies and then asymptotically fall with the asymptote inclination 6 dB/octave (10 dB/decade) for the 1-st order system and 12 dB/octave (20 dB/decade) for the 2-nd order system at high frequencies. Also they are stable, i.e. all zeros if any and poles of the transmitting response $W(p)$ must have a negative real part. There are no more plants of the 1-st order satisfying these requirements [\[87\]\[88\]\[89\]\[90\]\[91\]](#) [Figure 4.11 c\)](#). In other words, the solution corresponding to the system of the 1-st order is unique.

On the other hand, one can develop different low pass filters of the 2-nd order, but our system has the overregulation property, which has to be satisfied. It excludes from the consideration the systems with two different negative poles on the real axis as far as they will behave similarly to the systems of the first order just some faster. Adding the imaginary components to the poles, i.e. $\zeta < 1$ in (4.14) will affect the oscillations of the step response, which has never been observed in our experiments. Thus the plant must have two identical negative real poles. If the zero of $W(p)$ would have the same or greater negative value as the poles, the system would behave like the system of the 1-st order. Thus, the only way is to have a zero more closely to the origin than the poles are, see [Figure 4.8 c\)](#)

As we have discussed above, two repeating poles correspond to the dumping

parameter $\zeta = 1$ in (4.14). A very meticulous one could notice that the small changes of ζ should not dramatically change the behavior of the system. Indeed, there is the quite narrow range of ζ where the behavior of formally oscillating system (with two complex conjugated poles) as well as the system with two different real negative poles would be almost the same or at least very similar to the system with two repeating real poles, see [Figure 4.14](#). Note that this adds one more parameter to the system, i.e. ζ . It means incrementing the degrees of freedom of the optimization problem and by this reducing the robustness and general complication. By the way, three different equations must be parameterized and tested for the best fit of the experimental curves, namely (4.20), (4.21), and (4.22) which exactly corresponds to the (4.12) tested above. It does not look reasonable, especially because the systems behave really similarly; the same effect, i.e. greater thermoregulation for $\zeta < 1$ or lower thermoregulation for $\zeta > 1$ can be achieved using the model with $\zeta = 1$ varying the parameter Q in (4.12) or, the same, parameter β^{-1} in (4.14). It is reflected on the pole-zero map in [Figure 4.14 c](#)): while a change of ζ affects redistribution of poles on the map, then a change of β moves the zero along the real axis.

[Figure 4.14](#) illustrates the behavior of the different systems (4.14) in the narrow range of ζ close to 1. The parameters are reflected in the Table 4.3; the systems in the table and the colors correspond to the ones reflected in [Figure 4.14](#):

#	ω_0 , [rad * sec ⁻¹]	ζ , [rad * sec ⁻¹]	β	Poles	Zero
1.	0.0191	1	0.25	$\lambda_{1,2} = -0.0095$	$\varsigma = -0.0048$
2.		1.1	0.25	$\lambda_1 = -0.0149$ $\lambda_2 = -0.0061$	$\varsigma = -0.0048$
3.		0.9	0.25	$\lambda_{1,2} = -0.0086$ $\pm 0.0042i$	$\varsigma = -0.0048$
4.		1	0.2	$\lambda_{1,2} = -0.0095$	$\varsigma = -0.0038$
5.		1	0.3	$\lambda_{1,2} = -0.0095$	$\varsigma = -0.0057$

Table 4.3. The parameters of the systems reflected in [Figure 4.14](#).

Comparing the step responses of the systems in [Figure 4.7](#) with the first three ones in [Figure 4.14](#), one can see that for $\zeta \lesssim 1$ the damping is big enough to completely fade the oscillations with two complex conjugate poles in the third system in the table. It means that the real exponent in (4.20) fades faster than $\sin(\)$ and $\cos(\)$. On the other hand, $\zeta \gtrsim 1$ is small enough to still give overshooting for the non-repeating poles (4.21), the second system. The tricky thing is that moving the zero farther from the origin but not that far as the poles, see the system #5 in the table, one can reduce the overshooting even more than for the given system (4.21), and vice versa, the system #4.

This means that the obtained models with the order of the control system upper bounded by 2 are not unique in terms of the best fit, but are the simplest ones. The model of the 2-nd order (4.12) with the solution (4.13) is unique if to bound the maximum number of the parameters, i.e. fix the dumping factor $\zeta = 1$. It is natural from both physical and biological points of view: two different negative poles correspond to two real exponents with similar exponent factors. It requires two different but quite similar physical processes.

On the other hand, the couple of complex conjugant roots mean fading oscillations of thermal regulation, which also have not been observed. Moreover, as it is shown right below, see the Chapter 4.4, even the simplest system of the second order (4.12 – 4.13) appeared unnecessarily complex.

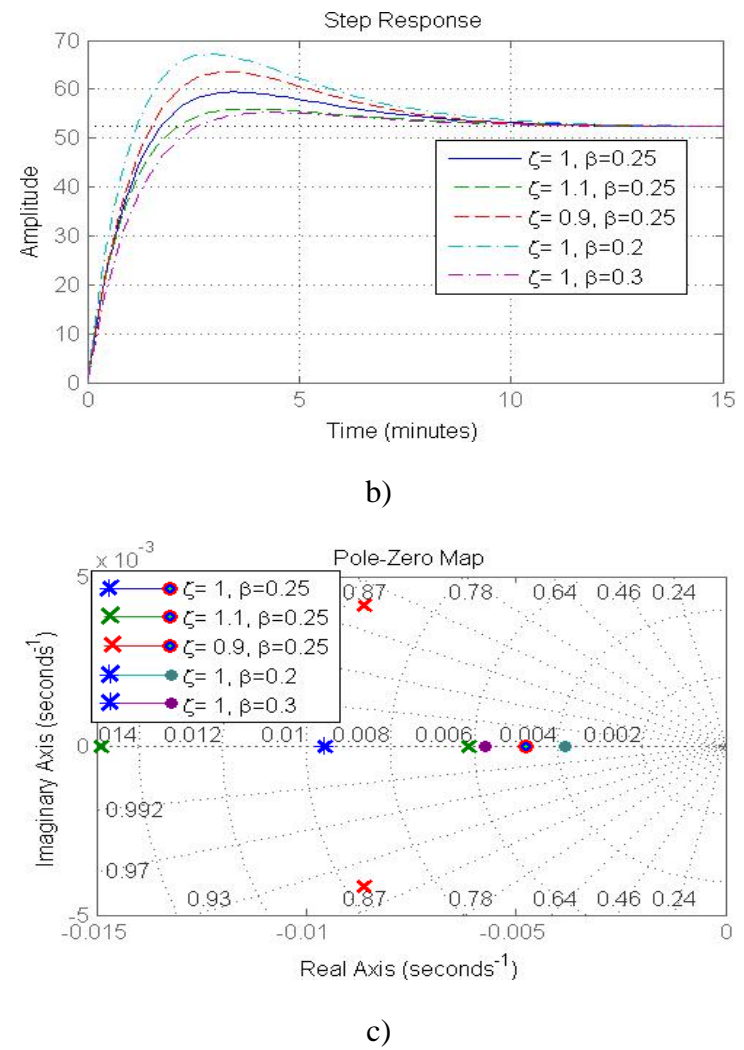
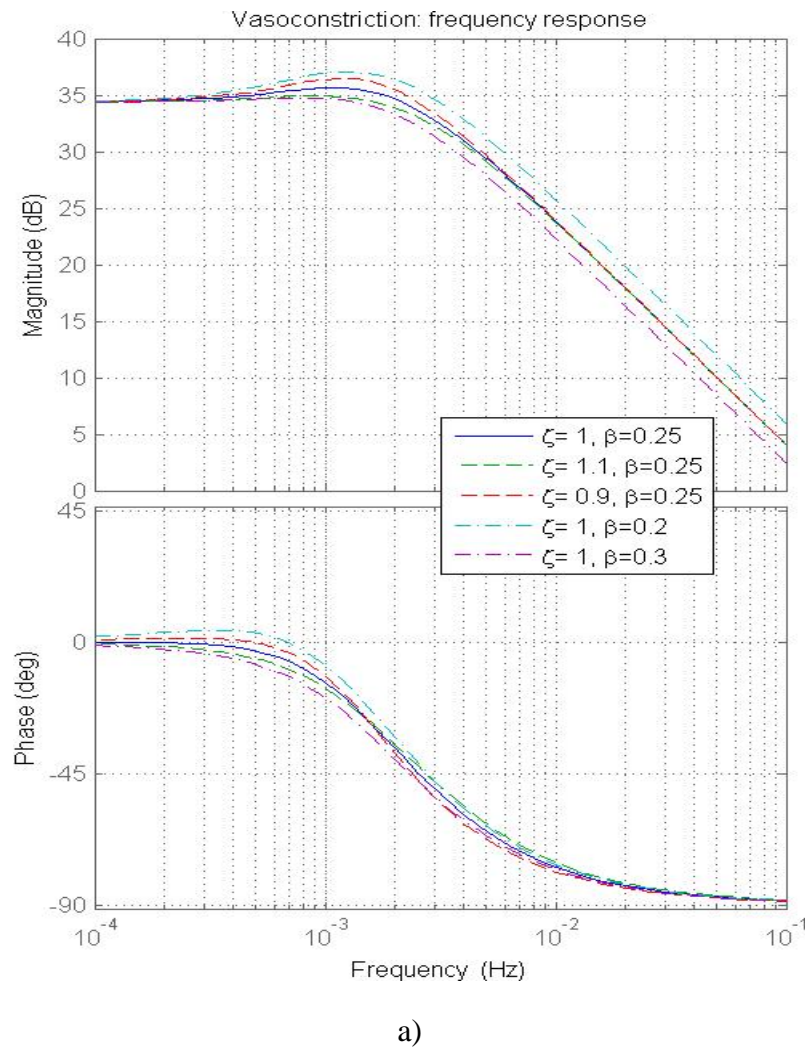


Figure 4.14. Sample 2-nd order control systems (4.14) with different damping factor ζ and amplification β^{-1} : frequency responses a), step response b), and pole-zero map c). The poles marked with x-crosses; the zeros are marked with the circles.

4.4 The biological sense of the thermoregulation models

4.4.1 The biological mechanisms of human thermoregulation

Precisely, by thermoregulation we are referring to the change of particular parameters accounted for by T depending on the temperature and time. The list of the human thermoregulation mechanisms includes the following ones: convection, conduction, radiation, goose bumps, and evaporation [93]. Our experiment includes three phases: control, cooling and recovery of the peripheral body part.

Go back to the equation (4.3). The radiation term (4.4) may be ignored in the model of a foot recovery in room temperature, as we discussed above in [Chapter 4.2](#). Similarly, in the short time cooling phase we may ignore evaporation (4.5). The goose bumps during cooling give almost no effect on thermoregulation because of direct contact between the human skin and cold pressor (through a thin bag of ice). Fat to energy transform in the mitochondria can also be neglected by local and short time cooling and also for adult humans [81].

The convection and conduction are related to the interaction of the tissue with both external media and blood. Let us discuss the thermal energy exchange with the environment first. The energy exchange for the given skin area by the conduction cannot be regulated. The change of the convection intensity in the room by the temperature change can also be neglected. Thus, the thermoregulation happens inside the human body, i.e. between the tissue and blood. Blood current corresponds to the convection. Naturally assuming the constant values for heat capacity and density for both tissue and blood during the 15-20 minutes of the experiment, one can claim that the change of blood perfusion

$\omega_b(t)$ is the main factor of thermoregulation.

Mechanically and hydrodynamically the blood current in a human body is absolutely analogous to the liquid current in the pumping hose, where the heart works as a pump, and the vessels as the hoses. Thus, we could name the heart pulse rate, and pulse amplitude as the general parameters related to the “pump” whereas the diameters of vessels are the parameters related to the local properties of the “hose”. The blood pressure indicates the interaction between the “pump” and the rest liquid distributing system. We will not solve the Navier-Stokes equation in 3D for the hydrodynamical (hemodynamical in our case) model together with the thermal conductivity equation with the boundary conditions determined by the vessels of changing diameters, but use the same principle of control theory as above, i.e. assume the whole complex system as a black box and try to get its parameters. It must be noted that we cannot differentiate the influence of each factor using just the data of the measurements we made. For example, to investigate the dependence between the thermoregulation and the pulse amplitude [94] the laser Doppler fluorometer has been used to measure the flux of the red cells in the fingers and toes, and the pulse amplitude has been measured with the photoelectrical pulse plethysmographs. One of the conclusions have been made in [94] is that these general factors do have the influence on the thermoregulation state. Particularly it means that the thermoregulation of the same subject will be quite different with different pulse amplitude and rate (and also with different breathing, and even with mental stress). One may conclude by this that it should be taken into account investigating repeatability. Nevertheless, the main goal of this research is to diagnose the peripheral neuropathy with the key word “peripheral”. It means that beyond of pulse rate, etc. the diameters of the vessels can almost literally be the

bottleneck for the blood current. Therefore, it is the main thermoregulation mechanism must be taken into account. Its local nature gives a possibility to differentiate healthy and problematic areas on the foot beyond of the body parameters.

Thus the major factors in thermal regulation are vasoconstriction, i.e. shrinking (constricting) of arterioles to reduce heat loss from the blood and vasodilation which is the opposite process. In contrast in the recovery stage all the mechanisms above should be switched back to the “normal” mode, i.e. vasodilation instead of vasoconstriction.

4.4.2 The correspondence between the biological mechanisms and the analytical models of thermoregulation

Let us compare two models in terms of the biological thermoregulation mechanisms. Observing the obtained model parameters after nonlinear fit in the legends in [Figure 4.13](#) one can see that the dimensionless intensity of thermoregulation denoted as Q is positive for the 2-nd order model whereas it is negative for the 1-st order model. Indeed, comparing the temperature dependences for the models [Figure 4.6 a\)](#) and [Figure 4.12a, b\)](#) clear that the neither the plots with $Q < 0$ for the 1-st order model nor the neither the plots with $Q > 0$ look similarly to each other and to the interpolated experimental curves. In contrary to these illustrations, Figure 4.14 shows only the parameters which have sense, i.e. $Q \geq 0$ for the 2-nd order model and $Q \leq 0$ for the other one. They are absolutely equal at $Q = 0$ which corresponds to the Newton’s law of cooling (4.2). Increasing the thermoregulation intensity $|Q|$, the temperature plots go above the asymptotic Newton’s plot for the 2-nd order model (4.10) Figure 4.14 a) and below for another one (4.16) Figure 4.14 b) whereas at the times corresponding to the beginning of recovery both models make

the temperature growth faster than the asymptote. There is no contradiction in this as far as the 2-nd order model later on slows down after the time $t = s^{-1}$. The main difference between the models is that they describe different biological mechanisms of thermoregulation. The 1-st order model Figure 4.14 d) is monotonically increasing, therefore it corresponds to vasodilation. It has greatest value of the derivative of (4.15) i.e. greatest intensity of thermoregulation at the beginning and that it exponentially goes to 0. The 2-nd order model Figure 4.14 c) reflects vasodilation at the beginning until the intersection of the thermoregulation curve with the asymptotic line at the time $t = 2s^{-1}$ and vasoconstriction later on.

Let us explain the simplest model first. As we have discussed above, the body part being cooled down gets less blood to preserve the heat energy of the human body under the cold stress [93]. Thus, the cold stress turns the vasoconstriction on. Then, the unit step function of heat at the beginning of the recovery process opens the vasodilation phase. This explanation is very clear and has neither doubts no contradictions with the known facts for the biology of human body.

In contrary to this simple explanation, the model of the second order describes the process of alternating of vasodilation and vasoconstriction, so called so called hunting response or Lewis reaction [94][95][96][97][98][98]. We did not measure the change of the vessel diameters directly, so we cannot claim the existence of the more complex biological process, especially the one has been criticized [100] [101] [102] [103] [104]. Moreover, Lewis reaction has been claimed as induced by cold, whereas recovery is the opposite process. That's why the model of the 1-st order has been chosen for further investigation. Both models are similarly robust, and give the same inter- and extrapolation

quality, but the control system of the first order is simpler, unique, and, more important, has a clear biological meaning.

4.5 Accuracy of the model of thermoregulation

Similarly to (4.3) for Newton's law of cooling, we will use the nonlinear least square fit to find the parameters of the solution independently for each ROI for each experiment:

$$\{k, s, Q, T_0, T_A\} = \underset{\text{subject to } lb \leq \{k, s, Q, T_0, T_A\} \leq ub}{\operatorname{argmin}} \{\|T(t) - T_{measured}(t)\|_2^2\} \quad (4.29)$$

where lb and ub are lower and upper bounds for the vector of parameters.

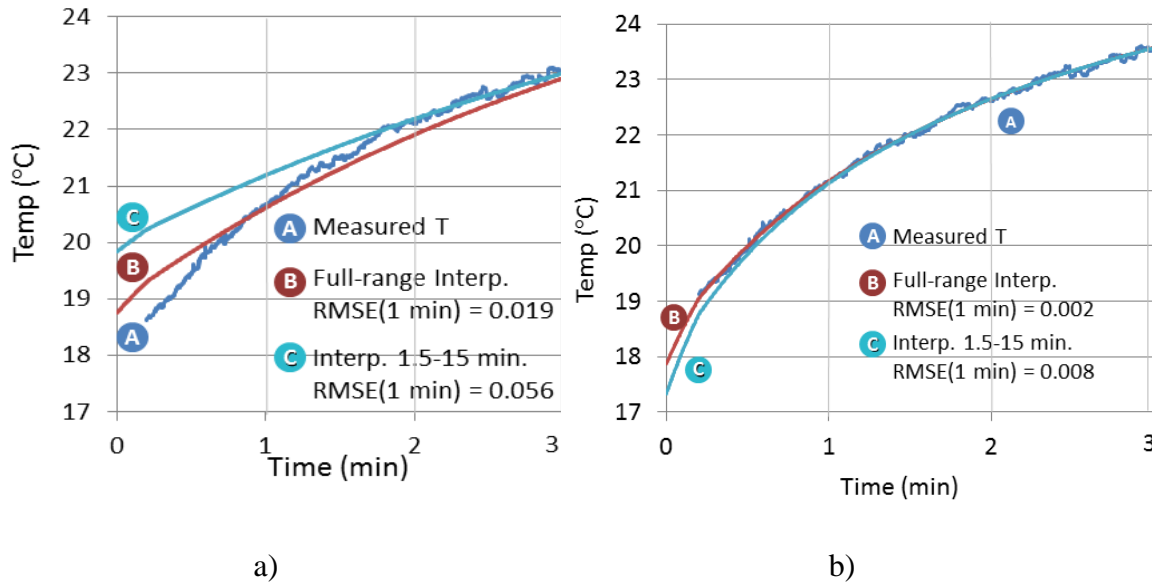


Figure 4.15. Interpolation quality with Newton's law of cooling a) and the TR-1 model b)

Let us compare the interpolation quality of the models for the full range of data, i.e. where the experimental measurement has been taken as close to the beginning of recovery as it is possible.

	ROI 5 Lateral Arch		
	$\Delta T_0, ^\circ\text{C}$	$\text{RMSE} \times 10^3$	
		$\leq 0.5 \text{ min}$	$\leq 2 \text{ min}$
No thermoregulation: Newton’s Law of Cooling			
Mean	0.96	40.04	17.58
STD	0.39	12.73	5.91
Median	0.86	39.38	17.46
Min	0.44	17.21	7.66
Max	1.90	62.82	30.92
The Model of Thermoregulation of the 1-st Order			
Mean	0.060	4.23	3.45
STD	0.056	1.78	0.77
Median	0.048	4.14	3.25
Min	0.003	1.87	2.27
Max	0.212	9.02	4.94

Table 4.2. Comparison of interpolation quality of TR-1 with Newton's Law of Cooling.

Also, for the same experiments, assume that the measurements started with the 0.5 min delay, and 1.5 min. delay. We need to know how sensitive the model is to the loss of data like this, which, unfortunately, happened quite often. Unsurprisingly, we see the same effect. Moreover, the mean error 0.26-0.60 $^\circ\text{C}$ for the TR-1 with incomplete data is less than the mean error of Newton's law of cooling with the complete data.

	ROI 5 Lateral Arch		
	$t \geq 0.5$ min	$t \geq 1$ min	$t \geq 1.5$ min
No thermoregulation: Newton's Law of Cooling			
Mean	1.26	1.61	1.89
STD	0.62	0.71	0.75
Median	0.98	1.44	1.80
Min	0.48	0.72	0.90
Max	2.90	3.61	4.00
The Model of Thermoregulation of the 1-st Order			
Mean	0.27	0.43	0.60
STD	0.25	0.41	0.56
Median	0.18	0.31	0.41
Min	0.00	0.01	0.00
Max	0.90	1.99	2.48

Table 4.3. Extrapolation quality of TR-1 and Newton's Law of Cooling with the loss of data.

Let us discuss the meaning of the model parameters. Whereas Q – the amplitude of regulation, and s – speed of regulation – depends on the properties of vessels, vessel muscles and reaction of peripheral nervous system on the stress, i.e. should vary for every experiment with different conditions, k rather depends on tissue, and should be very similar for the same subject. Thus, for the set of 27 experiments with the same volunteering subject we substituted $k = k_{mean}$, and let other model parameters vary. It means that the problem (4.29) became

$$\{s, Q, T_0, T_A\} = \begin{matrix} \underset{\text{subject to } lb \leq \{s, Q, T_0, T_A\} \leq ub, k = k_{mean}}{\operatorname{argmin}} \{ \|T(t) - T_{measured}(t)\|_2^2 \} \end{matrix} \quad (4.30)$$

The interpolation quality did not change a lot; see Table below.

ROI 5 Lateral Arch			
	$\Delta T_0, ^\circ\text{C}$	RMSE $\times 10^3$	
		$\leq 0.5 \text{ min}$	$\leq 2 \text{ min}$
The Model of Thermoregulation of the 1-st Order, $k = k_{mean}$			
Mean	0.082	4.58	3.66
STD	0.073	1.96	1.07
Median	0.064	4.43	3.52
Min	0.001	1.21	1.87
Max	0.288	8.51	6.48
The Model of Thermoregulation of the 1-st Order			
Mean	0.060	4.23	3.45
STD	0.056	1.78	0.77
Median	0.048	4.14	3.25
Min	0.003	1.87	2.27
Max	0.212	9.02	4.94

Table 4.3. Interpolation quality of TR-1 with fixed and varying parameter k .

All this means, first, that the thermoregulation model has in orders of magnitude greater accuracy and robustness comparing to the model without the thermoregulation, and second, it describes real biological processes, and its parameters can be used for their quantification.

Chapter 5 Heat transfer during the cooling phase

There did not seem to be so many pools of water under the snow on the left side of Henderson Creek, and for half an hour the man saw no signs of any. And then it happened. At a place where there were no signs, the man broke through. It was not deep. He was wet to the knees before he got out of the water to the firm snow.

Jack London, To Build a Fire.

5.1 Motivation

The standard measurement protocol described in Chapter 2 includes three main phases: control, cooling and recovery. The control and recovery phases in the room temperature air are quite similar, whereas cooling in the cold water is physically, biologically, and (based on many personal impressions of the tested subjects) even emotionally very different. In the previous chapter, we have developed thermal regulations models and tested the model using the temperature recovery curves. One would expect that the same model should also work with the cooling phase. In fact, one would expect applying the model to the data points of the cooling phase should improve the overall accuracy of the parameters.

5.2 The thermoregulation model of the cooling phase.

5.2.1 General solution.

The simple model (4.11, 4.25) obtained for the process of a foot recovery in the room temperature is based on the several assumptions. Most of them are still applicable to the cooling phase in water, but not all of them. The assumptions that need to be modified are mostly related to the environment. In the recovery phase, the impact to the surrounding air is negligible, while the impact of to the cold water bath is not. Because of these, the following two assumptions must be adjusted:

1. The constant environment temperature has been assumed in the recovery phase. It allows us to ignore the second equation from (4.3). While this is a valid assumption for room temperature, it is not the case for the cooling phase when the subject's foot is submerged in a 2-gallon bath of cold water. To ensure that this assumption is still valid, we will have to keep the water temperature constant. This is achieved by adding cold water or ice to keep the water temperature constant during the cooling.
2. The assumption $r_b \gg r_e$ in (4.6) is based on (1) the mass-specific heat capacity of air $c_a \approx 963 \text{ J/kg/}^\circ\text{K}$ is much less than for the blood which is within the range $c_b = 3594 \dots 4153 \text{ J/kg/}^\circ\text{K}$ [77], and (2) the blood is constantly circulating, whereas there is no artificial air current in our experiments. In the cooling phase, however, the mass-specific heat capacity of water is: $c_w = 4181.3 \dots 4186 \text{ J/kg/}^\circ\text{K}$. Also, we ask the subjects to move their feet to make the cooling more uniform.

Recall Equation (4.6) (denoted as Equation (5.1) in this Chapter):

$$\frac{dT(t)}{dt} = -r_1(t)(T(t) - T_b) - r_e(T(t) - T_e) \quad (5.1)$$

where $r_e = \frac{(\rho c)_e}{V\rho c} \omega_e$ [sec⁻¹] is the characteristic of the body (foot) with respect to the external media (here "e" stands for environment, *i.e.*, water in the cooling phase), and $r_1(t) = \frac{(\rho c)_b}{V\rho c} \omega_b(t)$ [sec⁻¹] accounts for all the biological and thermal dynamical parameters responsible for the heat transfer between the blood ("b") and tissue, as before.

Recall that the original of time t is the beginning of the recovery, *i.e.*, the end of cooling. To avoid negative times, let $t' = t - t_{cooling}$, where $t_{cooling}$ is the cooling time. After this change of variables, equation (5.1) is still a linear parametric equation with respect to t' , and has an explicit solution, which is:

$$T(t') = e^{-t'(k+r_e) + \frac{Qk}{s}e^{-st'}} \left(C_2 + \int \left(((1 + Qe^{-st'})T_b k + T_e r_e) e^{t'(k+r_e) - \frac{Qk}{s}e^{-st'}} \right) dt' \right) \quad (5.2)$$

Recall, k is the speed of cooling due to blood, Q , and s are the parameters of the thermoregulation, r_e is the speed of cooling due to the interaction with the environment.

Observe that substitute $Q = 0$ – no thermoregulation. This solution becomes:

$$T_{Newton's Law of Cooling}(t') = (T_e r_e + T_b k + C_2 e^{-t'(k+r_e)}) / (k + r_e) \quad (5.3)$$

for the initial conditions

$$T(t' = 0) = T_{ref}, \quad (5.4)$$

where the integration constant is

$$C_2 = T_{ref}(k + r_e) - T_e r_e - T_b k. \quad (5.5)$$

Thus, the new solution is consistent with the Newton's Law of Cooling.

Now observe that:

$$\begin{aligned} & \int \left(((1 + Qe^{-st'})T_b k + T_e r_e) e^{t'(k+r_e) - \frac{Qk}{s}e^{-st'}} \right) dt' \\ &= (T_b k + T_e r_e) \int \left(e^{t'(k+r_e) - \frac{Qk}{s}e^{-st'}} \right) dt' \\ &+ QT_b k \int \left(e^{t'(k+r_e-s) - \frac{Qk}{s}e^{-st'}} \right) dt' \end{aligned} \quad (5.6)$$

Let

$$b = \frac{Qk}{s} \quad (5.7)$$

$$a_1 = k + r_e \quad (5.8)$$

$$a_2 = -s + k + r_e \quad (5.9)$$

Then

$$\begin{aligned}
\int \left(e^{at' - be^{-st'}} \right) dt' &= \left| \begin{array}{l} x = e^{-st'} \\ t' = -\frac{1}{s} \ln x \\ dt' = -\frac{1}{s} \frac{dx}{x} \\ e^{at'} = x^{-a/s} \end{array} \right| = -\frac{1}{s} \int (x^{-a/s-1} e^{-bx}) dx \\
&= \left| \begin{array}{l} bx = y \\ dx = \frac{dy}{b} \end{array} \right| = -\frac{b^{a/s}}{s} \int (y^{-a/s-1} e^{-y}) dy
\end{aligned} \tag{5.10}$$

Let

$$t' = -\frac{1}{s} \ln \frac{y}{b} \tag{5.11}$$

$$y = be^{-st'} \tag{5.12}$$

The integral (5.10) is known as lower incomplete gamma function [78]:

$$\int_0^y y^{-a/s-1} e^y dy = \int_0^y y^{-a/s-1} e^y dy + C = \gamma_l(-a/s, be^{-st'}) + C \tag{5.13}$$

Recall that the complete gamma function $\Gamma(a)$ is:

$$\Gamma(a) \equiv \int_0^\infty t^{a-1} e^{-t} dt = \gamma_l(a, \infty). \tag{5.14}$$

The complete gamma-function can be split into the sum of a lower and an upper incomplete gamma-functions, i.e. $\int_0^\infty (\Gamma(a)) = \int_0^x (\Gamma(a)) + \int_x^\infty (\Gamma(a))$. The normalized lower incomplete gamma function is:

$$P_l(a, x) = \frac{\gamma_l(a, x)}{\Gamma(a)} = \frac{\int_0^x t^{a-1} e^{-t} dt}{\int_0^\infty t^{a-1} e^{-t} dt} \quad (5.15)$$

Thus, the items of (5.6) can be reduced to the following form:

$$(T_b k + T_e r_e) \int \left(e^{t'(k+r_e) - \frac{Qk}{s}} e^{-st} \right) dt' \quad (5.16)$$

$$= -\frac{(T_b k + T_e r_e) \left(\frac{Qk}{s} \right)^{(k+r_e)/s}}{s} \left(\gamma_l \left(-(k+r_e)/s, \frac{Qk}{s} e^{-st'} \right) + C_4 \right)$$

$$QT_b k \int \left(e^{t'(-s+k+r_e) - \frac{Qk}{s}} e^{-st'} \right) dt \quad (5.17)$$

$$= \frac{-QT_b k \left(\frac{Qk}{s} \right)^{(k+r_e-s)/s}}{s} \left(\gamma_l \left(-(k+r_e-s)/s, \frac{Qk}{s} e^{-st'} \right) + C_5 \right)$$

Substitute the formulae above to the general solution (5.2):

$$T(t') = e^{-(k+r_e)t' + \frac{Qk}{s} e^{-st'}} \left(C_1 \right. \quad (5.18)$$

$$\left. - \left(\frac{Qk}{s} \right)^{(k+r_e)/s} \left(T_b \left(\frac{k+r_e}{s} \gamma_l \left(-\frac{k+r_e}{s}, \frac{Qk}{s} e^{-st'} \right) \right. \right. \right.$$

$$\left. \left. + \gamma_l \left(1 - \frac{k+r_e}{s}, \frac{Qk}{s} e^{-st'} \right) \right) \right.$$

$$\left. \left. + (T_e - T_b) \frac{r_e}{s} \gamma_l \left(-\frac{k+r_e}{s}, \frac{Qk}{s} e^{-st'} \right) \right) \right),$$

where the integration constant C_1 is

$$C_1 = T_{ref} e^{-\frac{Qk}{s}} \quad (5.19)$$

$$\begin{aligned} & + \left(\frac{Qk}{s}\right)^{(k+r_e)/s} \left(T_b \left(\frac{k+r_e}{s} \gamma_l \left(-\frac{k+r_e}{s}, \frac{Qk}{s} \right) \right. \right. \\ & \left. \left. + \gamma_l \left(1 - \frac{k+r_e}{s}, \frac{Qk}{s} \right) \right) \right. \\ & \left. + (T_e - T_b) \frac{r_e}{s} \gamma_l \left(-\frac{k+r_e}{s}, \frac{Qk}{s} \right) \right) \end{aligned}$$

Notice herewith that (5.18-5.19) represent the explicit solution to (5.1). Nevertheless, it still does not look obvious and intuitively understandable, especially comparing with the solutions obtained in the previous chapter. Let us continue the reduction.

Using the following decomposition of the lower incomplete gamma function [79, 80]:

$$\begin{aligned} \gamma_l(a, x) &= e^{-x} x^a \left(\frac{x^0}{a} + \frac{x^1}{a(a+1)} + \frac{x^2}{a(a+1)(a+2)} + \dots \right) \quad (5.20) \\ &= a^{-1} e^{-x} x^a \left(\frac{x^0}{1} + \frac{x^1}{(a+1)} + \frac{x^2}{(a+1)(a+2)} + \dots \right) \end{aligned}$$

One can see from (5.20) that

$$a^{-1} e^{-x} x^a + a^{-1} \gamma_l(1+a, x) = \gamma_l(a, x) \quad (5.21)$$

Substitute (5.21) to (5.18-5.19). The solution will be reduced to the following:

$$\begin{aligned}
& T(t') \\
&= T_b + C_1 e^{-(k+r_e)t' + \frac{Qk}{s}} e^{-st'} \\
&- (T_b \\
&- T_e) \frac{r_e}{s} \left(e^{-(k+r_e)t' + \frac{Qk}{s}} e^{-st'} \left(\frac{Qk}{s} \right)^{(k+r_e)/s} \right) \gamma_l \left(-\frac{k+r_e}{s}, \frac{Qk}{s} e^{-st'} \right)
\end{aligned} \tag{5.22}$$

where the integration constant C_1 is

$$C_1 = (T_{ref} - T_b) e^{-\frac{Qk}{s}} + (T_b - T_e) \frac{r_e}{s} \left(\frac{Qk}{s} \right)^{(k+r_e)/s} \gamma_l \left(-\frac{k+r_e}{s}, \frac{Qk}{s} \right) \tag{5.23}$$

There is one more representation of incomplete gamma function [82]:

$$\gamma_l(a, x) = a^{-1} e^{-x} x^a M(1, 1+a, x) \tag{5.24}$$

Here $M(1, 1+a, x)$ is the confluent hypergeometric function of the first kind [78, 83]:

$$M(\alpha, \beta, z) = \sum_{n=0}^{\infty} \frac{(\alpha)_n}{(\beta)_n n!} z^n = 1 + \frac{\alpha}{\beta} \frac{z^1}{1!} + \frac{\alpha(\alpha+1)}{\beta(\beta+1)} \frac{z^2}{2!} + \dots \tag{5.25}$$

where the $(\alpha)_n$ and $(\beta)_n$ are Pochhammer symbols denoted as:

$$(x)_n \equiv \frac{\Gamma(x+n)}{\Gamma(x)} = x(x+1)(x+n-1). \tag{5.26}$$

Substitute (5.24) to (5.22 – 5.23) we obtain the solution on the following form:

$$T(t') = T_b + C_1 e^{-(k+r_e)t' + \frac{Qk}{s}} e^{-st'} \quad (5.27)$$

$$- (T_b - T_e) \frac{r_e}{k + r_e} M\left(1, 1 - \frac{k + r_e}{s}, \frac{Qk}{s} e^{-st'}\right)$$

where the integration constant C_1 is:

$$C_1 = \left(T_{ref} - T_b + (T_b - T_e) \frac{r_e}{k + r_e} M\left(1, 1 - \frac{k + r_e}{s}, \frac{Qk}{s}\right) \right) e^{-\frac{Qk}{s}} \quad (5.28)$$

Finally, using the decomposition to series we got the following formula:

$$T(t') = T_b + C_1 e^{-(k+r_e)t' + \frac{Qk}{s}} e^{-st'} \quad (5.29)$$

$$\begin{aligned} & - (T_b - T_e) \frac{r_e}{k + r_e} \left(1 + \frac{(Qk)e^{-st'}}{(s - k - r_e)} \right. \\ & + \frac{(Qk)^2 e^{-2st'}}{(s - k - r_e)(2s - k - r_e)} \\ & \left. + \frac{(Qk)^3 e^{-3st'}}{(s - k - r_e)(2s - k - r_e)(3s - k - r_e)} + \dots \right) \end{aligned}$$

where the integration constant C_1 is:

$$\begin{aligned}
C_1 = & \left(T_{ref} - T_b \right. \\
& + (T_b - T_e) \frac{r_e}{k + r_e} \left(1 + \frac{(Qk)}{(s - k - r_e)} \right. \\
& + \frac{(Qk)^2}{(s - k - r_e)(2s - k - r_e)} \\
& + \frac{(Qk)^3}{(s - k - r_e)(2s - k - r_e)(3s - k - r_e)} \\
& \left. \left. + \dots \right) \right) e^{-\frac{Qk}{s}}
\end{aligned} \tag{5.30}$$

Observe that the explicit solution in the form (5.29-5.30) is real, whereas the solution in the form (5.22 – 5.23) with incomplete gamma function has complex items for negative values of Q , which correspond to the cooling phase. The series in the parenthesis (5.29-5.30) obviously converges; the computations show that it is enough to compute just 3 items of series for the accuracy within 10^{-4} . That's why this form has been chosen for the implementation and computation.

5.2.2 The thermoregulation term.

As far as we did not introduce any new physical and biological mechanisms, the thermoregulation term must be in the general solution above as well. Note that the stronger interaction with the environment is still linear; it is the same Newton's law of cooling, but with the different exponent factor. Similarly, the thermoregulation depends on r_e . Denote the thermoregulation term of the 1-st order model with the strong interaction with the environment similarly to the previous models, i.e. as the exponent factor of (5.27) and (5.29):

$$r_{1e}(t) = (k + r_e)(1 - Qe^{-st}) \quad (5.31)$$

Introduce the dimensionless ratio r_e/k ; the equation (5.31) can be reduced to

$$r_{1e}(t) = k(1 + r_e/k)(1 - Qe^{-st}) \quad (5.32)$$

One can see that the difference between (5.32) and (4.27) is negligible for small r_e/k , and vice versa.

5.2.3 Important special cases.

To better understand the solutions as developed in this Chapter, we should demonstrate how the solution applies to some important special cases. Recall that k , r_e , and s are the parameters which have the dimension of frequency; they show how fast the tissue temperature changes by such factors as blood, environment, and thermoregulation, correspondently.

5.2.3.1 No thermoregulation (examples: DPN subjects, Newton's law of cooling):

$$Q = 0.$$

Substitute $Q = 0$ to any form of the general solution. We have:

$$T_{Newton}(t') = \frac{T_b k + T_e r_e}{k + r_e} + C_0 e^{-(k+r_e)t'} \quad (5.33)$$

where the integration constant C_0 is:

$$C_0 = T_{ref} - \frac{T_b k + T_e r_e}{k + r_e} \quad (5.34)$$

Not surprisingly, we arrive at the Newton's law of cooling, where the weighted

coefficient and averaged time constant account for independent interaction with two media, *i.e.*, blood and environment.

5.2.3.2 *Thermoregulation in the air: $r_e = r_{air} \ll r_e = r_{w[ater]}, r_{air} \ll k$.*

Substitute back to t for time instead of t' , r_{air} vs. $r_{w[ater]}$ for the temporal constant of the external media, T_0 for the initial temperature, and T_A for the stationary temperature, we end up with the same solution as in the previous chapter:

$$T_1(t) = T_A + C_3 e^{-kt + \frac{Qk}{s} e^{-st}} \quad (5.35)$$

where the integration constant C_3 is:

$$C_3 = (T_0 - T_A) e^{-\frac{Qk}{s}} \quad (5.36)$$

Note that this is due to the fact that incomplete gamma and confluent hypergeometric functions do not conflict with the nice and understandable exponents.

5.2.3.3 *Strong thermoregulation (example: normal subjects).*

Recall that for normal subjects with the good thermoregulation, $s \gg k$. At the same time, we may assume $r_w \approx k$ because the mass-specific heat capacity of blood and water are almost the same. Therefore $(s - k - r_w) \lesssim s$. Thus Equation (5.29-5.30) can be approximated as:

$$T_{normal}(t') \gtrsim T_b + C_1^{normal} e^{-(k+r_e)t' + \frac{Qk}{s} e^{-st'}} - \frac{r_e(T_b - T_e)}{k + r_e} e^{\frac{Qk}{s} e^{-st'}} \quad (5.37)$$

where the integration constant C_1^{normal} is:

$$C_1^{normal} = (T_{ref} - T_b)e^{-\frac{Qk}{s}} + \frac{r_e(T_b - T_e)}{k + r_e} \quad (5.38)$$

Note that this is also consistent with the results from Chapter 4.

5.3 Experimental results

5.3.1 Model verification for the recovery phase

As it has been shown above, the model (5.29-5.30) is a generalization of the model (4.11, 4.25). As a result, we obtained very similar quality curve fitting results with the data from the recovery phase. Figure 5.1 shows the comparison results for the two models. One can see that the difference between two interpolating curves is below the measurement noise. It means that two models are equally good in describing the recovery of the cooled feet to core body temperature.

Figure 5.2 shows the typical thermoregulation plots computed by these two models. Observe that the plots look quite similar, but not exactly.

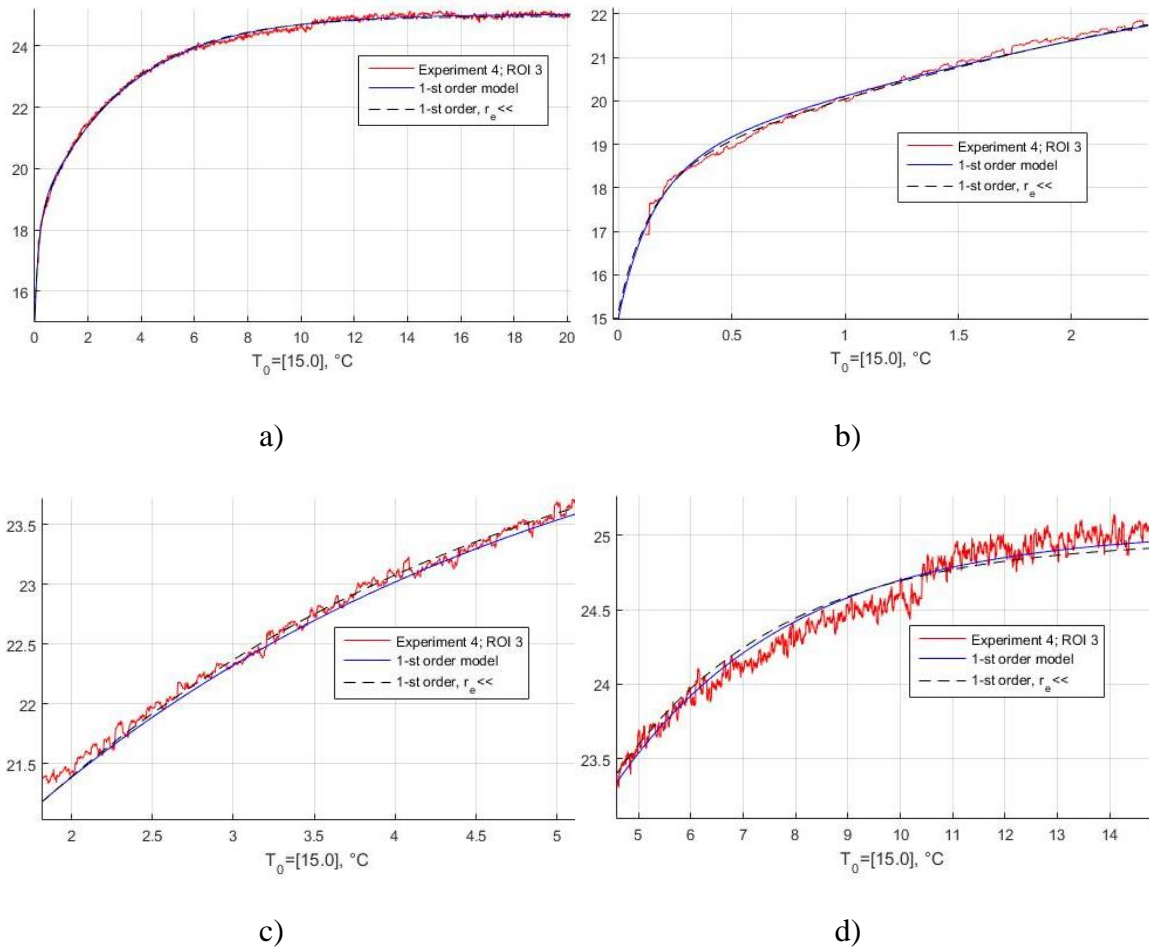


Figure 5.1. Nonlinear fit of the experimental data for TR-1_e and TR-1 $r_e \ll$: in the whole time range a) for 0...2 min b), 2...5 min c), and 5...15 min d).

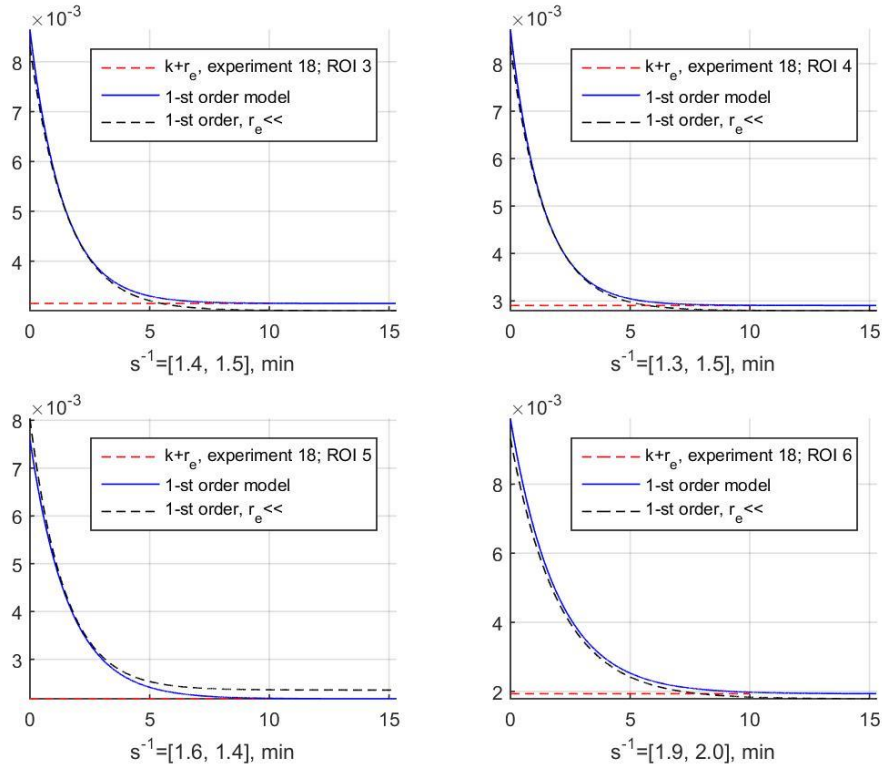


Figure 5.2. Sample thermoregulation plots for 4 ROIs computed with two different models; red dashed line shows the stationary value for the model (5.29-5.30), solid blue line; observe that is is some different for the model (4.11, 4.25), dashed black line.

5.3.2 Application of the general model to both cooling phase and recovery phase

For ≥ 15 minutes of measurements in the recovery phase with 8-9 Hz frame ratio one has a 7-8 thousands of control points obtained by direct measurements. For the cooling phase, we have two points of intersection of the interpolating curves obtained for the control and recovery phases, correspondently: T_{ref} at the beginning of cooling and T_0 at the end of cooling (i.e., the beginning temperature of the recovery, i.e. $t = 0$). The green dash almost horizontal line shows the change of water temperature, i.e. the quality of the satisfying the assumption of constant environment temperature. As can be seen, the water temperature change is within 1 degree and therefore can be ignored.

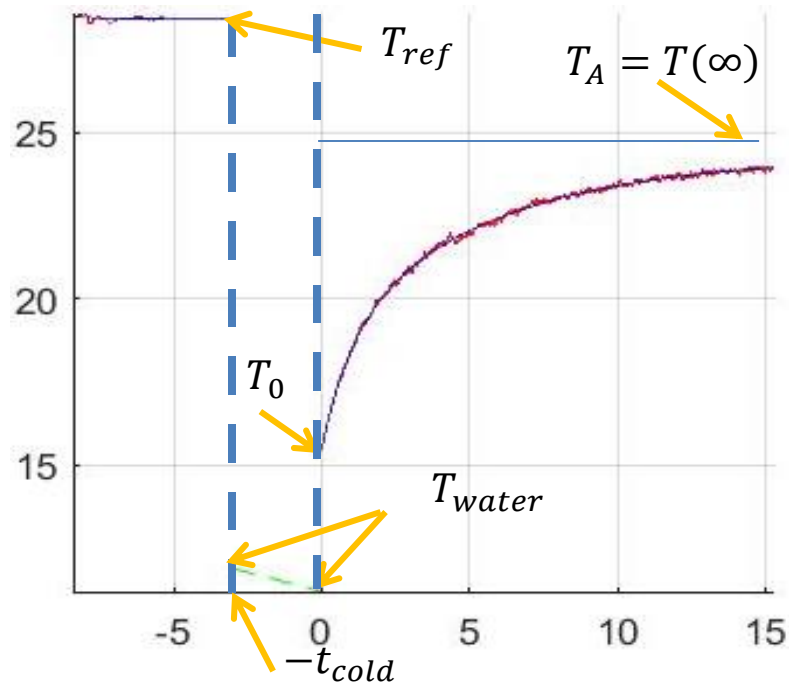


Figure 5.3. Sample plots illustrating three phases of the experiment.

When applying the model to the cooling phase, we have assumed that the model parameters for the same subject have [relatively] small variation between the cooling and the recovery phase. This is a valid assumption and has been experimentally verified; where we varied the starting conditions for the same subject and calculated the model parameters (see Table 5.1).

Cold stress duration, min	Cold stress temperature, °C							
	5.5	7.0-7.5	9.0-9.5	10.0-10.5	11.0-13.0	15.0	18.0	25.0
1			7			12		
2						10 _p	11	
3	27	[19, 20 ^R], [23, 24 ^R]	17 _p , [25, 26 ^R] _p	1	18 _p	13		
5			16 _p	2 _p , 8, 9 _p	3 _p , [21, 22 ^R] _p	4, 14, 15	5 _p	6 _p

Table 5.1. The initial conditions of the experiments with the normal subject VQB 04. Here the main index X means the number of the experiment (23 experiments total); two indices in the square parenthesis mark two feet placed into the water at the same time (4 such experiments gives 27 experiment indices); X^R means the right foot, and the indices without the superscript correspond to the left foot. X_p indicate the afternoon experiments, and the ones without the subscript done at the morning time.

With the above assumption, i.e., the same thermoregulation model parameter for the cooling phase and the recovery phase, one can find them as solution of the following optimization problem:

$$\{Q, s, k\} = \underset{\{Q, s, k\}}{\operatorname{argmin}} \left\{ \sum_{j=1}^N \left\| T^{(j)}(t) - T_{measured}^{(j)}(t) \right\|_2^2 \right\} \quad (5.39)$$

$$\text{subject to } lb \leq \{Q, s, k, T_0^{(j)}, T_A^{(j)}\} \leq ub$$

where $T_{measured}^{(j)}$ are data from the j-th experiment, $T^{(j)}$ are the correspondent model data, and $T_0^{(j)}$ are the initial temperatures interpolated for each experiment independently. We use the equation (5.39) to apply for the same thermoregulation model

as for the recovery phase in Chapter 4, i.e. the TR-1 assuming weak interaction with the environment. For the model Chapter 5.2 accounting the strong interaction with the environment one gets a very similar problem formulation:

$$\begin{aligned} \{Q, s, k, r_e\} = & \underset{\text{argmin}}{\left\{ \sum_{j=1}^N \left\| T^{(j)}(t) - T_{measured}^{(j)}(t) \right\|_2^2 \right\}} \\ & \text{subject to } lb \leq \{Q, s, k, r_e, T_0^{(j)}, T_A^{(j)}\} \leq ub \end{aligned} \quad (5.40)$$

Intuitively, the goal of this curve fitting is to minimize the difference between the interpolated and the actual temperature at the end of the cooling phase.

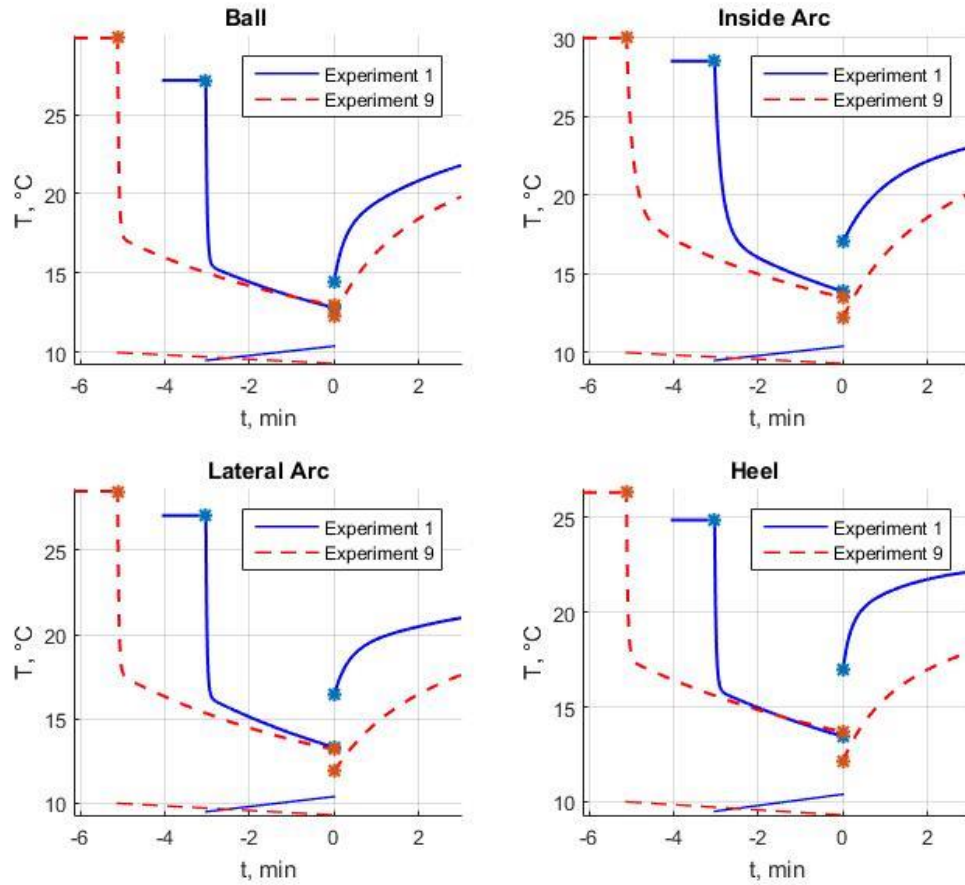


Figure 5.4. Sample plots illustrating the data and the residuals of the cooling phase.

The box plot Figure 5.6 below illustrates the residuals for all 26 experiments of Table 5.1. One can see the few outliers where the error is $> 4^{\circ}\text{C}$ or even more.

Experiment	Ball	Inner Arch	Lateral Arch	Heel
1	-0.33	-1.82	-1.79	-2.14
2	-3.75	-7.72	-2.03	-4.08
3	0.63	-0.89	-0.85	-1.27
4	2.32	1.57	0.78	1.31
5	1.90	2.30	1.26	2.14
6	0.61	0.98	0.34	0.33
7	0.15	-0.13	0.07	0.71
8	0.53	2.07	1.05	1.38
9	0.60	2.06	0.91	1.88
10	2.13	1.06	0.76	0.16
11	1.05	1.13	0.91	0.80
12	-0.68	-0.35	-0.31	-1.25
13	1.39	2.06	1.69	1.94
14	2.63	2.95	1.52	2.08
15	1.09	2.47	1.36	1.85
16	-0.40	-1.29	-0.91	-4.64
17	0.14	0.53	-0.05	-0.84
18	-0.72	-1.57	-0.17	-0.82
19	0.71	0.64	1.41	1.05
20	-1.02	0.13	-0.10	0.12
21	-0.51	0.49	0.53	0.83
22	-1.98	-2.83	-1.52	1.23
23	-1.44	-0.03	-0.58	-0.16
24	0.43	0.31	-0.61	0.38
25	0.31	1.03	0.28	1.37
26	-1.95	-1.28	-1.39	-0.78

Table 5.2. The residuals of cooling phase, all 26 similar experiments.

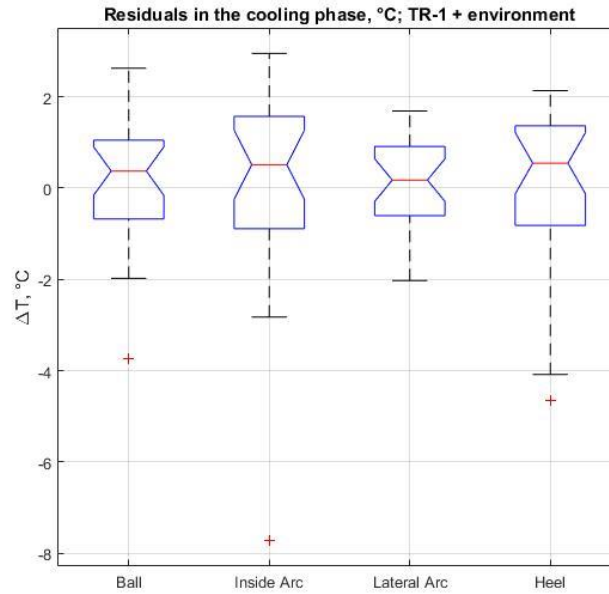


Figure 5.5. The residuals of the cooling phase reflected in Table 5.2 above.

A further investigation of the experimental data revealed that the most outliers correspond to abnormal experimental conditions. For example, two of such outliers correspond to 5-minute cooling into the colder water (9-10 °C). Note that normally, cooling is performed for 3 minutes and using (10 °C) water. Another one of such outliers corresponds to cooling with 25 °C water. One would assume that these experiments under fairly extreme conditions could be very different. Based on our record, we don't have explanation for the 4th outlier.

Figure 5.7 a) and Table 5.3 a) show the curve fitting results without the 4 outliers. For all 4 ROIs the medians are within 0.3 °C from 0; the main parts of the distribution (25%-75%, marked with the boxes) are within 1 °C from the corresponding medians; the worse cases are within 2.5 °C (marked with whiskers); no outliers found. This showed that our generalized model captures the cooling phase.

Experiment	Ball	Inner Arch	Lateral Arch	Heel		Ball	Inner Arch	Lateral Arch	Heel
1	-0.37	-1.97	-1.85	-2.10		-1.22	-2.75	-2.66	-2.97
3	-0.11	-2.39	-1.33	-2.39		-0.01	-2.28	-1.23	-2.26
4	1.69	0.31	0.36	0.35		2.07	0.69	0.74	0.77
5	1.36	1.31	0.94	1.45		1.59	1.52	1.15	1.67
7	0.44	-0.01	0.48	0.78		1.37	0.78	1.38	1.76
8	-0.20	0.62	0.53	0.18		0.66	1.47	1.40	1.11
9	-0.35	0.28	0.26	0.36		0.82	1.41	1.41	1.61
10	2.24	1.29	0.76	0.28		2.67	1.69	1.19	0.73
11	1.16	1.34	0.95	0.93		1.35	1.52	1.15	1.14
12	-0.32	-0.02	0.03	-0.88		-0.57	-0.28	-0.21	-1.13
13	1.25	1.82	1.54	1.77		1.27	1.86	1.57	1.80
14	2.06	1.71	1.15	1.25		1.76	1.44	0.86	0.95
15	0.41	1.15	0.91	0.83		0.81	1.54	1.31	1.27
17	0.05	0.34	-0.15	-0.90		-0.46	-0.12	-0.63	-1.40
18	-0.96	-1.88	-0.40	-1.18		-0.07	-1.03	0.48	-0.24
19	0.68	0.49	1.36	1.12		-0.57	-0.67	0.16	-0.14
20	-1.04	-0.03	-0.15	0.18		-2.30	-1.19	-1.35	-1.07
21	-1.05	-0.68	0.22	-0.02		-2.24	-1.82	-0.94	-1.19
23	-1.53	-0.31	-0.67	-0.18		-2.86	-1.54	-1.95	-1.52
24	0.33	0.04	-0.70	0.35		-0.99	-1.20	-1.97	-0.99
25	-0.12	0.51	-0.12	0.67		1.61	2.13	1.57	2.49
26	-2.39	-1.81	-1.79	-1.47		-0.66	-0.19	-0.09	0.35
	a)					b)			

Table 5.2. Residuals of the cooling phase, 22 experiments by the model with the strong interaction with the environment a), and by the model with the week interaction with the environment b).

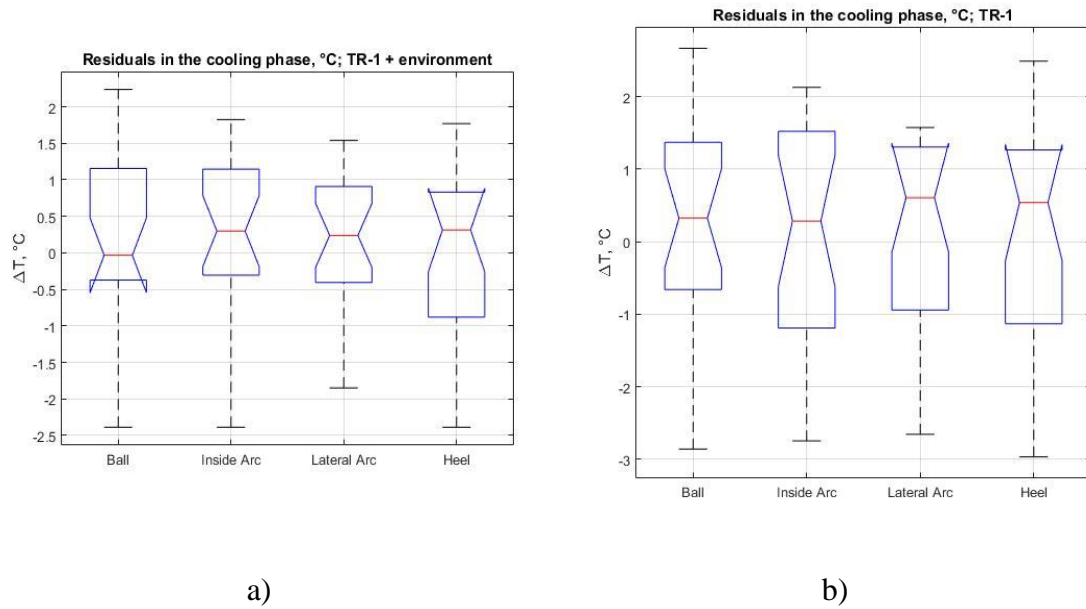


Figure 5.6. Residuals of the cooling phase, 22 experiments by the model with the strong interaction with the environment a), and by the model with the weak interaction with the environment b).

It is also worthwhile to point out that we have applied the model from Chapter 4 to the cooling phase as well for comparison with the general model. The fitting results Figure 5.7 a) and Table 5.3 a) in larger error in the following terms: the medians are farther from zero, the main part of distribution is visually wider, and the largest error is greater.

This is the only way to compare the quality of two models for the case where they should be different, i.e. for cooling, and we see that they really are. We can conclude that the model taking into account interaction with the environment (here – with water) is more accurate.

Observing the typical cooling curves Figure 5.5 one can visually separate two sub-phases of cooling. The model shows that being submerged to cold water, the tissue surface cools down rapidly (first sub-phase), and then – slowly (second sub-phase). It means that the thermoregulation reacts much faster for the negative temperature jump than for the

positive one in recovery phase, i.e. the vessels constrict fast; after the end of this sub-phase, i.e. after the end of thermoregulation, the tissue slowly colds down by the Newton's law of cooling. See the thermoregulation plots at Figure 5.8 below; compare the speed of thermoregulation for the recovery phase, Figure 5.3 – it is ~50 times faster at the beginning of cooling.

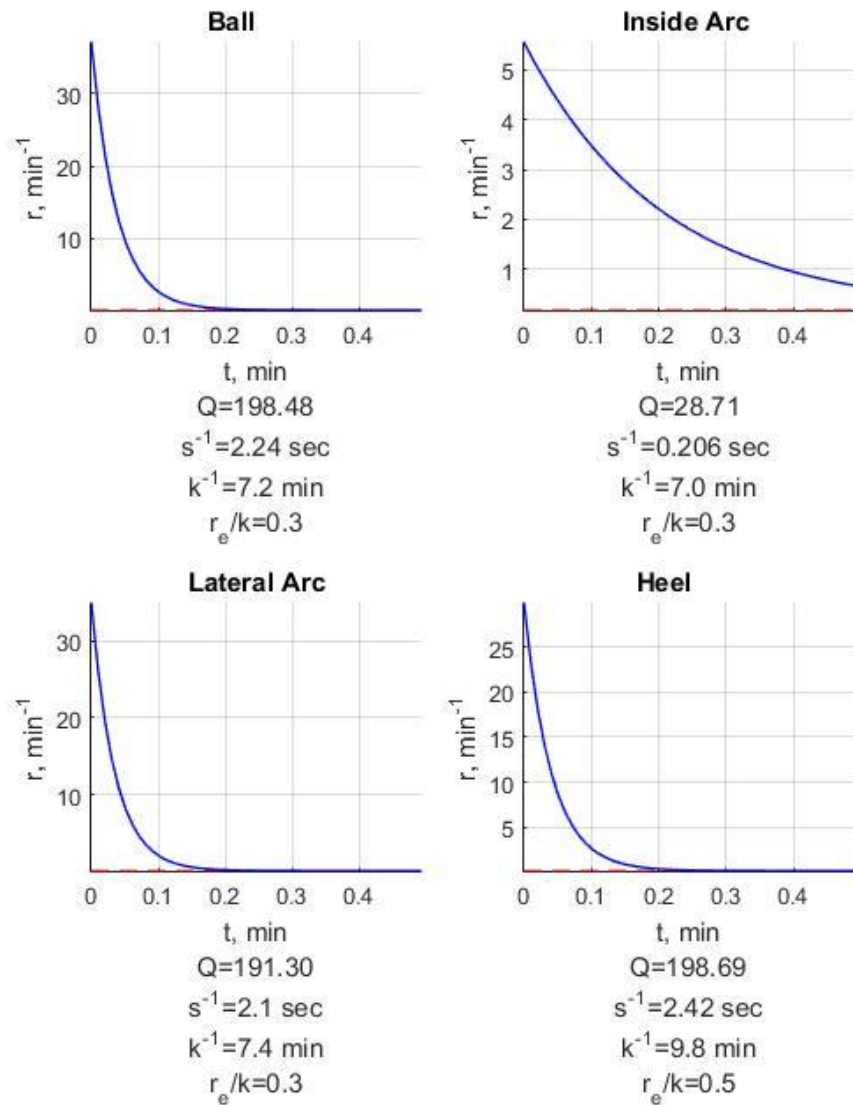


Figure 5.7. Parameters of thermoregulation and $r(t)$ for the cooling phase, 22 experiments.

5.4 Practical recommendations.

The cooling phase is much more difficult for measurements; also, the optimization described above is ill-posed because of the assumptions we made. Despite of this, one can get some practical recommendations from the results obtained above.

First, one can bound the temperature and the duration of required cold stress, which is important to save time, and even much more important to make the patients more comfortable. 3 minutes in 11-13 °C water is much easier for any tested subject than 5 minutes in 10 °C. On the other hand, the stress temperatures ≥ 20 °C are too high to switch the thermoregulation on with confidence.

Second, if one got the far outlying parameters of thermoregulation modeling for the cooling phase, it should indicate that the experiment requires more attention. It does not mean that the subject has a DPN, but it could be one of the reasons. Another reason could be that something went wrong during the experiment. Thus, if the cooling phase shows the far outlying parameters, and much more robust recovery phase shows the slow thermoregulation, the subject definitely suspected to be a DPN. If two phases show different results, especially if the cooling phase demonstrates far outlying, we could recommend repeating the experiment with this subject.

It must be noticed that the set of the experiments described above has been done with one subject. To bound the thermoregulation parameters of cooling phase more precisely, which is definitely required for the estimation of outliers, more experiments with different subjects are required.

5.5 Conclusion

1. The model of the feet thermoregulation taking into account interaction between the tissue and cooling water has been developed.
2. The model has been verified for the recovery phase, and demonstrated the same accuracy and robustness as the simplified model.
3. The model has been applied for the modeling of cooling phase. It demonstrates better accuracy than the model without strong interaction.
4. The model has been used to bound the cold stress conditions to minimize the discomfort of tested subjects, and to estimate variance of the thermoregulation parameters.
5. The additional criterion for the more robust diagnostics of DPN based on the estimation of thermoregulation parameters and modeling error in cooling phase is proposed.

Chapter 6 Classification

‘Who are YOU?’ said the Caterpillar.

This was not an encouraging opening for a conversation. Alice replied, rather shyly,

‘I—I hardly know, sir, just at present— at least I know who I WAS when I got up this morning, but I think I must have been changed several times since then.’

‘What do you mean by that?’ said the Caterpillar sternly. ‘Explain yourself!’

‘I can’t explain MYSELF, I’m afraid, sir’ said Alice, ‘because I’m not myself, you see.’

‘I don’t see,’ said the Caterpillar.

Lewis Carroll. Alice’s Adventures in Wonderland.

Carving is easy; you just go down to the skin and stop.

Michelangelo Buonarotti.

6.1 Motivation

The ultimate goal of this research is to investigate that if one can differentiate the DPN subjects from the non-DPN subjects using the parameters extracted from the thermal regulation models.

Since the beginning of this research, some 40 subjects have been measured using the protocol described in Section 2. The subjects are partitioned into different age-race-gender matched groups with the suggestion from an endocrinologist. The group of the 64-

72-year old white male subjects is shown here to demonstrate the classification with different criteria. The group is picked because it has the largest population so far in our current patient database. The group includes four control subjects and four subjects who have been diagnosed with diabetic peripheral neuropathy.

Let us describe herewith the various algorithms proposed for the diagnosing.

6.2 The first naïve expectation: slower recovery of PN comparing to the control group

Since we are measuring the quality of thermal regulation, an intuitive classifier is the speed of recovery. The idea has been proposed in [112] and later discussed in [113] [114] [115]. One would expect the foot of healthy subject without peripheral neuropathy should recover faster to the core temperature than a subject with peripheral neuropathy following cold stimulus, compare the plots at [Figure 6.1](#).

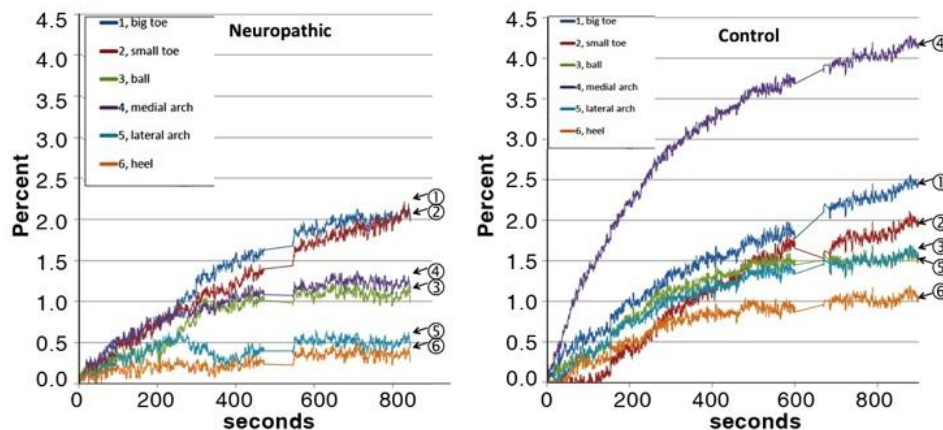


Figure 6.1. Different temperature change over time of the neuropathic subject (left), and the normal subject (right).

Let T_{ref} be the temperature of a particular region of interest (ROI) on a subject's foot before the cooling. Assume the ROI is cooled down to T_0 , and let $T(t)$ be the temperature recovery of the ROI over time t . See [Figure 6.2](#) for illustrations. In the plot,

the X-axis is time and Y-axis is temperature. The temperature before $t = 0$ is the original core temperature T_{ref} . Recovery starts at time $t = 0$. (Note that we are not imaging the cooling process.) The cool down temperature T_0 is the temperature at $t = 0$, and the recovery temperature $T(t)$ over time is the curve fitting result of temperature change extracted from the infrared video.

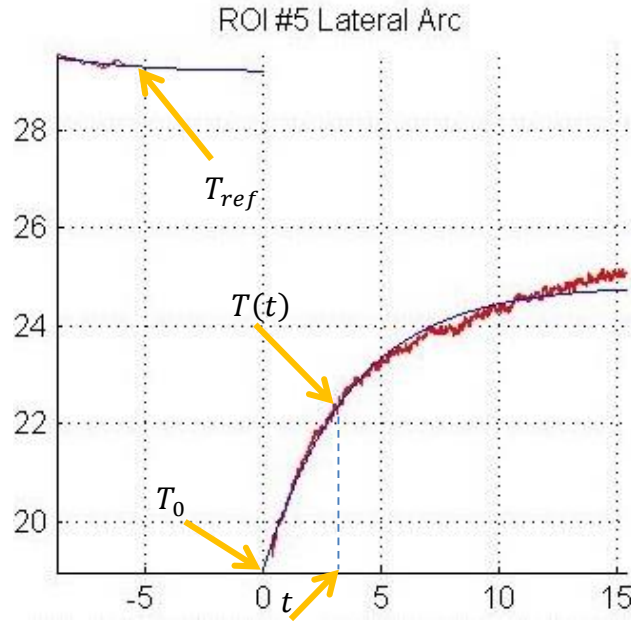


Figure 6.2. Illustrating T_{ref} , T_0 , and $T(t)$

Denote the recovery ratio at time t as

$$\epsilon(t) = \frac{T(t) - T_0}{T_{ref} - T_0}. \quad (6.1)$$

As mentioned in Chapter 2, we have 6 regions of interests (ROIs) identified. We shall denote the recovery ratio of the six ROIs as $\epsilon_j(t)$, where $j = 1, 2, 3, 4, 5, 6$. Since peripheral neuropathy affects the foot non-uniformly, i.e., some ROIs may have a good thermal regulation whereas others may not, and a patient is diagnosed with peripheral neuropathy if he or she has lost sensation at the any part of the foot, the classifier is chosen

as the minimum recovery ratio amongst all six ROIs, i.e.,

$$\epsilon_{min}(t) = \min\{\epsilon_j(t), j = 1, 2, 3, 4, 5, 6\}$$

[Figure 6.3](#) shows the scatter plot of the group of 64-72-year old white male subjects for ϵ_{min} at time $t = 3 \text{ minute}$. The blue diamonds represent the healthy subjects without peripheral neuropathy, and the red asterisks represent subjects with diagnosed peripheral neuropathy. [Figure 6.3](#) indicates that ϵ_{min} can potentially be used as a classifier for quantitative identification of peripheral neuropathy.

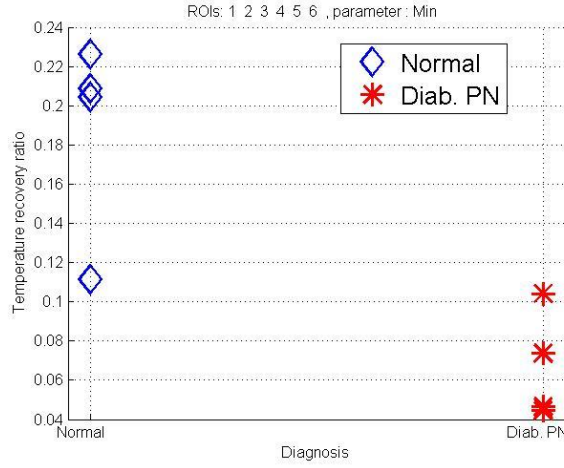


Figure 6.3. Scatter plot of $\epsilon_{min}(t)$ for $t = 3 \text{ minutes}$.

It is also worthwhile to note the following.

- 1) There is no particular reason for picking $t = 3 \text{ minutes}$. However, clinically it is ideal to use a shorter time t since it can help reduce the imaging time and thus improve patient throughput.
- 2) The recovery speed is determined more with the body parameters, which are different for different patients (like heart rate, body temperature, blood pressure) and the environment. The influence of the peripheral features in the

overall thermal signal is much smaller, almost noise-level; it is impossible to differentiate them. Mostly therefore the method is not robust.

6.3 The parametric classification

The methods based on the estimated parameters of the thermoregulation model discussed in Chapter 4 naturally differentiate the peripheral features of the foot.

6.3.1 Amplitude of regulation.

Remind the thermoregulation $r(t)$ which is (4.15) for the model of the first order TR-1. Denote the amplitude A_r of thermal regulation [116] [117] [118] as:

$$A_r = r(0) - r(\infty) = k|Q|. \quad (6.2)$$

See [Figure 6.4](#) for the illustration. Greater value of A_r means stronger thermoregulation. Therefore, for subjects without peripheral neuropathy, we expect stronger thermoregulation than for the ones with peripheral neuropathy $|Q| \approx 0$.

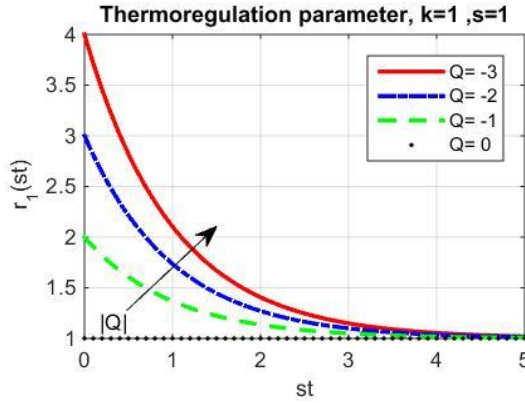


Figure 6.4. Illustration of the parameters of (5.2).
Here A_r changes from 0 for $|Q| = 0$ to 3 for $|Q| = 3$

As mentioned previously, since peripheral neuropathy affects the foot non-uniformly, the minimum of A_r for all ROIs is used as a classifier. [Figure 6.5](#) shows the scatter plot of the age group 64-72-year old white male for minimum A_r . Like in [Figure](#)

6.3, the blue diamonds represent healthy subjects without peripheral neuropathy and the red asterisks represent subjects with diagnosed peripheral neuropathy. Thus minimum A_r can be a good classifier for identifying peripheral neuropathy [117] [118].

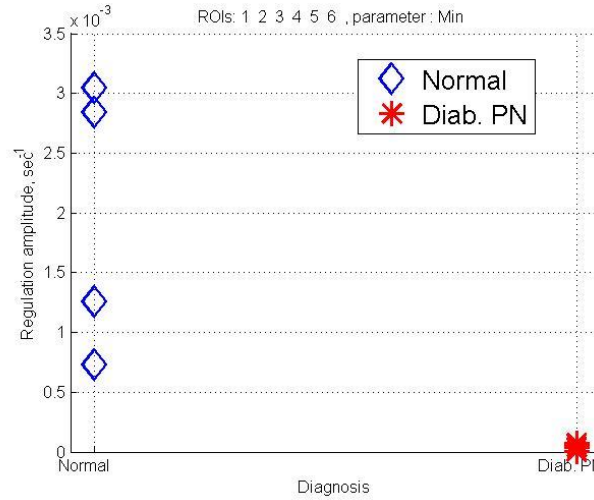


Figure 6.5. Scatter plot of A_r for the selected group.

It is also worthwhile to note the following. From [Figure 6.5](#) one can see that for all four subjects with diabetic peripheral neuropathy, the minimum of their A_r 's are close to 0. This implies at least one ROI has extremely small amplitude of thermoregulation. This is illustrated in the scatter plot of the A_r 's for individual ROIs in [Figure 6.6](#). As can be seen from [Figure 6.6](#), three out of four subjects with peripheral neuropathy has bad thermal regulation in their big toe [Figure 6.6 a\)](#) and two out of the four subjects with peripheral neuropathy have bad thermal regulation in their heel [Figure 6.6 b\)](#).

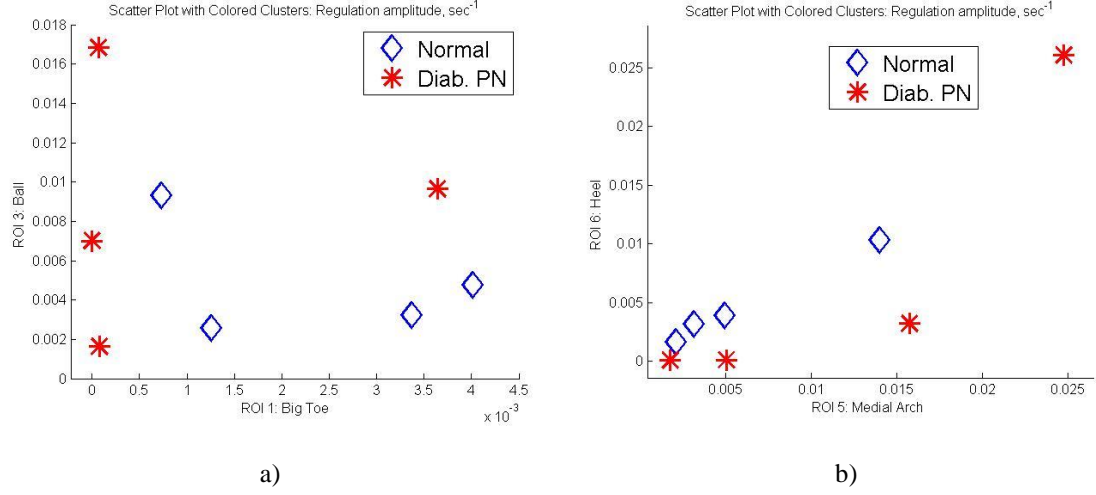


Figure 6.6. Scatter plots of A_r with different ROIs.

6.3.2 Inversed speed of regulation

One of the successful classifiers is the thermal regulation speed Δt [116]. It is equal to

$$\Delta t = 2s^{-1}. \quad (6.3)$$

Smaller value of Δt means faster time to reach maximum thermal regulation, and therefore a stronger thermoregulation.

Since peripheral neuropathy affects the foot non-uniformly, the maximum of Δt for four ROIs (excluding toes) is used as a classifier. [Figure 6.7](#) shows the scatter plot for maximum Δt for the same age-race-gender matched small group of 8 subjects (4 normal control and 4 with diabetic peripheral neuropathy). As can be seen, the maximum Δt shows promise as a classifier of peripheral neuropathy.

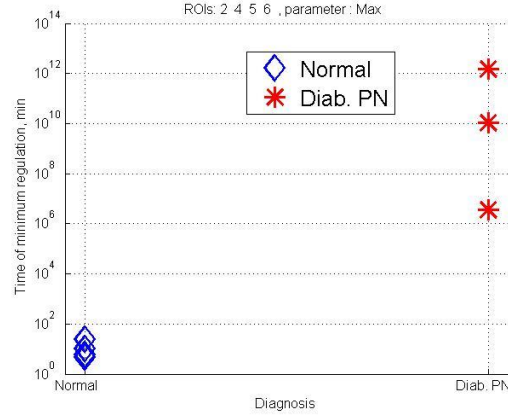


Figure 6.7. Scatter plots of $\max(\Delta t)$ for the selected group b).

6.3.3 Advantages and disadvantages

The main advantage of the parametric classification is the ability to separate the strongest signal component, which corresponds to the non-regulated warming from the area-specific regulation. Also they are the only ones usable for the low-cost IR diagnostic system described in Chapter 2.4 as far this camera does not produce an image. One can visually compare the regulation curves for the tested subjects and certain that the diabetic subject has greater value of Δt .

The first disadvantage is that the processing with these methods requires some manual operation, at least entering the positions of ROIs and the initial referencing for the registration.

The main disadvantage is common for all methods requiring discrete ROIs. Selection of ROIs is very approximate, very subjective, and very non-robust geometrically. The next day the same operator for the same subject could select some different and may be even non-overlapping ROIs inside the foot.

The problematic areas, which are strongly damaged with diabetes, i.e. the areas of

DPN are generally different on the foot for different PN subjects. The ROIs may not overlap with the problematic areas. Moreover, for the different patients they may overlap with the different problematic areas.

6.4 The “take attention” supplementary approach.

For the increasing of overall robustness of classification, it is proposed to complete the parametric classification with other methods, which let us filter the wrong experiments out, or, if it happens, take additional attention for such experiments and subjects.

6.4.1 Delay of capturing.

The TR-1 model gives a robust interpolation even with the absence of the initial data, i.e. with the delay of capturing of the recovery phase. Notice that the exponential solution of the model equation changes much faster namely at the beginning. It means that the investigators not measuring early stage are missing most important part of recovery signal. The model keeps robustness up to ~ 1.5 min of delay; if ≥ 2 min of data is lost the model cannot guarantee neither the good fit, nor correct values of the model parameters.

Therefore, the most correct approach is a) start capturing in time; b) repeat the experiment with the significant loss of data.

6.4.2 Parameters of the cooling phase.

As it has been notices at Chapter 5, if one got the far outlying parameters of thermoregulation modeling for the cooling phase, it should indicate that the experiment requires more attention. One needs to take more experiments with different normal subjects to bound so ill-posed cooling model with some confidence; nevertheless, we have enough data to bound one subject.

6.4.3 Parameters related to bounds.

The optimization problems (4.3, 4.29, 5.39) are constrained, because they are formulated as subject to bounds. It narrows the domain of search, keeps the parameters within their physical meaning, and let avoid meaningless local minima. If the optimization algorithm hits the bound during the computation, it means that the found parameters may be are mathematically optimal, i.e. correspond to a local minimum, but may be not physically reasonable. It could indicate either the error of the experiment or potentially problematic region.

The first bound is $\min(T_0 - T_{water})$ for all ROIs. Obviously, T_{water} is the lower bound for the foot temperature: the foot cannot be colder than the water. If the optimization finds the solution where $T_0 - T_{water} \cong 0$ it indicates a potential error, most often correlated either with the delay of capturing, or with the untracked strong foot shake, see Figure 6.8 a).

The second source of potential error is if $Q/Q_{bound} \approx 1$, see Figure 6.8 b), which could happen by the same reasons.

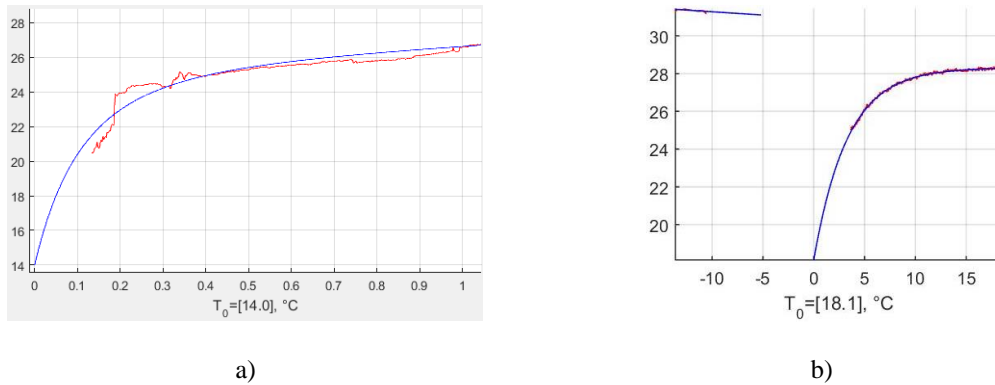


Figure 6.8. Examples of bounded solutions:
a) $T_0 - T_{water} \approx 0$; subject VQB-022 (diabetic); b) $Q/Q_{bound} = 1$; subject UNM-03 (normal).

6.4.4 Interpolation quality parameters.

Low interpolation quality means that the model does not fit the experiment well. It could happen due to untracked foot shake, or could indicate a potentially problematic region, see Figure 6.9. The natural metrics of the goodness of fit are mean error and root mean square error.

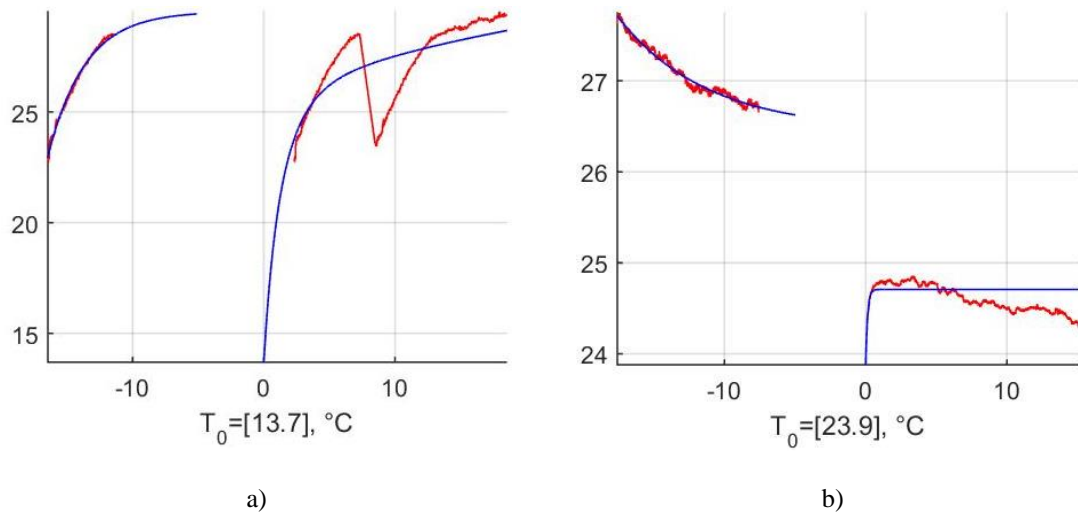


Figure 6.9. a) Experimental error (strong shaking); subject UNM-019 (diabetic).
b) Problematic region (heel); subject VQB-03 (diabetic).

6.5 Results of the parametric classification.

We have also experimented in setting up a classifier with the entire data set that include 17 for the normal control subjects, 20 diabetes subjects with no formal diagnosis of DPN, and 14 diabetes subjects with the diagnosed peripheral neuropathy (DPN), see Table 6.1.

#	Control subjects					Diabetic subjects					DPN subjects				
	Experiment ID	Initial H ₂ O Temp	End H ₂ O Temp	Cold pressor time, min.	Delay of capturing, min.	Experiment ID	Initial H ₂ O temp.	End H ₂ O temp.	Cold pressor time, min.	Delay of capturing, min.	Experiment ID	Initial H ₂ O temp.	End H ₂ O temp.	Cold pressor time, min.	Delay of capturing, min.
1	Test feet 001	13.1	13.4	5.05	1.67	Subject UNM 015	13.8	14.2	5.13	2.70	Test feet 016	13	13.5	5.32	1.28
2	Patient VQ 002	13.1	13.4	5.02	0.24	Subject UNM 016	13.7	13.9	5.00	1.49	Test feet 017	13.8	14.1	5.03	2.22
3	Subject UNM 01	11.3	12.3	4.82	0.77	Subject UNM 017	13.5	13.8	5.07	1.85	Test feet 018	13.6	14.7	5.05	1.08
4	Patient UNM-01	13.4	14	5.27	1.05	Subject UNM 019	13.5	13.7	5.07	2.31	Patient UNM-002	13.6	14	5.05	2.75
5	Patient UNM 03	13.4	13.7	5.15	3.65	Subject UNM 020	13.9	14.1	5.12	4.38	Patient UNM 004	13.4	13.4	5.70	1.70
6	Test feet 007	13.3	13.9	5.73	2.00	Subject UNM 021	13.7	13.9	5.10	2.66	Subject UNM 005	13	13.2	4.87	1.97
7	Subject VQB 01	12.2	13.1	5.02	0.25	Subject UNM 022	13.7	14.3	5.15	1.65	Subject UNM 006	13	13.4	5.00	3.09
8	Test feet pat 001	13.2	13.2	5.02	0.35	Subject UNM 023	13.8	14.2	5.82	2.23	Subject UNM 008	13.8	14.1	5.07	1.28
9	Test feet pat 005	13.2	14.1	5.17	0.22	Subject UNM 025	13.9	13.9	5.33	1.23	Subject UNM 009	13.5	13.5	5.88	3.42
10	Test feet pat 006	13.2	14.5	5.10	0.53	Patient VQ 019	11.7	12.8	5.03	0.37	Subject UNM 010	13.5	13.7	5.15	3.04
11	Test feet pat 007	13	13.4	5.08	0.41	Test feet VQ 03 1	12.9	13.4	5.03	1.62	Subject UNM 012	13.8	13.8	5.35	2.05
12	Test feet pat 009	13.5	13.5	5.17	0.40	Patient VQ 03 02	13.3	14.2	5.05	0.17	Subject UNM 013	13.5	13.9	5.02	3.14
13	Test feet pat 010	13	14	5.02	0.83	Patient VQ 03 03	13.2	14.4	5.05	0.10	Subject UNM 014	13.5	13.8	5.03	3.06
14	Test feet pat 011	13.6	14.3	5.05	2.01	VQB 22 01	13	14	5.02	0.23	Subject UNM 018	13.39	13.78	5.02	1.62
15	Test feet 001 p	13.4	14.2	5.23	1.90	VQB 22 02	13	14	5.05	0.13					
16	Subject VQB 04	11.2	12.5	5.00	0.22	Test feet pat 008	13.4	14.2	5.10	0.28					
17	p 06 24	11.9	12.1	5.02	0.08	Test feet 012	13.8	14.2	5.03	0.41					
18						Test feet 013	13.1	14.1	5.07	0.84					
19						Test feet 014	13.6	14.7	5.30	0.94					
20						Test feet 015	13.3	14.2	5.10	0.37					

Table 6.1. Data collected by the standard protocol

Cold stress duration, min	Cold stress temperature, °C							
	5.5	7.0-7.5	9.0-9.5	10.0-10.5	11.0-13.0	15.0	18.0	25.0
1			7			12		
2						10 _p	11	
3	27	[19, 20 ^R], [23, 24 ^R]	17 _p , [25, 26 ^R] _p	1	18 _p	13		
5			16 _p	2 _p , 8, 9 _p	3 _p , [21, 22 ^R] _p	4, 14, 15	5 _p	6 _p

Table 6.2. The initial conditions of the experiments with the normal subject VQB 04. Here the main index X means the number of the experiment (23 experiments total); two indices in the square parenthesis mark two feet placed into the water at the same time (4 such experiments gives 27 experiment indices); X^R means the right foot, and the indices without the superscript correspond to the left foot. X_p indicate the afternoon experiments, and the ones without the subscript done at the morning time.

6.5.1 Exclusion of the outliers.

The toe ROIs have been excluded in this study because they can't be reliably segmented and tracked due to motions.

The interpolation quality parameters for all experiments taken into consideration reflected in Figure 6.10 (max(ME) for 5 min) and 6.11 (max(RMSE) for 10 min). It looks like the diabetic subject VQB 22 (index 4) and DPN subjects UNM 22 (index 4) requires additional attention (which is true for both).

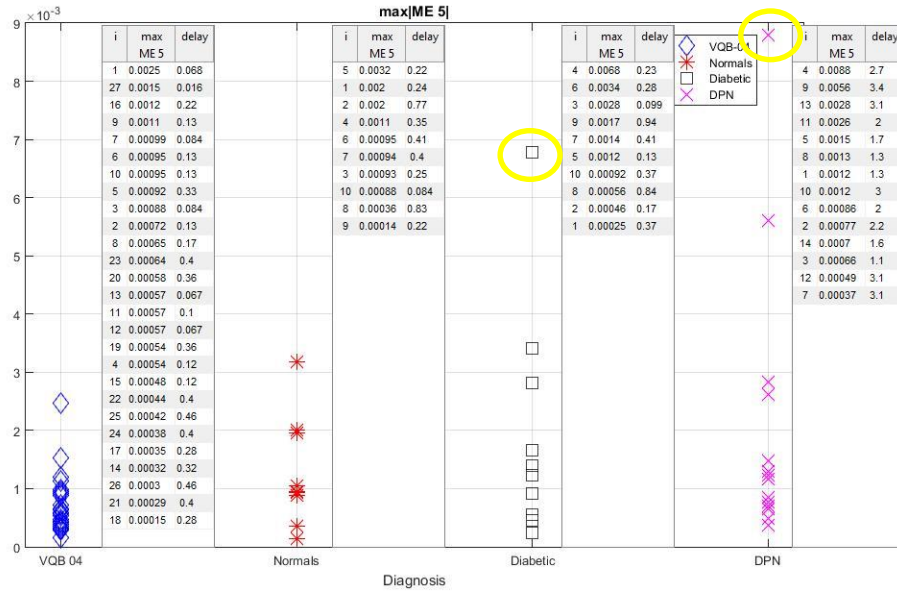


Figure 6.10. Interpolation quality parameter max|ME| for 5 min.

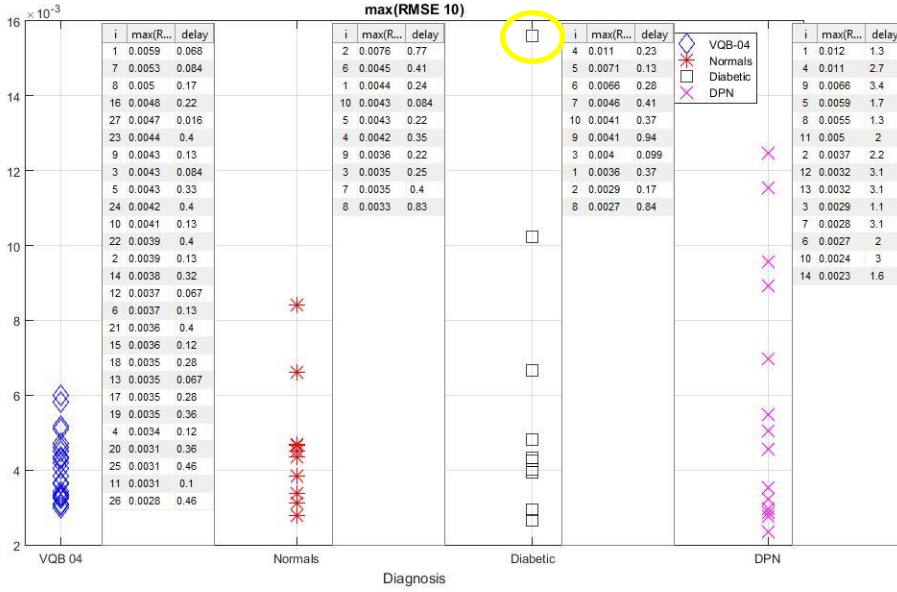


Figure 6.11. Interpolation quality parameter max|RMSE| for 10 min.

Figures 6.12 and 6.13 show the parameters related to bounds: $\min(T_0 - T_{water})$ and Q/Q_{bound} , correspondently. The first criterion marked as suspects 4 DPN and 2 diabetic subjects; the second one pointed to one diabetic subject (index 10) and 3 DPN subjects.

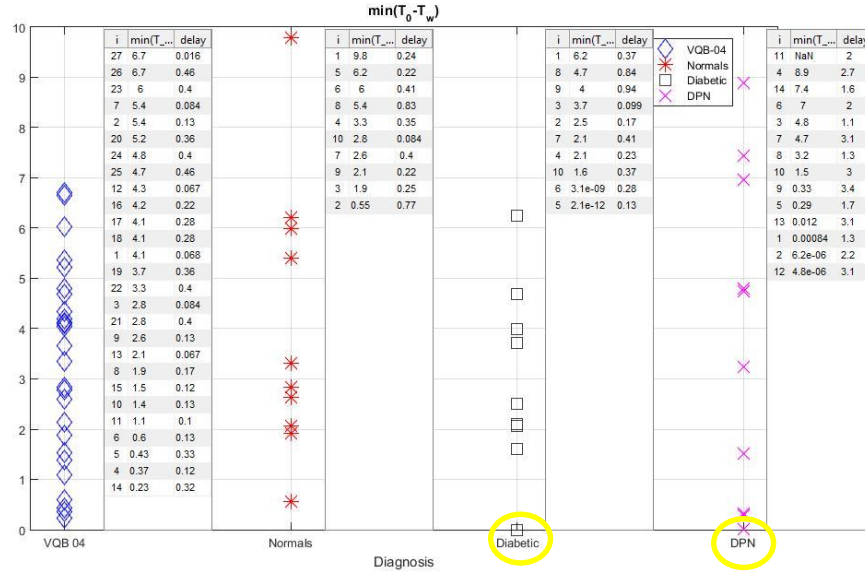


Figure 6.12. Bounded $\min(T_0 - T_{water})$

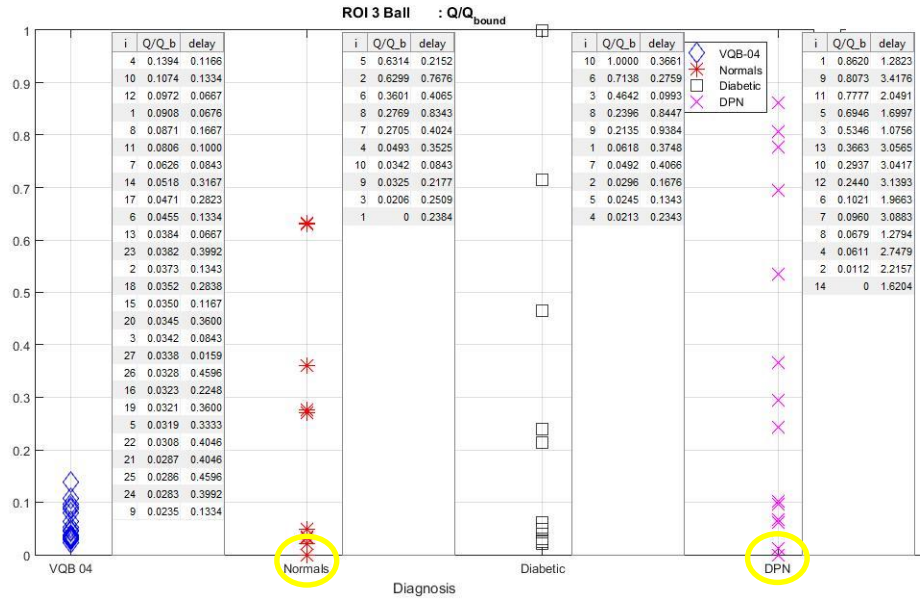


Figure 6.13. Bounded $\max(Q/Q_{bound})$

6.5.2 Classification by the thermoregulation model parameters.

The tables and scatter plots on Figures 6.14 and 6.15 demonstrates the classification with the parameters discussed above: $\min(k|Q|)$ and $\min(s)$, correspondingly. The horizontal level lines correspond to the optimal values of corresponding parameters. One

can use different criteria for thresholding; we used the Bayesian criteria to minimize the total probability of false positives (i.e., control subjects recognized as DPNs) and the false negatives (i.e., DPN subjects recognized as normal ones). By this, the threshold value for $\min(k|Q|)$ is 0.0031 sec^{-1} , and for $\min(s)$ it is equal to 0.0038 sec^{-1} . As far as there is no gap between these sets, we are not trying to classify diabetic subjects without DPN; they could be relatively “classified” so far as “rather DPN” or “rather not”.

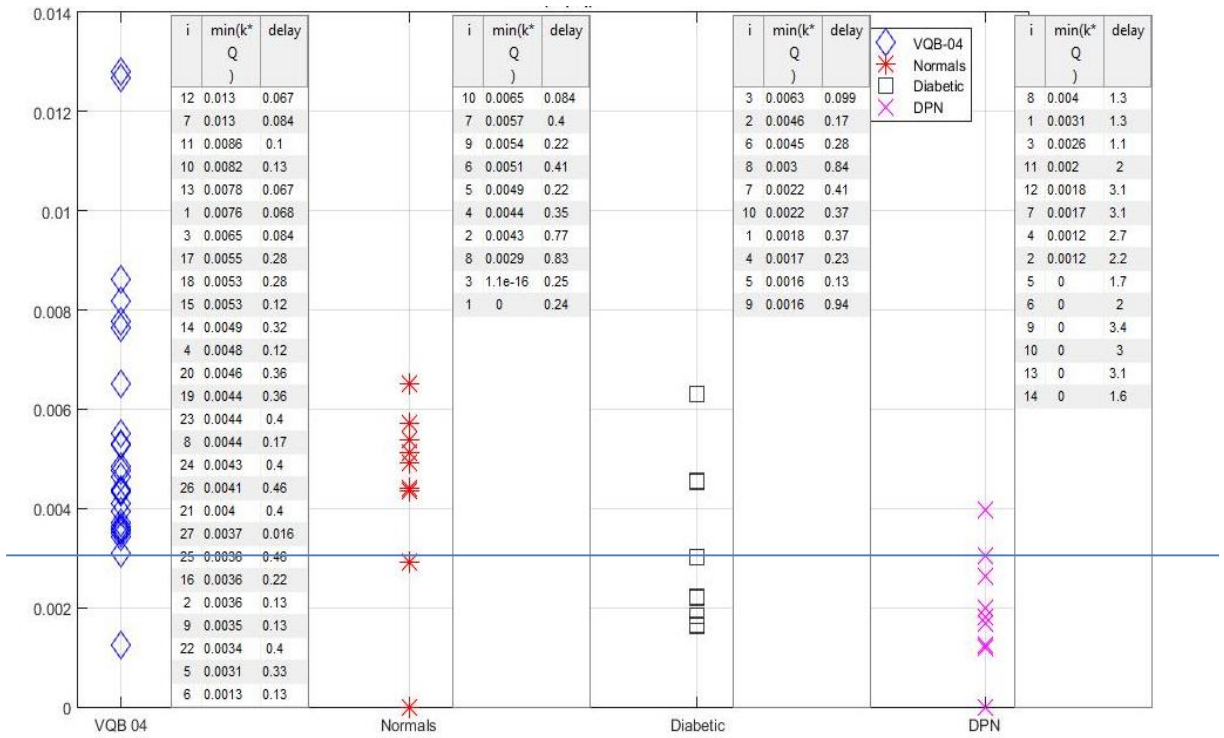


Figure 6.14. $\min(k|Q|)$

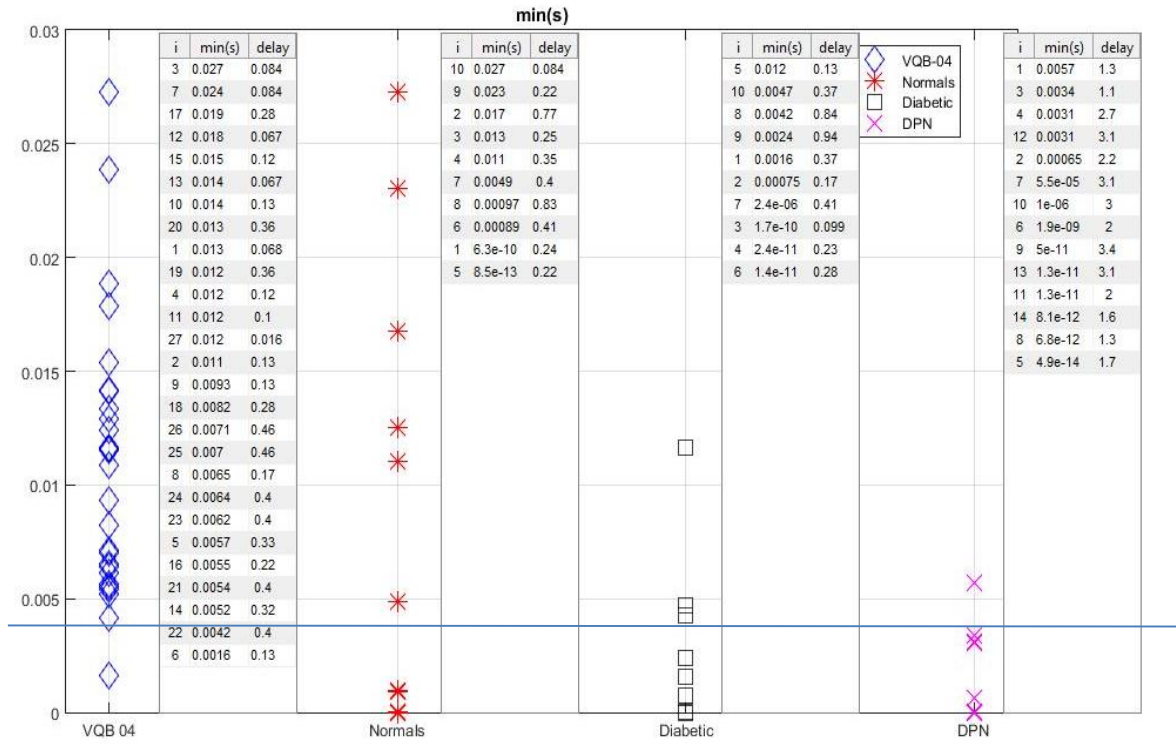


Figure 6.15. $\min(s)$

The tables in Figure 6.16-6.17 show the number of misrecognized subjects and the probabilities of errors, sensitivity and specificity. The number of classified experiments is 27 for VQB-04 + 10 for other control subject (37 control experiments total), and 14 DPN subjects.

Diagnosis	VQB 04	Controls	DPNs
No DPN	25	7	1 (8)
DPN	2 (6, 5)	3 (1, 3, 8)	13

a)

Diagnosis	Controls	DPNs
No DPN	0.86	0.07
DPN	0.14	0.93

b)

Figure 6.16. $\min(k|Q|)$. Number of correctly and incorrectly classified subjects, and the indices of incorrectly classified ones a); probabilities of errors, sensitivity and specificity.

Diagnosis	VQB 04	Controls	DPNs
No DPN	26	6	1 (1)
DPN	1 (6)	4 (1, 5, 6, 8)	13

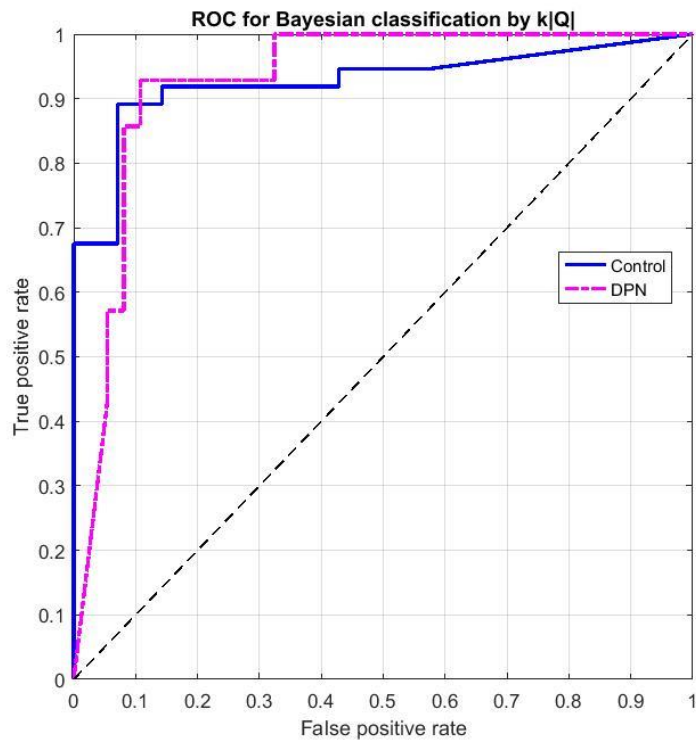
a)

Diagnosis	Controls	DPNs
No DPN	0.86	0.07
DPN	0.14	0.93

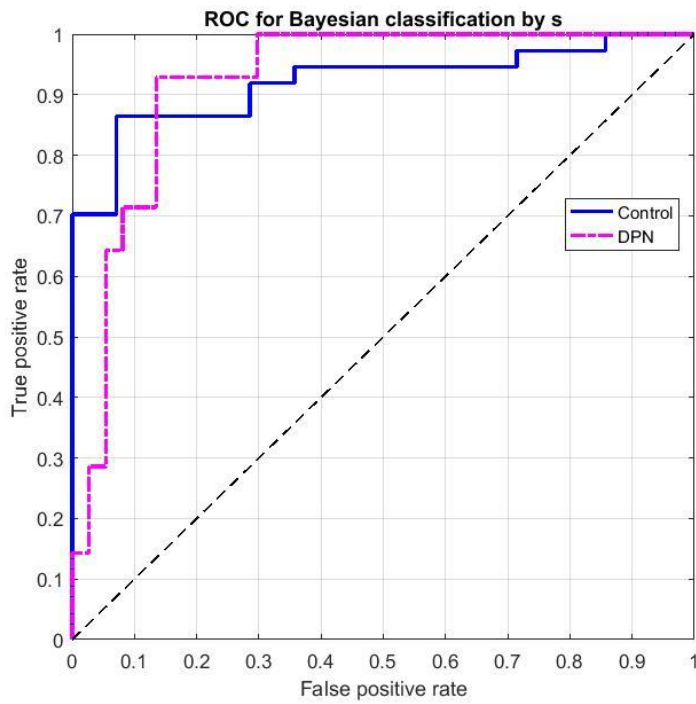
b)

Figure 6.17. $\min(s)$ Number of correctly and incorrectly classified subjects, and the indices of incorrectly classified ones a); probabilities of errors, sensitivity and specificity.

The receiving operating characteristic (ROC) curves for both parameters are presented on Figure 6.18. This curves shows true positive rate vs. false positive rate. The areas under the curves are 0.9266 and 0.9208, correspondingly (close to 1, i.e. good enough).



a)



b)

Figure 6.18. ROC curves for $\min(k|Q|)$ a), and $\min(s)$ b).

Observe similar scatter plots for both parameters for each of 4 ROIs, see Figures 6.19-6.26. If one would set the same threshold values as above, the sensitivity and specificity values will be predictable worse for each ROI than for minimum values shown above. One can see numerous false negatives as the \times symbols above the threshold at the right columns of all a)-d) subplots, for both chosen criteria. Notice that the indices of the misclassified subjects are different for different ROIs, see also Table 6.3-6.4. It happens because diabetes could affect different areas for different subjects. Therefore, we strongly recommend to use the minimum parameter values for classification to reflect the worse cases for each subject. In other words, to avoid the most serious diagnostic error: missing of DPN, a subject should be classified as a DPN one if he/she has any problematic area.

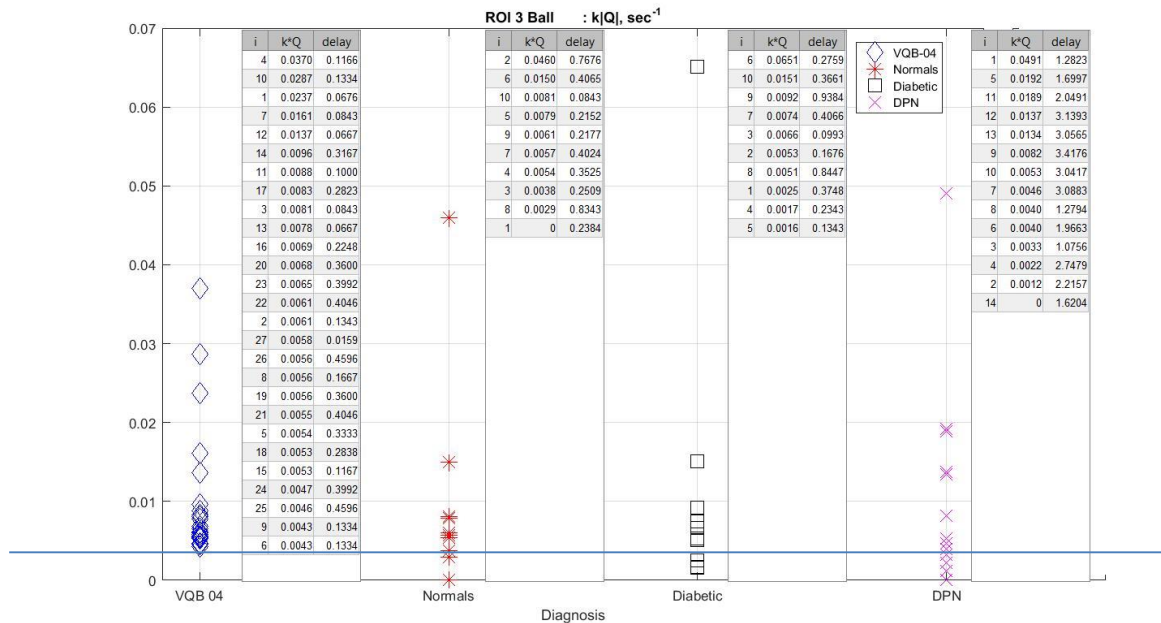


Figure 6.19. Classifier by $k|Q|$ for ball.

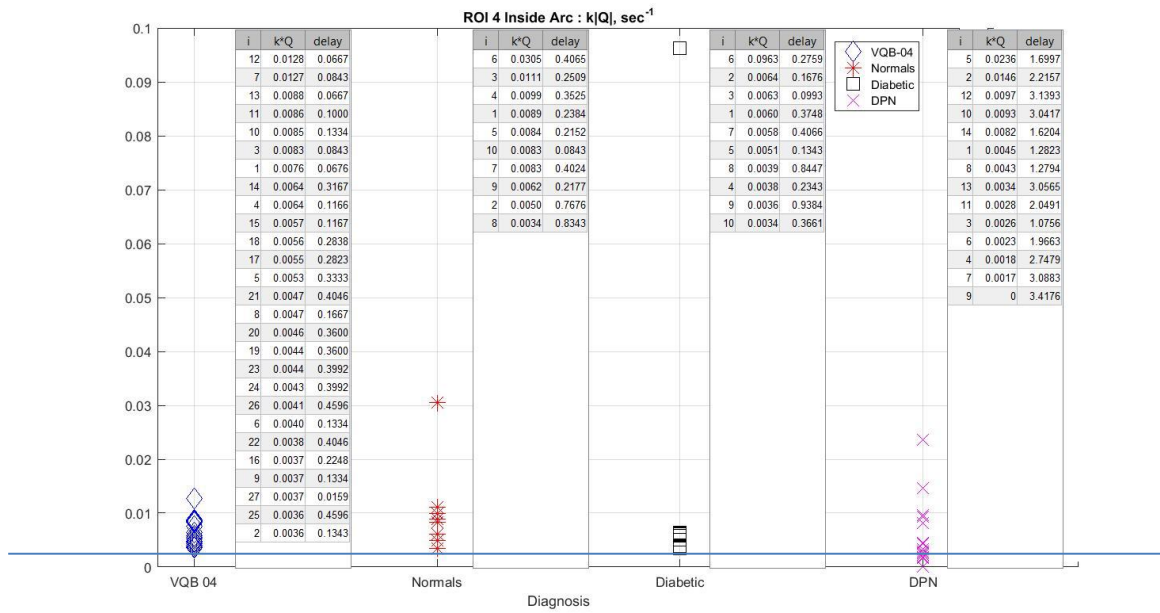


Figure 6.20. Classifier by $k|Q|$ for inside arch.

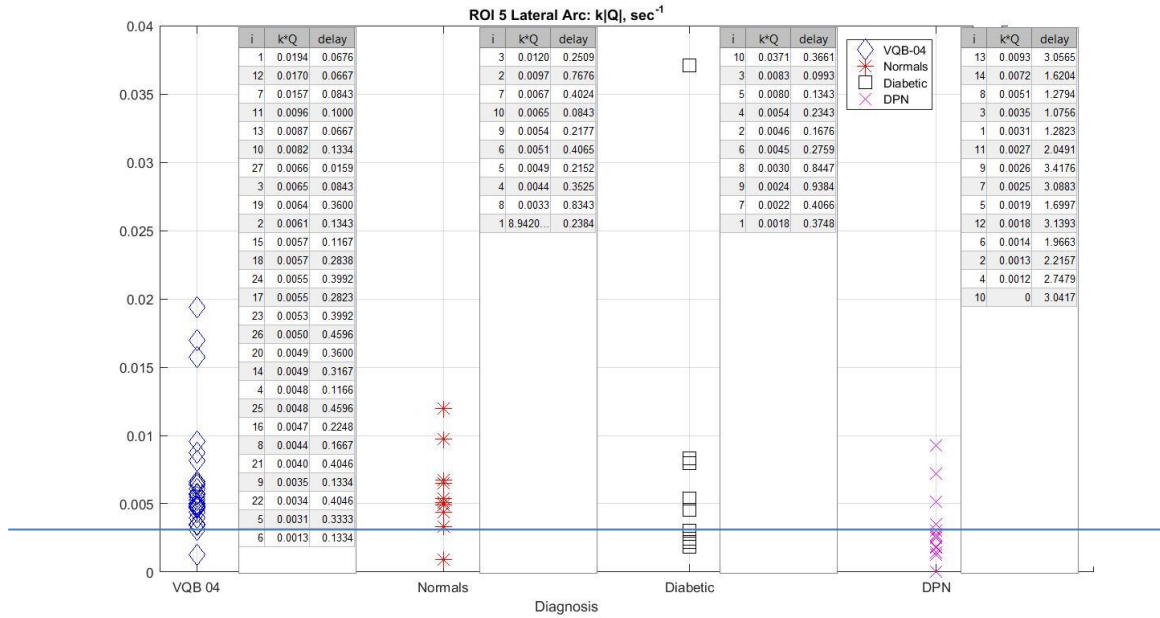


Figure 6.21. Classifier by $k|Q|$ for lateral arch.

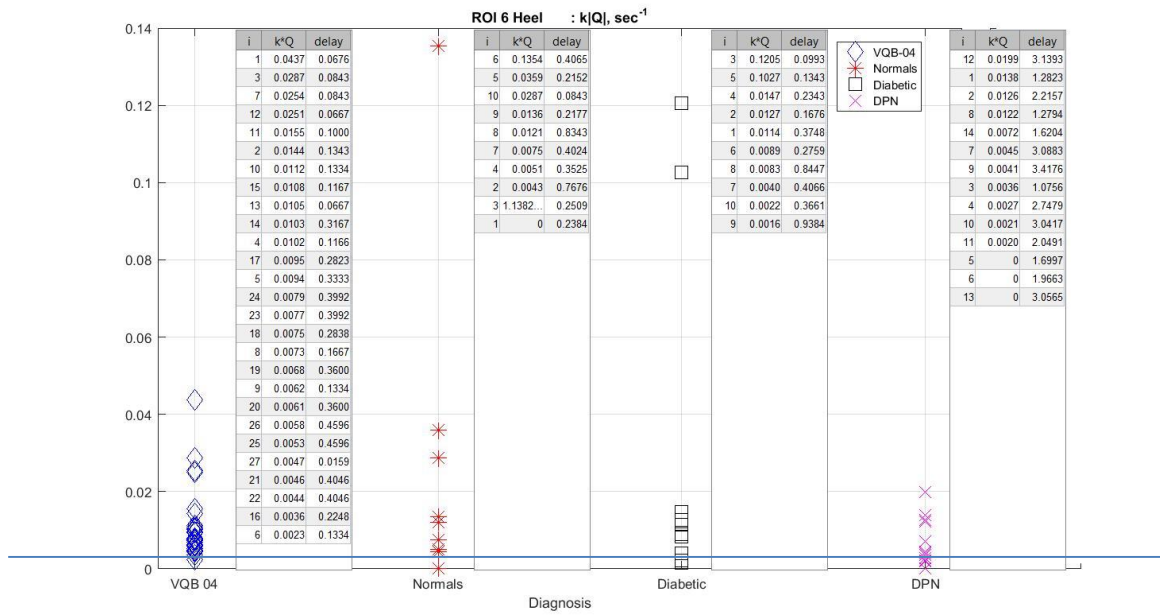


Figure 6.22. Classifier by $k|Q|$ for heel.

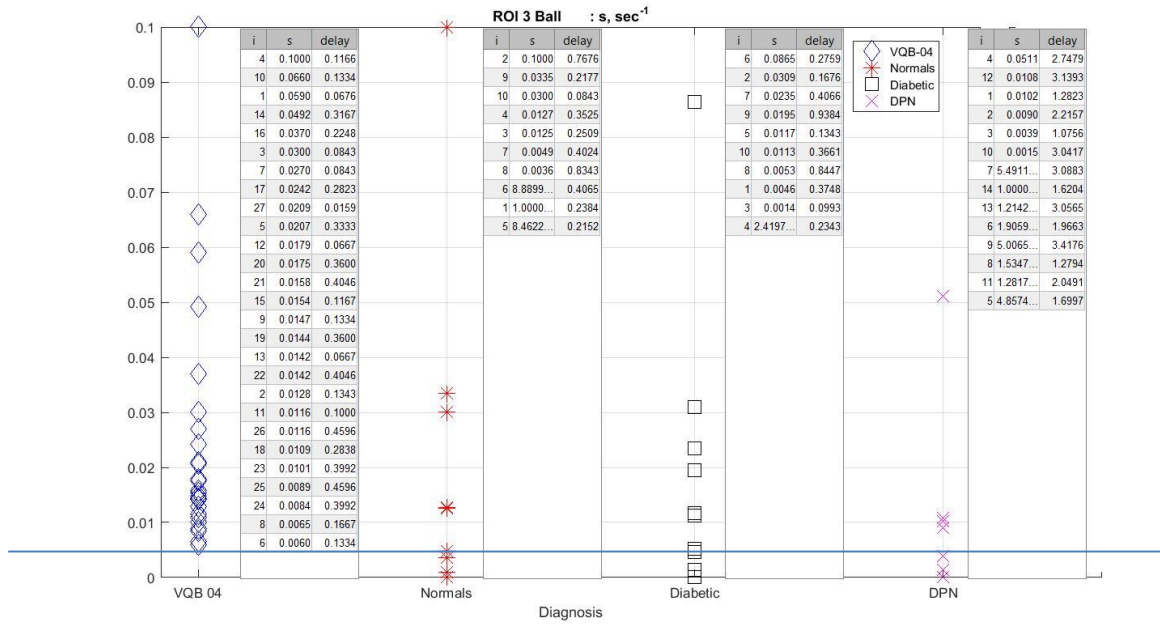


Figure 6.23. Classifier by s for ball.

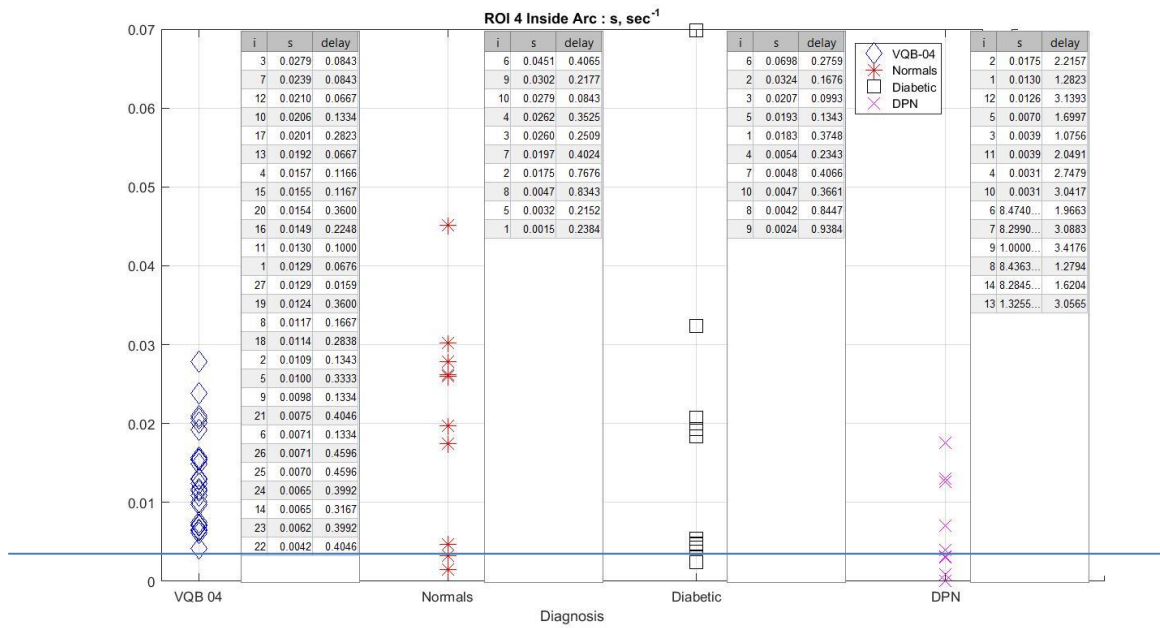


Figure 6.24. Classifier by s for inside arch.

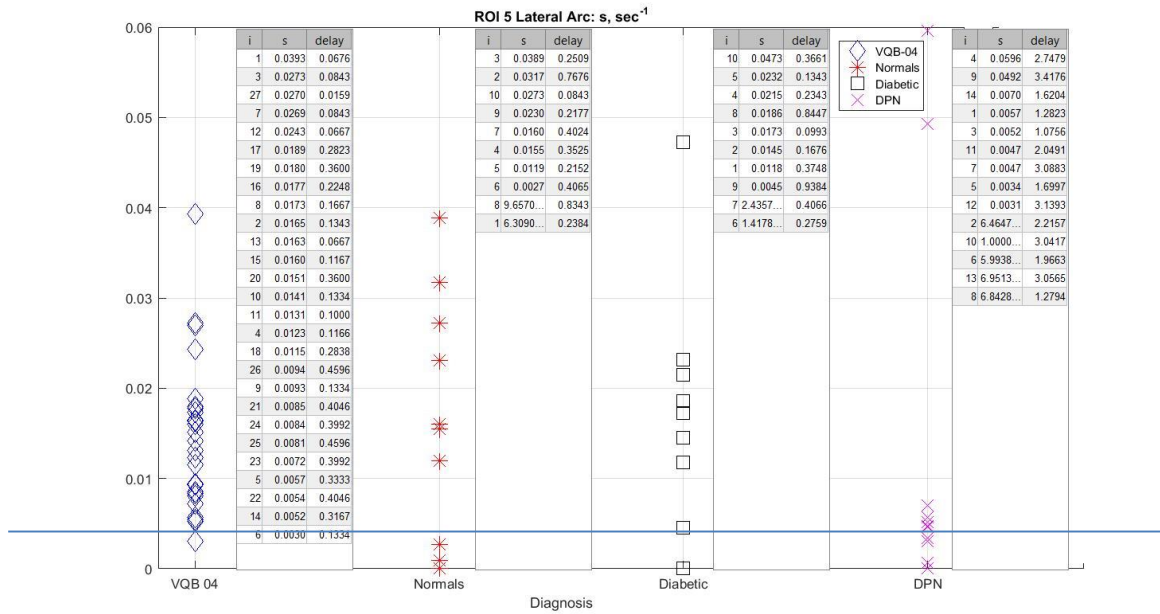


Figure 6.25. Classifier by s for lateral arch.

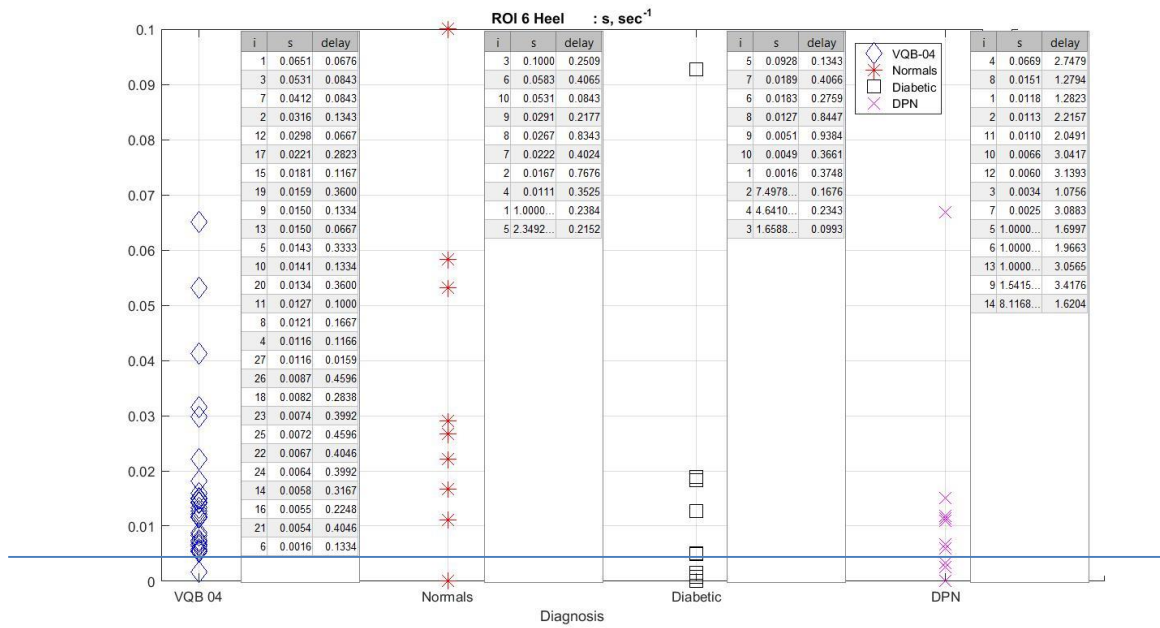


Figure 6.26. Classifier by s for heel.

ROI	Diagnosis	VQB 04	Controls	DPNs
Ball	No DPN	27	8	10 (1, 5, 6, 7, 8, 9, 10, 11, 12, 13)
	DPN	0	2 (1, 8)	4
Inside arch	No DPN	27	9	8 (1, 2, 5, 8, 10, 12, 13, 14)
	DPN	0	1 (8)	6
Lateral arch	No DPN	25	9	5 (1, 3, 8, 13, 14)
	DPN	2 (5, 6)	1 (1)	9
Heel	No DPN	26	8	8 (1, 2, 3, 7, 8, 9, 12, 14)
	DPN	1 (6)	2 (1, 3)	6
min(4 above)	No DPN	25	7	1 (8)
	DPN	2 (6, 5)	3 (1, 3, 8)	13

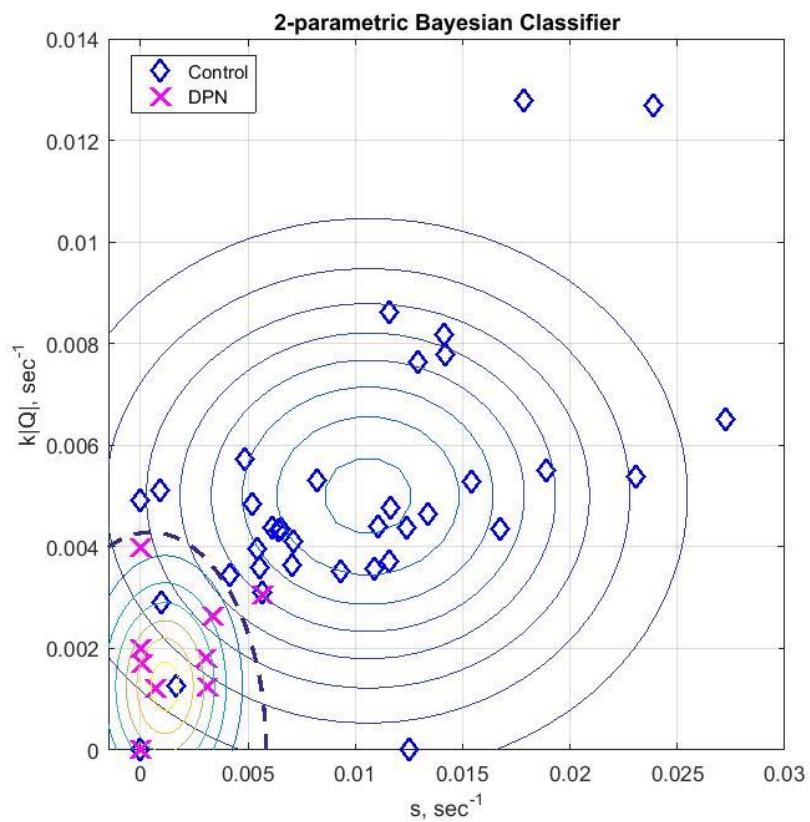
Table 6.3. $\min(k|Q|)$. ROI-specific number of correctly and incorrectly classified subjects, and the indices of incorrectly classified ones.

ROI	Diagnosis	VQB 04	Controls	DPNs
Ball	No DPN	27	6	5 (1, 2, 3, 4, 12)
	DPN	0	4 (1, 5, 6, 8)	9
Inside arch	No DPN	27	6	6 (1, 2, 3, 5, 11, 12)
	DPN	0	2 (1, 5)	8
Lateral arch	No DPN	26	7	7 (1, 3, 4, 7, 9, 11, 14)
	DPN	1 (6)	3 (1, 6, 8)	7
Heel	No DPN	26	8	7 (1, 2, 4, 8, 19, 11, 12)
	DPN	1 (6)	2 (1, 5)	7
min(4 above)	No DPN	26	6	1 (1)
	DPN	1 (6)	4 (1, 5, 6, 8)	13

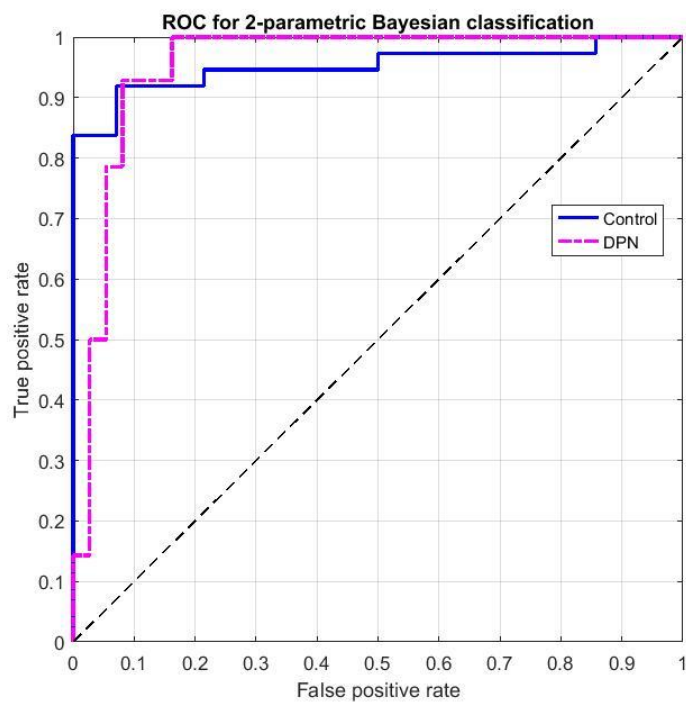
Table 6.4 *min(s)* ROI-specific number of correctly and incorrectly classified subjects, and the indices of incorrectly classified ones.

Investigating the scatter plots and corresponding tables above including the Table 6.1, it could be recommended to investigate additionally the subjects VQB_19 and VQB_13 (experiment indices 1 and 8 in the recent tables), which has been classified as DPNs by both criteria.

It is naturally to combine both successful criteria. The naïve Bayesian classifier in 2-D feature space for both *min(s)* and *min(k|Q|)* is shown at Figure 6.27. The values true and false positives and negatives and the misrecognized subjects shown on Figure 6.28. Observe increasing of sensitivity for 2-parameter classifier comparing to both 1-parameter ones. The discriminant curve of the classifier is shown as bold dashed line at Figure 6.27 a). The area under the 2-parametric ROC curve is 0.9517, i.e. some more close to 1.0 than the previous ones.



a)



b)

Figure 6.27. Classifier a) and ROC curves b) for 2-parametric classification.

Diagnosis	VQB 04	Controls	DPNs
No DPN	26	9	1 (1)
DPN	1 (6)	1 (1, 8)	13

a)

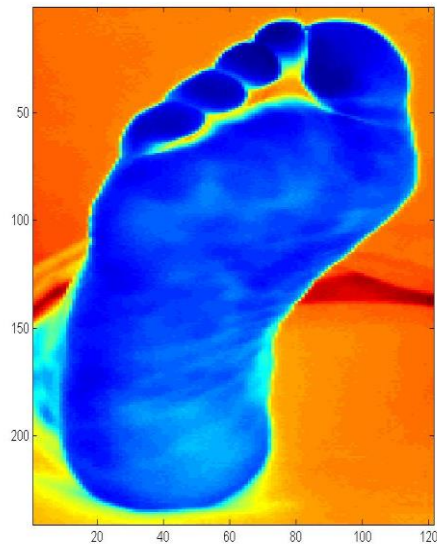
Diagnosis	Controls	DPNs
No DPN	0.92	0.07
DPN	0.08	0.93

b)

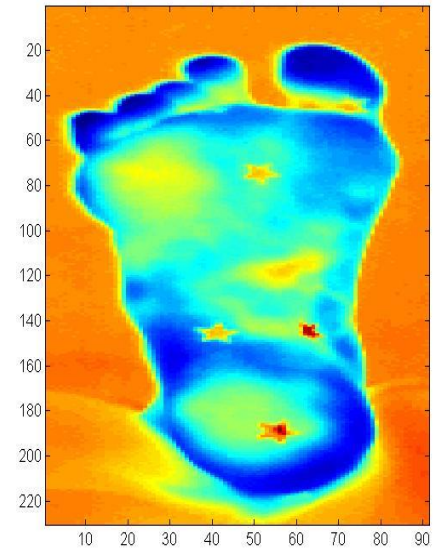
Figure 6.28. 2-parametric Bayesian classifier: number of correctly and incorrectly classified subjects, and the indices of incorrectly classified ones a); probabilities of errors, sensitivity and specificity b).

6.6 The pattern recognition approach

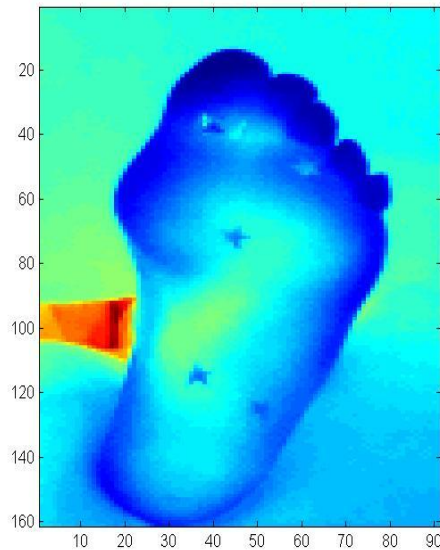
It has been observed [119] that the healthy subjects and DPN ones usually have visually different thermal foot signature. While the hot area of the control subjects is kidney-shaped, i.e. hot at the inner arch, and then smoothly and almost uniformly diffuses to the rest foot, the PN subjects often have more irregular pattern with visually recognized spots, [Figure 6.29](#). The irregular patterns are different for the different subjects.



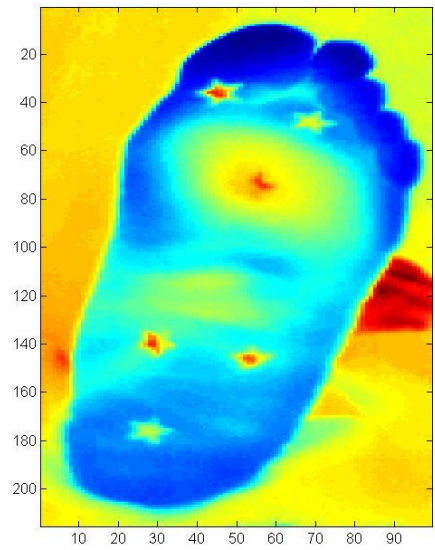
a)



b)



c)



d)

Figure 6.29. Sample thermal foot signatures. Control subjects, a), b), and the PN ones c) and d).

The metrics proposed for the classification of spotty and regular patterns is similar to the lossy compression quality. Most of the image compression algorithms use the smoothness of the images of natural origin; it is their main and principal difference to the

general compression algorithms [120] [121]. The first stage of image compression is some transform, i.e. projection from the spatial domain to the domain of the chosen transform. The great majority of the image information is concentrated into the few components in the new domain, so the lossy compression requires keeping and encoding just that few ones and ignoring the other ones. Decompression means inverse transform of the set of saved components back to the spatial domain. One can choose the transform between the traditionally applicable for image compression, for example principal component analysis (PCA), independent component analysis (ICA), Fourier transform, wavelet transform; for the last one there is a huge choice of the wavelet type [121]. The simple and natural metrics of compression quality is the measure of the nonzero (lossy compression!) difference between the initial image and the decompressed one; also there is a choice between Euclidian, Manhattan, Minkovsky distances, and other measures like standard deviation of the obtained difference, etc. It is not a big deal; all these things are really similar. The problem of choosing a right classification threshold requires a statistically significant data set.

Smooth images have better compression quality in all the domains named above. It must be noted that the compression quality depends on the edges very much. In our case the even the spots are much smoother than the foot edges, i.e. the contrast boundary between the foot and the background. Thus, instead of compressing of the whole image or the whole foot one have to make a rectangular selection inside of the investigated foot area and crop image by the selection.

For the illustration, see the compression quality for PCA. Initial fragment on the foot image has been compressed with the different number of PCA components. See the

compression quality and the difference between the initial and decompressed images [Figure 6.30](#). Top left subplots are the original images; bottom left is the result of the reconstruction by 4 first PCA components; bottom right is the difference between them; top right is the reconstruction by 30 first PCA components.

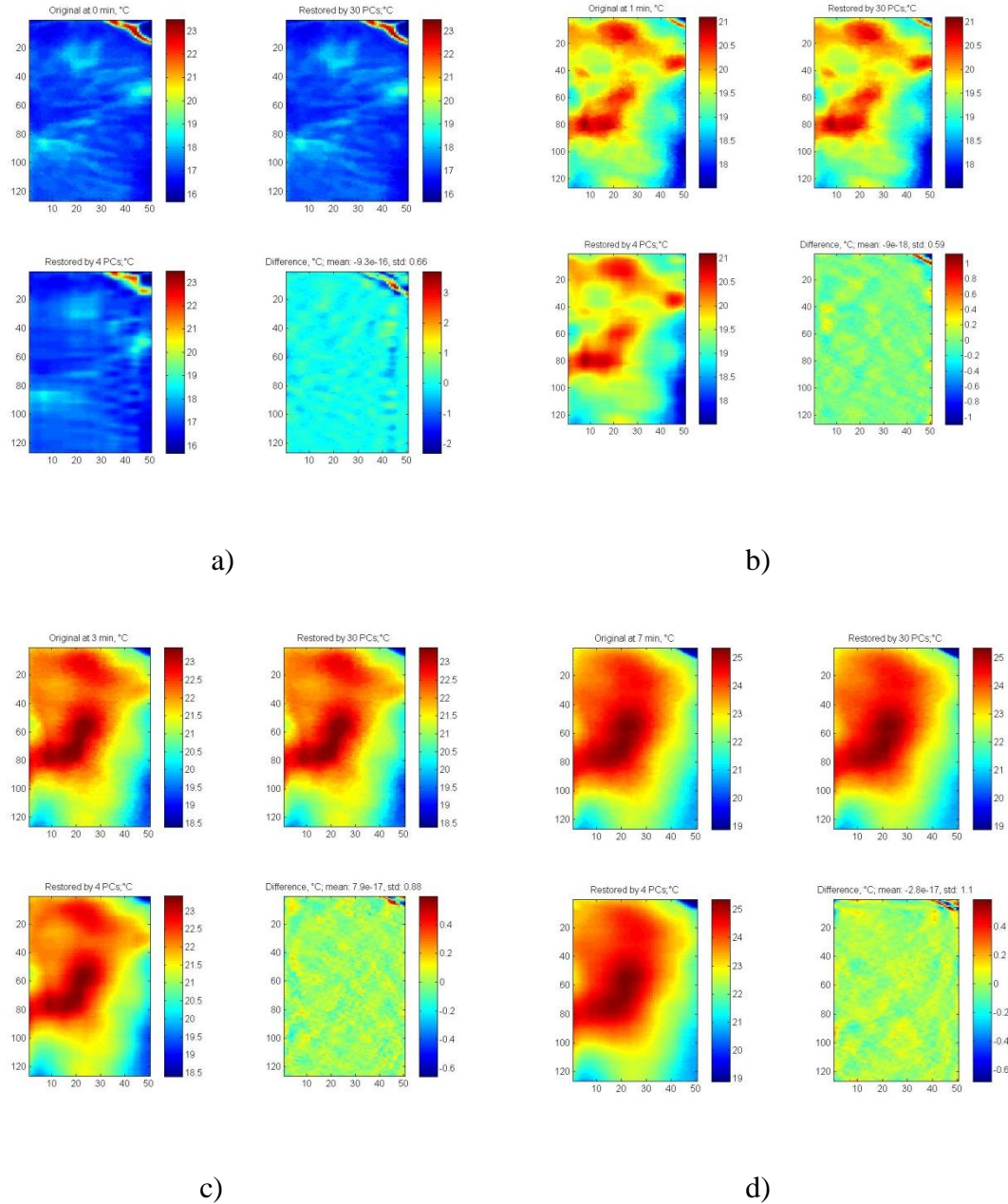


Figure 6.30. Illustration of the image compression quality at 0 a), 1 b), 3 c), and 7 min d).

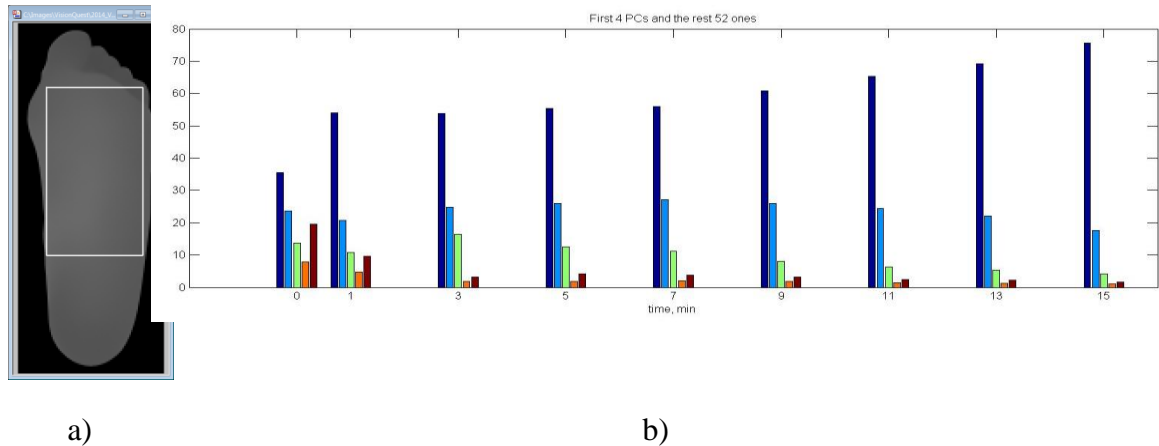


Figure 6.31. Segmented foot with the selection a), and the amount of the first 4 PCA components comparing to all others for the different frames b).

See the change of compression quality with increasing of the time, [Figure 6.31](#). Indeed, after the cold stress the thermal patterns of a foot should become smoother in time; therefore, for the later frames more information is concentrated in less number of PCA components. Let's be more specific and try the following metrics: compare the amount of all PCA components but the first 4 for the frame at 3 min. after beginning of recovery. 3 minutes has been chosen to try the method even for the subjects with the lost first 2 minutes of data; 4 PCA components chosen some intuitively; I don't claim that it is the best choice.

This method has been investigated less of all so far, that's why the robustness has been not investigated yet. Four cases at [Figure 6.29](#) reflect that it is less robust than we would like it to be: here there are two hits for two diagonal patterns and two classification errors of both kinds for the non-diagonal ones. By the way, it reflects what we see: the thermal signature of the normal subject [Figure 6.29 b\)](#) looks less smooth than thermal signature of the DPN subject [Figure 6.29 c\)](#). I don't claim by this that the method works with probability 50%. I made the pessimistic selection of the subjects now not to be disappointed later. The method definitely works better, but it is the subject for the further

investigation. The main break for this is that it requires a segmentation, registration and similar spatial orientation for all comparing frames; so far it is manual.

The potential advantages of this method are the following. Initial visual recognition is quite easy for the diagnostics, even for the observers who are not confident in the subject like the patients themselves. It can be easy explained to the doctors and to the patients; definitely more easily than the difference between the thermoregulation models of different order. The people like simple things! Just one frame required (optimistically) to initially estimate the diagnosis. Also, this approach is not sensitive to the missed frames. Additionally, it is extremely fast: it takes almost no computational time comparing to the initial data processing.

The disadvantages are the following. First, it's the overall feature, nothing ROI specific, i.e. no detail diagnostics is possible, just the integrated classification. Second, the compression quality metrics can be applied just to the inner part of the foot; the boundary effect with the foreground, which is generally different for each experiment, gives a huge error for any type of compression, even with the toes and the space between them, which are recommended to be excluded from the compression quality analysis. Third, the manual selecting of the areas inside the foot is very operator-specific. Also, it is natural to compare images decomposed to the same amount of PCAs, so the size of the selection in pixels must be the same for all comparing selections. Note that generally the feet have size on the IR image.

The classification metrics is not patient – specific; the “healthy – PN” threshold has to be chosen by analyzing of the statistically significant number of the experiments which

we don't have yet.

It looks interesting to make it applicable for the more detail diagnostics with the potential geometrical resolution compatible with the spot size. The metrics for description of the spots taking into account their geometrical position is required for this. The idea to compare this potentially interesting method with the area-specific diagnostics with high resolution (see right below) looks attractive, especially if the methods would be mutually supplementing.

6.7 The foot segmentation approach

6.7.1 Segmentation

As mentioned previously, peripheral neuropathy does not affect the diabetic foot uniformly. So far we limit the scope of the investigation to six regions of interests marked manually by reflective stars. In order to demonstrate a truly useful computer aided system for detecting peripheral neuropathy, we must be able to analyze the entire foot and identify problematic regions. To study the whole foot requires an image-processing algorithm that is capable of segmentation and registration of the foot for a given infrared video. Once the video frames are registered, the temperature recovery of each point on the feet plantar can then be extracted and analyzed using our bio-thermal model. The regions that exhibit abnormal ability to recover can then be detected. It means that the overall resolution of the system in the domain of the model parameters will be increased explosively: from just 6 ROIs to the $O(N)$, where N is upper bounded by the number of the pixels on the foot; $N \sim 2 * 10^4$ for the FLIR SC 305 camera.

Also by the foot segmentation one can dramatically reduce the registration error.

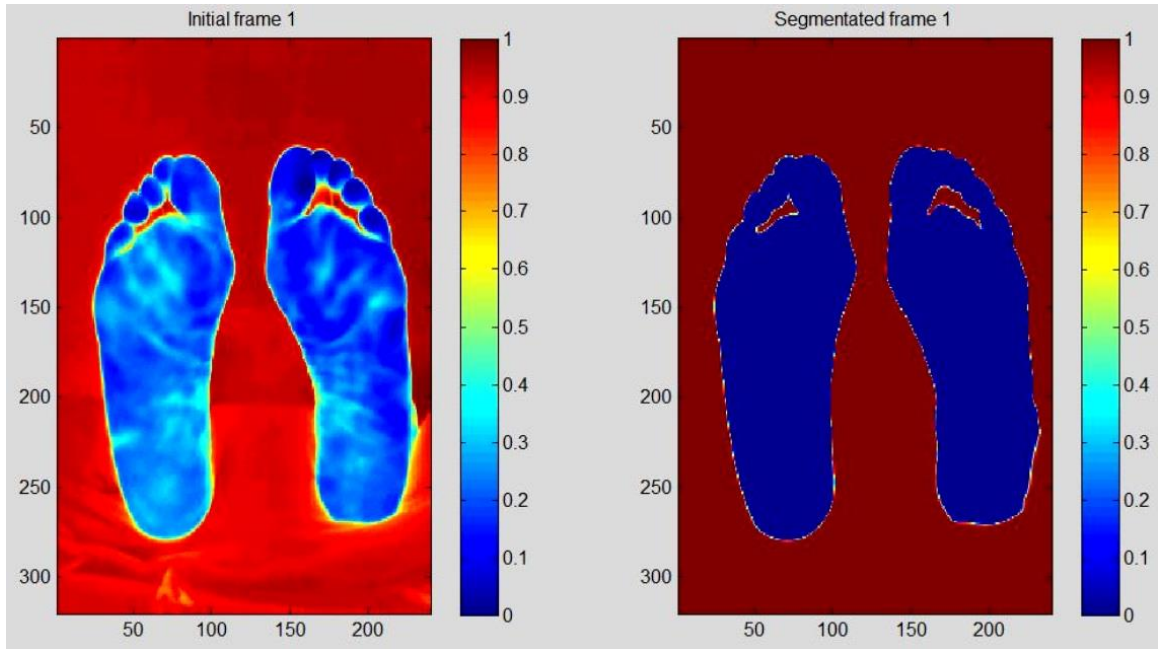
By this, the range of trustful times can be reduced, as well and the robustness of the model will be increased. Also the actual resolution in the domain of the model parameters will be increased.

Comparing to the segmentation of a digital video in a visible band, the segmentation of IR video of the thermally changing object like the recovering foot is really challenging. The main challenges are the following.

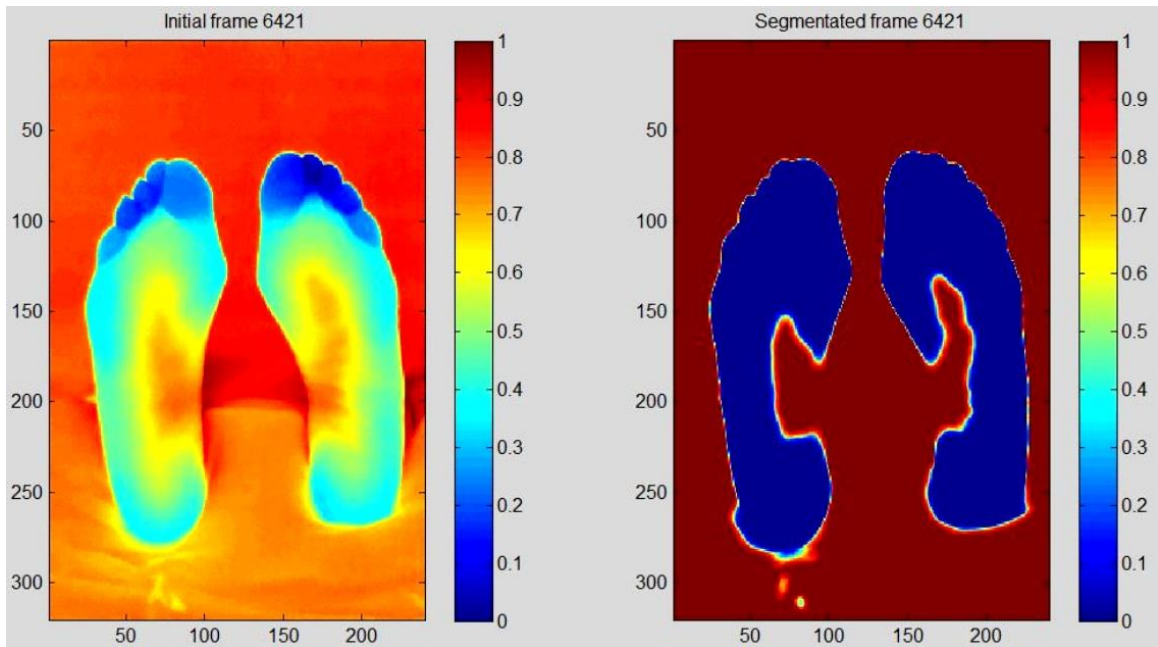
1) As the foot warms up, it creates an ever-changing contrast. More specifically, at for the most cases the beginning of the recovery process, the foot is colder than the surrounding, [Figure 6.32 a](#)). However, as the foot temperature warms up, the contrast between the foot and the surrounding decreases to a point where there is almost no contrast at all. Beyond this point, the foot becomes warmer than the surrounding. One can observe the loss of contrast in 10 minutes at the inner arch area, which usually is the warmest part of the foot in [Figure 6.32 b](#)).

2) As the foot warms up, it also warms up the surrounding. Thus, there is no thermally stable background. This effect mostly happens due to the thermal interaction between the heel and the supporting bench, especially if the subject moves the foot during the recovery; see [Figure 6.33](#).

3) Sometimes the feet and the background are not enough contrast even at the beginning; see [Figure 6.34](#). It happened mostly in winter in the relative cold room.

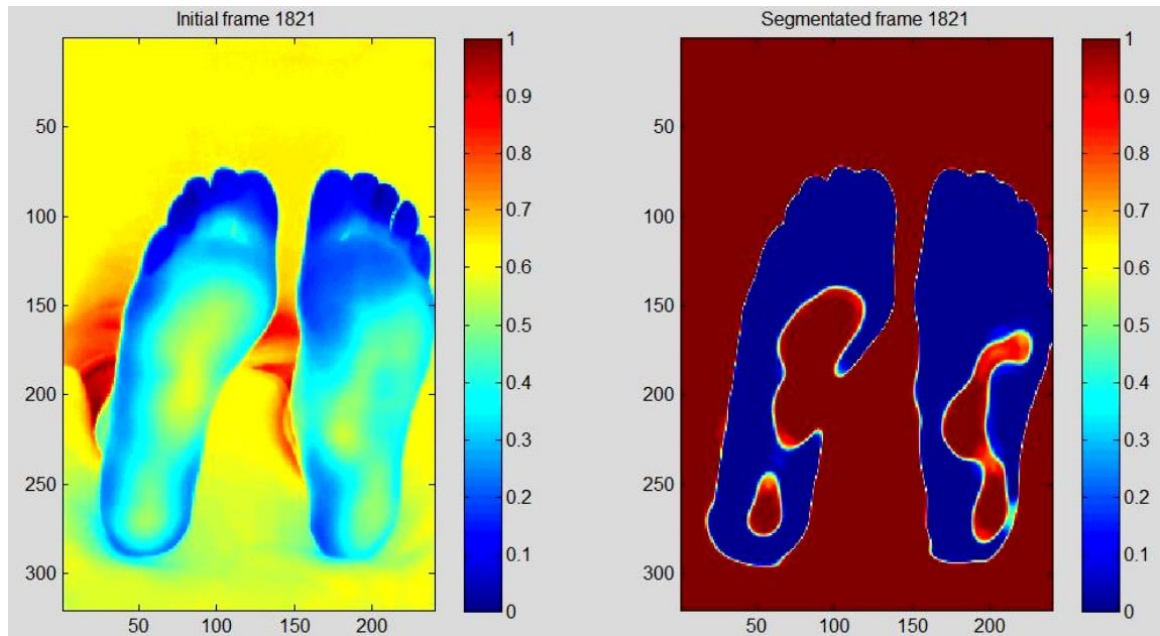


a)

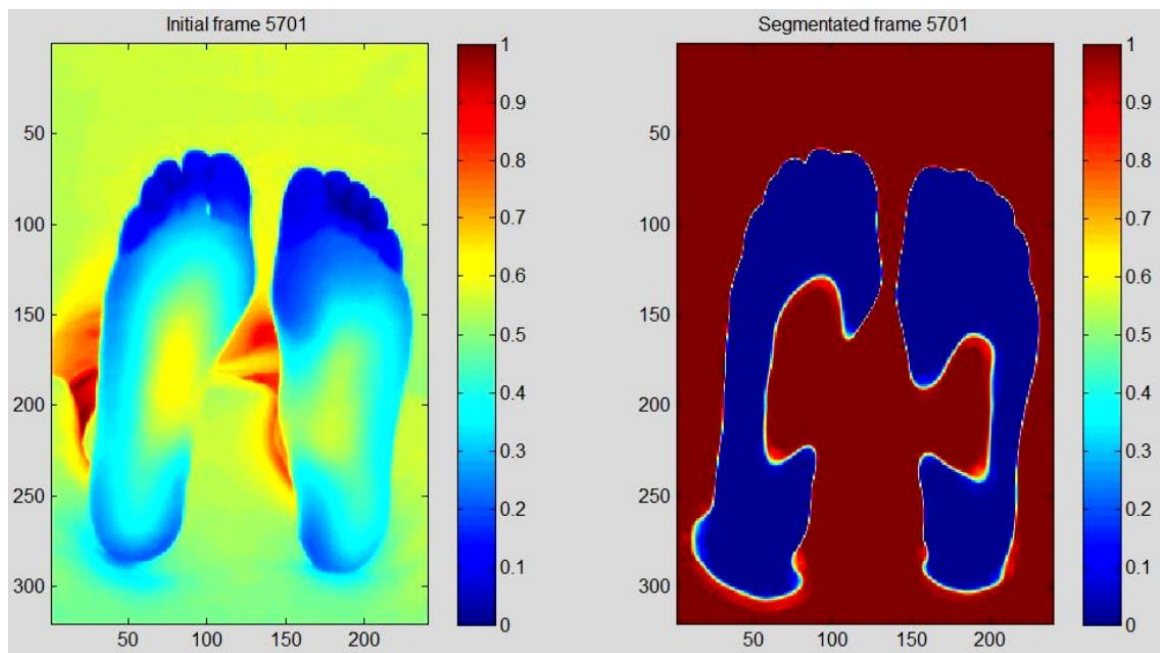


b)

Figure 6.32. Very contrast feet at the beginning a) and the loss of the contrast at the inner arch area b). Also observe some shape distortion below the heel area b).



a)



b)

Figure 6.33. Illustration of the thermal interaction between the heel and the supporting bench.

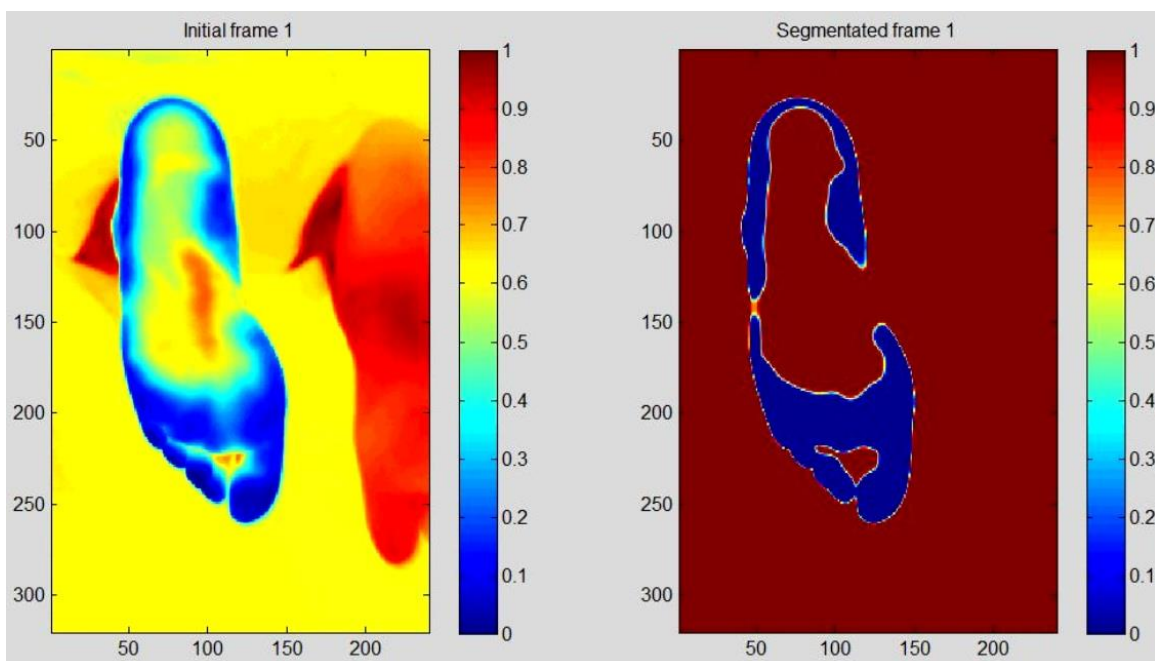


Figure 6.34. Initially low contrast foot at the very beginning of recovery.

All of these factors make it difficult to segment all the frames of the non-fixed patient's feet independently, see Figure 6.35.

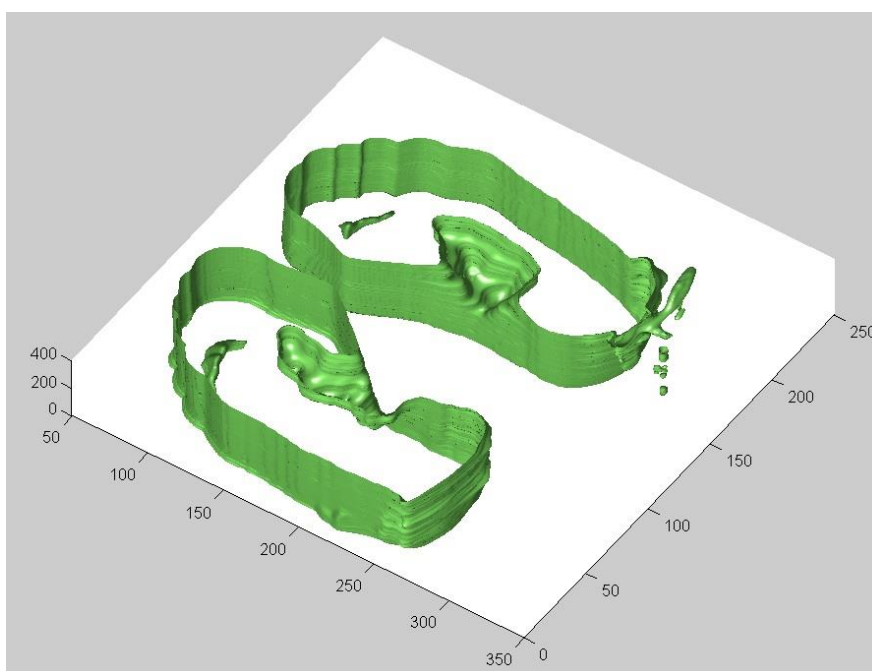


Figure 6.35. Frame-by-frame segmentation of two feet; z-axes corresponds to time. Observe the deformations described above.

To overcome these challenges, we have developed the following palliative solution.

1) Apply the continuous max-flow method [122] to segment the foot at the very beginning of the recovery by taking advantage of the high contrast created by the cold foot. We have experimented with a number of other segmentation algorithms before decided to use max-flow method because the boundary contours are not biased by the choice of computational grid. As with most segmentation algorithm, max-flow method also requires a temperature threshold. To avoid manual tuning, the temperature of the cold water for cooling, the environment temperature and the initial tissue temperature before cooling are incorporated to set up the threshold. Also the temperatures are normalized to within the given range.

2) Based on the segmentation of the first frame, we apply shape extraction to create the geometric foot model as a smooth simple polygon.

3) For the successive frames, we use numerical optimization to search for the best fit of the foot model similarly to the registration and tracking discussed in Chapter 3.4.

Let $P_0(x, y)$ be the foot model obtained from the first frame $f_0(x, y)$. Let $f(x, y)$ be the current frame to be segmented. The goal of the optimization is to find a transformation A when applied to $P_0(x, y)$ generates the foot polygon $P(x, y)$ that best “fits” the frame f .

After several trials, the affine transformation without scaling and shearing, i.e., $A =$

$\begin{bmatrix} \cos(\theta) & -\sin(\theta) & \Delta x \\ \sin(\theta) & \cos(\theta) & \Delta y \\ 0 & 0 & 1 \end{bmatrix}$ is seems to give very good result and chosen for the optimization.

Interested readers may wonder why only rotation and translation is needed. This is because: (1) there is no deformation of the foot. (2) The foot doesn't warm up uniformly. In fact, the medial (inner) arch warms up so fast and quickly blend in with the surrounding. More advanced transforms A will not only increase computation time, but introduces unnecessary deformations of the foot model that results in a bad segmentation.

(3) The patient's feet may move during the recovery period. The transformation matrix automatically accounts this motion.

6.7.2 Labeling

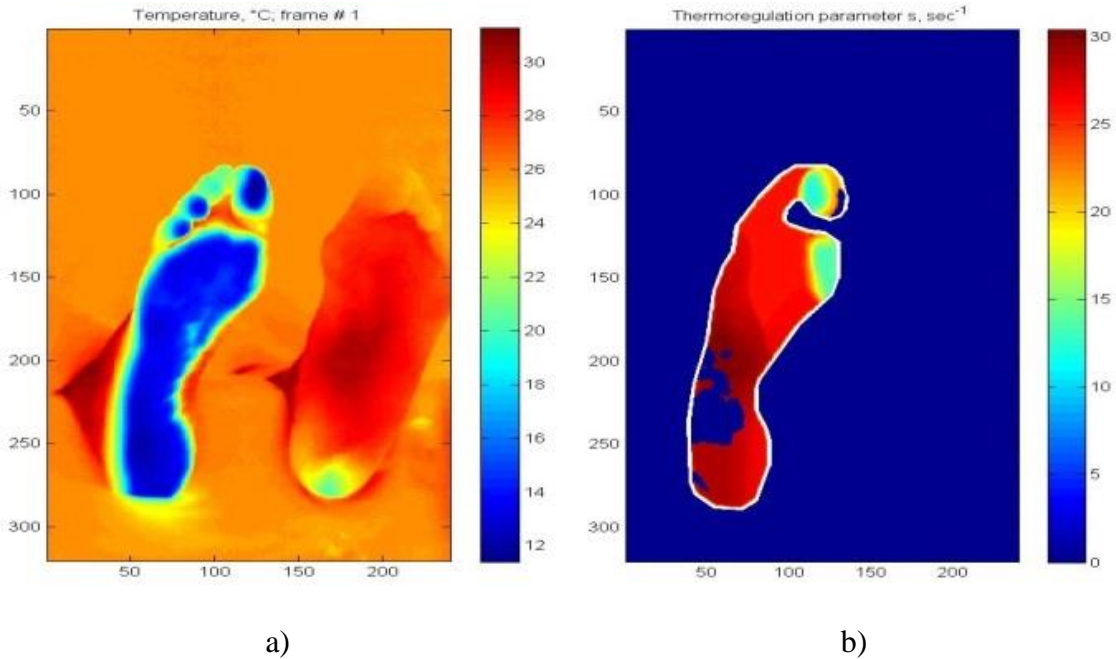
Using the segmentation of the feet at each frame, we can do more than just classify the subjects. The thermoregulation model can be applied to every point of the observed foot surface. By this, one can classify every pixel of the segmented foot. In other words, the problem areas of the foot will be visualized for the client. It gives an additional degree of freedom for the practical diagnostics comparing to the classification by 3 classes.

[Figure 6.36](#) illustrates this approach. The pictures on the left are the initial frames of the infrared video, while the pictures on the right are the result of the processing which includes registration and tracking, segmentation, modeling and the extracting of the thermoregulation model parameters at every pixel, and finally mapping of the model parameters to the segmented frame.

The geometric accuracy of the segmentation has been evaluated with manually placed star-shaped markers. Even though in our current CAD system, the reflective stars are no longer used for diagnostic purpose, but the markers do come handy for evaluating the geometric accuracy of the segmentation. The affine transform for each frame has been

applied to the initial coordinates of the geometric centers of the markers, which are then compared to their actual positions at every frame. The geometric accuracy of the segmentation is within 1-2 pixels (less than 1 mm), which is more than sufficient for the CAD system. We have also compared the automatic segmentation with manual segmentation, which also shows good agreement.

With the foot segmented and registered, we can extract the temperature change for each point on the foot plantar. By analyzing the temperature changes with our thermoregulation model as described in Chapter 4, we can obtain the map of thermoregulation at each point of the feet, see [Figure 6.36](#) b) and d). The colored areas correspond to the healthy foot areas, while the dark blue ones do not show thermoregulation (as well as the background), so they have been classified as the problematic areas.



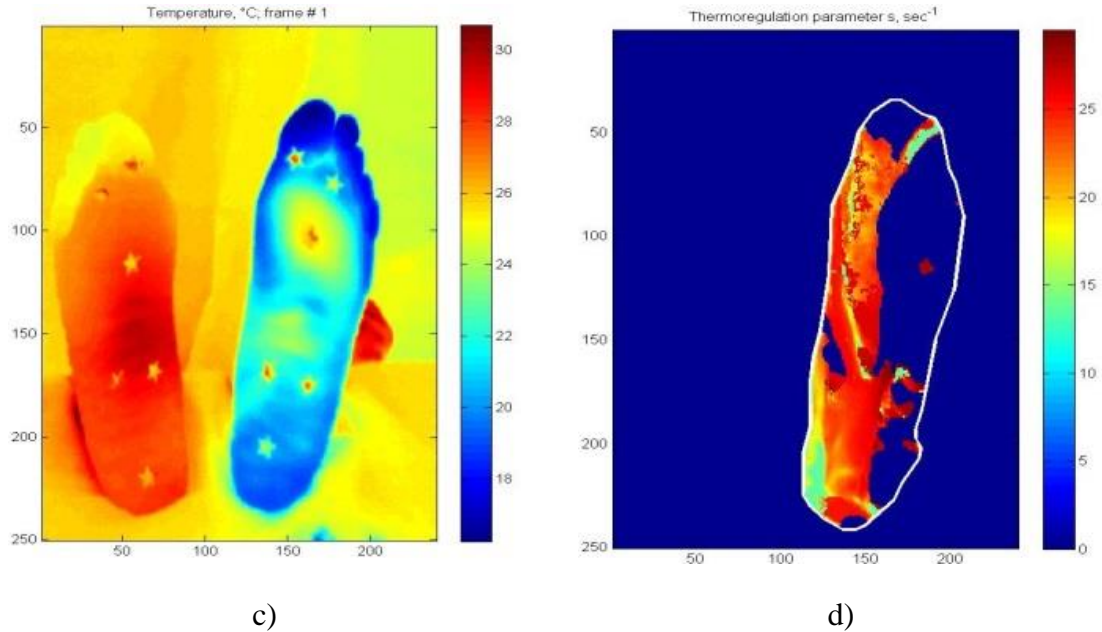


Figure 6.36. Initial frames a), c) and the mapping of the thermoregulation parameter to the whole segmented area b), and d). Here a) and correspondently b) belong to the normal subject whereas c) and d) belong to the DPN subject.

This is the illustration of the main advantage of this method: one obtains not just the integrating diagnosis but the quantitative diagnostics virtually for each point of the foot. Also the number of manually inputted parameters is reducing a lot: no need for pointing of ROIs. If we could obtain the fully automatic segmentation, the manual input can be excluded.

The principal disadvantage is the increasing of the computation times for the modeling proportionally to the number of the pixels. The computation time can be reduced by the natural parallelism of the processing, i.e. in the frames of our “1D” model every pixel is assumed independent.

The main disadvantage of the palliative approach virtually comparing with the ideal segmentation is the geometrical accuracy of the registration. With the accuracy ± 1 pixel we reduce the actual spatial resolution in the model parameters domain 4 times and,

correspondently 16 times with the accuracy ± 2 pixels. Also, the non-rigid foot transformations (like tow moves) are not taken into account.

Chapter 7 Conclusions and Future Work

The repose in being still warm.

The present thinks keep me for
tomorrow tomorrow tomorrow tomorrow.

César Vallejo, Trilce.

Osgood Fielding III: “Well, nobody's perfect”.

Robert Thoenen, Michael Logan, Some like it hot.

7.1 Conclusions

1. The protocol of the experiment has been developed.
2. The original low cost camera has been designed, calibrated and investigated.
3. The noise of the cameras has been investigated in detail; particularly the noise stationarity has been proven.
4. The robust estimation of the power α of the $1/f^{2-\alpha}$ flicker noise has been proposed.
5. The trustful numerical model of the camera noise has been developed.
6. The required preprocessing of the thermal IR video has been developed. It includes spatial and temporal filtering, synchronization, registration and tracking.
7. The original problem specific algorithms for adaptive filtering and tracking has been developed, implemented and investigated.
8. The novel model of the human body thermoregulation has been derived from the equation of the bio heat transfer.
9. The applicability of the model to the real vascular processes, i.e. vasodilation

(recovery phase) and vasoconstriction (cooling phase), has been explained from the various points of view including the control theory, physiology, and experimental data fit.

10. The robustness of the model has been investigated in detail including the robustness of the experimental data fit, and the robustness of the model parameters.
11. The uniqueness and fullness of the model has been discovered within the assumption of the bounded model complexity.
12. The requirements to the experiment to satisfy the given criteria of accuracy of the model parameters estimation has been derived using the analytical methods, processing of the data of the natural experiments, and the numerical modeling of the experiment. More specifically, they include the requirements to the camera, to the geometric accuracy of the video frames tracking, and to the time of capturing.
13. The type of error of the model parameter estimation due to the reducing of the experimental data has been shown.
14. The model of the feet thermoregulation taking into account strong interaction between the tissue and external environment has been developed.
15. The model has been verified for the recovery phase, and demonstrated the same accuracy and robustness as the simplified model.
16. The model has been applied for the modeling of cooling phase. It demonstrates better accuracy than the model without strong interaction.
17. The model has been used to bound the cold stress conditions to minimize the discomfort of tested subjects, and to estimate variance of the thermoregulation parameters.

18. The additional criterion for the more robust diagnostics of DPN based on the estimation of thermoregulation parameters and modeling error in cooling phase is proposed.
19. Different classification algorithms have been proposed and tested, including the following: classification by estimation of the thermoregulation model parameters for ROIs and for the whole foot; classification by the analysis of the lossy compression quality of the thermal signatures.

7.2 Future work

For future research, our team will work in the following two areas. First, we need to collect more patient data. Our statistical power analysis has indicated that we may need hundreds of patients in order to make stronger clinical claims. Secondly, we would like to improve the performance and accuracy of our segmentation and tracking system. It would also help if we can localize the patient's feet to reduce the impact of the motions. Thirdly, we would like to perform longer-term repeated measurements for diabetes patient. We believe thermal regulations, like the blood pressure, needs to be continuously monitored. Therefore, as part of the future research, we would like to perform monthly measurements of diabetes patients and track the progression of DPN.

REFERENCES

- [1] Boulton AJM: The diabetic foot: a global view. *Diabetes Metab Res Rev* 16:S2–S5, 2000
- [2] Palumbo P J, Melton L J. Peripheral vascular disease and diabetes. In: Harris, Hamman, editors. *Diabetes in America*. 1st ed. Washington, D.C.: US Government Printing Office; 1985.
- [3] Mancini L, Ruotolo V: The diabetic foot: epidemiology. *Rays* 22:511–523, 1997.
- [4] Palubo P, Melton L. Peripheral vascular disease and diabetes. In: Hamman R, editor. *Diabetes in America*. Washington, DC: Government Printing Office; 1985. p. 1-21
- [5] Reiber G E, Boyko E J, Smith D C. Lower extremity foot ulcers and amputations in diabetes. In: Harris, Cowie, Stern, Boyko E J, Reiber G E, Bennet, editors. *Diabetes in America*. 2nd ed. Washington, D.C.: US Government Printing Office; 1995. p. 402-428.
- [6] Ramsey S D, Newton K, Blough D, McCulloch D K, Sandhu N, Reiber G E, et al. Incidence, outcomes, and cost of foot ulcers in patients with diabetes. *Diabetes Care* 1999; 22(3):382-7.
- [7] Reiber G E, Boyko E J, Smith D C. Lower extremity foot ulcers and amputations in diabetes. In: Harris, Cowie, Stern, Boyko E J, Reiber G E, Bennet, editors. *Diabetes in America*. 2nd ed. Washington, D.C.: US Government Printing Office; 1995. p. 402-428.
- [8] Pecoraro R E, Reiber G E, Burgess E M. Pathways to diabetic limb amputation. Basis for prevention. *Diabetes Care* 1990; 13(5):513-21.

- [9] Morbach S, Lutale J, Viswanathan V, Mollenberg J, Ochs H, Rajashekar S, et al. Regional differences in risk factors and clinical presentation of diabetic foot lesions. *Diabet Med* 2004;21:91-5.
- [10] Viswanathan V, Snehalatha C, Sivagami M, Seena R, Ramachandran A. Association of limited joint mobility and high plantar pressure in diabetic foot ulceration in Asian Indians. *Diabetes Res Clin Pract* 2003;60:57-61.
- [11] American Diabetes Association Fast Facts Data and Statistics about Diabetes 2013.
- [12] Flynn M, Edmonds M, Tooke J, Watkins P. Direct measurement of capillary blood flow in the diabetic neuropathic foot. *Diabetologia* 1988; 31:652-6..
- [13] Rayman G, Williams S, Spencer P, Smaje L, Wise P, Tooke J. Impaired microvascular hyperaemic response to minor skin trauma in type 1 diabetes. *Br Med J* 1986; 292:1295-8.
- [14] Flynn M, Tooke J. Diabetic neuropathy and the microcirculation. *Diabet Med* 1995; 12:298-301.
- [15] Cobb J, Claremont D. Noninvasive measurement techniques for monitoring of microvascular function in the diabetic foot. *Int J Low Extrem Wounds* 2002;1:161-9.
- [16] Cobb JE. An in-shoe laser Doppler sensor for assessing plantar blood flow in the diabetic foot [dissertation] in DEC. Bournemouth (UK): Department of Design, Engineering, and Computing, Bournemouth University; 2000.
- [17] Belcaro G, Vasdekis S, Rulo A, Nicolaides AN. Evaluation of skin blood flow and venoarteriolar response in patients with diabetes and peripheral vascular disease by laser Doppler flowmetry. *Angiology* 1989 ;40:953-957.

- [18] Bornmyr S, Svensson H, Lilja B, Sundkvist G. Skin temperature changes and changes in skin blood flow monitored with laser Doppler flowmetry and imaging: a methodological study in normal humans. *Clin Physiol Funct Imaging* 1997;17:71-82.
- [19] Miranda-Palma B, Sosenko J, Bowker J, Mizel M, Boulton A. A comparison of the monofilament with other testing modalities for foot ulcer susceptibility. *Diabetes Res Clin Pract* 2005;70:8-12.
- [20] Singh N, Armstrong DG, Lipsky BA: Preventing foot ulcers in patients with diabetes. *JAMA* **293**:217–228, 2005.
- [21] Abbott CA, Carrington AL, Ashe H, Bath S, Every LC, Griffiths J, Hann AW, Hussain A, Jackson N, Johnson KE, Ryder CH, Torkington R, Van Ross ER, Whalley AM, Widdows P, Williamson S, Boulton AJ: The North-West Diabetes Foot Care Study: incidence of, and risk factors for, new diabetic foot ulceration in a community-based patient cohort. *Diabet Med* **19**:377–384, 2002.
- [22] Boulton A.J.M. *et al.* Comprehensive Foot Examination and Risk Assessment. A report of the Task Force of the Foot Care Interest Group of the American Diabetes Association, with endorsement by the American Association of Clinical Endocrinologists. *Diabetes Care*, 31(8), 1679-1685, 2008.
- [23] Young MJ, Breddy JL, Veves A, Boulton AJ: The prediction of diabetic neuropathic foot ulceration using vibration perception thresholds: a prospective study. *Diabetes Care* 17:557–560, 1994.
- [24] Armstrong DG, Lavery LA, Vela SA, Quebedeaux TL, Fleischli JG: Choosing a practical screening instrument to identify patients at risk for diabetic foot ulceration. *Arch Intern Med* 158:289–292, 1998.

- [25] Stess RM, Sisney PC, Moss KM, Graf PM, Louie KS, Gooding GA, et al., "Use of liquid crystal thermography in the evaluation of the diabetic foot," *Diabetes Care* 1986; 9:267-72.
- [26] Benbow S, Chan A, Bowsher D, Williams G, Macfarlane I. "The prediction of diabetic neuropathic plantar foot ulceration by liquid-crystal contact thermography," *Diabetes Care* 1994; 17:835-9.
- [27] Fisher A, Gilula L, McEnery K. Imaging of the diabetic foot. In: Bowker J, Pfeifer M, editors. *The diabetic foot*. St. Louis (MO): Mosby; 2001. p. 333-54.
- [28] Aspres N, Egerton I, Lim A, Shumack S. Imaging the skin. *Aust J Dermatol* 2003; 44:19-27.
- [29] Minamishima C, Kuwaki K, Shirota E, Matsuzaki M, Yamashita K, Kamatani M, et al. Thermal imaging properties of toes after walking stress test in diabetic patients. *Rinsho Byori* 2005; 53:118-22.
- [30] Armstrong D, Lavery L, Wunderlich R, Boulton A. Skin temperatures as a one-time screening tool do not predict future diabetic foot complications. *J Am Podiatr Med Assoc* 2003;93:443-7.
- [31] Armstrong D, Sangalang M, Jolley D, Maben F, Kimbriel H, Nixon B, et al. Cooling the foot to prevent diabetic foot wounds. *J Am Podiatr Med Assoc* 2005;95:103-7.
- [32] National Institute of Neurological Disorders and Stroke (NINDS). Peripheral neuropathy fact sheet. Jan 10, 2008b. Accessed Jan 29, 2008. Available at URL address:
http://www.ninds.nih.gov/disorders/peripheralneuropathy/detail_peripheralneuropathy.htm.

- [33] Perkins B.A., Olaleye D., Zinman B., et al. Simple screening tests for peripheral neuropathy in the diabetes clinic. *Diabetes Care* 2001; 24:250-6.
- [34] Boulton AJ, Armstrong DG, Albert SF, et al. Comprehensive foot examination and risk assessment: a report of the task force of the foot care interest group of the American Diabetes Association, with endorsement by the American Association of Clinical Endocrinologists. *Diabetes Care* 2008, vol. 31, no. 8, 1679-1685.
- [35] D. Chirtea, Current concepts in vascular therapies. 2013 Mid-Atlantic Conference, April 26 - 27, 2013, Hilton Virginia Beach Oceanfront.
- [36] FLIR A325sc datasheet. (C) FLIR Systems, Inc.
- [37] Specification for Thermopilearrays HTPA8x8, HTPA16x16 and HTPA32x31, rev. 12. Heimann Sensor GMBH. (c) 2010
http://www.heimannsensor.com/Heimann_Sensor_complete_Datasheet_HTPA_Rev1_2.pdf
- [38] Greg Iven, Viktor Chekh, Shuang Luan, Abdullah Mueen, Peter Soliz, Wenyao Xu, Mark Burge. Non-contact Sensation Screening of Diabetic Foot using Low Cost Infrared Sensors, 27th International Symposium on Computer-Based Medical Systems (CBMS'14), New York, May 2014.
- [39] Melexis NV. MLX90614 family. Single and Dual Zone. Infrared Thermometer in TO-39. 2012. www.melexis.com
- [40] <http://en.wikipedia.org/wiki/Eye>
- [41] http://en.wikipedia.org/wiki/Stefan-Boltzmann_law
- [42] Miniature Blackbody Calibration Source Portable Design and High Temperature Range. <http://www.omega.com/pptst/BB703.html>

- [43] W.A. Lenz. Characterization of Noise in Uncooled IR Bolometer Arrays. MIT, Department of Electrical Engineering and Computer Science, 1998
- [44] Lawrence M. Ward, Priscilla E. Greenwood. The mathematical genesis of the phenomenon called “1/f noise”, 6 June 2010-12 June 2010
- [45] Jørgensen, Bent (1997). The theory of dispersion models. Chapman & Hall. ISBN 978-0412997112.
- [46] FLIR systems. Infrared Imaging. Digital Imaging Systems, lecture 15, January 2009.
- [47] W. Schottky, "Ueber spontane Stromswankungen in vershiedenen Elektrizitatsleitern" ("On Spontaneous Current Fluctuations in Various Electric Conductors"), Ann. d. Phys., v. 57, 1918, p. 541-67
- [48] J.B. Johnson, The Schottky effect in low frequency circuits, Phys. Rev. 26 (1925) 71-85.
- [49] W. Schottky, Small-Shot Effect and Flicker Effect, Phys. Rev. 28 (1926) 74
- [50] B. Mandelbrot. Some noises with 1/f spectrum, a bridge between direct current and white noise. IEEE Trans. Inf. Theory, 13(2):289–298, 1967.
- [51] Markus Niemann, Holger Kantz, and Eli Barkai. Fluctuations of 1/f Noise and the Low-Frequency Cutoff Paradox. Phys. Rev. Lett. 110, 140603 – Published 2 April 2013
- [52] <http://www.nslj-genetics.org/wli/1fnoise/index.html>
- [53] M. Stoisiek and D. Wolf. Recent investigations on the stationarity of 1/f noise. J. Appl. Phys. 47, 362 (1976); doi: 10.1063/1.322327
- [54] F.N. Hooge, P.A. Bobbert. On the correlation function of 1/f noise. Physica B 239 (1997) pp. 223-230.

- [55] S. Watanabe. Multi-Lorentzian model and $1/f$ noise spectra. *Journal of the Korean Physical Society*, Vol. 46, No. 3, March 2005, pp. 646-650.
- [56] M. Li and S. C. Lim, “A rigorous derivation of power spectrum of fractional Gaussian noise,” *Fluctuation and Noise Letters*, vol. 6, no. 4, pp. C33–C36, 2006.
- [57] B. B. Mandelbrot and J. W. van Ness, “Fractional Brownian motions, fractional noises and applications,” *SIAM Review*, vol. 10, pp. 422–437, 1968.
- [58] P. Flandrin, “On the spectrum of fractional Brownian motions,” *IEEE Transactions on Information Theory*, vol. 35, no. 1, pp. 197–199, 1989.
- [59] M. Li, “Fractal time series—a tutorial review,” *Mathematical Problems in Engineering*, vol. 2010, Article ID 157264, 26 pages, 2010.
- [60] S. V. Muniandy and S. C. Lim, “Modeling of locally self-similar processes using multifractional Brownian motion of Riemann-Liouville type,” *Physical Review E*, vol. 63, no. 4, Article ID 046104, 7 pages, 2001.
- [61] V. M. Sithi and S. C. Lim, “On the spectra of Riemann-Liouville fractional Brownian motion,” *Journal of Physics A*, vol. 28, no. 11, pp. 2995–3003, 1995.
- [62] S. C. Lim and S. V. Muniandy, “On some possible generalizations of fractional Brownian motion,” *Physics Letters A*, vol. 266, no. 2-3, pp. 140–145, 2000.
- [63] J. P. Chiles and P. Delfiner, *Geostatistics, Modeling Spatial Uncertainty*, Wiley Series in Probability and Statistics: Applied Probability and Statistics, JohnWiley & Sons, New York, NY, USA, 1999.
- [64] M. Li, C. Cattani, and S. Y. Chen, “Viewing sea level by a one-dimensional random function with long memory,” *Mathematical Problems in Engineering*, vol. 2011, Article ID 654284, 13 pages, 2011.

- [65] M. Li and W. Zhao. On 1/f Noise. Review article. Hindawi Publishing Corporation Mathematical Problems in Engineering Volume 2012, Article ID 673648, 23 pages
- [66] J. Dudas, M. L. La Haye, J. Leung, G.H. Chapman, "A Fault-Tolerant Active Pixel Sensor to Correct In-Field Hot-pixel Defects", Proc. IEEE Int. Symposium on Defect and Fault Tolerance, pp 526-534, Rome, Italy, Oct. 2007.
- [67] Haykin, Simon (2002). Adaptive Filter Theory. Prentice Hall. ISBN 0-13-048434-2.
- [68] Hayes, Monson H., Statistical Digital Signal Processing and Modeling, John Wiley & Sons, 1996, 493–552.
- [69] Richard Szeliski, Image Alignment and Stitching: A Tutorial. Foundations and Trends in Computer Graphics and Computer Vision, 2:1-104, 2006.
- [70] Croft, H. T.; Falconer, K. J.; and Guy, R. K. Unsolved Problems in Geometry. New York: Springer-Verlag, p. 3, 1991.
- [71] Jan Kybic. Elastic Image Registration using Parametric Deformation Models. Thèse #2439 (2001) École Polytechnique Fédérale De Lausanne.
- [72] Gonzales, Rafael C. and Richard E. Woods. Digital Image Processing. 2nd ed. Englewood Cliffs, NJ: Prentice-Hall, 2002.
- [73] Kendall, David G. "A Survey of the Statistical Theory of Shape." Statistical Science. Vol. 4, No. 2, 1989, pp. 87–99.
- [74] L.G. Brown. A Survey of Image Registration Techniques. ACM Computing Surveys, Vol. 24, No. 4, December 1992
- [75] Rodgers JL and Nicewander WA. Thirteen ways to look at the correlation coefficient. The American Statistician, 42(1):59–66, February 1988.

- [76] Brown LG. A survey of image registration techniques. *ACM Computing Surveys*. 24(4), 325-376, 1992.
- [77] Louis C. Burmeister, (1993) “Convective Heat Transfer”, 2nd ed. Publisher Wiley-Interscience, p 107.
- [78] T. Strutz: Data Fitting and Uncertainty (A practical introduction to weighted least squares and beyond). Vieweg+Teubner, ISBN 978-3-8348-1022-9.
- [79] Durkee JW Jr et al. Exact solutions to the multiregion time-dependent bioheat equation. I: Solution development. 1990 *Phys. Med. Biol.* 35 847. DOI= 10.1088/0031-9155/35/7/004
- [80] Frank P. Incropera, David P. DeWitt, Theodore L. Bergman and Adrienne S. Lavine. *Introduction to Heat Transfer*. Willey, 2006, 5th ed.
- [81] Krane, Kenneth (2012). *Modern Physics*. John Wiley & Sons.
- [82] Guyton, A.C., & Hall, J.E. (2006), *Textbook of Medical Physiology* (11th ed.), Philadelphia: Elsevier Saunders, p. 890
- [83] Chato J.C. Heat transfer to blood vessels. *J Biomech Eng.* 1980; 102(2):110-8.
- [84] T.L. Bergman, A.S. Lavine, F.P. Incropera, D.P. DeWitt. *Fundamentals of Heat and Mass Transfer*. Wiley, 7th Edition, April 2011.
- [85] Richard H. Pletcher, John C. Tannehill and Dale Anderson. *Computational Fluid Mechanics and Heat Transfer*, Third Edition. September 11, 2012 by Taylor & Francis.
- [86] V.I. Arnold. *Ordinary Differential Equations*. Springer, 1992 - Mathematics.
- [87] P. J. Antsaklis, A.N. Michel. *Linear systems*. Birkhauser, 2006.
- [88] Kalmykov G.F. *Radioautomatics*. Moscow, “Visshaja shkola”, 1990 (in Russian).

- [89] K.J. Astrom, Control Systems Design. (c) K.J. Astrom, 2002
- [90] J. Doyle, B. Francis, A. Tannenbaum. Feedback Control Theory. (c) Macmillan Publishing Co., 1990.
- [91] J.W. Polderman, J.C. Willems. Introduction to the Mathematical Theory of Systems and Control.
- [92] Steel, R. G. D. and Torrie, J. H., Principles and Procedures of Statistics, New York: McGraw-Hill.
- [93] A.L. Nilsson. Blood Flow, Temperature, and Heat Loss of Skin Exposed to Local Radiative and Convective Cooling. *Journal of Investigative Dermatology* (1987) 88, 586–593; doi:10.1111/1523-1747.ep12470202
- [94] J. Oberle, M. Elam, T. Karlsson and B. Gunnar Wallin. Temperature-dependent interaction between vasoconstrictor and vasodilator mechanisms in human skin. *Acta Physiol. Scand.* 1988, 132, p. 459-469.
- [95] Lewis T (1930) Observations upon the reactions of vessels of the human skin to cold. *Heart* 15: 1031-1034.
- [96] Li X, Tokura H & Midorikawa T (1994) The effects of two different types of clothing on seasonal cold acclimation of thermophysiological responses. *Int J Biometeorol* 38: 40-43.
- [97] Livingstone SD (1976) Changes in cold-induced vasodilatation during Arctic exercises. *J Appl Physiol* 40(3): 455-457.

- [98] Shin-ichi Sawada, Shunichi ARAKI and Kazuhito Yokoyama. Changes in Cold-induced Vasodilatation, Pain and Cold Sensation in Fingers Caused by Repeated Finger Cooling in a Cool Environment. *Industrial Health* 2000, 38, 79–86
- [99] Catherine O'Brien. Reproducibility of the cold-induced vasodilation response in the human finger. *J Appl Physiol* 98: 1334–1340, 2005.
- [100] Therapeutic Modalities: The Art and Science (Second Edition), by K.L. Knight, D.O. Draper. Lippincott Williams & Wilkins, 2008.
- [101] Knight K.L. Bryan K.S, Halvorsen J.M. Circulatory changes in the forearm during and after cold pack application and immersion in 1 degree C, 5 degrees C, and 15 degrees C water. *Int. J. Sports. Med.*, 1981, 4:1-2.
- [102] Knight K.L., Aquino J., Johannes S.M., Urban C.D. A re-examination of Lewis' cold-induced vasodilatation-In the finger and ankle. *Athl. Train.*·1980;15:248-250.
- [103] Clarke R.S.J., Hellon R.F., Lind A.R.: Vascular reactions of the human forearm to cold. *Clin. Sci.* 17:165-179, 1958. In: Knight K.L., Londeree B.R.: Comparison of blood flow in the ankle of uninjured subjects during therapeutic applications of heat, cold, and exercise. *Med. Sci. Sports. Exer.* 12(1):76-80. 1980.
- [104] M.A. Kowal. Review of Physiological Effects of Cryotherapy. *The Journal of Orthopaedic and Sports Physical Therapy*, September/October 1983. p. 66-73.
- [105] Blake A.S., Petley G.W., Deakin C.D. Effects of changes in packed cell volume on the specific heat capacity of blood: implications for studies measuring heat exchange in extracorporeal circuits. *Br J Anaesth.* 2000 Jan;84(1):28-32.

- [106] Handbook of Mathematical Functions: with Formulas, Graphs, and Mathematical Tables. Abramowitz M. (Editor), Stegun I. (Editor). Dover Books on Mathematics – June 1, 1965.
- [107] U. Blahak. Efficient approximation of the incomplete gamma function for use in cloud model applications. *Geosci. Model Dev.*, 3, 329–336, 2010.
- [108] M.T. Boudjelkha and M.A. Chaudhry. On the Approximation of a Generalized Incomplete Gamma Function Arising in Heat Conduction Problems. *Journal of Mathematical Analysis and Applications* 248, 509-519, 2000.
- [109] Introduction to MatLab. R.L. Spencer. Department of Physics and Astronomy, Brigham Young University, 2000.
- [110] Numerical Recipes in C: The Art of Scientific Computing / Edition 2 by W.H. Press, B.P. Flannery, S.A. Teukolsky, W.T. Vetterling. Cambridge University Press, 1992.
- [111] Chistova, E.A. (2001), in Hazewinkel, Michiel, *Encyclopedia of Mathematics*, Springer, ISBN 978-1-55608-010-4
- [112] G. Zamora, V. Chekh, M. R. Burge, E. S. Barriga, S. Luan, P. Heintz, A. Edwards, E. McGrew, P. Soliz, “Optical Measurements of Microvascular Circulatory Function in the Foot for Detection of Peripheral Neuropathy,” *Photonics West, BIOS*, San Francisco, CA, January 2012.
- [113] M. Burge, K. Colleran, S. Barriga, V. Chekh, E. McGrew, A. Edwards, P. Soliz
"Dynamic infrared imaging to quantitate thermoregulatory function in individuals with

- diabetes for preclinical detection of peripheral neuropathy," ADA, 73rd Scientific Sessions, June 21-25, 2013, Chicago, IL.
- [114] S. Barriga, V. Chekh, C. Carranza, M. Burge, A. Edwards, E. McGrew, G. Zamorra, P. Soliz. "Computational Basis for Risk Stratification of Peripheral Neuropathy from Thermal Imaging," 34th Annual IEEE Engineering in Medicine and Biology Society, EMBC, San Diego, August 28-September 1, 2012
- [115] P. Soliz, V. Chekh, M. Burge, A. Edwards, E. McGrew, G. Zamora, and S. Barriga "Computational Basis for Risk Stratification of Peripheral Neuropathy from Thermal Imaging," The 25th IEEE International Symposium on Computer-Based Medical Systems, Rome, Italy, June 2012.
- [116] V. Chekh, P. Soliz, S. Barriga, E. McGrew, M. Burge, S. Luan. Computer Aided Diagnosis of Diabetic Peripheral Neuropathy. Accepted to SPIE Medical Images, 15-20 February 2014, San Diego, CA.
- [117] V. Chekh, P. Soliz, S. Barriga, E. McGrew, N. Kanagy, S. Luan. Novel model of thermoregulation based on control theory used to evaluate peripheral microvascular function. Experimental Biology 2013
- [118] Chekh V, Luan S, Burge M, Carranza C, Soliz P, McGrew E and Barriga S. Quantitative Early Detection of Diabetic Foot. ACM-BCB 2013, Washington DC, 2013.
- [119] M. Burge, G. Zamora, E. S. Barriga, V. Chekh, S. Luan, P. Heintz, A. Edwards, E. McGrew and P. Soliz "Thermal Functional Imaging for Screening of Peripheral Neuropathy in the Diabetic Foot," American Diabetes Association, 72nd Scientific Session, Philadelphia, PA, June 8-12, 2012.

- [120] M. Rabbani, P. W. Jones. Digital Image Compression Techniques. SPIE Press, Jan 1, 1991 - Technology & Engineering - 221 pages
- [121] K.K. Shukla, M.V. Prasad. Lossy Image Compression. Domain Decomposition-Based Algorithms. SpringerBriefs in Computer Science, 2011, ISBN: 978-1-4471-2217-3.
- [122] Yuan J, Bae E, and Tai XC. A study on continuous max-flow and min-cut approaches. In CVPR, USA, San Francisco, 2010.
- [123] V. Chekh, P. Soliz, S. Barriga, E. McGrew, N. Kanagy, S. Luan. Novel model of thermoregulation based on control theory used to evaluate peripheral microvascular function. Experimental Biology 2013.